LOW-FREQUENCY ELECTROMAGNETIC FIELDS FOR THE DETECTION OF BURIED OBJECTS IN THE SHALLOW SUB-SURFACE

By

JAMES DORIAN CROSS

A thesis submitted to the
University of Birmingham
for the degree of
DOCTOR OF PHILOSOPHY

School of Electronic, Electrical and Computer Engineering
College of Engineering and Physical Sciences
The University of Birmingham

February 2014

ABSTRACT

This thesis explores the application of low-frequency electromagnetic fields, which may be excited within a buried pipe, for the detection of underground utilities.

Low-cost network analyser technology, which can be applied to field-measurements of the relative-permittivity of soil, is evaluated. These technologies are compared to laboratory-grade alternatives whose cost prohibits their use for field work. Methodologies for the measurement of the relative-permittivity of soil are discussed with reference to the low-cost technology, including use of a novel coaxial cavity which incorporates a step-discontinuity. It is shown that there is potential for use of low-cost network analysers in measuring relative-permittivity, but that further research is required to formulate a complete methodology.

The propagation of electromagnetic waves in layered media is discussed. The recent literature relating to this field is extensively reviewed, with several errors and omissions highlighted. A new calculation is presented which allows the calculation of the electromagnetic field due to a vertical electric dipole in a four-layered medium. Example results, including an approximation of a leaking pipe, are presented.

Finally, two sets of field trials are reviewed. The first field trials looked to observe waves propagating with low-velocity in the ground, by measuring the phase change along an array of receiving probes. Waves, propagating with low-velocity, were observed. However, direction of arrival measurements were not achievable due to a combination of signal-to-noise ratio, and the expected phase change at the observed propagation-velocity, across an array of realistic size.

The second field trials measured low-frequency electromagnetic fields, excited within a buried pipe, which were used to detect the location of the pipe with good correspondence to the ground truth. Furthermore, comparison with a ground-penetrating radar survey indicated that some anomalous results in the low-frequency electromagnetic survey corresponded to shallow targets detected using ground-penetrating radar.

ACKNOWLEDGEMENTS

I am grateful to a number of people, without whom this work would not have been possible.

I would like to thank my supervisor Phil Atkins, for his support and guidance, talents for acquiring funding, and endless enthusiasm for the unknown. But mostly for the good humour with which he viewed those stumbling blocks met along the way.

I am grateful to Andrew Foo, Giulio Curioni, Andrew Thomas, and Alan Islas-Cital for help and encouragement, and the colleagues on the MTU team whose ongoing work continues the project that funded this PhD. My thanks also go to those staff in the School of Engineering who supported this work; Warren Hay for manufacturing my increasingly eclectic requests, Alan Yates, Mary Winkles, and Clare Walsh for help at various times.

I would also like to thank my friends and family for their encouragement, and occasional endurance, throughout this process, especially Adam Mummery-Smith for accommodating me throughout the final year of this work.

I am most indebted to Mel, for her support, insight, and belief.

To those I have not mentioned, and to those who will be disappointed that the solution did not require a rucksack bearing fish, boldly exploring the world's buried pipes, I apologise.

TABLE OF CONTENTS

LIST OF ILLUSTRATIONS

LIST OF TABLES

CHAPTER 1: INTRODUCTION

1.1 BACKGROUND

Street works are estimated to cost the economy of the United Kingdom £7 billion per annum (McMahon *et al.*, 2005). The work described by this thesis is a part of the Mapping the Underworld project which researched new technologies for detection and assessment of buried utilities, as part of the effort to manage the impact of street works (Metje *et al.*, 2007; Metje *et al.*, 2011).

Low-frequency electromagnetic technologies have been used for a number of years, for agriculture (Corwin and Lesch, 2003) and archaeology (Imai *et al.*, 1987; Tabbagh *et al.*, 1993), amongst others (Samouëlian *et al.*, 2005). Primarily, low-frequency electromagnetic surveying has taken the form of resistivity surveys which may be used to estimate three dimensional maps of the subsurface (Earl, 1998; Samouëlian *et al.*, 2005). However, in recent years capacitive sensors have been used, in place of buried probes, to reduce the time required to take resistivity measurements (Kuras *et al.*, 2006; Foo *et al.*, 2010).

There are some key advantages to using low-frequency electromagnetic fields in this context: Attenuation of an electromagnetic plane-wave is approximately proportional to $1/\sqrt{frequency}$, giving increased potential for signal detection at low-frequencies (Jackson, 1975, pp. 222-225). Furthermore, velocity of propagation is predicted to be much reduced at low frequencies, either due to increased effect of conductivity (Paul and Nasar, 1987) or due to exceptionally high relative-permittivity recorded in soils at low-frequencies (Smith-Rose, 1934; Lesmes and Morgan, 2001; Cosenza *et al.*, 2008). The predicted reduction in velocity would allow measurable phase change across distances of the order of metres, making estimations of velocity and direction of arrival feasible with small arrays of receiving probes.

In order to facilitate the measurement of soil properties at low-frequencies, technology to measure the frequency-dependent relative-permittivity of soils is reviewed. At present, time-

domain reflectometry is widely used for the measurement of the permittivity and conductivity of soils (Topp and Davis, 1985; Robinson *et al.*, 2003). However, time-domain reflectometry is limited in the frequency-domain, particularly at low-frequencies (Friel and Or, 1999), making alternative technologies appealing. Recent advances have resulted in the marketing of new, low-cost, network analysers with the potential to measure the dielectric properties of soils in the frequency-domain (Baier, 2009). The use of this technology to support low-frequency, in-situ, measurements is explored in this thesis.

Modelling the propagation of electromagnetic signals in soil is exceptionally difficult; soil is a fundamentally inhomogeneous, non-stationary, dispersive medium which may also be non-linear and anisotropic (Santamarina *et al.*, 2001). One method of modelling soil is to assume a layered medium, in which different components are assumed to be homogenous within the defined layers (King and Sandler, 1994; Wait, 1998a; Li, 2009). This thesis derives a model for the propagation of electromagnetic fields in a four-layered medium which is shown to be useful for approximating a leaking pipe, or buried utility.

The possibility of exciting low-frequency electromagnetic fields from within a buried pipe has not received research attention. Signal excitation from within a pipe is beginning to emerge in the fields of ground penetrating radar (Pennock and Redfern, 2007) and acoustics (Muggleton and Brennan, 2008). The advantages of these techniques are significant: By placing the excitation at the pipe, all of the transmitted energy originates at the buried object; the propagation distance is reduced, approximately by a factor of two; and the interfering, direct propagation path - which dominates when the transmitter and receiver are collocated on the surface - is removed. Chapters 5 and 6 present the results of field trials which evaluated the efficacy of in-pipe excitation for locating buried-utilities, both in terms of phase and magnitude measurements.

1.2 CONTRIBUTION

The contributions to knowledge developed through this thesis are summarised here:

- The use of low-cost vector network analysers for the in-situ measurements of the relative-permittivity of soils is evaluated in detail. This technology could facilitate the acquisition of frequency-domain measurements in demanding environments, which are currently unavailable.
- A new calculation for the electromagnetic field due to a vertical electric dipole in a four-layered media is presented. This represents an extension to a significant body of previous research (King and Sandler, 1994; Zhang and Pan, 2002; Zhang *et al.*, 2004; Xu *et al.*, 2008). This analysis can be used for scenarios including a leaking pipe or large voids in the subsurface.
- The previous research calculating the electromagnetic field in layered media is critiqued, and a number of errors and omissions are discussed, which will greatly increase the ability of future researchers to utilise earlier methods.
- The possibility of waves propagating with low-velocities in the shallow subsurface, due to unusual dielectric properties of soil at low-frequencies, in assessed. A number of publications have noted very large relative-permittivity of soil at frequencies between 10^{-3} and 10^{1} Hz (Smith-Rose, 1934; Lesmes and Morgan, 2001; Cosenza *et al.*, 2008). The feasibility of using direction of arrival measurements to detect buried utilities, given the low velocity of propagation, predicted at low frequencies, is explored.
- In-pipe excitation for the detection of buried utilities is a relatively new area of study, that has not utilised low-frequency electromagnetic fields (Cook, 1999; Muggleton and Brennan, 2008). Results are presented which show that a low-frequency signal, excited within a buried pipe, may be detected at the surface, and used to locate the pipe.

1.3 STRUCTURE OF THE THESIS

This work is presented in seven chapters: Chapter 1 sets out the context of the research, the original contributions to knowledge and the structure of the remaining thesis.

Chapter 2 provides a review of the relevant literature, including appropriate background information to enable soil scientists to readily access the techniques familiar to electrical engineers and vice-versa. Chapter 3 presents a study of low-cost network analyser technologies for improving the in-situ measurement of the electromagnetic properties of soil. This includes a comparison of the specifications of the low-cost technologies, as well as showing comparative measurement results and calculated soil properties. The methodology presented includes the use of a novel coaxial cavity, incorporating a step-discontinuity. Chapter 4 derives a novel, quasi-analytical, technique for calculating the electromagnetic field in four-layered media due to a vertical electric dipole. The four-layered scenario enables the modelling of leaking utilities and large voids in the sub-surface.

Chapter 5 presents field-work which aimed to establish the feasibility of locating buried assets using direction of arrival estimation. Direction of arrival estimation requires slow propagating waves so that reliable phase measurements may be made with equipment which is not prohibitively large. The theoretical prediction of slowly propagating waves due to the unique dielectric properties at low-frequencies is presented. Chapter 6 describes a second set of field-trials which measured the response at the surface due to a field excited from within a buried pipe. This method has not been previously attempted and good initial results are presented showing the location of the buried-pipe with good agreement to its known position.

Finally, chapter 7 draws conclusions from the thesis and suggests further avenues for research. Four appendices are included to support the remainder of the thesis, and are referenced in the text.

CHAPTER 2: LITERATURE REVIEW

2.1 INTRODUCTION

That street works have large cost to the economy has been known for many years; McMahon *et al.* (2005) calculated the cost to the UK economy as £7 billion per annum. Whilst estimates vary, in part due to the fragmented nature of the calculation (Gilchrist and Allouche, 2005), it is agreed that significant social benefit could be achieved through changes to the practices surrounding street works (Read, 2004; Goodwin, 2005). This thesis investigates the use of low-frequency electromagnetic technology to detect buried utilities, to increase the effectiveness, and reduce the associated disruption, of street works.

This chapter discusses the relevant research relating to the electromagnetic (EM) properties of soil, which must be considered before the evaluation of any method to explore the subsurface using EM fields. Methods available for examining the EM properties of soil are then covered, considering both time-domain and frequency-domain methods. The signal processing techniques which support the work in the remainder of this thesis are then described. A survey of current methods for detecting utilities in the shallow-subsurface is then given, followed by a more extensive survey of relevant low-frequency methods, forming a summary of the state-of-the-art.

Improved detection of utilities forms part of a range of options for achieving a reduction in the impact of street works. These include increased use of trenchless technology; seen as increasingly important given public pressure to reduce highway congestion (Erez and Samuel, 2002; Najafi and Kim, 2004; Jung and Sinha, 2007). However, for trenchless technologies to be effective the operator must be able to accurately control the position of the drilling equipment and have full knowledge of the subsurface, neither is trivial (Royal *et al.*, 2010; Manacorda *et al.*, 2010). Other high-level strategies may reduce the social cost of street-works, or provide greater incentive for utility providers to do so. These include timing of the works to coincide with low traffic demand (Ober-Sundermeier and Zackor, 2001), the use of multi-utility tunnels when installing new utilities (Hunt *et al.*, 2012), the prohibition of open trench work (Read, 2004), or

environmental taxes (Metje *et al.*, 2011) even though the administration of such policies is not always practical (Ogus, 1999).

2.2 ELECTROMAGNETIC PROPERTIES OF MATERIALS

Any sensor which measures the electromagnetic (EM) field present in a medium relies on knowledge of the EM properties of the medium to draw conclusions about the source or transmission of the signal. This section defines the EM – or dielectric – properties of materials and their impact on propagating signals. These are then applied to soils with a discussion about the parameters affecting the dielectric properties of soils.

2.2.1 Definition of Electromagnetic Properties

The movement of charge within a medium is described by Maxwell's equations, which are given in differential form below (Santamarina *et al.*, 2001, pp. 313 - 315):

$$\nabla \cdot \boldsymbol{E} = \frac{1}{\varepsilon}\rho_v^{<free>} \tag{2-1}$$

$$\nabla \cdot \boldsymbol{H} = 0 \tag{2-2}$$

$$\nabla \times \boldsymbol{E} = -\mu\frac{d\boldsymbol{H}}{dt} \tag{2-3}$$

$$\nabla \times \boldsymbol{H} = \sigma\boldsymbol{E} + \varepsilon\frac{d\boldsymbol{E}}{dt} \tag{2-4}$$

$$\boldsymbol{D} = \varepsilon\boldsymbol{E} \tag{2-5}$$

$$\boldsymbol{B} = \mu\boldsymbol{H} \tag{2-6}$$

$$\boldsymbol{J} = \sigma\boldsymbol{E} \tag{2-7}$$

Where $\boldsymbol{E}$ is the electric-field strength, $\boldsymbol{D}$ is the electric flux density, $\boldsymbol{H}$ is the magnetic-field strength, $\boldsymbol{B}$ is the magnetic flux density, $\boldsymbol{J}$ is the current density, ε is the permittivity, μ is the magnetic permeability, σ is the electrical conductivity, and $\rho_v^{<free>}$ is the volumetric, free charge density.

It would be impossible to cite all the developments which have stemmed from these equations, but a large number of texts have been published which present an overview of the subject, see Jackson (1975), King and Smith (1981), or Elliott (1995). The properties which govern the

behaviour of electromagnetic phenomena in materials are permittivity, permeability, polarization and conductivity. These properties are very well known, but are included for those readers more familiar with soils than electromagnetics:

2.2.1.1 Permittivity (ε)

Permittivity is defined as "the ability of a material to store electrical potential energy under the influence of an electric field" (Merriam-Webster, 2013b). The constitutive relations quoted with Maxwell's equations, (2-5) - (2-7), show that the permittivity of a material determines the electric-field resulting from the electric-flux, or charge density.

Permittivity has units of Farads per meter, but is usually quoted as a dimensionless ratio to the permittivity of free-space ($\varepsilon_0 = 8.8541 \times 10^{-12} Fm^{-1}$) known as relative-permittivity (ε_r)

However, permittivity is only a real number in a lossless medium. If a medium is lossy, that is that a wave loses energy as it propagates through the medium, the permittivity of that material will be complex, with the complex permittivity given as (Paul and Nasar, 1987, p. 305):

$$\varepsilon^* = \varepsilon_r' + \frac{\sigma}{j\omega} \tag{2-8}$$

Where ω is the angular permittivity ($rads\ sec^{-1}$), and j is $\sqrt{-1}$.

2.2.1.2 Conductivity (σ)

Conductivity is familiar as the material parameter which relates current flow to applied voltage in an electric circuit, having units of Siemens per meter (Sm^{-1}). When considering electromagnetic fields, conductivity causes loss due to the current density induced by an electric-field in the presence of a material with non-zero conductivity (2-7).

2.2.1.3 Permeability (μ)

Fundamentally, the permeability of a material, μ, is the constant of proportionality between magnetic flux density and the magnetic field, equivalent to permittivity in the context of an

electric-field (Jackson, 1975, p. 153). The permeability of a material determines how much energy is stored in the magnetic field due to a movement of charge.

The unit of permeability is Henries per meter. However, as with permittivity, it is usual to quote the permeability of a material (μ_r) relative to that of free space ($\mu_0 = 1.2566 \times 10^{-6} Hm^{-1}$). A non-magnetic material has a relative permeability of 1. Soils are commonly assumed to be non-magnetic (Santamarina *et al.*, 2001), and the assumption that $\mu_r = 1$ is used throughout this work.

2.2.1.4 Polarization (χ)

Polarization may be electric or magnetic, but in this work electric polarization is considered. Santamarina *et al.* (2001) state that "polarization arises when a force displaces a charge from some equilibrium position, thus, storing energy". Santamarina *et al.* go on to describe a number of polarization methods: Electronic polarization is the movement of electrons with respect to the positive nucleus in a polarized atom; ionic polarization is the movement of charged ions within a polarized molecule; and orientational polarization is the rotation of a polarized molecule from its random orientation.

Each polarization mechanism, including those not mentioned above, is governed by different mathematical rules. However, each polarization type represents a loss-mechanism for the electric field. Energy is used to move or rotate electrons, atoms or molecules. For further information about specific polarization mechanisms, with a focus on soils, the reader is referred to the works of Kirkwood (1939); Levitskaya and Sternberg (1996a) and (1996b); Santamarina *et al.* (2001); Oh *et al.* (2007).

When considering polarization, in relation to the electric field in a medium, the following equations are pertinent (Santamarina *et al.*, 2001):

$$\boldsymbol{P} = \chi_e \varepsilon_0 \boldsymbol{E} \tag{2-9}$$

$$\varepsilon = (1 + \chi_e)\varepsilon_r \varepsilon_0 \tag{2-10}$$

Where $\boldsymbol{P}$ is the polarization of bound charges, χ_e is the electrical susceptibility of the medium, and ε is the effective permittivity of the medium accounting for polarization. It is clear from (2-10) that the susceptibility of the material can have a significant impact on the electromagnetic fields in that material.

2.2.2 Electromagnetic Properties of Soil

A large number of factors affect the electromagnetic properties of soil. Furthermore, many of the underlying assumptions which allow easy analysis of the EM field in a medium are invalid in soil. This section explains the factors that affect the dielectric properties of soil, gives some expected values for the electromagnetic properties of soil, and then defines the terms used to explain the various imperfections which must be considered.

2.2.2.1 Factors which Change the Electromagnetic Properties of Soils

A vast body of literature has sought a model for the dielectric properties of soil, the so-called mixing model. It was noted in 1934 that temperature, frequency, and soil type are required to predict the dielectric properties of soil (Smith-Rose, 1934). Whereas, in an extensive literature review Thomas (2010) (citing van Dam *et al.*, 2005) noted that more than 22 mixing models now exist and that none can be expected to accurately predict the dielectric properties of all soil in all situations. The purpose of this section is not to provide a definitive, predictive, model for the dielectric properties of soil; it is to give an indication of the range of factors affecting electromagnetic fields within soil, and provide an appreciation for the unique difficulties of working in this medium.

Some of the most commonly cited works which seek to predict the dielectric properties of soil are briefly explored here. The work by Topp *et al.* (1980), motivated by the potential of time-domain reflectometry (TDR), found that relative-permittivity was strongly related to water content, and weakly related to salinity, temperature, density and soil-type. Later, the papers by Hallikainen *et al.* (1985), Dobson *et al.* (1985), and Peplinski *et al.* (1995) gave more consideration to the soils' components, and considered soil as a combination of particles, water, and air voids. Furthermore,

they distinguished between bound-water – water adsorbed onto the surface of particles – and bulk-water – water which may move within the soil. Hallikainen, Dobson, Peplinski *et al*. concluded that frequency, soil-composition, temperature, salinity, density, bound-water content and free-water content are all factors in the prediction of the relative-permittivity of soils. The properties significantly affecting the dielectric properties of soil are reviewed here.

Frequency

It can be seen from (2-8) that there is frequency-dependence in the definition of complex permittivity. Furthermore, the widely cited Debye model predicts the frequency-dependent permittivity of soil as a function of low and high-frequency permittivities, conductivity, and material relaxation frequencies (Curioni, 2013). Many papers have been published showing significant increases in permittivity as frequency is reduced, in accordance with the Debye model; values for ε_r' of up to 50 and ε_r'' of up to 70 have been reported (Smith-Rose, 1934; Campbell, 1990; Heimovaara, 1994; Heimovaara *et al.*, 1994). However, at frequencies in the sub-Hz to low kHz range, some studies report exceptionally high values of permittivity. For example, in a study on sandstone samples Lesmes and Morgan (2001) report measuring ε_r' at around 10^9 at a frequency of 10^{-3} Hz. Whilst Cosenza *et al.* (2008), measured the clay based rock Argillite and reported comparable results, shown in Figure 2-1 and Figure 2-2.

The reason for such high relative-permittivity at low-frequency remains uncertain. Explanations proposed include different polarizations of different grain sizes at different frequencies (Lesmes and Morgan, 2001); or electrical phenomena on the surface of the particles which make up the soil (Cosenza *et al.*, 2008). Whatever the cause, it is clear that highly unusual electromagnetic effects could be observed if the reported results are representative across the bulk of a soil. This will become apparent as the expression for velocity of propagation is derived below, and this possibility forms the basis of the work undertaken in Chapter 5.

Soil Composition

The mixing models described by Hallikainen *et al.* (1985), Dobson *et al.* (1985), and Peplinski *et al.* (1995) classify soil based on their particulate content; specifically the percentage, measured by weight, of sand, silt, and clay. This classification is a simplification of the unified soil classification systems which defines clay as having particle size of less than 0.002 mm, silt between 0.002 mm and 0.005 mm, and sand between 0.005 mm and 2.00 mm (U.S. Department of Agriculture, 2013, p. 618-A.43). A commonly presented diagram which demonstrates this classification system is shown in Figure 2-3. However, it has been noted that the soil composition is unlikely to be known prior to measurement, making its use in predicting relative-permittivity difficult (Thomas, 2010).

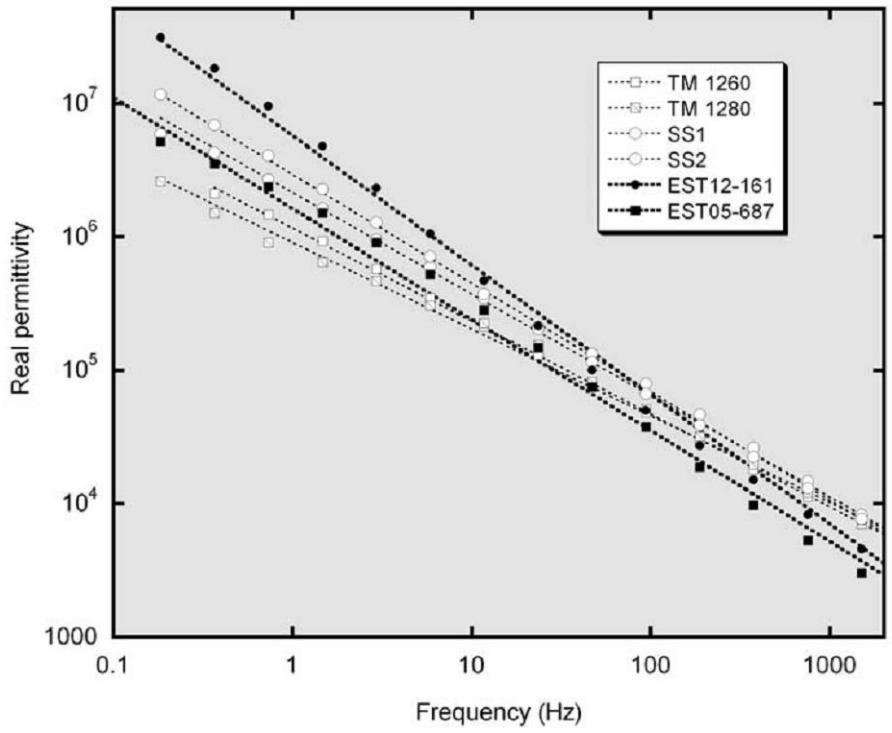

Figure 2-1: Real permittivity measured in clay based Argillite rock (after Cosenza *et al.*, 2008) © 2008 by the American Geophysical Union

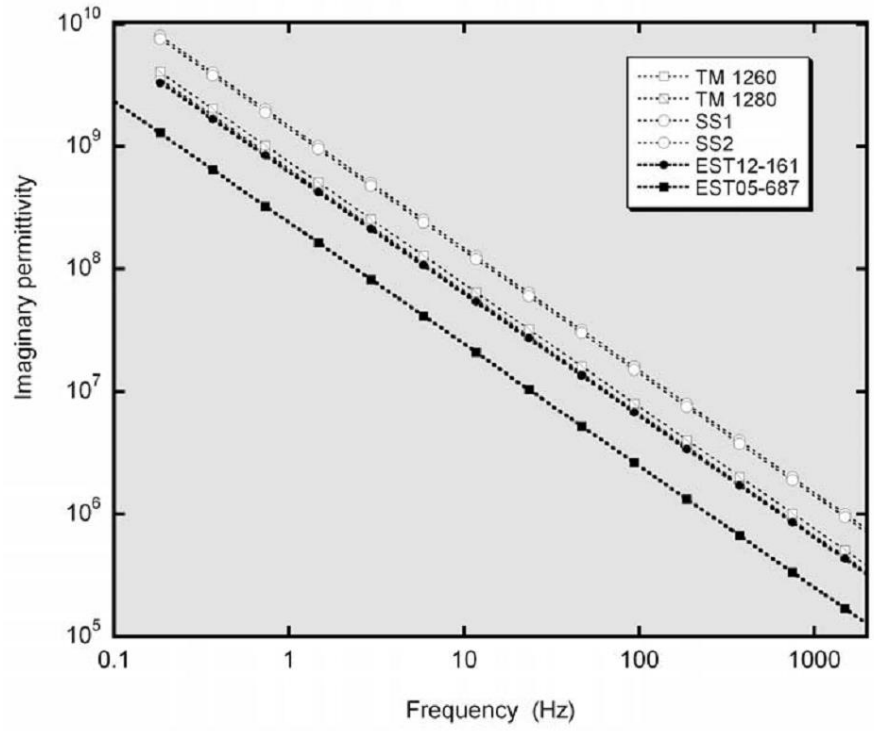

Figure 2-2: Imaginary permittivity measured in clay based Argillite rock (after Cosenza *et al.*, 2008) © 2008 by the American Geophysical Union

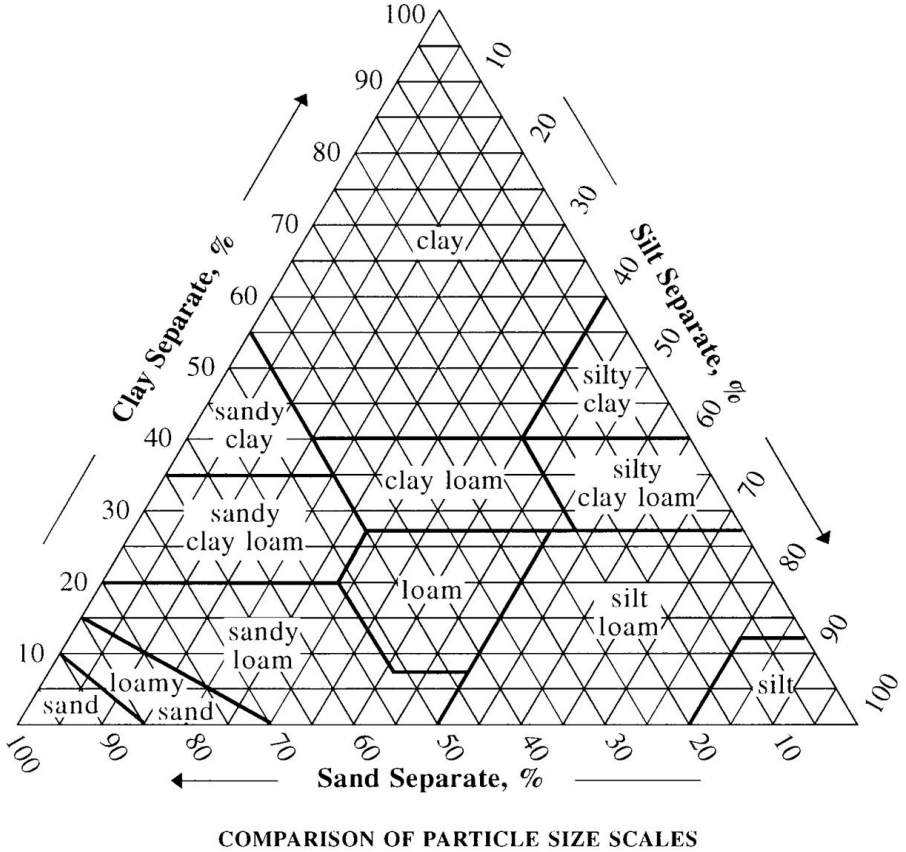

Figure 2-3: Soil classification by ratio of constituent particulate sizes. (U.S. Department of Agriculture, 2013)

Water Content

Whether considering water-content as a bulk property (Topp *et al.*, 1980) or as separate bound-water and free-water contents (Hallikainen *et al.*, 1985; Dobson *et al.*, 1985; Peplinski *et al.*, 1995) it seems intuitive that water-content will have a significant effect on the relative-permittivity of a soil. Water has a relative-permittivity around 80 (Topp, 2003) and dry soil has a permittivity of between 2 and 4 (Santamarina *et al.*, 2001, p. 375), it seems evident that adding water to dry soil will increase the permittivity. Indeed, the model proposed by Topp *et al.* (1980) has allowed scientists to measure the soil-water content, by means of measuring permittivity, with little need to consider other soil properties (Robinson *et al.*, 2003). The strength of the relationship between soil water content and relative-permittivity is demonstrated in Figure 2-4.

In an environment where rain is common, time constraints must apply which allow a measurement to be considered stationary. Gray (1973) gives figures for the infiltration rate in soils, these range from 0.02 inches per hour for soil over shallow bedrock to 1 inch per hour for coarse soil over very coarse base materials. Therefore, it is reasonable to assume that unless significant rainfall occurred immediately prior to – or during – measurements, the soil water content is stationary. This assumption is further supported by the results of Curioni (2013, pp. 178-180) which show stable soil permittivity and conductivity during dry weather, and changes shortly after large rainfall events which stabilise within hours.

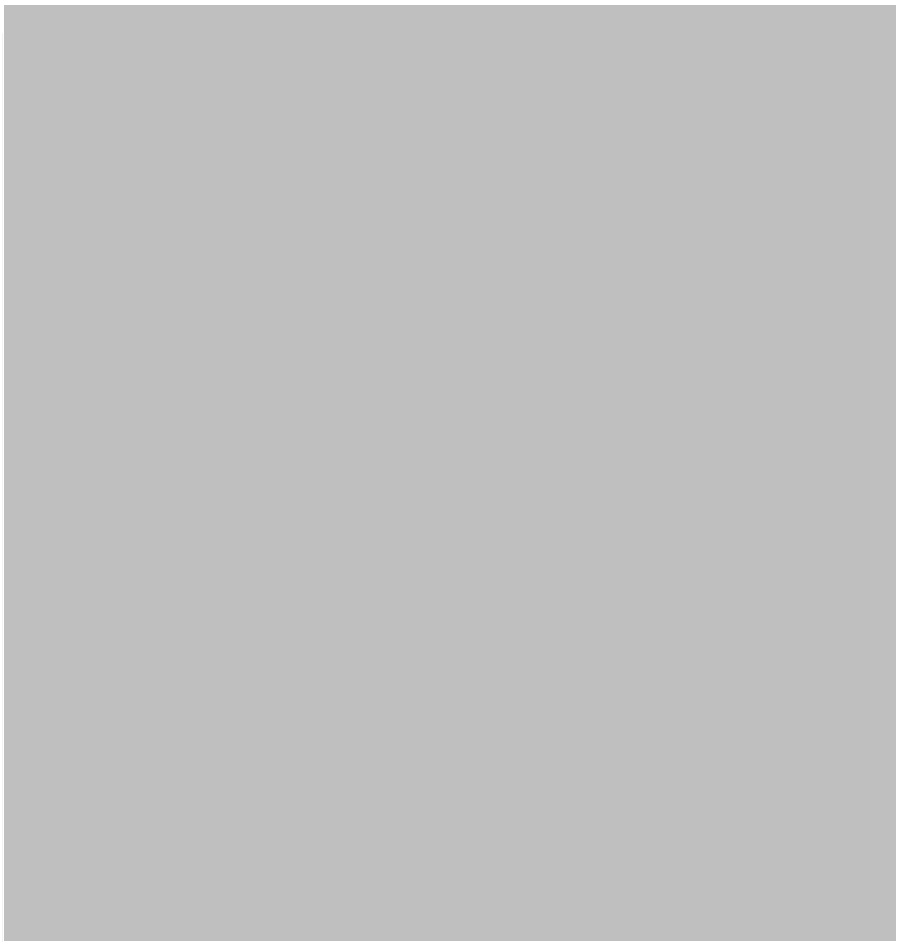

Figure 2-4: Relative-permittivity as a function of soil water content, for a number of materials (after Topp *et al.*, 1980). Measured using TDR with an effective-frequency between 0.7 GHz and 1 GHz (Robinson *et al.*, 2005). © 1980 by the American Geophysical Union

Temperature

It has been reported that the apparent conductivity and relative-permittivity of both dry soil and air are temperature insensitive within the natural range of temperatures encountered in environment (Topp *et al.*, 1980; Friedman, 2005). However, the dielectric properties of water do exhibit small temperature dependence meaning the dielectric properties of wet soil do the same. The temperature-dependence of the dielectric properties of water has been quantified and is expressed in (2-11) and (2-12) (Wraith and Or, 1999).

$$\varepsilon_w(T) = 78.54[1 - 4.579 \times 10^{-3}\Delta + 1.19 \times 10^{-5}\Delta^2 - 2.8 \times 10^{-8}\Delta^3] \quad (2\text{-}11)$$

Where $\varepsilon_w(T)$ is the relative-permittivity of water, $\Delta = T - 25$, and T is the temperature in Celsius.

$$\sigma_w(T) = \sigma_{w(25^\circ C)} \exp[-\Delta'(2.033 \times 10^{-2} + 1.266 \times 10^{-2}\Delta' + 2.464 \times 10^{-6}\Delta'^2)] \quad (2\text{-}12)$$

Where σ_w is the bulk electrical conductivity of water, and $\Delta' = 25 - T$.

The temperature dependence of the dielectric properties of soil is dependent on the water content of the specific soil; experimental examples are illustrated by Topp *et al.* (1980), Or and Wraith (1999), and Wagner *et al.* (2011) .

2.2.2.2 Assumptions about Electromagnetic Properties of Soil

Introductory electromagnetic texts would have the reader hope that all measurements can be taken in environments which are homogenous, isotropic, linear, and stationary. In soil it is rare for this to be accurate. In this section, these terms are defined, and the mathematics which allows the removal of these assumptions is introduced.

Homogenous

Homogeneity is perhaps the largest, most important, and yet least valid assumption made when considering electromagnetic fields in soil. A homogenous material is one which maintains the same properties throughout its bulk. It will be seen that an anisotropic, non-linear material may be accounted for by relatively simple extra mathematics. However, the same is not true for a material which is inhomogenous. Indeed, Chapter 4 of this thesis is entirely concerned with the propagation of EM fields through a four-layered medium where it will be seen that the EM field is fundamentally different to that in a homogenous medium.

It can be argued that inhomogeneous media may be considered by applying Maxwell's equations with permittivity, permeability, or conductivity described as spatially dependant functions (Paul and Nasar, 1987). However, this approach cannot accurately consider two important types of inhomogeneity discussed here:

Stratified Media

There is a vast body of research considering the propagation of electromagnetic waves in stratified media, the reader is referred to the excellent review by Wait (1998a) for the historical context. The seminal work by King *et al.* (1992) considered the propagating EM field in stratified media, and formalised the integral equations which describe them. A later review of published work, gave valuable insight into several specific cases including propagating along an earth-air

boundary, and propagation in three-layered media (Li, 2009). The papers which form the basis of the work by Li (2009), along with the methods of King *et al.*, are extensively reviewed in Chapter 4.

It is now accepted that in a stratified media the electromagnetic energy will take the form of direct and reflected waves in the layer where the energy source is located. In addition, lateral waves propagate along each layer; and trapped surface waves propagate along the boundaries between each layer (King and Sandler, 1994; Wait, 1998b; King and Sandler, 1998; Zhang and Pan, 2002). Fundamentally, these mathematical descriptions of the electromagnetic field are derived from Maxwell's equations. However, it is clear from the literature that a specific method is advantageous for successful evaluation of the EM fields in stratified media.

Soil

Soil is fundamentally inhomogeneous, consisting of particulates, air and water (Hallikainen *et al.*, 1985). By seeking to measure the dielectric properties of soil, one attempts to measure the bulk properties of this fundamentally inhomogeneous material. However, the type of particulate and the ratio of the constituent components of soil fundamentally vary due to water infiltration, and temperature variation, amongst a long list of "physical, chemical, and biological processes" (Santamarina *et al.*, 2001). These factors cause the medium to be inhomogeneous, but also non-stationary.

Stationary

A stationary medium is one whose dielectric properties have no time-dependence. It has been shown that soil cannot be assumed to be stationary. However, it has also been shown that measurements can be conducted under the assumption that soil is stationary, due to the relatively slow rate of change.

It has been demonstrated, as discussed above, that the single largest factor affecting the dielectric properties of soil is its water content (Topp *et al.*, 1980). It follows, that to assume soil to be

stationary would be to assume its water content stationary. The same is true of temperature, salinity, and density, amongst others.

Water infiltration into soil is well researched; Miller and Gardner (1962) presented a laboratory study of water infiltration into soil under constant pressure (case A in Figure 2-5), while Rubin and Steinhardt (1963) modelled the infiltration due to steady rainfall using differential equations (case D in Figure 2-5). By 1973, researchers were noting several different cases for water infiltration, due to a saturation point; which, once reached, means that no water can be absorbed into the soil (cases B and C in Figure 2-5) (Mein and Larson, 1973). The present state-of-the-art is one where water infiltration in soil is well understood, and covered extensively in textbooks (Gray, 1973; Hanks *et al.*, 1991). However, research is still published in specialist areas such as infiltration through frozen – or partially frozen – soil (French and Binley, 2004); to explore the efficacy of different soil treatments for agriculture (Franzluebbers, 2002); or to observe water infiltration over measurement periods spanning years (Curioni *et al.*, 2012; Curioni, 2013).

Clearly, in an environment where rainfall occurs soil cannot be considered stationary. However, the rate of water infiltration into soil is such that it may be considered stationary over the periods of minutes required for measurements to occur, particularly if rainfall has not occurred in the immediate period prior to measurement.

Figure 2-5: Different types of water infiltration into soil (after Mein and Larson, 1973). © 1973 by the American Geophysical Union

Isotropic

An isotropic material is one which has the same properties regardless of the direction of observation or propagation. In an anisotropic medium, the constitutive relationships (2-5) - (2-7) may be replaced so that permittivity, permeability, conductivity, or susceptibility are replaced by a matrix such as (2-13) (Paul and Nasar, 1987):

$$\begin{bmatrix} D_x \\ D_y \\ D_z \end{bmatrix} = \begin{bmatrix} \varepsilon_{xx} & \varepsilon_{xy} & \varepsilon_{xz} \\ \varepsilon_{yx} & \varepsilon_{yy} & \varepsilon_{yz} \\ \varepsilon_{zx} & \varepsilon_{zy} & \varepsilon_{zz} \end{bmatrix} \begin{bmatrix} E_x \\ E_y \\ E_z \end{bmatrix} \tag{2-13}$$

Using this matrix formulation, the electric-field resulting from the electric flux density is dependent on the directional components of the electric flux density and the permittivity. Equivalent expressions may be applied to the other constitutive equations. Santamarina *et al.* (2001) state that a material which is "geometrically anisotropic" is likely to exhibit anisotropic behaviour in their electromagnetic properties. Santamarina *et al.* (2001) demonstrate this with experimental results showing the effective conductivity of aligned mica flakes mixed with electrolytes changes in different alignments with the electric field, unfortunately they give little insight into the anisotropic properties of soils.

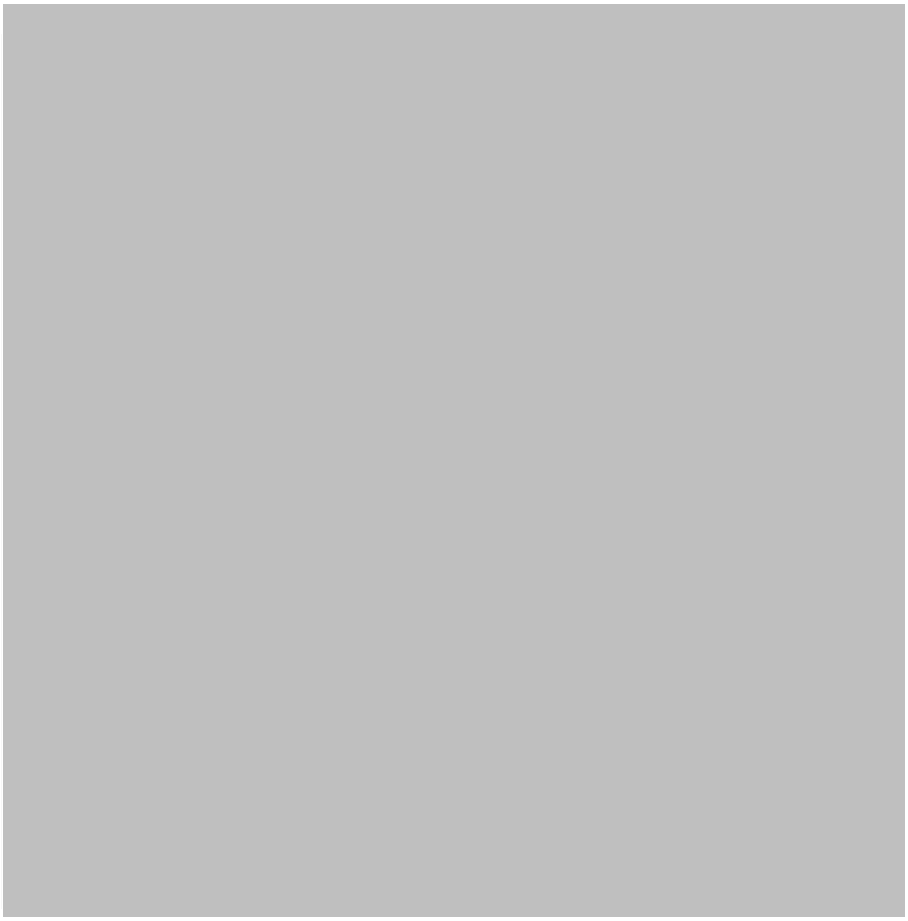

Figure 2-6: Change in permittivity perpendicular (++) and parallel (--) to the geometric alignment of the rock under test (Tillard, 1994) © 2006, John Wiley and Sons

A literature search has revealed a paucity of research documenting the anisotropic properties of soil. Vasco *et al.* (1997) conducted a study into signal processing techniques for GPR in slightly heterogeneous and anisotropic media; and noted that where anisotropy is exhibited for acoustic waves it is likely that anisotropy will occur in electromagnetic properties. Supporting their argument, Vasco *et al.* cited work by al Hagrey (1994) and Tillard (1994). One of these works studied a site where the anisotropy was caused by fracturing in the ground, and noted slight increase in conductivity between the longitudinal and transverse components (al Hagrey, 1994). The study by Tillard (1994) showed significant change in complex permittivity, and propagation distance, depending on the orientation of the electric field relative to the granular orientation of the schist rock under test, see Figure 2-6. Both of these examples studied areas of rock with clear geometric alignment. In the test sites used for this thesis no such geometric properties were observed, consequently the measurements were assumed to have been carried out in isotropic media.

Linear

A linear material is one whose dielectric properties do not exhibit dependence on the magnitude of the field in the medium (Paul and Nasar, 1987). The assumption that the dielectric properties of soil behave linearly is widespread, and is maintained throughout this work.

2.3 MEASUREMENT OF THE ELECTROMAGNETIC PROPERTIES OF SOIL

This section explores the current research in measuring the electromagnetic properties of soils. The first question considered is why there is a need to measure the EM properties of soils. Methods which exist to measure EM properties are then explored and the well-established time-domain methods are briefly considered. Frequency-domain methods, capable of measuring frequency-dependent material properties, are given greater emphasis than their time-domain equivalents because they are better suited to applications with dispersive soils.

2.3.1 Why Measure the Electromagnetic Properties of Soil?

When considering the complex and extensive field of the dielectric properties of soil, it is easy to lose sight of why it is undertaken. The applications for the knowledge of the dielectric properties of soils are numerous, but significant examples are given here.

2.3.1.1 Soil Water Content

It was shown above that soil water content is the dominant factor affecting relative-permittivity of a soil (Topp *et al.*, 1980). A large number of measurements are made, purely to measure the soil water content for a range of purposes including water distribution in agriculture, and the water levels in plant roots (Or and Jones, 2002). A number of physical properties influence the dielectric properties of soils and measurements are sometimes made to study these, but the uses are limited by the strength of the influence of soil water content on permittivity. Examples include measuring salinity in agriculture using conductivity (Corwin and Lesch, 2003); or measuring polarization in rocks for prospecting (Levitskaya and Sternberg, 1996a; b).

2.3.1.2 Ground Penetrating Radar

Ground penetrating radar (GPR) results typically show measured reflection as a function of time and antenna location (Annan, 2002). However, in order to relate the measurement time to depth, the velocity of propagation of the wave, excited by the GPR, must be estimated. The high-quality review by Davis and Annan (1989) illustrates the difference in expected velocity of propagation in Figure 2-7.

Figure 2-7: Illustration of velocity of propagation in soil as a function of frequency and conductivity (after Davis and Annan, 1989) © 2006, John Wiley and Sons

The other parameter of interest when using GPR is the range of operation, determined by the attenuation in the soil and the sensitivity of the equipment. Attenuation varies significantly, at 10 MHz attenuation could be expected to vary between 10^{-1} dB and 10^{2} dB per metre (Davis and Annan, 1989). Clearly, a GPR survey where attenuation is 10^{2} dB per metre requires significantly greater sensitivity to achieve useable results than an equivalent measurement where attenuation is 10^{-1} dB per metre.

2.3.1.3 Direction of Arrival Estimates

Direction of arrival (DoA) estimation refers to methods of estimating the bearing of a propagating signal, and is covered in detail below. The common methods for DoA estimation using an array

of sensors rely on the knowledge of the signal wavelength (Godara, 1997). Wavelength can only be known if the velocity of propagation is known, which relies on the EM properties of the soil (Paul and Nasar, 1987).

2.3.2 Methods for Permittivity Measurements

Although there is no difference in information content between the time and frequency-domains, the measurement of the dielectric properties of materials tends to be accomplished wholly in the time or frequency-domain.

2.3.2.1 Time-Domain Reflectometry

A good review of time-domain reflectometry (TDR) for permittivity and conductivity measurements is given by Robinson *et al.* (2003) who gave a historical context in the development of TDR for soil measurements. TDR measurements transmit a short pulse down a transmission line which contains the material under test and measure the reflected signal. The transmission line can be a coaxial line (Topp *et al.*, 1980; Jones *et al.*, 2005), but is usually a line consisting of 2 or more parallel rods which have been inserted into the measurement medium (Jones *et al.*, 2002; Robinson *et al.*, 2003). By measuring the time delay before reflections, and the magnitude of those reflections, permittivity and conductivity are measured, a good explanation of this process is given by Curioni (2013).

2.3.2.2 Frequency-Domain Consideration of TDR

Conventional TDR gives little information about the frequency range of its measurements, this is a significant disadvantage when considering soil, which is often dispersive. Research has been conducted which considers the frequency-domain information available from TDR results. The most fundamental comparison is to calculate the effective frequency, f_{eff}, of a TDR measurement which can be used to compare results with frequency-domain equivalents, this is calculated using (2-14), where t_r is the rise time of the TDR pulse (Robinson *et al.*, 2005).

$$f_{eff} = \frac{\ln\left[\frac{0.9}{0.1}\right]}{2\pi t_r} \quad (2\text{-}14)$$

A more sophisticated method is to utilise the spectral content of the TDR pulse to calculate a frequency-domain response from the material which may be compared to direct frequency-domain measurements (Friel and Or, 1999).

2.3.2.3 Frequency-Domain Methods

Frequency-domain methods give specific results across a range of frequencies, in the case of dispersive soils the variation can be large, justifying the use of such techniques (Hallikainen *et al.*, 1985; Dobson *et al.*, 1985; Klein and Santamarina, 1997). The following techniques are given in chronological order so that the reader may appreciate their development. However, the first method – known as Nicoloson-Ross-Weir – is still widely used, and cited. It should be noted that most of the methods discussed here utilise reflection and transmission measurements. This is not always advantageous and the second half of this section considers methods which only use reflection measurements, despite some inherent difficulties with the method.

Transmission-Reflection Measurements

The following methods consider the calculation of the dielectric properties of a material, by measuring the transmitted and reflected signals from a waveguide filled with the material.

Nicolson-Ross-Weir

Traditionally, frequency-domain permittivity methods used a slotted transmission-line to measure the standing wave within a waveguide. Nicolson and Ross (1970) published a method removing the need for a slotted line, by using an open-ended transmission line. Using a time-domain method, Nicolson and Ross (1970) measured the reflection-coefficient of a waveguide with a dielectric filled section. After calibration, Nicolson and Ross were able to transform their measurements to obtain frequency-domain scattering parameters of their system, from which they calculated the permittivity and permeability of the dielectric under test. This is calculated

by solving simultaneous equations similar to those given by Baker-Jarvis *et al.* (1990) and shown below in (2-15) and (2-16).

A further advance in this method was made when a network analyzer was used to remove the need for transforming the time-domain pulse into the frequency-domain (Weir, 1974). Use of a network-analyser enabled Weir to directly measure S_{11} and S_{21} across a range of frequencies. This method of determining the permittivity and permeability of a sample embedded in a transmission line became known as the Nicolson-Ross-Weir (NRW) method (Baker-Jarvis, 1990).

When evaluating the NRW method, several comments are commonly made. Firstly, an optimal sample length exists due to uncertainty at half-wavelength frequencies (Baker-Jarvis *et al.*, 1990). The review by Stuchly and Stuchly (1980) observes that "the optimum sample thickness is an odd number of one-eighth of the wavelength in the dielectric". If the aim of the measurement is to determine the permittivity of a material, the wavelength will be unknown and multiple measurements will be required. It has been shown that reducing the sample size to avoid the occurrence of half-wavelength frequencies increases measurement uncertainty. Finally, the NRW has a 2π phase ambiguity which must be resolved, this obstacle is rarely mentioned in the literature (Baker-Jarvis, 1990).

Iterative Methods

In a series of papers Baker-Jarvis *et al.* showed that the permittivity and permeability of a sample in a waveguide may be calculated without errors due to the low magnitude of S_{11} at half-wavelength frequencies (Baker-Jarvis, 1990; Baker-Jarvis *et al.*, 1990). Baker-Jarvis *et al.* (1990) give the following set of equations which demonstrate the difference between the iterative method and the NRW method.

$$|S_{11}| = \left|\frac{\Gamma(1-z^2)}{1-z^2\Gamma^2}\right| \tag{2-15}$$

$$|S_{21}| = \left|\frac{z(1-z^2)}{1-z^2\Gamma^2}\right| \tag{2-16}$$

$$\frac{S_{21}}{S_{21}^0} = \exp(\gamma_0 L)\frac{z[1-\Gamma^2]}{1-z^2\Gamma^2} \tag{2-17}$$

$$S_{21}S_{12} - S_{11}S_{22} = \exp[(-2\gamma_0)(L_{air} - L)]\frac{z^2-\Gamma^2}{1-z^2\Gamma^2} \tag{2-18}$$

Where γ_0 is the wavenumber in free space, L_{air} is the length of the waveguide filled with air, L is the length of the dielectric sample within the waveguide, Γ is the reflection-coefficient at the air-dielectric interface in the waveguide, $z = \exp(-\gamma L)$ is the transmission-coefficient.

The NRW method solves (2-15), but this is unreliable at half-wavelength frequencies where $S_{11} \rightarrow 0$ and results in erroneous results at these frequencies. The Baker-Jarvis method, solves (2-17) and (2-18) iteratively, treating length of the waveguide and sample as unknowns.

Using the example of a PTFE sample, Baker-Jarvis *et al.* showed that the iterative solution is able to supply good estimates of permittivity over a large frequency range without erroneous results at the half-wavelength frequencies. The disadvantages of the Baker-Jarvis method include the obvious computational effort required for an iterative solution, the loss of an analytical solution, and the requirement for an estimate for permittivity to seed the iteration (Boughriet *et al.*, 1997).

A Non-Iterative NRW Variation

The most recent variation on the NRW method was published by Boughriet *et al.* (1997), who showed that different derivations of the equations used by Nicolson, Ross, and Weir could remove the instability inherent in their equations. Boughriet *et al.* also showed that their method achieved comparable accuracy to the Baker-Jarvis method. Since its publication, the Boughriet method has been used successfully to achieve new permittivity measurements (Hasar, 2008a; b). It is believed that the Boughriet method represents the best available solution for measuring the dielectric properties of a material using scattering measurements of a transmission line.

Reflection Only Measurements

In a number of cases, it is not possible to fill a waveguide with the material under test: Examples include measuring living tissue, or measuring soil before it is excavated. For a comparison of

methods using open-ended waveguides terminated by the material under test, the reader is referred to the review paper by Stuchly and Stuchly (1980). Two methods are discussed which use a short-circuited transmission line to calculate the dielectric properties of materials using reflection measurements.

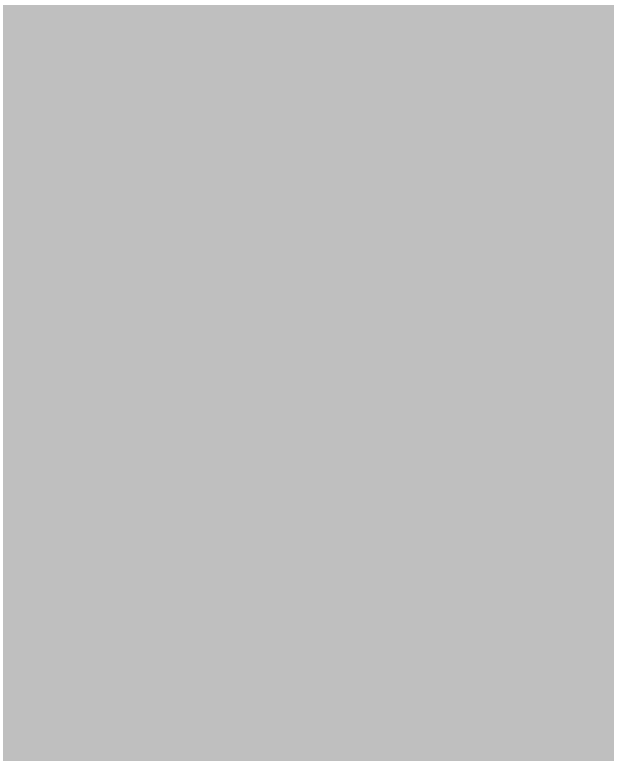

Figure 2-8: The operating principles of the experiment conducted by Roberts and Von Hippel. Note the slot and travelling detector used to measure the wavelength of the standing wave. (After Roberts and Von Hippel, 1946). © 1946 The American Institute of Physics

As early as 1946, Roberts and Von Hippel (1946) showed that a short-circuit terminated waveguide, partially filled with a sample of a dielectric, could be used to measure the relative-permittivity of the dielectric. The method involved using a slot to measure the voltage along the waveguide and determine the wavelength of the standing wave. The operating principle is shown in Figure 2-8. Later Nelson *et al.* (1974) provided algorithms to radically increase the speed of the Roberts and Von Hippel method, but this was overtaken by the NRW method using networks analysers.

Quarter-Wavelength Analysis

Despite only giving results at specific frequencies, quarter-wavelength analysis (QWA) is exceedingly robust. Thomas *et al.* (2008) (citing Heimovaara *et al.*, 1996) stated (2-19) which

defines the quarter-wavelength frequencies, f_n^{QWA}. That is, the frequencies at which a local maximum in reflection-coefficient occurs, due to the summation of transmitted and reflected wave in the coaxial cavity.

$$f_n^{QWA} = \frac{(2n-1)c}{4\sqrt{\varepsilon^*}L} \tag{2-19}$$

Where n is an integer between 0 and ∞, c is the speed of light in free space, L is the length of the coaxial cavity, and ε^* is the complex relative-permittivity of the dielectric in the transmission line.

By plotting the measured S_{11}, the researcher is able to identify the quarter wavelength frequencies, and by simple algebraic manipulation of (2-19) calculate the relative-permittivity at those frequencies. However, measurement resolution is very low, leading to preference for the inversion methods, despite their increased complexity.

Iterative Solutions

The second half of the excellent review paper by Baker-Jarvis (1990) focuses on permittivity measurements using a short-circuit terminated transmission line. Baker-Jarvis *et al.* show derivations for S_{11} in terms of the geometry and the dielectric properties of the sample (2-20) - (2-22), these equations are then iteratively solved for a given measurement. If the sample is assumed non-magnetic ($\mu = \mu_0$) then only one measurement is required, otherwise two measurements, of different sample length, are required.

$$S_{11} = \rho = \frac{-2\beta\delta + [(\delta+1) + (\delta-1)\beta^2]\tanh(\gamma L)}{2\beta + [(\delta+1) - (\delta-1)\beta^2]\tanh(\gamma L)} \tag{2-20}$$

$$\beta = \frac{\gamma\mu_0}{\gamma_0\mu} \tag{2-21}$$

$$\delta = \exp(-2\gamma_0\Delta L) \tag{2-22}$$

Where γ and γ_0 are the wavenumbers in the sample and free-space, respectively; μ and μ_0 are the permeability of the sample and free-space, respectively; L is the length of the sample; and ΔL is the distance between the sample and the short circuit.

As with the iterative transmission-reflection method, this procedure requires an initial estimate, more computation power than an analytical solution, and removes the use of an analytical solution for other applications.

2.3.2.4 Practical Considerations

Practical considerations for taking measurements must be made, notably that containing a liquid or highly granular material within a waveguide requires additional design effort. It has been shown that additional constraining layers need not negatively influence measurements despite additional calculations, providing the constraining layer is of known material and size (Bois *et al.*, 1999).

2.4 ELECTROMAGNETIC WAVE PROPAGATION

Maxwell's equations, together with the constitutive equations describe the properties of electromagnetic energy propagating through all media. However, it is not trivial to take Maxwell's equations and deduce the expected voltage induced on, or current induced through, a receiving antenna as a result of a transmitting antenna at a point in space. This section explores the literature which allows the researcher to predict experimental results, based upon Maxwell's equations and a very large body of subsequent work. The first section considers the challenges at exceedingly low frequencies:

2.4.1 When is a Wave a Wave?

By considering Maxwell's equations, it can be seen there is no fundamental lower-limit for the frequencies to which they apply. However, when a signal has very low frequency do its properties cease to be wave-like? A signal propagating in air at a frequency of 1 Hz has a wavelength of approximately 3×10^8 m. While a signal with frequency 0.1 Hz must be sampled for 10 seconds to measure a single wavelength, but could conceivably be sampled at 5 second intervals. To the electrical engineer, used to working in the millimetre band, for whom kHz represents very low-frequencies, these distances and times make gathering useful information seem most difficult.

However, published research exists which uses frequencies well below 0.1 Hz. For instance, Schneider *et al.* (2001) use gravitational waves with frequencies between 5×10^{-6} and 5×10^{-5} Hz to characterise distant stars. Electromagnetic fields have been measured in the ionosphere, due to seismic activity, at frequencies between 10^{-2} and 10^{2} Hz; these fields are used to monitor and predict earthquake activity (Molchanov *et al.*, 1995). Chang and Wait (1974) considered propagation at ELF frequencies, defined as 1 Hz to 3 kHz (Wait, 1962), along the earth's surface. It was shown that an ELF signal can propagate along a wire on the surface of a dissipative earth, with a wavenumber equal to the root-mean-square of the wavenumbers of the earth and the air.

2.4.2 Important Concepts for EM Propagation

2.4.2.1 The Difference between the Near and Far Fields

The treatment of electromagnetic propagation is split into fundamentally different bodies of work; that is near-field, and the far-field. In a succinct explanation, Bienkowski and Trzaska (2012) define the boundaries between the near and far fields, explaining the far-field region is the region where the EM field is accurately described as a plane-wave and where the E and H fields are orthogonal and related by the characteristic impedance.

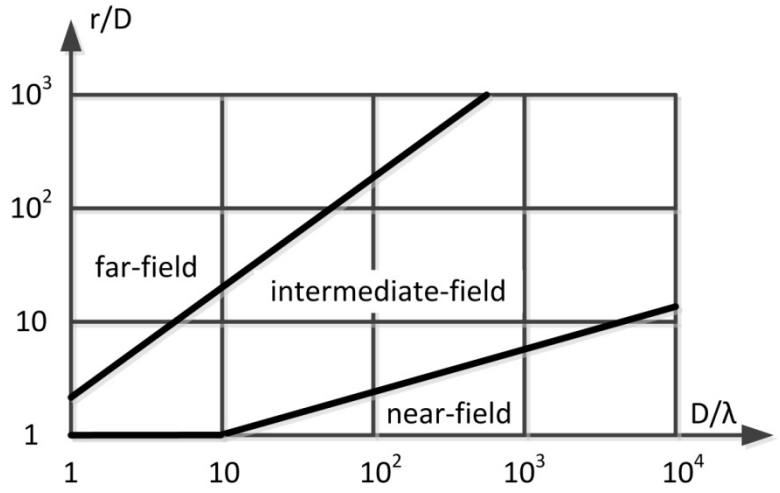

Figure 2-9: Boundaries of near, intermediate, and far field areas where r is the distance between transmitter and receiver, D is the size of the receiver, and λ is the EM field wavelength (after Bienkowski and Trzaska, 2012).

The far-field assumptions are employed where:

$$R \geq \frac{2D^2}{\lambda} \tag{2-23}$$

Where R is the distance between transmitter and receiver, D is the size of the receiver, and λ is the EM field wavelength. Whereas, the near-field is defined as the region where the E and H fields are independent, and a spherical-wave approximation is required, where:

$$R \leq \frac{D}{4} + \frac{D}{2}\left(\frac{D}{\lambda}\right)^{1/3} \tag{2-24}$$

Bienkowski and Trzaska (2012) go on to explain the difficulties encountered when working in the near-field. The work in this thesis assumes far-field measurements. Figure 2-9 shows the near, intermediate, and far field regions as a function of the geometry of the system.

2.4.2.2 Guided Waves

Maxwell's equations may be readily applied to a wave propagating in an infinite uniform medium. However, this is of little practical use; structures which guide a wave are of huge practical importance and variety, ranging from the smallest cables to the earth itself.

Transmission Lines

Transmission lines may be defined as "the interconnections that convey electromagnetic energy from one point to another" (Kraus *et al.*, 1999). Transmission lines can be coaxial, PCB mounted, or one of number of other physical implementations, but the study of their properties has led to methods of analysis which remove the need to begin with Maxwell's equations when implementing a transmission line system. Transmission lines are fundamentally defined using the transmission line equations (Pozar, 1990):

$$\frac{\partial v(z,t)}{\partial z} = -Ri(z,t) - L\frac{\partial i(z,t)}{\partial t} \tag{2-25}$$

$$\frac{\partial i(z,t)}{\partial z} = -Gv(z,t) - C\frac{\partial v(z,t)}{\partial t} \tag{2-26}$$

Where *v* and *i* are the voltage and current on the transmission line, *R*, *L*, *G*, and *C* are the equivalent circuit parameters shown in Figure 2-10.

By modelling transmission lines as networks of inductors, resistors and capacitors, it is possible to determine properties such as the impedance of a transmission line (Paul and Nasar, 1987). From the concept of impedance, reflection-coefficients due to the load and intrinsic-impedance of terminated transmission lines are calculated (Kraus *et al.*, 1999):

$$Z_x = Z_0 \frac{Z_L + Z_0 \tanh \gamma x}{Z_0 + Z_L \tanh \gamma x} \tag{2-27}$$

Where Z_x is the impedance at the start of a transmission line of length x, intrinsic impedance Z_0, terminated by a load impedance Z_L, and γ refers to the propagation constant in the waveguide.

Waveguides

A waveguide is a structure which support EM waves and shares many properties with transmission lines, although the precise definition changes considerably depending on the source. The definition taken for this thesis is that of Paul and Nasar (1987) who simply state that a waveguide is a structure which "serve[s] to guide energy from one point to another".

A waveguide may not have been designed to support a wave (such as the surface of the earth), or may have been designed to support very specific types of wave (such as resonant cavities) but the analysis of waveguides is relatively universal in its approach. With knowledge of the geometry of the waveguide, boundary conditions are applied to Maxwell's equations which allow the derivation of the propagation constant for the waveguide in question. Examples of this process for a number of simple waveguides are given by Pozar (1990).

Modes

The method of applying boundary conditions to Maxwell's equations does not give unique results. By assuming $E_z = 0$ and/or $H_z = 0$, different propagation-constants are found. This variation gives rise to different *modes*. There are three categories of mode, the transverse electromagnetic (TEM), the transverse magnetic (TM), and the transverse electric (TE). In the TEM mode $E_z =$

$H_z = 0$, meaning that both electric and magnetic fields are orthogonal to the direction of propagation, similarly in TM modes $H_z = 0$, and in TE modes $E_z = 0$.

There are an infinite number of possible modes, both TE and TM, referring to the number of wavelengths with exist within the waveguide, satisfying the boundary conditions. For example, considering the TM modes in a lossless rectangular waveguide with cross-sectional dimensions *a*, *b*, Paul and Nasar (1987) define the TM modes using (2-28).

$$\hat{E}_z = \hat{C} \sin[Mx] \sin[Ny]\, e^{-j\beta_{mn}z} \tag{2-28}$$

Where $\hat{C}$ is the field magnitude; *x*, *y*, and *z* are the Cartesian coordinates; $\beta_{mn} = \omega\sqrt{\mu\varepsilon}$ is the phase constant; *m* and *n* are positive integers such that:

$$M = \frac{m\pi}{a} \tag{2-29}$$

$$N = \frac{n\pi}{b} \tag{2-30}$$

As frequency increases, so do the number of possible modes. This idea leads to the concept of a cut-off frequency, which is the highest frequency at which a waveguide will support a single mode of propagation. When using a waveguide, or transmission line, it is often desirable to maintain a single mode of operation to maintain the validity of the analysis undertaken at the design stage. The waveguides used in Chapter 3 will be subject to this analysis.

2.4.3 Methods of Modelling EM Propagation

2.4.3.1 Maxwell's Equations

It is well established that Maxwell's equations accurately describe the electromagnetic field in a medium. From Maxwell's equations, the wave or Helmholtz equations are derived. In an isotropic, linear, homogenous, source-free region (Pozar, 1990):

$$\nabla^2 \bar{E} + \omega^2 \mu\varepsilon \bar{E} = 0 \tag{2-31}$$

$$\nabla^2 \bar{H} + \omega^2 \mu\varepsilon \bar{H} = 0 \tag{2-32}$$

Where $k = \omega\sqrt{\mu\varepsilon}$ is the propagation constant.

In a lossy medium, or a good conductor, these equations differ. If the medium has multiple layers, then boundary conditions must be observed relating the field incident on the boundaries to those reflected and transmitted. If more than one boundary is present, then the reflected and transmitted waves will be incident on another boundary, and so on.

When applying Maxwell's equations to a real world scenario significant complexity can be created very easily. Consequently, researchers have methods which allow familiar tools of circuit theory to be used.

2.4.3.2 Circuit Theory

When considering a system as a transmission line, circuit theory may be applied. A surprisingly large number of systems may be described as transmission lines: coaxial geometries, two conductor geometries, and single conductors over a ground plane all readily conform to the transmission line methodology (Kraus *et al.*, 1999). Consider the following representation of a transmission line segment:

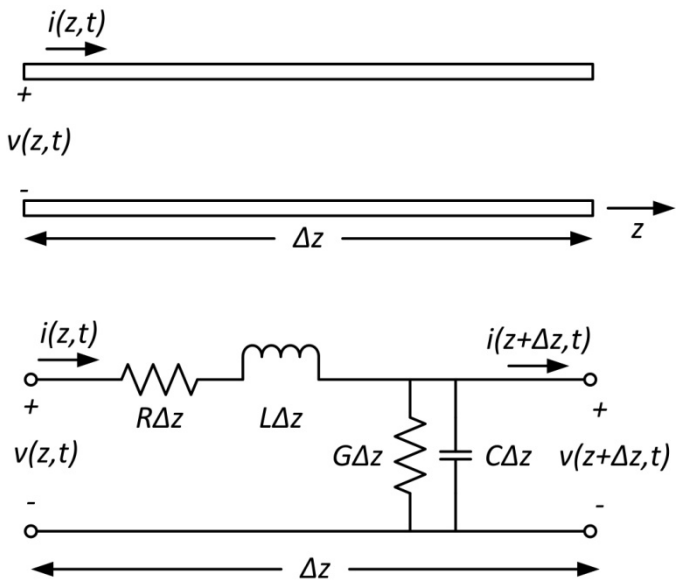

Figure 2-10: Circuit Representation of a Section of Transmission Line (after Pozar, 1990, p.49)

Definition of the equivalent lumped circuit elements allows calculation of the characteristic impedance of the line, propagation constant, wave velocity, and transmission line wave equation (2-25), (2-26) (Kraus *et al.*, 1999, pp. 120-123). Where a system can be defined as a transmission

line network, circuit theory presents an easy selection of tools to evaluate the propagating electromagnetic field. However, circuit theory assumes a single mode of propagation (usually TEM) and so should not be used if a more complete field evaluation is required.

2.4.3.3 Network Analysis

Circuit theory, and its representation of transmission lines, allows easy calculations in place of a full-field solution using Maxwell's equation. However, as multiple transmission lines are connected it becomes more difficult to maintain the validity of a circuit theory approximation. When two transmission lines with different geometries are connected, the resulting field cannot purely be described as a result of the mismatch in impedance, the reactance associated with a discontinuity must also be accounted for. Furthermore, while a series cascade of two-port networks is easily analysed, multi-port networks rapidly lead to unwieldy analyses (Pozar, 1990).

A variety of network analysis techniques exist, but they all rely on the concept that a network with *n* ports can be represented by a square *n*×*n* matrix, describing the relationship between the inputs and outputs of each port. Once a component in a network has been described using these methods, multiple components may be evaluated as a system based on their matrix definitions as components. The network analysis tools used in this thesis are scattering-matrices, and transition-matrices. These will be described here, but the reader is referred to the work of Pozar (1990, p.192) for an in depth discussion of other available techniques.

For a two port system, Pozar (1990) defines scattering parameters using (2-33):

$$\begin{bmatrix} b_1 \\ b_2 \end{bmatrix} = \begin{bmatrix} S_{11} & S_{12} \\ S_{21} & S_{22} \end{bmatrix} \begin{bmatrix} a_1 \\ a_2 \end{bmatrix} \tag{2-33}$$

Where S_{xy} is the measured response at port *y* in to an input at port *x*, a_x and b_x are the input and output from port *x*, respectively. Equations for the outputs from the system in terms of its inputs may be easily derived from (2-33). Increasing the number of ports in the system increases the size of the scattering-matrix but the principle is consistent, this work is restricted to two port systems.

Transition-matrices are related to scattering-matrices and are defined using (2-34). Transition-matrices allow the properties of a system to be found by multiplying the transition-matrices of its components.

$$\begin{bmatrix} b_1 \\ a_1 \end{bmatrix} = \begin{bmatrix} T_{11} & T_{12} \\ T_{21} & T_{22} \end{bmatrix} \begin{bmatrix} a_2 \\ b_2 \end{bmatrix} \tag{2-34}$$

Transition-matrices are related the scattering-matrices by the following relation (Edwards, 1981; Agilent, 2004):

$$\begin{bmatrix} T_{11} & T_{12} \\ T_{21} & T_{22} \end{bmatrix} = \begin{bmatrix} -\dfrac{\det(S)}{S_{21}} & \dfrac{S_{11}}{S_{21}} \\ -\dfrac{S_{22}}{S_{21}} & \dfrac{1}{S_{21}} \end{bmatrix} \tag{2-35}$$

$$\begin{bmatrix} S_{11} & S_{12} \\ S_{21} & S_{22} \end{bmatrix} = \begin{bmatrix} \dfrac{T_{12}}{T_{22}} & \dfrac{\det(T)}{T_{22}} \\ \dfrac{1}{T_{22}} & -\dfrac{T_{21}}{T_{22}} \end{bmatrix} \tag{2-36}$$

The power of network analysis lies in the ability to study a component in a system from measurements of the system as a whole. In networks where electromagnetic waves propagate, it is difficult to measure a single component in isolation, so being able to *de-embed* a component is a vital tool. The system shown in Figure 2-11 is a representation of a 3 components system, the device under test can be evaluated from a system measurement using (2-38), if the connector properties are known.

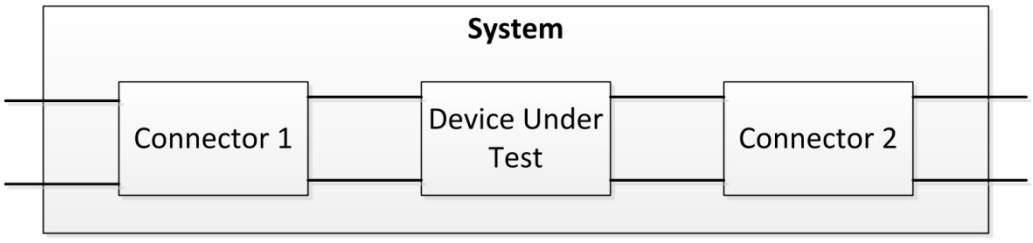

Figure 2-11: Matrix representation of a 3 component system using network analysis methods

Where the transition matrices of the system are defined using:

$$\boldsymbol{T}_{system} = \boldsymbol{T}_{C1}\boldsymbol{T}_{DUT}\boldsymbol{T}_{C2} = \begin{bmatrix} T_{11}^{C1} & T_{12}^{C1} \\ T_{21}^{C1} & T_{22}^{C1} \end{bmatrix} \begin{bmatrix} T_{11}^{DUT} & T_{12}^{DUT} \\ T_{21}^{DUT} & T_{22}^{DUT} \end{bmatrix} \begin{bmatrix} T_{11}^{C2} & T_{12}^{C2} \\ T_{21}^{C2} & T_{22}^{C2} \end{bmatrix} \tag{2-37}$$

Leading to a matrix calculation for the device under test:

$$\boldsymbol{T}_{DUT} = \boldsymbol{T}_{C1}^{-1}\,\boldsymbol{T}_{System}\,\boldsymbol{T}_{C2}^{-1} \tag{2-38}$$

2.4.3.4 Numerical Methods

When faced with a complex system, it is often desirable to compute the electromagnetic field by numerical methods rather than expending considerable effort in deriving and solving the appropriate wave equation. The numerical work in this thesis has been completed using the finite-element method, due to availability of commercial software but the other two methods discussed are very common and are included for completeness (Booton, 1992).

Finite-Difference

Finite-difference methods use a Taylor series expansion of the differential wave equation to approximate the solution to the wave equation at a grid of points. The finite-difference method may be applied to simplified one, two or three dimensional systems, and is commonly applied in the time-domain to increase computational efficiency (Weiland, 1996). A very large body of research giving results using the finite-difference method has been published, good example applications include simple antenna radiation (Maloney *et al.*, 1990) and EM field penetration into cavities (Taflove, 1980).

Finite-Element

The finite-element method divides the system into small, tessellating, regions known as finite-elements. An integral across the region, may then be approximated by summing the value of the integral for each finite-element. Whilst the function across the whole region can be very complex, each finite-element can be described simply using the values of the surrounding finite-elements. Given boundary conditions, the values on each successive element are iteratively calculated, and so the system can be approximated (Booton, 1992).

As with finite-difference methods, a very large body of research exists discussing finite-element modelling. Results which are relevant to this thesis include a finite-element method for evaluating the electromagnetic field in inhomogeneous media (Mur and de Hoop, 1985), and calculating the scattering-matrix of coaxial waveguide junction (Marouby *et al.*, 1990).

This thesis makes use of a commercial finite-element software package for electromagnetic field predictions. This software is easily used and very powerful, but can lead to the impression that finite-element modelling is possible with no understanding of the underlying physics. Clearly a finite-element model is only as accurate as its underlying equations – something which must not be forgotten (COMSOL, 2013).

Method of Moments

The method of moments is another well used numerical method, which looks to solve a function by projecting it onto the domain of a linear function and performing a numerical minimization (Harrington, 1987). The history of the method of moments – in the context of electromagnetic fields – is concisely given by Harrington (1990) who cites Harrington (1961) for the original development of the method. However, as with much research, the more informative references come in the form of later review papers. In this instance, the works of Ney (1985) and Harrington (1987) give a good introduction to the method of moments.

2.4.4 Propagation in Stratified Media

There is significant motivation for solutions to wave equations in stratified media, modelling the earth as such as system allowed prediction of radio wave propagation over the earth (Wait, 1953), and under the sea (Mott and Biggs, 1963). In the years since these papers, a very large body of work has built up around this subject, and the excellent review paper by Wait (1998a) is highly recommended for the reader interested in a full history of those developments, which is beyond the scope of this work. An appendix of the paper by Wait (1998a) also contains useful definitions of the various types of waves which propagate in layered media, this is most instructive as the terminology in this area is not consistent across the literature.

For the situation where a wave is excited above a boundary, it is well known that the boundary can guide that wave, usually with a wavenumber between the wavenumber of the media either side of the boundary (Harrington, 1961). However, in the situation with multiple layers, the

waves which propagate along the boundaries, through each layer, and directly between source and excitation form a complex system which is well reviewed by King *et al.* (1992).

2.5 SIGNAL PROCESSING

In the context of this thesis, signal processing refers to the treatment of measured or simulated signals to infer information about their source or propagation path. Much of the signal processing used in later chapters is based on relatively simple concepts which are covered here. This section gives an introduction to the relevant fundamentals of signal processing; the literature covering signal detection is then explored; the extensive research relating to the estimation of the direction of arrival is reviewed; and finally, suppression of noise and interference is covered.

These topics are not meant to be a complete review of signal processing literature, but a distillation of the selected topics used in this thesis. The reader is referred to the vast body of literature for a generalised overview, see Baher (2001), for example.

2.5.1 Fundamentals

The following concepts are familiar to the majority of electrical engineers, and have long since passed from state-of-the-art to useful tools. Consequently, they will be concisely described with references which can provide supplemental coverage.

2.5.1.1 Signal Decomposition and Notation

Signal Decomposition

In 1822 Fourier published work showing that any real function may be described as a summation of an infinite number of sine and cosine functions, which exists in the range $\pm l$. This is the Fourier series (Baher, 2001):

$$f(x) = \frac{a_0}{2} + \sum_{k=1}^{\infty} \left(a_k \cos\frac{k\pi x}{l} + b_k \sin\frac{k\pi x}{l} \right) \tag{2-39}$$

Where a_k and b_k are the magnitude coefficients of the Fourier series.

For data which is sampled, and non-infinite, the discrete Fourier transform (DFT) makes a similar summation possible, leading to the Fourier pair which describe a periodic, sampled, function in time and frequency domains (Baher, 2001):

$$f(n) = \frac{1}{N}\sum_{k=0}^{N-1} \mathrm{F}(k) \exp\left(\frac{j2\pi kn}{N}\right) \rightleftharpoons F(k) = \sum_{n=0}^{N-1} \mathrm{f}(n) \exp\left(\frac{-j2\pi kn}{N}\right) \qquad (2\text{-}40)$$

Where $f(n)$ is a time-domain sequence of N elements, $\mathrm{F}(k)$ is the equivalent frequency-domain sequence, and j is the square-root of -1.

In practical terms, this means that a real signal of N samples may be represented as a sum of $N/2$ independent sinusoids whose frequencies are determined by the length of the sample and the sampling frequency. These sinusoids have both magnitude and phase, leading to the representation of the frequency-domain using complex numbers.

The method used in this thesis to achieve the discrete Fourier transform, and its inverse, is known as the fast Fourier transform (FFT). First devised by Cooley and Tukey (1965) the FFT algorithm has come become the usual implementation of the DFT (Oppenheim and Schafer, 1989).

Frequency-Domain Notation

The fundamental notation for a signal in the time and frequency-domain is given in (2-41) (Baher, 2001):

$$f(t) \rightleftharpoons F(\omega) \qquad (2\text{-}41)$$

Where $f(t)$ is a time-domain signal dependant on time, t, and $F(\omega)$ is a complex frequency-domain signal dependant on angular frequency ω. It is important to note that no information is lost in the conversion between these notations.

The two properties of data-points in the frequency-domain are magnitude and phase. The summation of sinusoids representing the time-domain signal requires that each sinusoid may be of any magnitude and offset by any phase. Standard vector notation is employed to describe the

magnitude and phase of a sinusoidal signal, and the terms are used throughout this thesis (Kreyszig *et al.*, 1999).

Factors to Consider when Using the Frequency-Domain

Properties of the DFT

Baher (2001) gives simple explanations for several important properties of the DFT, these include:

- Linearity: That signals may be summed in either the time or frequency-domain with equal success.
- Phase or time shifting: A shift in the time-domain of a signal by m samples is equivalent to multiplication by $\exp(j2\pi mk/N)$ in the frequency-domain.
- Other properties defined include the power in a waveform; correlation in time and frequency-domains; and the equivalence between convolution in the time-domain and multiplication in the frequency-domain.

Windowing

When taking a finite sample of a stationary time-domain function, the frequency-domain function is defined as the sum of a finite of number of sinusoids. If the sampling is modelled as multiplication by a weighting function, then the effect of this distortion is easily calculated. A DFT performed with a rectangular window –that is no windowing applied except for taking a discrete sample – the frequency-domain signal is convolved by the DFT of a rectangular window. The DFT of a rectangular window is given by Baher (2001):

$$w_r(t) \rightleftharpoons NT\frac{\sin(\omega NT/2)}{\omega NT/2} \tag{2-42}$$

Where w_r is the rectangular weighting function between $\pm NT/2$, N is the number of samples, and T is the sampling period. The effect of this windowing is to spread the spectrum across a wider range of frequency bins than might have been anticipated.

The excellent paper by Harris (1978) provides a thorough review of different windowing functions, which is summarised for some common windows below (Table 2-1). The window functions are defined as $w[n]$ where n is the sample number, falling between 0 and M. Each window function is zero where n is greater than M or less than 0. Comparison is made using the difference in amplitude between the main-lobe and greatest side-lobe (dB); the -3 dB bandwidth (BW) which indicates the width of the main-lobe; and the coherent gain. Coherent gain is the summation of the weighting-function across all the samples and indicates the amplitude-loss due to the application of the window.

Window Type	Window Function	Side-Lobe Amplitude (dB)	-3 dB BW (frequency bins)	Coherent Gain
Rectangular	$w[n] = 1$	-13	0.89	1.00
Bartlett	$w[n] = \begin{cases} 2n/M, & 0 \leq n \leq M/2 \\ 2 - 2n/M, & M/2 \leq n \leq M \end{cases}$	-27	1.28	0.50
Von Hann	$w[n] = 0.5 + 0.5\cos(2\pi n/M)$	-32	1.44	0.50
Hamming	$w[n] = 0.54 - 0.46\cos(2\pi n/M)$	-43	1.30	0.54

Table 2-1: Properties of a selection of common windowing functions (after Harris, 1978)

Aliasing

A DFT may be well described by the sum of sinusoids between $\pm\,\omega_s/2$, where ω_s is the angular sampling frequency. However, it would be equally well described by $\omega_s \pm \omega_s/2$. Therefore, one must assume and ensure that all signals measured have been sampled at a rate sufficient to ensure that the frequency-domain representation is accurate. This is the well-known Nyquist criterion (Kreyszig *et al.*, 1999).

2.5.1.2 Correlation

Time-Domain

A significant area within signal processing involves measuring the nature of the received signal. Consequently, the measure of the similarity of two signals is of vital importance. Furthermore, it will be shown that by applying correlation methods, a signal may be detected in situations with

low signal-to-noise ratios. The correlation coefficient, r_{fg}, of two complex variables, $f(t), g(t)$, is defined by Dupraz (1986):

$$r_{fg} = \frac{C(t)}{\sigma_f \sigma_g} \tag{2-43}$$

Where σ_f is the standard deviation of variable f, and the covariance, $C(t)$ of functions $f(t)$ and $g(t)$, is defined as:

$$C(t) = \overline{(f(t) - \bar{f})(g(t) - \bar{g})^*} \tag{2-44}$$

Frequency-Domain

The correlation coefficient of two variables may also be determined in the frequency-domain. The cross-energy spectrum, is a Fourier pair with the cross-correlation (Baher, 2001):

$$C(t) \rightleftharpoons \mathcal{E}_{fg}(\omega) = F^*(\omega)G(\omega) \tag{2-45}$$

The normalised complex cross-spectrum is then given by Bendat (1978):

$$\hat{\gamma}_{fg}^2(f) = \frac{\left|\hat{C}_{fg}(f)\right|^2}{\hat{C}_{ff}(f)\hat{C}_{gg}(f)} \tag{2-46}$$

The process of normalisation, reduces the complex cross-spectrum magnitude to between 0 and 1. The accents in (2-46) indicate that the function can be averaged across multiple measurements. This is a common method to increase system performance, which is also utilised in array signal processing.

SNR can be measured from the complex cross spectrum magnitude as follows (Quazi, 1981):

$$(SNR)^2 \approx \frac{S^2}{(S+N)^2} \Big/ \left[1 - \frac{S^2}{(S+N)^2}\right] = \frac{|\gamma(f)|^2}{1 - |\gamma(f)|^2} \tag{2-47}$$

Combining (2-47) with the work of Bendat (1978) gives an expression for phase error in the complex cross spectrum, as a function of number of averages, n_d, and SNR:

$$\Delta\hat{\phi}_{xy} = \frac{1}{SNR\sqrt{2n_d}} \tag{2-48}$$

These equations give the impression that phase accuracy for a given measurement can be arbitrarily increased, for a sample of fixed length, by increasing the number of averages. However, by increasing the number of averages, the SNR at the frequency of interest is reduced as the frequency bin is widened, leading to the same accuracy. Therefore, to increase phase accuracy in the complex cross-spectrum, the SNR or the number of samples must be increased.

2.5.1.3 Array Signal Processing

An array is defined by Johnson and Dudgeon (1993) as "a group of sensors located at distinct spatial locations". A large number of applications exist for array signal processing, including seismic, acoustic and electromagnetic applications, the reader is referred to the useful book by Haykin *et al.* (1985) for selected examples. By utilising an array of sensors, more information may be gained about a measured signal than could have been achieved with a single sensor. This is achieved in a number of ways:

Increased Signal-to-Noise Ratio

Simply by averaging the output of each sensor in an array, the signal-to-noise ratio is increased by a factor proportional to the number of sensors in the array and the joint-statistics of the noise. This is due to the simple process of the signal amplitude remaining unchanged after averaging, while uncorrelated noise amplitude is degraded linearly (Johnson and Dudgeon, 1993).

Signal Characterisation

In addition to increased signal-to-noise ratio, an array may measure the speed of propagation or the direction of arrival of a propagating wave. This is discussed in greater depth below. In addition to locating targets, an array may differentiate between a number of targets, up to the number of elements in the array Johnson and Dudgeon (1993).

Array Configurations

A vast number of different array configurations exist. The work in this thesis is limited to a linear array. For details of square, circular, or even cubic array configurations see chapter 3 of the work by Johnson and Dudgeon (1993).

2.5.2 Signal Detection

"Signal detection and estimation…deals with the processing of information-bearing signals for the purposes of extracting information from them" (Poor, 1994). Any system which receives signals operates in an environment without certainties, consequently signal detection looks to probability theory to achieve its aims. On a very fundamental level, the problem of signal detection is well defined by Brillinger (1985), consider (2-49):

$$Y(x,y,t) = \rho\cos(\alpha x + \beta y + \gamma t + \delta) + \epsilon(x,y,t) \qquad (2\text{-}49)$$

Where $Y(x,y,t)$ is the measured signal, α and β constitute the wavenumber, γ is the angular frequency of the signal, and $\epsilon(x,y,t)$ is the additive noise signal. Assuming that $Y(x,y,t)$ and γ are known, signal detection is the process of testing whether $\rho \neq 0$. All other signal processing problems may be considered as estimating the unknown parameters in (2-49). Clearly, this analysis assumes a single narrowband signal, without dispersion or interference, but the purpose of signal detection is consistent regardless of the function used to describe the propagating wave.

The signal detection and processing in this thesis is comparatively simple, the aim is to determine if a signal has been received and measure its phase. For treatments of more sophisticated signal detection methods, the reader is referred to the well written books by Poor (1994) or Wickens (2002).

2.5.3 Direction of Arrival Estimation

A common requirement of signal processing is to estimate the location or bearing of the source. This section focuses on direction of arrival (DoA) estimation using signals received from an array of omnidirectional antennas. Several other assumptions are made initially, most importantly that

the signals received by the antennas are well approximated by plane waves. The validity of this assumption is explored in Chapter 5, and the literature studying the additional complexity of a near-field source is covered below. This section primarily considers the methods used with a linear array of antennas, shown in Figure 2-12, but also notes the other configurations available to the researcher and their relative merits.

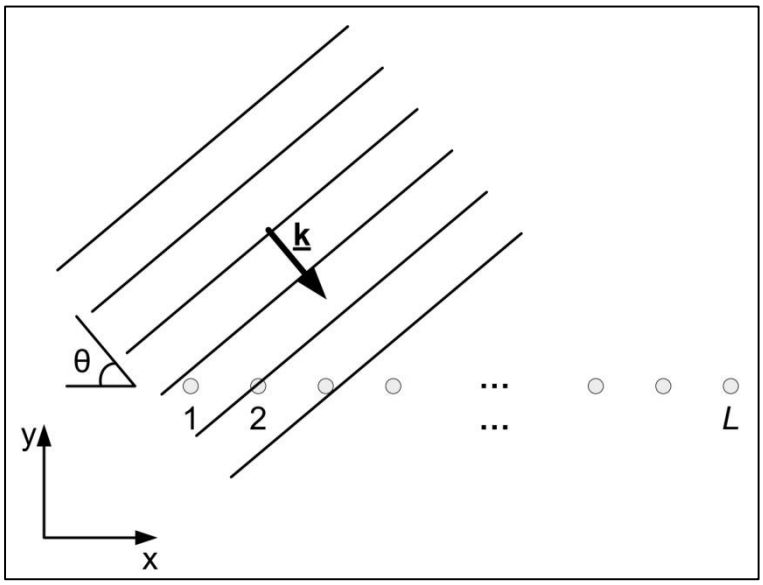

Figure 2-12: Illustration of the configuration used to calculate the direction of arrival at an antenna array, the measured signal is shown as a single plane wave with wave-number k arriving at angle θ.

2.5.3.1 Plane Wave Signals

In his extensive review of antenna arrays for beamforming and DoA estimation Godara (1997) notes that the signal on one element of an array may be described in terms of a plane wave signal measured on the preceding element as follows:

$$y_\ell(t) = x_\ell(t)e^{j2\pi\Delta_0 \cos\theta} \tag{2-50}$$

Where $y_\ell(t)$ and $x_\ell(t)$ are the signals measured on the current and previous array elements, respectively, Δ_0 is the array spacing as a number of wavelengths, and θ is the DoA of the signal. In a review paper on DoA estimation and array beamforming, Godara (1997) cites over 500 references and explores more than 10 methods for DoA estimation, whose basis is the coherence matrix between array elements, which includes the calculation of the relative phase change along the array.

The techniques used to estimate the DoA have been developed for a wide range of applications, including SONAR (Johnson, 1982; Shengli and Willett, 2007), oceanography (de Moustier and Alexandrou, 1991; Paduan *et al.*, 2006) and geosciences (Şahin and Miller, 2001; Ebihara and Sato, 2001), but the field which most driven progress in this area is mobile communications (DeGroat *et al.*, 1993; Godara, 1997).

Measuring the Effectiveness of DoA Estimation Methods

DoA estimation methods may be compared using several metrics including resolution, bias, variance, and probability of resolution (Godara, 1997). To aid the understanding of these metrics Figure 2-13 is given which show the difference between different DoA methods graphically.

The first measure of the effectiveness of a method of DoA estimation is resolution, which in this context is "the ability of an estimate to reveal the presence of two equal-energy sources which have nearly equal bearing" (Johnson, 1982). That is to say, resolution is less concerned with the precision of the estimate of the DoA, than with the necessary difference in bearing between two signals for two sources to be estimated, rather than a single combined source. In the case shown in Figure 2-13, the linear predictive measure has a resolution of less than 10 degrees at SNR = 0 dB, whereas it is apparent that the Bartlett method has a resolution of greater than 10 degrees.

However, Seligson (1970) (cited by Cox, 1973) published work in which he showed that, under certain conditions, high-resolution methods may show behaviour which would be thought of as low-resolution in the more general sense of the term. Seligson (1970) notes that the Bartlett method can have smaller angles between the -3dB points either side of a DoA estimate than the maximum-likelihood method, one of the "super-resolution" beamformer methods (Johnson and Miner, 1986). In other words, the peaks shown in Figure 2-13 may be wider under, some circumstances, with high resolution techniques.

The second measure of the effectiveness of a DoA estimation method is bias, defined as "the error in location of the spectral peak" (Johnson, 1982). The mathematical analysis of bias is more complex than that of resolution, especially when considering the eigen-decomposition required

for the super-resolution methods (Godara, 1997). The expressions for bias for a number of DoA methods were derived by Xu and Buckley (1994).

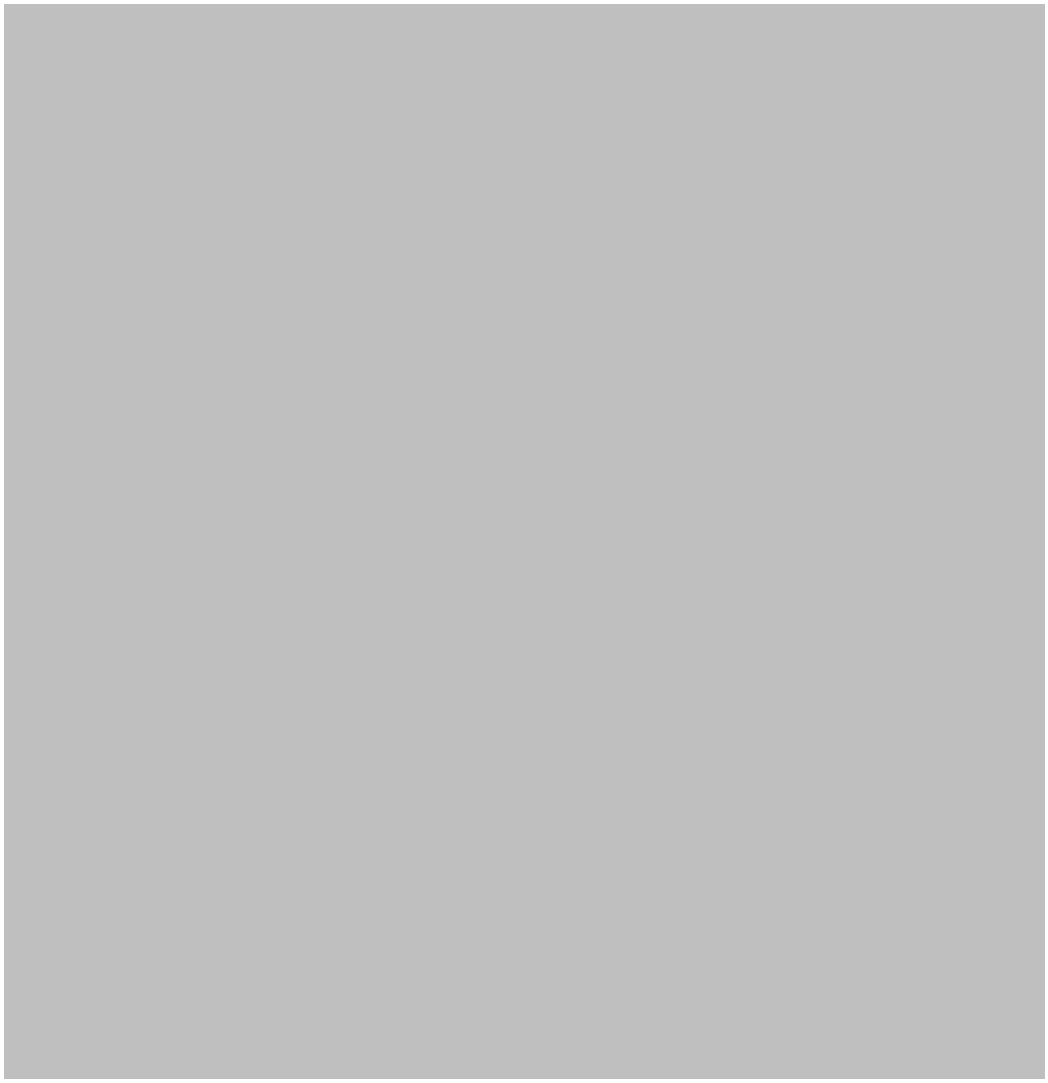

Figure 2-13: Results of three different DoA estimation methods, for data due to two signals 10 degrees apart with 0dB SNR for each signal. DoA estimates used are the Bartlett method (a), the maximum-likelihood method (b), and the linear-predictive method (c) (after Johnson, 1982). © 1982 IEEE

A final measure of effectiveness is the noise tolerance of an estimation method. All methods will be less effective with reduced SNR, but performance of different methods does not degrade in a uniform manner (Gething, 1978; Walker, 1985).

Error in Direction of Arrival Measurements

The accuracy of DoA estimate is dependent on a number of factors, and the methodology used to make the calculation. In the case of the, well used, MUSIC algorithm Srinath and Reddy (1991) calculated that the standard deviation of a DoA estimate using a linear sensor array is:

$$E(\Delta\theta_1^2) = \frac{12\sigma_p^2}{M(M^2-1)}\left(\frac{\lambda}{2\pi d\cos\theta_1}\right)^2 \quad (2\text{-}51)$$

Where σ_p^2 is the variance in the received signal phase measurements, M is the number of sensors in the array, λ is the signal wavelength, d is the sensor separation, and θ_1 is the true direction of arrival. The phase variance may be more usefully expressed in terms of the signal-to-noise ratio (SNR) as (2-52) (Bendat and Piersol, 1971; Bendat, 1978; Quazi, 1981). A derivation of this equation is shown in Chapter 5.

$$\sigma_p = \frac{1}{SNR\sqrt{M}} \quad (2\text{-}52)$$

Substituting (2-52) into (2-51) gives an expression for the error in a DoA estimate including the dependence on SNR:

$$E(\Delta\theta_1^2) = \frac{12}{SNR^2M^2(M^2-1)}\left(\frac{\lambda}{2\pi d\cos\theta_1}\right)^2 \quad (2\text{-}53)$$

The accuracy required of any DoA estimate will be determined by the application. However, in order to give an indication of the potential accuracy in situations relevant to this work, Figure 2-14 and Figure 2-15 show standard deviation of a DoA estimate as a function of SNR, number of sensors and true direction of arrival, for a typical signal used in the later chapters of this work. In many cases the standard deviation is shown to be less than 5 degrees. However, at low signal-to-noise ratios, or low numbers of sensors errors are significantly greater.

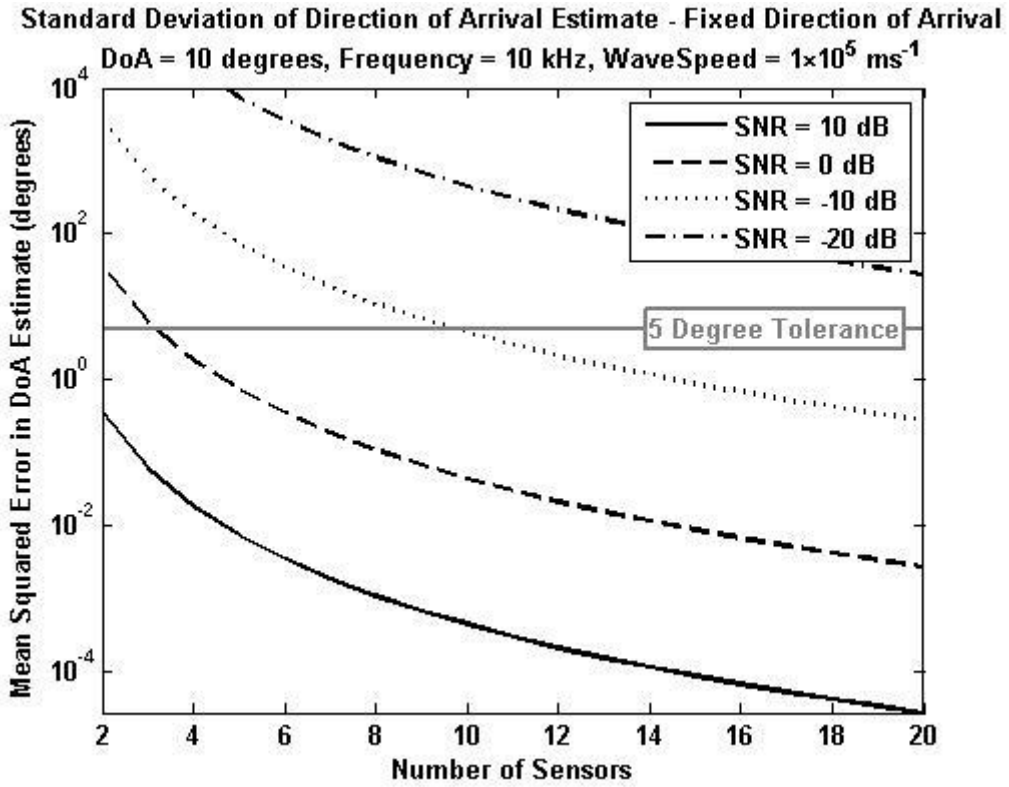

Figure 2-14: Standard deviation of direction of arrival estimates as a function of number of sensors and signal-to-noise ratio.

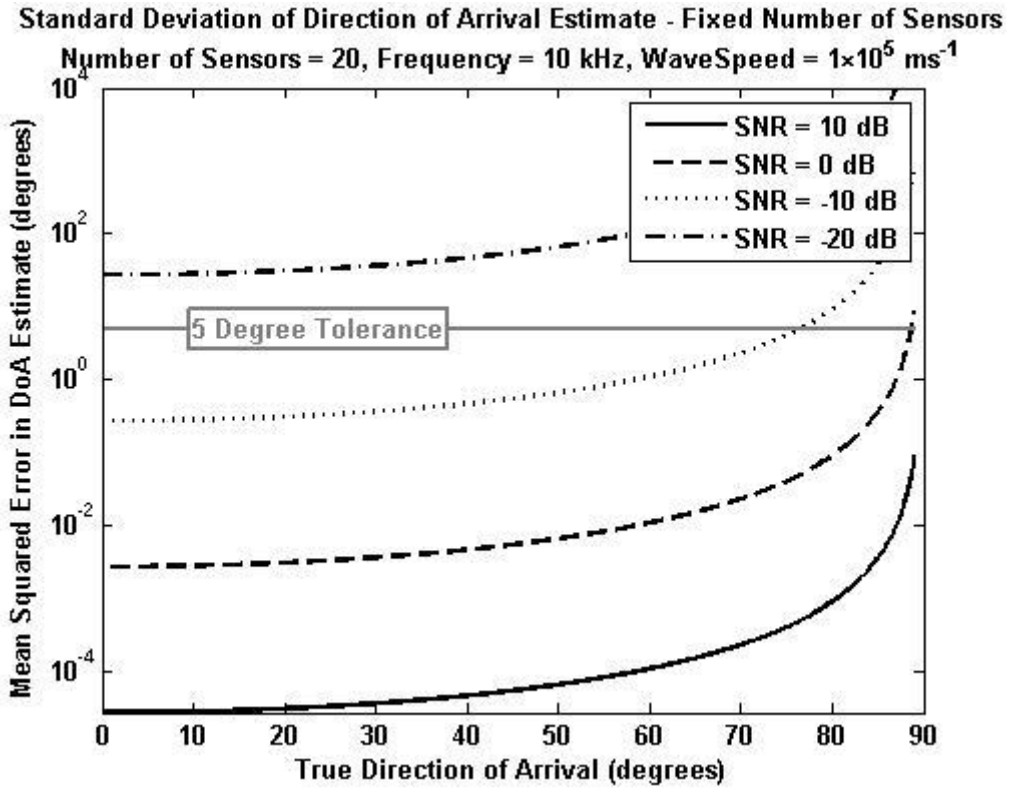

Figure 2-15: Standard deviation of direction of arrival estimates as a function of the true direction of arrival and signal-to-noise ratio.

Summary of Methods

"Spectral estimation methods" for the estimation of DoA have been in use for many years. The work by Johnson (1982) is often cited, and provides a good comparison of a number of spectral estimation techniques. These techniques rely on "steering" the array towards a particular direction by applying a weighting function which reinforces signals whose phase delay is consistent with that direction. This weighting is known as the steering vector, which is derived differently in different methods.

Other methods are available which utilise eigen-values and eigenvectors of the spatial correlation matrix to further enhance the signals propagating in the desired direction. See Chen *et al.* (2010) for further details.

2.5.3.2 Direction of Arrival in Unknown Media

The fundamental equation of DoA estimation in the far-field (2-50) relies on known wavelength. In the event that the wavelength is unknown, it must be estimated in the same process as the DoA. A large body of work aims to correct for small errors in sensor location, as a function of wavelength (Flanagan and Bell, 2001). However, fewer publications tackle the challenge of completely unknown wavelength.

The work by Ng (1995) uses signals of known bearing to calibrate an array where wavelength is unknown, but this approach is often impractical. Algorithmic methods have been published which allow the sensor positions to be estimated with the DoA by iteratively adjusting position to reduce an associated cost function. However, errors never fall to the values expected for known sensor position and significant complexity is encountered when implementing these algorithms (Flanagan and Bell, 2001). However, this is an area of active research and performance has improved significantly in recent years (Aktas and Tuncer, 2010).

2.5.3.3 Direction of Arrival Estimation in the Near-Field

The previous sections all consider DoA estimation methods which rely on the plane-wave assumption, implicit in (2-50). When the measured signal is due to the near-field, the plane-wave assumption must be replaced by a spherical approximation and different methods are required. Godara (1997) cites the work of Weiss *et al.* (1988) - who present a DoA algorithm which does not assume uniform signal magnitude along the array – as a method for processing near-field measurements. However, this methodology does not account for the non-linear phase change expected when measuring a spherically propagating wave. A better solution is to adjust the algorithm to account for quadratically changing phase along the array (Grosicki *et al.*, 2005). A concise review of several near-field methods is given by El Korso and Pesavento (2012).

2.5.4 Noise and Interference Suppression

The relevant text books are remarkably reluctant to define noise, Skomal (1978) takes 3 pages to define man-made radio noise. The definition which is used throughout this work is "an unwanted signal or a disturbance (as static or a variation of voltage) in an electronic device or instrument" (Merriam-Webster, 2013a). This definition includes random variations due to physical phenomena, but also propagating signals which are unwanted.

Signal-to-noise ratio (SNR) is the factor which limits the performance of transmitting and receiving systems. In the case of phase-measurements using correlation techniques, (2-48) gives the standard deviation of the phase measurement as a function of SNR. Similarly, in the case of digital communication, the probability of error in receiving data bits is dependent on the SNR (McDonough and Whalen, 1995, p. 210). Many advanced signal processing techniques have been developed, but the fundamental limitation is always the ratio of signal power to noise power.

2.5.4.1 Noise Properties

There are so many types of noise that a full coverage of their properties here is impossible. The properties of several of the most relevant types of noise are summarised. The reader is referred to the works of Van Der Ziel (1955) for a summary of noise due to physical phenomena; Skomal

(1978) for an in-depth coverage of man-made noise; or Robins (1983) for an introduction to noise caused by signal processing techniques. It will also be shown that increasing the understanding of noise properties increases the researcher's ability to suppress it.

Quantisation Noise

In any system where analogue data is measured and represented digitally, an inherent error exists between the original analogue signal and its digital representation. A digital system is fundamentally limited by its sampling frequency, and the number of bits representing each sample. This noise has been well studied, the work of Bennett (1948) is often cited as an early study of quantisation noise. Whilst Bennett may not have envisaged 24-bit ADCs operating at gigahertz frequencies, his methods still apply. However, when considering a 24-bit ADC operating between ±10 V, the maximum error for a sample is 5.96×10^{-7} V. Assuming the received signal is uniformly distributed, this gives a signal to quantisation-noise ratio of 144 dB, rendering quantisation noise negligible (Gray, 1990).

Interfering Signals

Interfering signals are a noise source which is almost impossible to predict. These are signals which are intentionally transmitted but are not of interest or use to the measurement. The frequency, amplitude, and direction of these sources is entirely dependent on the transmission, over which the researcher has no influence.

Electrical- Generation and Transmission-Line Noise

Chapter 3 of the work by Skomal (1978) gives a detailed description of the source of electrical-generation and transmission-line noise. Most energy of this noise is at 50 Hz, but there is also significant energy at harmonics of 50 Hz. Measurements have been published which show field-strength due to transmission-line noise exceeding thermal-noise by 40 dB at 10 MHz, in the immediate vicinity of high-voltage power lines. The ubiquitous nature of this noise source forces the researcher to avoid transmitting at frequencies of multiples of 50 Hz as a priority.

2.5.4.2 Receiving Signals in Noise

Receiving a signal in the presence of noise could be as simple as applying a moving-average filter to recover a good estimate of the original waveform. However, a more common problem is to adapt the receiving system to discriminate between noise and the desired signal. This task is simplified if the signal or noise are well characterised.

Filtering for Known Signal Properties

The most common method of filtering is by frequency, when receiving a signal of known spectral content, the receiver can filter to attenuate all frequencies outside of the desired frequency range. The imperfect filter is likely to introduce some distortion into the waveform, but the increase in SNR can be very large. Filtering a narrowband signal is discussed in detail by McDonough and Whalen (1995, Ch. 3).

Frequency is not the only characteristic by which a signal may be filtered. If the waveform of the expected signal is known, then correlation analysis can detect signals which would otherwise be obscured by noise. It has been shown, that when deciding between two known signals, applying a correlation based detector can significantly increase the probability of correct detection (McDonough and Whalen, 1995, pp. 202 - 207).

Antenna Directionality

If an omnidirectional antenna is used to transmit and receive the measured signal, then a large proportion of the transmitted power is wasted, and a large proportion of the received noise is due to signals from different bearings to the desired signal. By transmitting using a directional antenna, or beamforming an array of antennas, the signal strength at the receiver can be greatly improved (Hall and Vetterlein, 1990). Similarly, by using a directional antenna to receive, or calculate a signal's direction of arrival, the measured SNR can be greatly improved (Godara, 1997).

2.6 CURRENT METHODS FOR DETECTING UTILITIES IN THE SHALLOW SUB-SURFACE

This work was funded as part of the *Mapping the Underworld* (MTU) project, an EPSRC funded project to develop a multi-sensor device to locate and identify buried utilities. Several of the publications introducing MTU provide a good overview of the technologies selected to form part of that project (Metje *et al.*, 2007; Royal *et al.*, 2011). The following sections will introduce those technologies, their maturity, and relative performance.

2.6.1 Ground Penetrating Radar

Ground penetrating radar (GPR) is the most mature of the technologies presented in this section. Research on GPR began with "ice radio echo sounding" in the 1960s in response to reports of altimeter errors above the polar ice caps due to radio waves penetrating the ice (Annan, 2002). Since that time, GPR has been used for a wide range of applications including sedimentology (Neal, 2004), measurement of soil water content (Huisman *et al.*, 2003; Lambot *et al.*, 2006; Minet *et al.*, 2010), archaeology (Leckebusch and Peikert, 2001; Leckebusch, 2003), and for oil exploration (Sixin *et al.*, 2004; Ebihara and Hashimoto, 2007). A history of the development of GPR is beyond the scope of this work, and the reader is referred to the work by Annan (2002) for an in depth history.

Physically, GPR systems usually consist of two or more antennas, often co-located on the same chassis, one transmitting and the others receiving, at a frequency range of between 10 MHz and 1 GHz (Huisman *et al.*, 2002). The operating frequency, antenna design, and antenna configuration all contribute to the specific performance of the GPR system. Common performance metrics include spatial-resolution, usable-depth for a particular material, and spectral leakage outside of the designated frequency. Any discontinuity in the dielectric properties of the measured area will result in reflections; the phase and amplitude of these reflections may then be resolved to give position or properties of the reflector (Neal, 2004). Results are presented in a number of ways, raw GPR data is very difficult to interpret without significant experience, a process known as migration is commonly employed which presents a 2 or 3 dimensional image

of the subsurface which is more easily interpreted by the user, examples of this process are given by Leckebusch and Peikert (2001).

2.6.2 Acoustic Technologies

Acoustic technologies use mechanical waves, which may be audible to the human ear, to detect utilities. Acoustic technologies have been used for subsurface detection in applications including mine hunting (Korman and Sabatier, 2004), and leak detection (Fuchs and Riehle, 1991). The focus of acoustics in detection of utilities has been pipe, or soil, configurations which have traditionally been challenging for GPR or electromagnetic technologies, such as plastic pipes or water saturated soils (Muggleton and Brennan, 2008). The research being undertaken as part of the Mapping the Underworld project utilises low-frequency excitation and an array of geophones to measure the accelerance of the ground. Accelerance is defined as a measure of the acceleration in the ground compared to the applied excitation force (Muggleton *et al.*, 2012).

2.6.3 Magnetic Field Sensors

The magnetic field sensor work undertaken as part of the Mapping the Underworld project uses "fields of opportunity" to detect buried cables and any metallic objects which may re-radiate the magnetic field generated by current flow in buried cables. The Mapping the Underworld magnetic field sensor is a passive technology, relying on detecting the "fields of opportunity" (Metje *et al.*, 2007; Ping *et al.*, 2010). A more prevalent application of magnetic field technology is the cable avoidance tool (CAT) which is a handheld tool that passively detects the magnetic fields from buried cables, and also has higher frequency active modes. The use of this device is widespread and long standing, it was reported to be in wide use in the 1980s by Garnett (1984), and its operating principles are well understood (Lee, 2002; Metje *et al.*, 2007).

2.6.4 Low-Frequency Electromagnetic Technology

The research presented in this section forms the specific background for the work presented in Chapters 5 and 6, consequently this section is presented in more depth than the previous sections which serve mainly to provide background and context.

2.6.4.1 Electrical Resistivity Surveys

Introduction

Electrical resistivity surveys have been undertaken for many years; Shepard (1934) patented a device for measuring the resistivity of soil, as a method of detecting corrosion along buried pipelines. The patent claimed that significant changes in resistivity along a pipeline could indicate corrosion or pipe damage. A more recent paper by Samouëlian *et al.* (2005) presents a good review of electrical resistivity surveying, the underlying principles of which are given here.

Common configurations include the Wenner and Wenner-Schlumberger configurations, shown in Figure 2-16, which utilise 4 electrodes. By injecting a current into the ground using electrodes C1 and C2, and measuring the resulting voltage at different points using electrodes P1 and P2, the electrical resistivity may be calculated. These calculations are not complex in a homogenous medium, relying on the position of the electrodes, the definition of resistivity in a planar medium, and Ohm's law, see Samouëlian *et al.* (2005, pp.175-176).

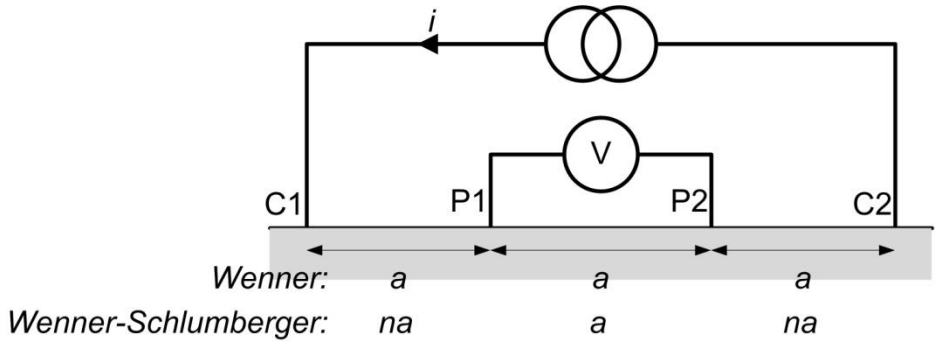

Figure 2-16: Wenner and Wenner-Schlumberger resistivity survey configuration (after Earl, 1998; Samouëlian *et al.*, 2005)

2.6.4.2 Frequencies Used

A range of frequencies have been used in the measurement of electrical resistivity. Initially, DC was used. The obvious advantage of simplicity, both in signal generation and voltage measurement, made this the obvious choice for early researchers. However, the use of DC does present difficulties; particularly that the electrodes become prone to polarization. Electrode polarization occurs when the potential on an electrode causes a build up of charge in the soil

around the electrode due to the change from electronic to ionic conduction, which dominates in soils (Santamarina *et al.*, 2001). Several methods allow the researcher to overcome this problem, including the use of higher frequencies; altering the experimental method whilst still using DC; or the use of non-polarizing electrodes (Levitskaya and Sternberg, 1996a). The use of higher frequencies is an easy and low-cost option with modern electronics (You *et al.*, 2010), but does not completely remove polarization effects at frequencies below 1 MHz (Logsdon, 2005) which are high enough for the complex permittivity of soil to cause very different results to those expected of DC measurements. It is, therefore, common to use low frequencies of less than 50 Hz to counteract the worst of the polarization effects (Hobbs, 1999). Kearey *et al.* (2002) (cited by Earl, 1998) present Figure 2-17 which shows the transition from "DC" resistivity to higher frequency measurements, and the qualitative impact on the measured resistivity.

Dahlin (2000) demonstrated that by using DC measurements and switching the direction in which the current flows, polarization may be overcome by noting the equal but opposite voltage bias due to polarization, and fitting appropriate curves to the measured data. This method is very simple, but care must be taken to allow time for the electrodes to depolarize, especially when the electrode functions are not consistent throughout the measurements.

The final option is the use of non-polarizing electrodes, which surround the electrode in a compatible salt solution – such as copper sulphate for copper electrodes, or silver nitrate for silver electrodes – which allow electronic conduction with the soil (Hobbs, 1999). The chemistry which allows electronic conduction into the soil is beyond the scope of this work, the reader is referred to the review papers by Levitskaya and Sternberg for an overview of the underlying chemistry (Levitskaya and Sternberg, 1996a; b).

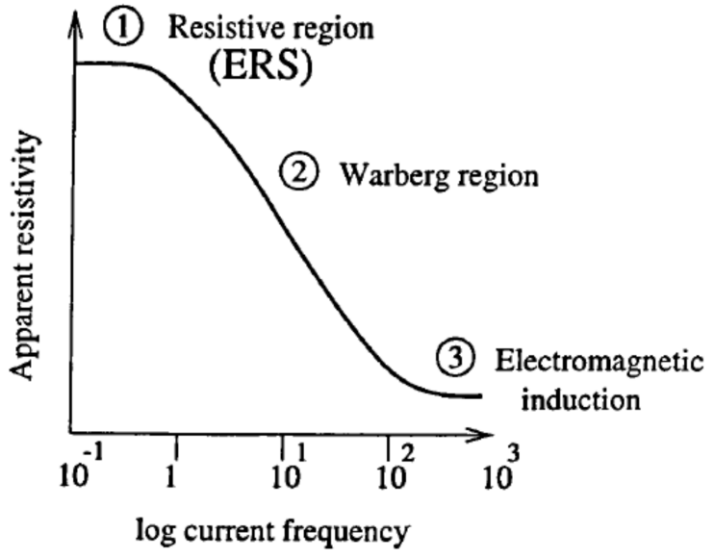

Figure 2-17: Frequency ranges used in resistivity surveys after Kearey *et al.* (2002) (cited by Earl, 1998)

2.6.4.3 Depth of Investigation

The depth of investigation of a resistivity survey is determined by the geometric factor of the probe configuration and the resistivity of the ground, for example in the Wenner configuration (Figure 2-16) the geometric factor is given by $2\pi a$ where a is the electrode separation, whereas if the Wenner-Schlumberger configuration is used the geometric factor is $\pi n(n+1)a$, where n is the factor determining the increase in separation between the current and voltage electrodes (see Figure 2-16) (Samouëlian *et al.*, 2005, p. 182). Barker (1989) presented a concise study of the effects of different probe configurations and their spacing on the depth of investigation, as well as discussing the precise definition of "depth of investigation" which can be misleading. It is easy to see how a three-dimensional picture may be built up by repeating measurements with different probe spacing, although the precise depth is strongly dependant on the structure and resistivity of the soil (Samouëlian *et al.*, 2005).

2.6.4.4 Applications and Limitations

Electrical resistivity tomography has a wide range of applications, this literature survey is limited to geophysical surveying applications but the extensive literature outside of this limitation should be noted. This includes the use in process engineering where resistivity can indicate the progress of a variety of mixing processes (Dickin and Wang, 1996); and medical applications where the

resistivity, measured simply across the chest (Harris *et al.*, 1987) or with complex three-dimensional imaging (Metherall *et al.*, 1996), of the human anatomy can provide a range of diagnostically significant information (Pethig, 1984).

Measurement of Soil Properties

A detailed review of the electromagnetic properties of soil is given above. However, one major use of electrical resistivity surveys is to identify electromagnetic properties of soil. Particularly when combined with some existing knowledge, the electrical conductivity of the soil can give the researcher information about the soil water content, constituent materials, temperature, or salinity (Samouëlian *et al.*, 2005). For small and shallow samples, time-domain reflectometry (TDR) has become a popular tool for measuring the electromagnetic properties of soil samples (Topp *et al.*, 1980), but electrical resistivity surveys have advantages including variable depth of survey, greater frequency control, and greater ability to survey large areas. Two illustrative examples of the uses of electrical resistivity surveys are given. However, the maturity of electrical resistivity technology, and its wide ranging applications, makes a comprehensive overview unrealistic.

Agriculture

Corwin and Lesch (2003) present a review of the use of electrical resistivity surveys in precision agriculture, defined as "Precision agriculture…utilizes rapidly evolving electronic information technologies to modify land management in a site-specific manner as conditions change spatially and temporally." Whilst limiting their focus to the Wenner array configuration, Corwin and Lesch (2003) explain the principles of electrical resistivity surveys and present example results of large scale surveys. These surveys monitor salinity in irrigated agricultural land, including the use of mobile, continuous monitoring. In addition, Corwin and Lesch (2003) give a detailed discussion of the difficulties in determining soil salinity from electrical resistivity, noting the need for prior or assumed knowledge of parameters including temperature, constituent soil materials, and

water content. This is an apt demonstration of the disadvantages of what Samouëlian *et al.* (2005) describe as the "numerous applications" of electrical-resistivity measurements.

Hydrology

In the area of hydrology, electrical resistivity has been used extensively to chart ground water movements. The paper by French and Binley (2004) presented an extensive study into groundwater flow, due to snow melt, in Norway using an array of 96 electrodes, split between the surface and boreholes. By monitoring electrical resistivity at varying depths, in conjunction with temperature sensors, the researchers were able to chart the infiltration of melt water into the water table against time, air temperature, and weather conditions. Given the complexity of a modelled solution, this presents another case of important knowledge gained using electrical resistivity techniques.

Limitations

Several of the limitations associated with electrical resistivity surveys have already been explained. The need to consider electrode polarization, or take measures to avoid it, is a key challenge for any survey (Hobbs, 1999). In addition, when interpreting data for the calculation of geotechnical properties such as soil type, or water content, the large range of properties which can influence the electrical resistivity of the ground will always challenge the researcher (Samouëlian *et al.*, 2005). Finally, the depth of investigation for a particular measurement can only be estimated once the resistivity and structure of the soil is established, when taking three-dimensional measurements this is also a significant obstacle (Zhou *et al.*, 2000).

The other main source of error in electrical resistivity surveys is the geometric uncertainty. In a situation where the measurement dimensions are of the order of metres, positioning error which is likely to be of the order of centimetres may seem insignificant. Oldenborger *et al.* (2005) investigated the sensitivity of resistivity results to spatial errors in the position of the electrodes. It was shown that errors of greater than 5% are possible as a result of 10 cm vertical error in the electrode positioning when measuring depths of 10 m. The precise error magnitude depends

upon the resistivity of the ground, the type of electrode and measurement depth. The results of Oldenborger *et al.* (2005) are complemented by Wilkinson *et al.* (2008) who use real data to demonstrate that certain configurations of electrodes when placed in boreholes give extreme sensitivity to spatial error. In particular, the "in-hole" configuration, where both voltage-electrodes are located in one borehole and both current electrodes are located in the other, shows errors two orders of magnitude greater than the "cross-hole" configuration, where one electrode of each type is located in each borehole.

2.7 RELEVANT TECHNOLOGY

Much of this thesis relies on modern electronic technology for their outcomes or methods. This section summarises the relevant research, and background reading which supports the use of this technology.

2.7.1 Sigma-Delta Data Acquisition

The field trials described in Chapters 5 and 6 use highly sensitive analogue to digital converters (ADCs) to take digital voltage measurements from sensors. The ADCs used were by National Instruments, with 24-bit resolution using a sigma-delta method (National Instruments, 2012). The sigma-delta method is well suited to high-precision, low-frequency measurements; and works by sampling at low resolution, at very high-frequencies, and digitally filtering the resulting digital data to produce the digital representation of the input signal (Barker and Texas Instruments, 2011a; b). A good overview of sigma-delta analogue-to-digital conversion is given by Aziz *et al.* (1996) who include the use of multi-bit sampling and cascaded sigma-delta modulation in their paper.

2.7.2 Electric Field Sensors

The measurement of electric fields in air has been underway for many years, Bassen and Smith (1983) reviewed the use of dipole antennas to measure electric field strength at frequencies above 0.2 MHz. Similarly, Kanda (1993) reviewed the use of a number of predictable dipoles and loops for electromagnetic field measurements between 2 kHz and 400 MHz.

At low-frequencies, reported measurement techniques rely on measuring the charge difference between two probes, or the induced current due to the electric-field. Examples of this technique include use for ULF measurements in space (Heppner *et al.*, 1978) and measuring the electric field in biological bodies (Shimizu *et al.*, 1989). The method is reviewed by Misakian (1993) for measurements of the electromagnetic field due to high-voltage power lines.

In order to measure the voltage between two points, to calculate the electric field, probes must be used. Initially, the field trials described in this thesis used metal probes inserted into the ground. However, inserting probes into the ground when taking a large number of measurements at different spatial positions becomes impractical. Therefore, large capacitive plates, similar to those patented by Vosteen (1973), were used to measure the voltage by measuring the charge induced on the plate by the voltage in the ground.

2.7.3 Vector Network Analysers

Agilent (2000) give a well-written application note detailing the principles of vector network analysis. They state that network analysis is the characterisation of components by measuring the incident, reflected, and transmitted wave at each port. A vector network analyser (VNA) measures the magnitude and phase of these signals at each measurement frequency, usually in a stepped-frequency signal. Measurements are usually returned in the form of complex scattering-parameters, which define the relationship between a signal incident on one port and received at another. It is then possible to calculate a range of other measurements from the scattering-parameters; including impedance, and equivalent circuits (Pozar, 1990). Scattering parameters were discussed in the context of electromagnetic measurements earlier in this chapter.

Chapter 3 studies the performance of a number of VNAs with the intention of measuring permittivity; the specification of several VNAs is discussed and the mathematical basis of scattering-parameters is given.

CHAPTER 3: LOW-COST VECTOR NETWORK ANALYSERS FOR IN-SITU MEASUREMENTS OF THE DIELECTRIC PROPERTIES OF SOIL

3.1 INTRODUCTION

The aim of this chapter is to investigate the application of low-cost vector network analysers (VNAs) to the measurement of the dielectric properties of soil. Chapter 2 discussed a range of applications for the measurement of the dielectric properties of soil, which include measuring soil water-content (Topp *et al.*, 1980); monitoring the performance of ground-penetrating radar (Davis and Annan, 1989); and predicting wavelength for direction of arrival estimates (Godara, 1997).

The standard method for measuring the dielectric properties of soils, in-situ, is time-domain reflectometry (TDR). TDR is a low-cost, robust, system which measures the response of a short transmission-line to a stepped-voltage signal which is used to calculate complex-permittivity. TDR is described fully in Chapter 2 and by Curioni (2013). However, TDR does not measure dielectric properties at all frequencies, the best a TDR measurement can achieve is a frequency-domain representation which interpolates between the frequencies present in a TDR waveform (Heimovaara, 1994; Friel and Or, 1999; Robinson *et al.*, 2005).

There are a range of methods for measuring the complex-permittivity of a material using VNAs (Baker-Jarvis, 1990; Klein and Santamarina, 1997; Gorriti and Slob, 2005a). However, VNAs are high-cost, delicate, items of equipment not suited to in-situ measurements, especially for high-risk tasks such as land-mine detection, or in demanding environment where particulates and liquids are likely to damage the equipment. Given the dispersive nature of soils (Santamarina *et al.*, 2001), there is a requirement for accurate, frequency-domain, measurements of the dielectric properties of soil, using a method which does not introduce risk to delicate, high-cost, equipment.

This chapter gives a description of VNA equipment, with specific focus on low-cost VNAs. A modified method for measuring the complex-permittivity of soil, which appears suited to low-

cost VNAs, is presented. This method includes significant coverage of calibration methods for coaxial cavities which are required before an inversion can be attempted. Calibration, one, and two-port measurement results are presented, with error analyses. Results are shown which allow a direct comparison of the low-cost VNAs. Finally, the application of low-cost VNAs to measurement of the dielectric properties of soil is discussed.

The new results presented in this chapter are:

- Use of two calibration techniques, one of which is extended, to explore the use of a coaxial cavity which includes a step-discontinuity for the measurement of relative-permittivity.
- Comparison of low-cost VNAs with laboratory-grade equivalents.
- Evaluation of two methods for calculating relative-permittivity of soils using low-cost VNAs with a coaxial-cavity including a step-discontinuity.

3.2 VECTOR NETWORK ANALYSERS

3.2.1 What is a Vector Network Analyser?

Vector network analysers (VNAs) measure the response of a component to a stepped-frequency signal, between one or more ports, with a matrix result showing the response at each port to an input at any other. The *vector* term refers to the complex nature of the measurement, which records amplitude and phase of the response. Agilent (2000) put it succinctly by defining vector network analysis as "a method of accurately characterizing components by measuring their effect on the amplitude and phase of swept-frequency and swept-power test signals". The value returned by a VNA, the S_{xy} of a system, refers to the response of port *x* to an input at port *y*, and is usually presented as a square-matrix with dimensions of the same length as the number of ports in the system.

There are a large number of commercial VNAs on the market. Important considerations for choosing between them include cost, frequency range and resolution, dynamic range, and number of ports.

3.2.2 Specific Vector Network Analysers Used In This Work

This chapter presents research which compares low-cost (≤$500), almost disposable, units against a high-cost laboratory-grade unit. The VNAs used are described in this section, the specific details of these units are summarised in Table 3-2, and compared in a later section.

3.2.2.1 MiniVNAPro

Many advances have been made in semiconductor devices aimed at low-cost signal analysis. One of these is the Analog Devices AD8302 (Analog Devices Inc, 2008), which can provide scaled voltage outputs representing magnitude and phase difference between two signals. The AD8302 is especially relevant here as it is capable of operating over frequencies in general use by GPR devices; up to 2.7 GHz. The AD8302 has been used to develop a very low-cost VNA operating between 200 kHz and 200 MHz, allowing measurement of both reflected and transmitted signals, the MiniVNA. This has subsequently been refined to the current product marketed as the MiniVNAPro which has an extended bandwidth of 200 MHz. Both units have USB communication capability and open source control software allowing easy operation with a PC (Figure 3-1).

Figure 3-1: The MiniVNAPro. Two ports with SMA connectors are visible, USB connection, power switch, and indicator LEDs are at the rear of the unit.

The MiniVNAPro has some significant weaknesses, the most obvious being the limited upper frequency of 200 MHz imposed by the Direct Digital Synthesis (DDS) semiconductor devices

available for low-cost circuitry at the time of its development. This frequency range encompasses "low-frequency GPR", given as 50 MHz to 100 MHz by Huisman *et al.* (2003), it also includes the frequency range Heimovaara *et al.* (1996) noted as being most significant when modeling dielectric relaxation in soil. However, it is known that signals at frequencies around 1 GHz give significant improvement for water-content measurements, in commonly encountered fine-grained soils. At such frequencies, the relationship between water content and the desired electromagnetic properties have been well established (Wensink, 1993; Thomas *et al.*, 2008).

The MiniVNA Pro inherit a significant phase measurement weakness in common with other simple circuits based on the AD8302; they are only capable of determining modulus phase differences (Analog Devices Inc, 2008). Therefore, any autonomous monitoring software would have significant difficulty determining whether the measured phase is positive or negative, compared to the test signal. The AD8302 also suffers significant errors close to 0° and 180° phase that increase with measurement frequency (Kantz *et al.*, 2005; Analog Devices Inc, 2008). However, the difficulty in resolving phase differences can be overcome using more sophisticated circuits; for instance, Kantz *et al.* (2005) took measurements between 500 MHz and 2 GHz by utilizing two AD8302 devices separated by a 90° delay line.

3.2.2.2 VNWA2

Addressing the limitations of the MiniVNAPro, and the AD8302, has led to a more recent low-cost VNA, the VNWA2 shown in Figure 3-2 (Baier, 2009). The VNWA2 utilizes two DDS devices whose outputs are multiplied to provide a frequency range covering 1 kHz to 1.2 GHz, making it suitable for wide-band soil measurements and many GPR applications. Furthermore, this more sophisticated circuit allows the resolving of the phase sign. The most significant weakness of the VNWA2 is the precise timing requirements it imposes on the host PC, requiring a parallel port interface. However, this has been improved with the release of the VNWA3 which uses a USB connection and synchronized audio signals to overcome some of the previous timing problems.

Figure 3-2: The VNWA2. It is shipped in circuit board form, requiring additional work to make usable in a field environment. Port connections are visible on the near side with power and parallel connections on the far side.

The VNWA2 and 3, use two multipliers to mix the reflected, transmitted, and reference signals into the audio band, they are then sent to the controlling PC via the soundcard. This method means that the device cannot measure transmission and reflection simultaneously, due to the limit of two channels of data, of which one must be the reference signal.

The software provided with the VNWA2 allows the user to perform calibration measurements, control the measurement parameters, and change the format for the display of measurement results.

3.2.2.3 Rohde and Schwarz ZVL3

The laboratory-grade Rohde and Schwarz ZVL3 is used as the benchmark for this test, shown in Figure 3-3. The stated performance is significantly greater than either of low-cost VNAs, in terms of dynamic-range, accuracy, and frequency-range. Unsurprisingly, the cost is also significantly greater. It is the only VNA tested which does not require a PC for operation, but measurements can be saved to external devices via its USB ports, and it may be operated with a PC via a network connection.

Figure 3-3: Rohde and Schwarz ZVL3, used as the benchmark for testing the low-cost VNAs.

3.2.2.4 Other VNAs

There are a large number of VNAs on the market, by a number of manufacturers and it would not be useful to explore the properties of all of them. However, the Agilent Fieldfox is included in Table 3-2. This device comes in a handheld, ruggedized, form-factor which is the most suited to field-work of any high-cost VNA that has been used by the author and is included for this reason. However, even with these advantages the Fieldfox is still a high-value, relatively fragile piece of equipment.

3.3 THEORETICAL BASIS OF THE INVERSION CALCULATIONS

3.3.1 Characterisation of a Coaxial Cavity

In order to calculate the dielectric properties of the sample material, it is important to understand the behaviour of the electromagnetic field within the coaxial cavities. Appendix 1 demonstrates that a transmission line approach is equivalent to using scattering-matrices. However, the scattering-matrix approach may be more convenient to conceptualise the different sections of the coaxial cell, and extract the section which contains the sample. Figure 3-4 shows a block diagram of the different components of the coaxial cavity; the scattering-parameter method allows each section to be characterised separately and matrix multiplication used to quantify the system.

However, a transmission line method requires the impedance to be calculated by working incrementally from the load to the source (Norgren and He, 1996). The underlying assumption, when the transition region includes a step-discontinuity, is that an accurate scattering-parameter matrix can be derived for the step-discontinuity, which causes significant phase and magnitude change to the signal despite occupying almost no space in the transmission line.

Regardless of the method of derivation, the response of a short-circuited coaxial-cavity when filled with a dielectric, and excited by an air-filled coaxial line of the same geometry, is given by Clarkson *et al.* (1977):

$$S_{11}|_{short\ circuit} = \frac{\rho - \exp[-2\gamma l]}{1 - \rho \exp[-2\gamma l]} \tag{3-1}$$

Where ρ is the reflection coefficient between a coaxial line equal intrinsic-impedance to the air-filled coaxial cavity, but of infinite length; l is the length of the coaxial cell; $\gamma = -j\omega/c_0$; and c_0 is the velocity of light in free-space.

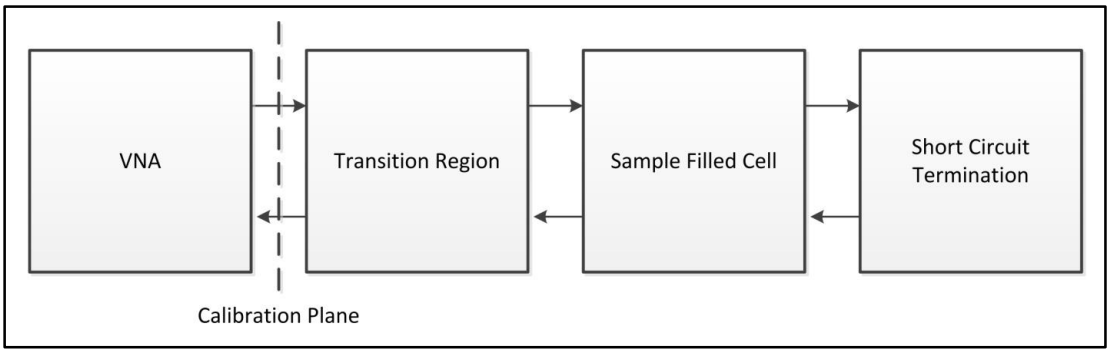

Figure 3-4: Block diagram of short-circuited coaxial cavity

3.3.2 De-embedding

The concept of de-embedding was introduced in section 2.4.3.3. To measure a component which may not be directly connected to the measurement equipment, the properties of the surrounding components can be used to calculate the response of the component under test from the measurement of the whole system (Agilent, 2004). Using transition-matrices defined in section 2.4.3.3 (Edwards, 1981), the de-embedding process is reduced to matrix inversion and multiplication. The key limitation for de-embedding is that the other components of a system must be well known to accurately calculate the properties of the component under test.

3.3.3 Modelling a Step Change in a Transmission Line

The reflection-coefficient of a change in a transmission line is often calculated using (Pozar, 1990):

$$\Gamma = \frac{Z_L - Z_0}{Z_L + Z_0} \tag{3-2}$$

Where Γ is the reflection-coefficient, Z_L is the load impedance, and Z_0 is the intrinsic line impedance (both in Ohms).

However, this calculation is incomplete where the transmission-line contains a step-change discontinuity. A step-change between two sections within a transmission line will result in reflections which are not accounted for by a mismatched impedance, this reflection is modelled as a capacitance across the transmission-line (Pozar, 1990). This area has long been an area of research, Whinnery *et al.* (1944) published a frequently-cited paper presenting graphs for the equivalent capacitance as a function of the ratio between the inner and outer diameters due to step-changes on the inner and outer conductors of a coaxial-line. The work by Whinnery *et al.* (1944) was updated using the more powerful computation available in the 1960s by Somlo (1967) who gave formulae for the equivalent capacitance:

$$C_{step\ on\ inner} \approx \frac{\epsilon}{100\pi}\left[\frac{\alpha^2+1}{\alpha}\ln\frac{1+\alpha}{1-\alpha} - 2\ln\frac{4\alpha}{1-\alpha^2}\right] + 1.11\times10^{-15} \times (1-\alpha)(\tau-1)\,F/cm \tag{3-3}$$

$$C_{step\ on\ outer} \approx \frac{\epsilon}{100\pi}\left[\frac{\alpha^2+1}{\alpha}\ln\frac{1+\alpha}{1-\alpha} - 2\ln\frac{4\alpha}{1-\alpha^2}\right] + 4.12\times10^{-15} \times (0.8-\alpha)(\tau-1.4)\,F/cm \tag{3-4}$$

Where α and τ are defined by the geometry as shown in Figure 3-5 and (3-5) - (3-8).

The equivalent capacitance of a step-discontinuity on both inner and outer conductors is well approximated by as summation of the two discontinuities modelled separately (Whinnery *et al.*, 1944).

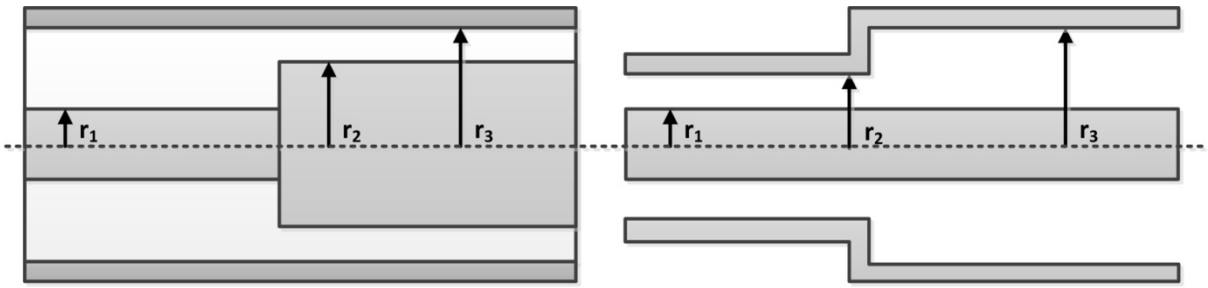

Figure 3-5: Geometry factors in calculating the equivalent capacitance a step-discontinuity in a coaxial-line (after Somlo, 1967)

$$\alpha_{\text{step on inner}} = \frac{r_3 - r_2}{r_3 - r_1} \tag{3-5}$$

$$\tau_{\text{step on inner}} = \frac{r_3}{r_1} \tag{3-6}$$

$$\alpha_{\text{step on outer}} = \frac{r_2 - r_1}{r_3 - r_1} \tag{3-7}$$

$$\tau_{\text{step on outer}} = \frac{r_3}{r_1} \tag{3-8}$$

3.3.4 Measurement Zeros

When measuring the response of a coaxial cavity to a stepped-frequency signal, it is likely that zeros will be encountered. A zero occurs where the standing wave inside the cavity sums to 0 V at the measurement port.

The Nicolson-Ross-Weir methodology (Nicolson and Ross, 1970; Weir, 1974) includes a division by S11 as part of the inversion process, when S11 tends to zero this causes very large, erroneous, results. Furthermore, the specified accuracy of VNAs reduces with the signal magnitude (Table 3-2).

Baker-Jarvis (1990) and Boughriet *et al.* (1997) published iterative, and non-iterative, advances to the NRW method which do not include a division by S11, which significantly reduces the error at measurement zeros. However, the increased error in measured S11 due to low magnitude remains. The difference between the NRW, Baker-Jarvis, and Boughriet methods are graphically demonstrated in Figure 3-6. Figure 3-6 was plotted by applying the above methods – as outlined by Baker-Jarvis (1990) and Boughriet *et al.* (1997) – to simulated data calculated using (3-1) with a small amount of random noise (SNR 30 dB) added to simulate measurement uncertainty.

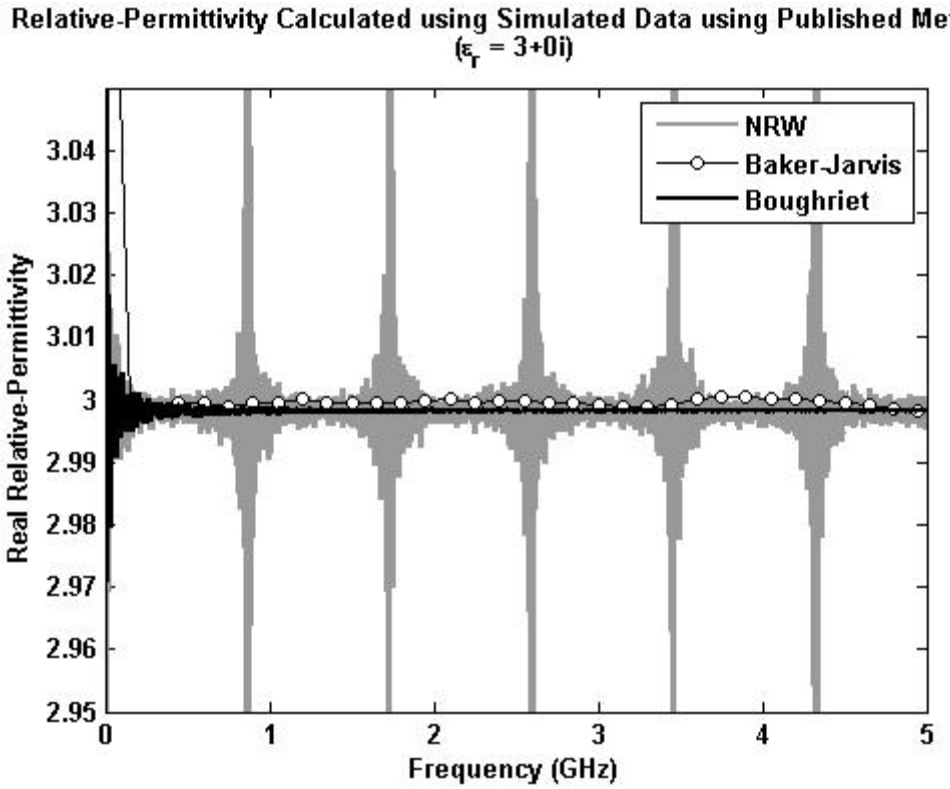

Figure 3-6: Results of NRW, Baker-Jarvis, and Boughriet methods. Errors are shown in the NRW method at the frequencies which produce zeros in S11.

3.3.5 Bandwidth of a Cavity

The concept of modes and cut-off frequencies was described in section 2.4.2.2. All of the inversion methods described, and used, in this chapter rely on the assumption that the only propagating mode in the coaxial transmission-line is the TEM mode. As a result, the effective bandwidth of the coaxial-cavity is between 0 Hz and the lowest frequency at which a second mode can propagate. The cut-off frequency for the TE_{11} mode in a coaxial waveguide is given by Pozar (1990) as:

$$f_c \approx \frac{c_0}{\pi\left(\frac{a+b}{2}\right)\sqrt{\mu_r \varepsilon_r}} \tag{3-9}$$

Where a and b are respectively the inner and outer radii of the coaxial line, μ_r is the relative permeability of the dielectric in the waveguide and ε_r is its relative permittivity. f_c (Hz) is derived from the wave-equation in cylindrical coordinates, making it a function of the differential Bessel function of the first and second kind. In the case of a first order solution, (3-9) is used as an approximate solution. For the derivation see Pozar (1990).

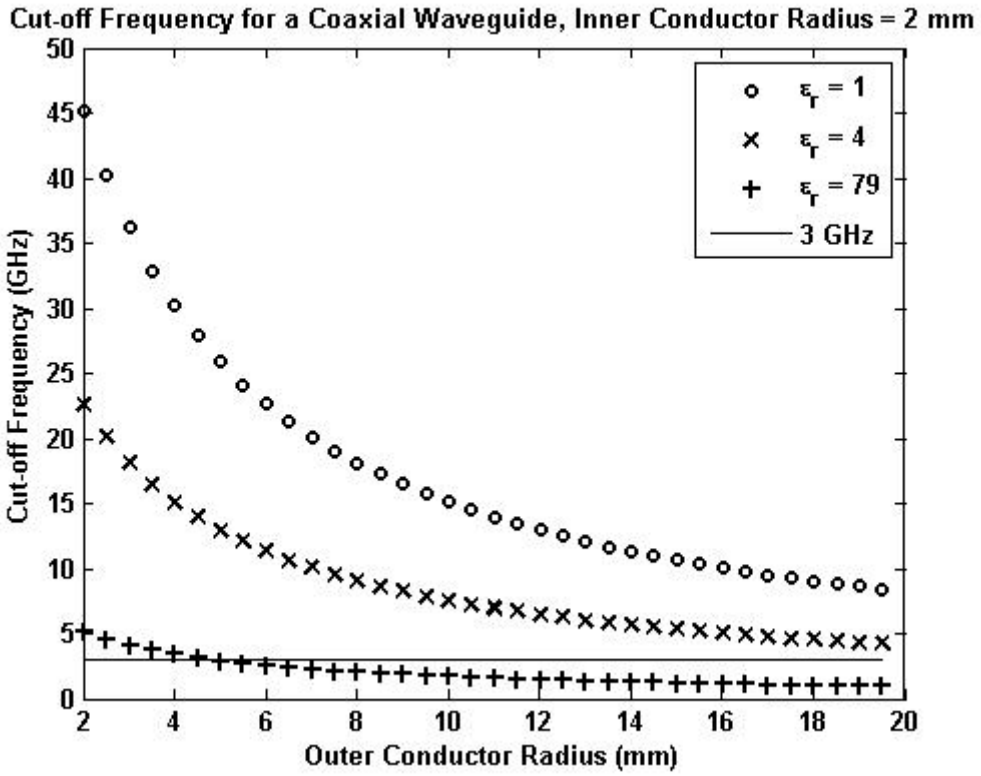

Figure 3-7: Cut-off frequency of a coaxial transmission-line for different dielectrics.

The cut-off frequency was calculated using equation (3-9), with a 5% margin of error. Figure 3-7 shows cut-off frequency as a function of the ratio of inner to outer conductor radii, where inner conductor radius is 2 mm. Where the relative permittivity is 1, no higher-order modes can propagate. However, where the relative-permittivity is close to that of water the cut-off frequency can be within range of the VNAs used in this experiment. Despite this, it may be worth operating near to the cut-off frequency due to the practical difficulties of filling a small coaxial transmission-line with soil.

3.3.6 Using a Transmission-Line not well Matched to the VNA

This section briefly outlines the relevant works which have taken similar measurements using transmission-lines which are not well matched to the VNA used. The works considered here used frequency-domain measurements, with large sample-holders to measure the dielectric properties of soil. The use of large sample-holders is necessary to prepare soil samples (Logsdon, 2005). The work by Logsdon (2005) cites others for the development of the method, and demonstrates the calculation of complex-permittivity from measurement of scattering-

parameters (Kraft, 1987; Campbell, 1990; Logsdon and Laird, 2002). Unfortunately, despite showing accurate results, Logdson *et al.* do not give significant attention to the challenge of calibrating the transmission-line, only Campbell (1990) mentions "adjustments" using measurements from three known dielectrics.

A thorough review by Gorriti and Slob (2005a) explores several methods for calibrating a transmission-line measurement. Including utilising a combination of short, and open-circuit terminations at different positions in the transmission-line (Chew *et al.*, 1991; Huang, 2001). By utilising these different terminations, it is possible to analytically compute scattering-parameters for the transition regions. However, these methods can become inaccurate at resonant frequencies or where results become very similar at low frequencies (Chew *et al.*, 1991; Gorriti and Slob, 2005a).

Gorriti and Slob (2005a) also cite their work (Gorriti and Slob, 2005b) which they claim does not require separate calibration measurements. However, this is slightly misleading: The method published by Gorriti and Slob (2005b) uses measurements with two known materials, and a fitting process which adjusts parameters in the model to reduce the difference between calculated and measured values, for known dielectrics. The parameters adjusted were the relative-permittivity of the dielectric in the transition region, the geometry of the model, and the losses in the transmission-line due to imperfect dielectrics and conductors. This method was adopted in part by Thomas *et al.* (2008) who adjusted the phase-delay parameter to calculate the separation between sample and calibration planes. These methods have been shown to give good results, but do not account for higher order modes or the equivalent capacitances due to transitions or imperfections in the transmission lines.

The majority of the methods discussed here used a customised, tapered, coaxial-cavity to minimise the reflections due to the transition. In this work a step change was adopted to reduce manufacturing cost, and simplify sample preparation. No research has been found which

examines the efficacy of these calibration methods for a step-discontinuity in the transmission-line.

3.4 METHODS

The methods presented in this chapter are designed to calculate complex relative-permittivity from scattering-parameters measured using a VNA. This section describes the VNA calibration, measurement calibration methodology, and presents one and two-port inversion methods, which are considered separately. The state-of-the-art was summarised in Chapter 2; this section aims to give the reader enough information to repeat the methods used here, and find relevant supporting publications.

3.4.1 Cavity Design

Previously published works which used large coaxial cavities to measure complex-permittivity usually used a tapered cavity to increase the cross-sectional dimensions to a size where preparing soil samples was possible. Three publications which do not use a tapered cavity were those of Logsdon (2005), Logsdon and Laird (2002), and Campbell (1990) who did not explore the need to model or control the transition from the VNA cabling to the measurement cavity. The work by Thomas *et al.* (2008) applies a phase-shift to account for the separation of the calibration-plane and the beginning of the sample, prior to calculating relative-permittivity using quarter-wavelength analysis. None of these works give significant support to the design of a new coaxial cavity. However, Thomas *et al.* (2008) did make a large number of measurements on soil with their coaxial cavity, albeit using quarter-wavelength analysis rather than a full inversion method. Consequently, the coaxial-cavities used in this chapter were based on that design, knowing that the size of the cavity was sufficient for soil preparation and that the length was not so great as to result in overly large attenuation for lossy soils.

Designing a coaxial-cavity with a good electrical connection at both short-circuit and the connecting ports presented some challenges. The central conductor was soldered into the base of the main cavity; the lid was bolted to the cavity using threaded holes in the side walls; and the

central conductor of the N-type connector was soldered directly to the centre conductor of the cavity such that removing the lid left it in place. The N-type connector was bolted to the lid assembly, although the bolts did not protrude into the cavity. A technical drawing of the N-type connector is included in Appendix 2 for reference. An exploded diagram is shown in Figure 3-8, with a photo of a completed cavity shown in Figure 3-9. The physical dimensions of the transmission line in the cavities are given in Table 3-1.

The two port cavity was of identical construction to the one-port cavities, but the lid assembly was repeated at both ends and the hollow cavity extended fully through the structure. An exploded diagram is shown in Figure 3-10, with a photo in Figure 3-11.

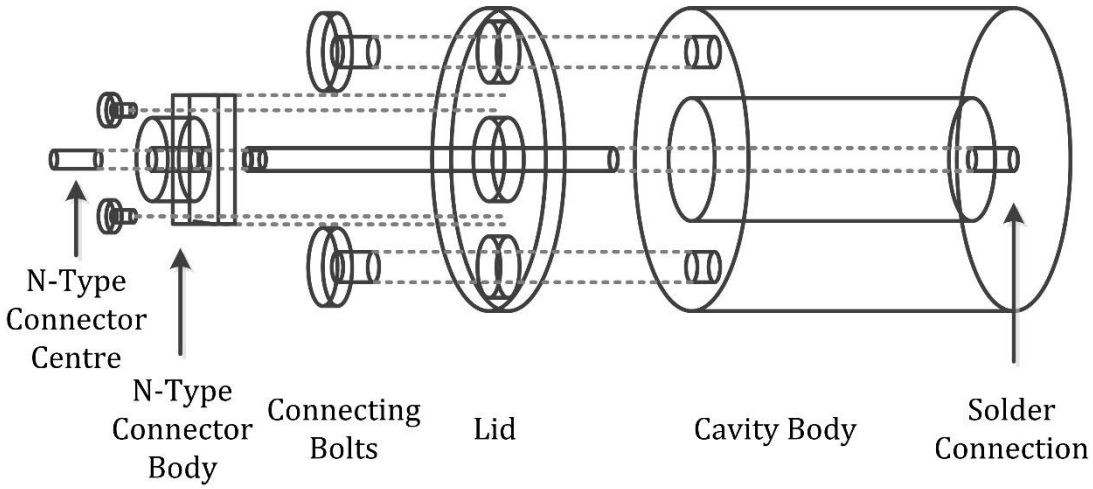

Figure 3-8: Exploded diagram showing the construction of a one-port coaxial cavity.

Number of Ports	Inner Conductor Radius (mm)	Outer Conductor Radius (mm)	Cavity Length (mm)
1	2	12	30
1	2	12	50
1	2	12	70

Table 3-1: One-port coaxial cavity dimensions

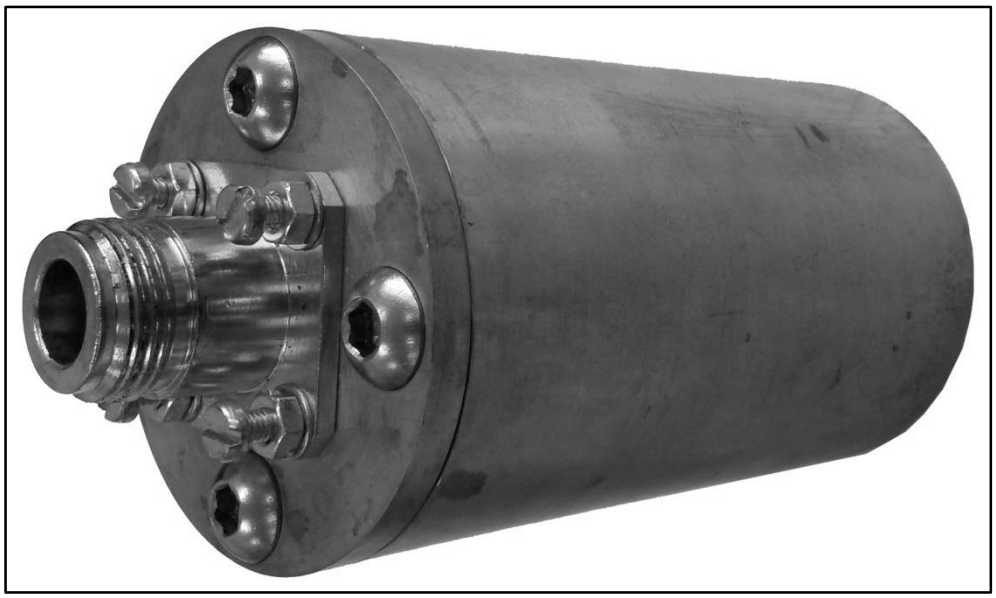

Figure 3-9: Photo of the short-circuited coaxial cavity showing the N-type connection and lid bolted to the brass cavity, the short-circuit termination is out of shot. Note the screws attaching the N-type connector to the lid do not protrude into the cavity.

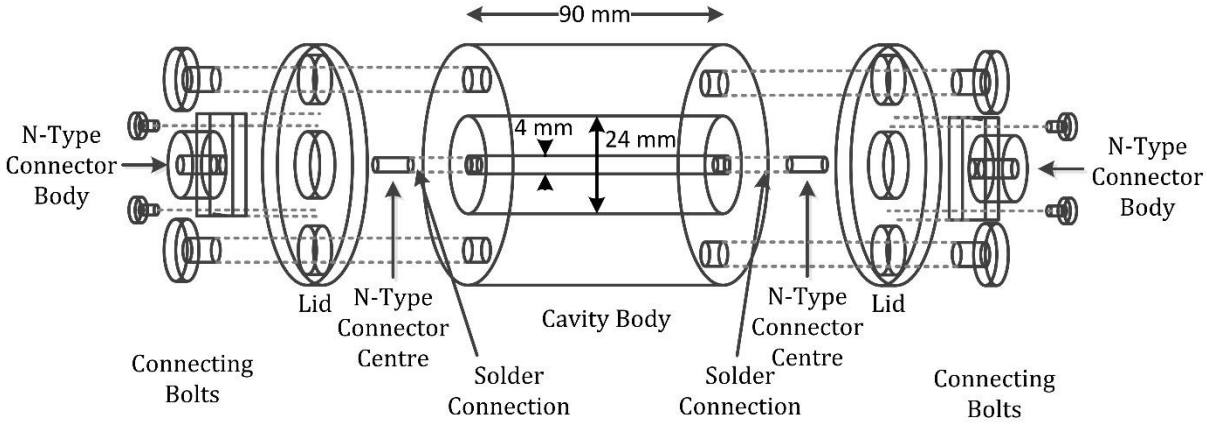

Figure 3-10: Exploded diagram of the two-port cavity. Mechanical connections are made in the same way as for the one-port cavity.

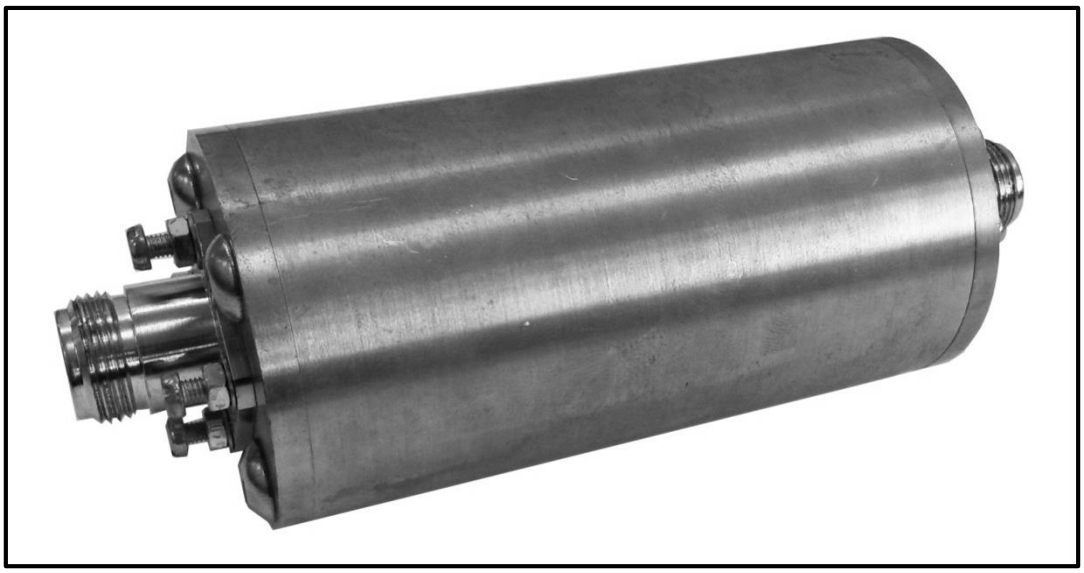

Figure 3-11: Photo of the two-port coaxial cavity, shown in Figure 3-10.

3.4.2 VNA Calibration

The measurements taken using multiple VNAs were compared by utilising calibration to compare like measurements, even where adaptors were required to connect an SMA terminated VNA to the N-type terminated coaxial cavity.

A number of calibration methods have been demonstrated in the literature (Hiebel, 2008) but the method used here the short-open-load-through (SOLT) method, described below. Given the potential for human error, each calibration was verified by connecting a short-circuit load followed by a matched load and visually confirming the measurements were those expected.

3.4.2.1 One-Port Calibration

In order to calibrate a one-port measurement, calibration measurements were taken of a short-circuit, open-circuit, and matched (50 Ω) load. These measurements allowed the VNA to account for three sources of error in the VNA measurement (Hiebel, 2008).

3.4.2.2 Two-Port Calibration

In order to calibrate for a two-port measurement, a short-circuit, open-circuit and matched load calibration measurement was taken for both ports. In addition, a "through" calibration measurement was taken, where a short coaxial line was used to connect the two ports. This configuration allows the error source associated with the individual ports to be accounted for, as well as the losses between the ports (Hiebel, 2008).

3.4.3 Measurement Calibration

Two calibration methods were utilised: Calibration using 3 short-circuit terminations at different positions to calculate the scattering-parameters of the transition-region (Chew *et al.*, 1991; Shang *et al.*, 1999; Huang, 2001); and adjusting model parameters to minimise the error between prediction and a measurement of a known dielectric (Campbell, 1990; Gorriti and Slob, 2005b).

3.4.3.1 Scattering-Parameter Calculation

The scattering-parameter calculation measures the properties of the transition region by taking three measurements of a known transmission line. In this case, an air-filled coaxial cavity with short-circuit terminations at different positions was used. Once three measurements were taken, algebraic methods were used to calculate the scattering-parameters of the transition regions. The simultaneous equations presented here were derived by Huang (2001) but similar methods are widely used (Chew *et al.*, 1991; Shang *et al.*, 1999). Consider three reflection-coefficient results $[\Gamma_{in}, \Gamma_{Ln}]$ where n is the number of the measurement, Γ_{in} are the VNA measurements at the calibration plane, and Γ_{Ln} are the predicted reflection-coefficient of the short-circuit terminated coaxial cavity, with reference to Figure 3-4:

$$\Gamma_i = S_{11T} + \frac{S_{12T}^2 \Gamma_L}{1 - S_{22T}\Gamma_L} \tag{3-10}$$

Where S_{xyT} are the scattering-parameters of the transition region, and the reflection-coefficient Γ_L is calculated using a reduced version of (3-1):

$$\Gamma_L = \left.\frac{\rho - \exp[-2\gamma l]}{1 - \rho \exp[-2\gamma l]}\right|_{\rho=0} = \exp[-2\gamma l] \tag{3-11}$$

Given three measurements, and three air-filled short-circuit terminated coaxial cavities of known geometry, the scattering-parameters of the transition region are calculated (Huang, 2001):

$$a = \frac{(\Gamma_{L3} - \Gamma_{L2})(\Gamma_{i1} - \Gamma_{i2})}{(\Gamma_{i2} - \Gamma_{i3})(\Gamma_{L1} - \Gamma_{L2})} \tag{3-12}$$

$$S_{22T} = \frac{a - 1}{a\Gamma_{L1} - \Gamma_{L3}} \tag{3-13}$$

$$b = \frac{\Gamma_{L1}(1 - S_{22T}\Gamma_{L2})}{\Gamma_{L2}(1 - S_{22T}\Gamma_{L1})} \tag{3-14}$$

$$S_{11T} = \frac{b\Gamma_{i2} - \Gamma_{i1}}{b - 1} \tag{3-15}$$

$$S_{12T}^2 = \frac{\Gamma_{i1} - S_{11T}}{\Gamma_{L1}}(1 - S_{22T}\Gamma_{L1}) \tag{3-16}$$

Using this method, the scattering-parameters for the transition region were calculated at each measurement frequency, these were then applied to calculate the response of the dielectric-filled coaxial cavity.

3.4.3.2 Adjusting Model Parameters

This method was formalised by Gorriti and Slob (2005b) who showed that the error of the theoretical model can be significantly reduced by adjusting the geometry of the transmission line, relative-permittivity of the connection materials, and loss tangent within the cavity. An accurate theoretical model of the cavity may be used to calibrate, and calculate complex-permittivity.

The model used in this chapter is different to that presented by Gorriti and Slob (2005b) due to the effective capacitance of the step discontinuity. However, the adjusted parameters are similar: geometry of the cavity, geometry of the connection, relative-permittivity of the cable dielectric, and loss tangent in the cavity. The model used is described and its relationship to the calibration is given, the results of the calibration are presented in section 3.6.1.

It has been shown that any transmission line, in which only one mode is propagating, is made up of sections which have impedance and propagation parameters, the performance of the whole is predicted by the combination of the impedance and propagation parameters (Gorriti and Slob, 2005b). However, it is also well known that a transmission line discontinuity cannot be described solely with the parameters of the components adjacent to the discontinuity (Pozar, 1990). This section shows a calibration method which attempts to apply the methods of Gorriti and Slob (2005b) to a transmission line which includes a discontinuity.

To calculate the input-impedance, or reflection-coefficient, of a terminated transmission line it is easiest to calculate from the load to the source. This method is used here, initially the input-impedance to a terminated coaxial cavity is stated (Pozar, 1990, p. 81):

$$Z_{in} = Z_0 \frac{Z_L + Z_0 \tanh(\gamma L)}{Z_0 + Z_L \tanh(\gamma L)} \tag{3-17}$$

Where Z_L is the load impedance which is 0 Ω, L is the length of the cell, Z_0 is the characteristic impedance of the line (Ohms), which is the impedance of the cavity when filled with air (3-18), and γ is the propagation constant (3-19) (Gorriti and Slob, 2005b):

$$Z_0 = \frac{1}{2\pi}\sqrt{\frac{\mu}{\varepsilon}}\ln\left(\frac{b}{a}\right) \tag{3-18}$$

$$\gamma = \frac{j\omega}{c}\sqrt{\varepsilon_r - \delta} \tag{3-19}$$

Where ω is the angular frequency, μ and ε are respectively the permeability and permittivity of the dielectric in the cavity, b and a are the outer and inner conductor radii, c is the velocity of light, ε_r is the real relative permittivity of the medium, and δ is the loss tangent due to dielectric and conduction losses.

The impedance of a capacitor is well known as $1/j\omega C$ where the capacitance is calculated as a function of the geometries of the cable and cavity (3-3), (3-4). The input-impedance of the system is calculated using the geometry of the transition region and its load impedance. The load impedance is calculated as the parallel combination of the capacitor and the cavity. Equations (3-17) - (3-19) are then used to calculate the input impedance of the transition region, whose intrinsic impedance is 50 Ω. Finally, the measured reflection-coefficient (S11) is given by Pozar (1990):

$$S_{11} = \Gamma = \frac{Z_{input} - Z_0}{Z_{input} + Z_0} \tag{3-20}$$

Where the intrinsic impedance of the VNA, Z_0, is 50 Ω.

Having calculated a predictive model for the cavity and its transition region, the researcher can adjust the parameters to improve the fit of the model for measurements of known dielectrics. The minimisation was performed using a simplex minimisation constrained to the known tolerance of the parameters (Lagarias *et al.*, 1998).

There are several methods of deriving the scattering-parameters of the transition region, having found an accurate predictive model: They may be analytically calculated using the parameters

above, or three solutions can be found and the scattering-parameters can be calculated using the simultaneous equations in section 3.4.3.1. The algorithm to solve the simultaneous equations had already been developed so that method was used.

3.4.3.3 Using the Calibration Calculations

In order to use the inversion methods described below, the response of the transmission-line filled with soil must be computed from the measurements. The process of de-embedding to extract the response of the coaxial cavity was described in Chapter 2 and section 3.3.2. This matrix algebra is applied to both one and two-port measurements using the scattering-parameters for the transition regions, calculated using either calibration method.

3.4.4 <u>One-Port Measurements</u>

Given the results presented in section 3.5, one-port calculations are preferred to two-port calculations for inversion using low-cost VNA measurements. It is likely that using the measurements with lower error will result in lower error for calculated relative-permittivity. In order to calculate the dielectric properties of a soil from one-port measurements, relative-permeability must be assumed to be one. Without this assumption, the inversion would be required to calculate two parameters for each measurement. Fortunately, the assumption that soils are non-magnetic is well founded (Santamarina *et al.*, 2001). The following method is adapted from the excellent work by Baker-Jarvis (1990):

For a short-circuit terminated coaxial cavity, the following equation predicts the measured reflection coefficient (Clarkson *et al.*, 1977):

$$S_{11}|_{short\ circuit} = \frac{\rho - \exp[-2\gamma L]}{1 - \rho \exp[-2\gamma L]} \tag{3-21}$$

Where:

$$\rho = \frac{1 - \sqrt{\varepsilon_r}}{1 + \sqrt{\varepsilon_r}} \tag{3-22}$$

The reflection coefficient, ρ, is defined by (3-22) in the case where the preceding transmission line has the same intrinsic impedance as the air-filled coaxial cavity. This assumption is valid if the calibration procedure is correct.

No analytical solution has been found, or published, to directly calculate relative-permittivity in terms of measured reflection-coefficient. Therefore, a numerical inversion technique is necessary. The prevalence of numerical techniques make a review of the subject unnecessary for this thesis, the reader is referred to Mathews (1992) or Press *et al.* (1992) for an introduction. The rearrangement given in (3-23) is made to cast (3-21) - (3-22) into a form to which a numerical minimisation may be applied, the cost function minimised is given by (3-24).

$$f(\varepsilon_r) = \frac{\rho - \exp[-2\gamma L]}{1 - \rho \exp[-2\gamma L]} - S_{11}^{measured} \tag{3-23}$$

$$\text{Cost} = \{Real\,[f(\varepsilon_r)]\}^2 + \{Imag\,[f(\varepsilon_r)]\}^2 \tag{3-24}$$

A simplex minimisation algorithm was used at each frequency step of the measurement (Lagarias *et al.*, 1998), and a low-pass filter was applied to the overall result. The previously published error analysis is valid for this method, assuming that a numerical solution is found for each frequency (Baker-Jarvis, 1990):

$$\frac{\Delta\varepsilon_r^*}{\varepsilon_r^*} = \frac{1}{\varepsilon_r^*}\sqrt{\left(\frac{\partial\varepsilon_r^*}{\partial|S_{11}|}\Delta|S_{11}|\right)^2 + \left(\frac{\partial\varepsilon_r^*}{\partial\theta_{11}}\Delta\theta_{11}\right)^2 + \left(\frac{\partial\varepsilon_r^*}{\partial L}\Delta L\right)^2} \tag{3-25}$$

Where $\Delta|S_{11}|$ is the uncertainty in scattering-parameter magnitude, and $\Delta\theta_{11}$ is uncertainty in scattering-parameter phase, ΔL is the uncertainty in the sample length. The partial derivatives are calculated as follows:

$$\frac{\partial\varepsilon_r^*}{\partial|S_{11}|} = \frac{\exp j\theta}{\frac{\partial f}{\partial\gamma}\frac{\partial\gamma}{\partial\varepsilon_r^*}} \tag{3-26}$$

$$\frac{\partial\varepsilon_r^*}{\partial\theta} = \frac{j|S_{11}|\exp j\theta}{\frac{\partial f}{\partial\gamma}\frac{\partial\gamma}{\partial\varepsilon_r^*}} \tag{3-27}$$

$$\frac{\partial \varepsilon_r^*}{\partial L} = \frac{\frac{\partial f}{\partial L}}{\frac{\partial f}{\partial \gamma}\frac{\partial \gamma}{\partial \varepsilon_r^*}} \tag{3-28}$$

Where:

$$\frac{\partial f}{\partial L} = \frac{\gamma_0 \gamma \operatorname{sech}^2(\gamma L)}{\gamma_0 \tanh(\gamma L) + \gamma}\left[1 - \frac{\gamma_0 \tanh(\gamma L) - \gamma}{\gamma_0 \tanh(\gamma L) + \gamma}\right] \tag{3-29}$$

$$\frac{\partial f}{\partial \gamma} = \frac{1}{\gamma_0 \tanh(\gamma L) + \gamma}\left[(\gamma_0 L \operatorname{sech}^2(\gamma L) - 1) - \frac{\gamma_0 \tanh(\gamma L) - \gamma}{\gamma_0 \tanh(\gamma L) + \gamma}[\gamma_0 L \operatorname{sech}^2(\gamma L) + 1]\right] \tag{3-30}$$

$$\frac{\partial \gamma}{\partial \varepsilon_r^*} = -\frac{\mu_0 \varepsilon_0 \omega^2}{2\gamma} \tag{3-31}$$

The uncertainty shown in the results section is calculated using this methodology. The uncertainty in measured scattering-parameters is found in the VNA specifications or from the results in section 3.5.2.

3.4.5 Two-Port Measurements

Chapter 2 explored a number of published methods for calculating relative-permittivity from transmission and reflection measurements. The method used in this chapter was that of Boughriet *et al.* (1997) who presented an adaption to the Nicolson-Ross-Weir (NRW) method (Nicolson and Ross, 1970; Weir, 1974) in order to remove erroneous results at half-wavelength frequencies. An iterative method has been published but it was felt that an analytical solution provided a better theoretical basis from which to compare the low-cost VNAs (Baker-Jarvis, 1990; Baker-Jarvis *et al.*, 1992).

The following derivation was presented by Boughriet *et al.* (1997) and shown to give equivalent accuracy the iterative method presented by Baker-Jarvis *et al.*:

$$K = \frac{S_{11}^2 - S_{21}^2 + 1}{2S_{11}} \tag{3-32}$$

$$\Gamma = K \pm \sqrt{K^2 - 1} \tag{3-33}$$

$$T = \frac{S_{11} + S_{21} - \Gamma}{1 - (S_{11} + S_{21})\Gamma} \tag{3-34}$$

$$\frac{1}{\Lambda^2} = \left[\frac{j}{2\pi L}\right]^2 \tag{3-35}$$

Where T and Γ are the transmission and reflection coefficients at the interface between the air and sample filled transmission-lines. If the soil is assumed non-magnetic then:

$$\varepsilon_{eff}^* = \left(\frac{\lambda_{0g}}{\Lambda}\right)^2 \tag{3-36}$$

Where:

$$\lambda_{0g} = \frac{1}{\sqrt{\frac{1}{\lambda_0^2} - \frac{1}{\lambda_c^2}}} \tag{3-37}$$

Where λ_0 is the free-space wavelength, and λ_c is the cut-off wavelength which tends to infinity in a coaxial waveguide. The effective permittivity can then be transformed into the sample permittivity:

$$\varepsilon^* = \left(1 - \frac{\lambda_0^2}{\lambda_c^2}\right)\varepsilon_{eff}^* + \frac{\lambda_0^2}{\lambda_c^2} \tag{3-38}$$

This method does not rely on a division by S11 which could tend to infinity at half-wavelength frequencies, a clear advantage over the NRW method. A similar error analysis to the one-port measurement is made, and (3-25) applies although it applies to S_{11} and S_{21}. The following partial derivatives are then used (Boughriet *et al.*, 1997):

$$\frac{\partial \varepsilon_{eff}^*}{\partial |S_\alpha|} = \left(\frac{\partial \varepsilon_{eff}^*}{\partial \Gamma}\frac{\partial \Gamma}{\partial S_\alpha} + \frac{\partial \varepsilon_{eff}^*}{\partial T}\frac{\partial T}{\partial S_\alpha}\right)\exp(j\theta_\alpha) \tag{3-39}$$

$$\frac{\partial \varepsilon_{eff}^*}{\partial \theta_\alpha} = j|S_\alpha|\frac{\partial \varepsilon_{eff}^*}{\partial |S_\alpha|} \tag{3-40}$$

$$\frac{\partial \varepsilon_{eff}^*}{\partial d} = \frac{\partial \varepsilon_{eff}^*}{\partial T}\frac{\partial T}{\partial d} \tag{3-41}$$

$$\frac{\partial \Gamma}{\partial S_{11}} = \left(1 \pm \frac{K}{\sqrt{K^2 - 1}}\right)\left(\frac{2S_{11}^2 - 2S_{21}^2 + 1}{2S_{11}^2}\right) \tag{3-42}$$

$$\frac{\partial \Gamma}{\partial S_{21}} = \left(1 \pm \frac{K}{\sqrt{K^2 - 1}}\right)\left(-\frac{S_{21}}{S_{11}}\right) \tag{3-43}$$

$$\frac{\partial T}{\partial S_\alpha} = \frac{1 - \Gamma^2 + \frac{\partial \Gamma}{\partial S_\alpha}((S_{11} + S_{21})^2 - 1)}{(1 - (S_{11} + S_{21})\Gamma)^2} \tag{3-44}$$

$$\frac{\partial \varepsilon_{eff}^*}{\partial \mathrm{T}} = 2\left(\frac{j\lambda_{0g}}{2\pi d}\ln(T)\right)\left(\frac{j}{2\pi d}\frac{\lambda_{0g}}{T}\right) \tag{3-45}$$

3.5 COMPARISON BETWEEN DIFFERENT VNAS

Before reviewing results of the inversion process, it is necessary to assess the utility of the low-cost VNAs. This section compares the low-cost VNAs in terms of specification, and then presents measurements from several VNAs to allow comparison of the accuracy of the different VNAs.

3.5.1 Specifications

The specifications of the relevant VNAs are shown in Table 3-2, where it is clear that the high-cost VNAs attain significantly greater dynamic-range, compared to the low-costs VNAs. It has not been possible to compare accuracy because the low-cost VNAs do not state measurement accuracy in their documentation. For this reason, the following two sections will compare the accuracy using measurement results.

The final comparison is cost, the difference between the laboratory-grade VNAs and the low-cost VNAs is as much as a factor of 40. This work does not suggest replacing laboratory equipment with low-cost VNAs, but there is clear potential for increased use of VNAs for field-work with such reduced equipment cost.

VNA	Approximate Cost	Form Factor	Dynamic Range	Frequency Range	Maximum Number of Measurement Points	Frequency Resolution	Available Measurements
Rohde & Schwarz ZVL3	$21,000	Desktop	9 kHz - 1 MHz: >75 dB 1 MHz - 7 MHz: >85 dB 7 MHz - 20 MHz: >105 dB 20 MHz - 3 GHz: >115 dB	9 kHz to 3 GHz	4,001 points per trace	1 Hz	S11, S12, S21, S22 Magnitude and Phase
Agilent Fieldfox N9913A-210	$12,000	Handheld	< 300 kHz: >63 dB 2 MHz – 9 MHz: >85 dB >9 MHz: >95 dB	30 kHz to 4 GHz	10,001 points per trace	1 Hz	S11, S12 Magnitude and Phase
MiniVNAPro	$500	USB connection to PC	> 50 dB in Reflection > 90 dB in Transmission	100 kHz to 200 MHz	Not given, results have been obtained using up to 2,000 points per trace	Not Given	S11, S12 Magnitude and Phase
VNWA2/3	$500	Parallel/USB Connection to PC	<500 MHz: >90 dB > 500 MHz: 50dB	1 kHz to 1.2 GHz	8,192 points per trace	Not Given	S11, S12 Magnitude and Phase

Table 3-2: Summary of the properties of the different VNAs used, as specified by their manufacturers.

3.5.2 One-Port Measurements

This section compares several one-port, reflection-only, measurements made using the different VNAs. The aim was to quantify the error of the low-cost VNAs by comparison with the laboratory-grade VNA. Two measurements were taken, measuring a short-circuited coaxial cavity, filled with air and tap-water. By comparing these two measurements, the performance of the VNAs for both low and high attenuation measurements is demonstrated. The cavities used were those described in section 3.4.1.

3.5.2.1 Air-Filled Coaxial Cavity

Results are shown here for magnitude (Figure 3-12) and phase (Figure 3-13) measurements of an air-filled, short-circuit terminated coaxial cavity. The frequency axis is presented on a log-scale to maximise the comparison at the lower frequencies. Air is a very low-loss dielectric, so the comparison is mainly achieved using phase. Magnitude measurements appear consistent for both low-cost VNAs apart from a region of high error between 600 MHz and 800 MHz for the VNWA2. This region corresponds to the switch over from using 1 DDS component to 2. The phase measurements are consistent but error does increase with frequency, the erroneous region, between 600 MHz and 800 MHz, in VNWA2 measurement is present in the phase results. The error is more clearly presented in Figure 3-14, where the error between the low-cost and laboratory-grade VNAs shown. The results show that the miniVNAPro and the VNWA2 have low magnitude errors (around 1%) up to 200 MHz and 600 MHz, respectively. While the phase error for the VNWA2 increases linearly to 0.2 rads at 600 MHz with the MiniVNAPro performing similarly up to 200 MHz. Between 600 and 800 MHz the VNWA2 shows high error for both magnitude and phase, but above 800 MHz error falls to around 5% for magnitude and to around 0.5 rads for phase, following the linear approximation seen at lower-frequencies.

3.5.2.2 Water-Filled Coaxial Cavity

The S11 measurement were repeated for a coaxial-cavity filled with tap-water. Much greater attenuation occurs in tap-water than air due to greater conductivity, so this presents a better

comparison for high-loss measurements. The results for magnitude and phase are shown in Figure 3-15 and Figure 3-16. Again, the results for both magnitude and phase agree well, apart from a region between 600 MHz and 800 MHz where significant error is shown for the VNWA2 results. The difference between the magnitude and phase results of the laboratory-grade VNA and the two low-cost VNAs is plotted in Figure 3-17. This gives a better comparison than examining the data directly, and shows that the MiniVNAPro presents significantly greater error than the VNWA2 for high attenuation measurements. This is consistent with the lower dynamic range specified by the MiniVNAPro. The phase error for the VNWA2 is consistent with that of the air measurements, showing the same rate of increase with frequency, and the same erroneous region between 600 and 800 MHz.

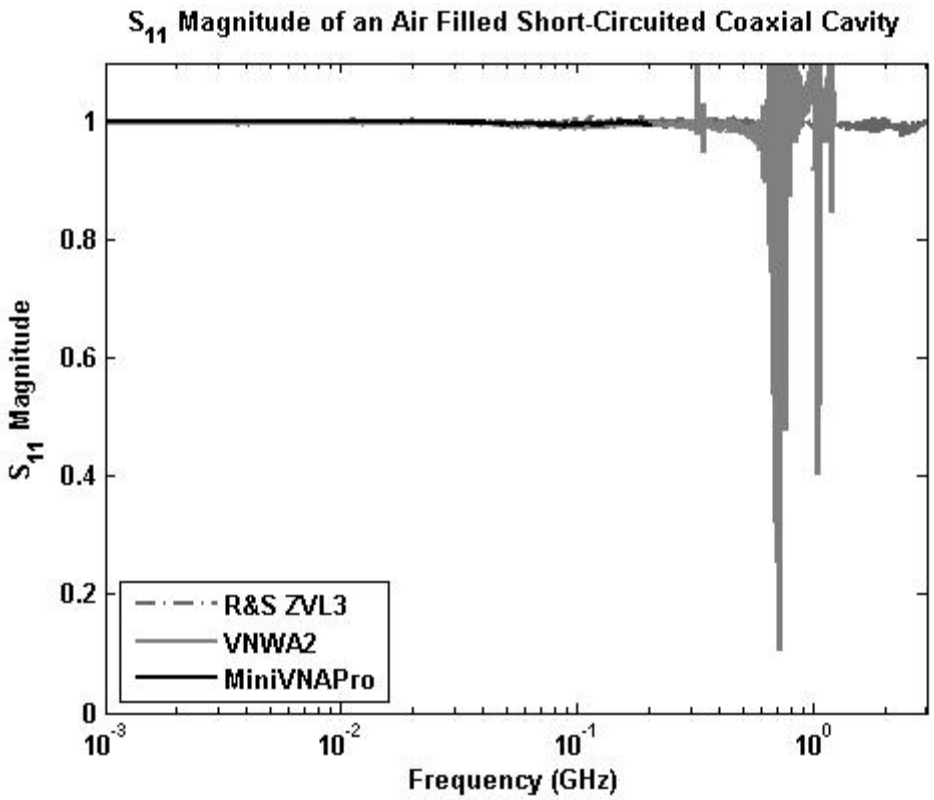

Figure 3-12: S11 magnitude for a short-circuited, air-filled, coaxial cavity measured using three VNAs.

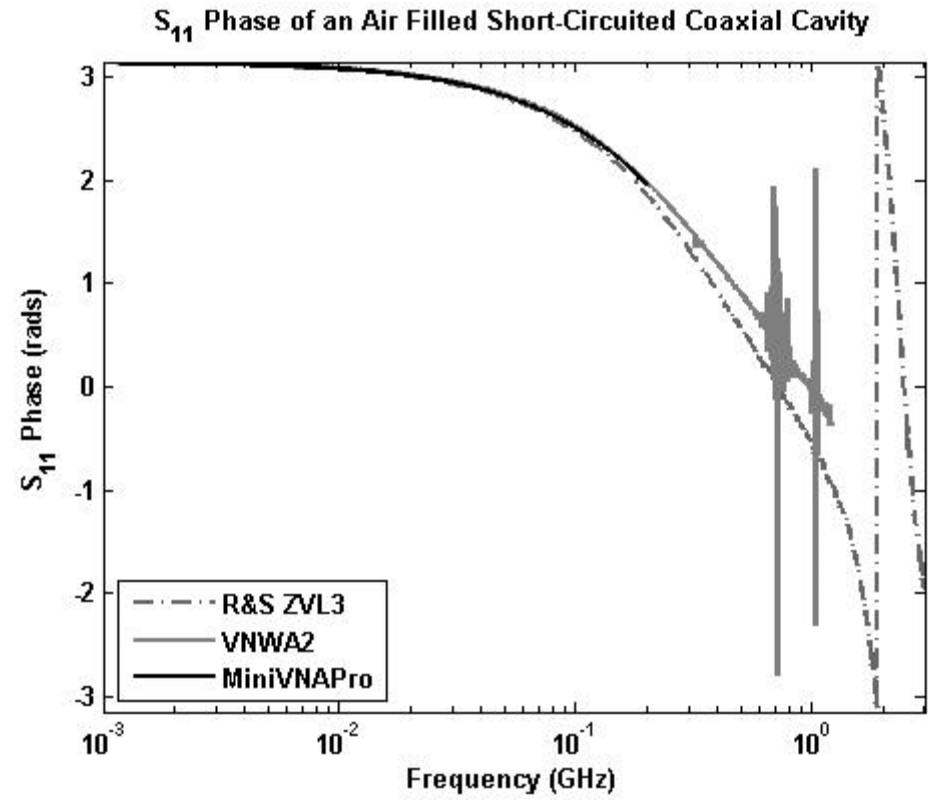

Figure 3-13: S11 phase for a short-circuited, air-filled, coaxial cavity measured using three VNAs.

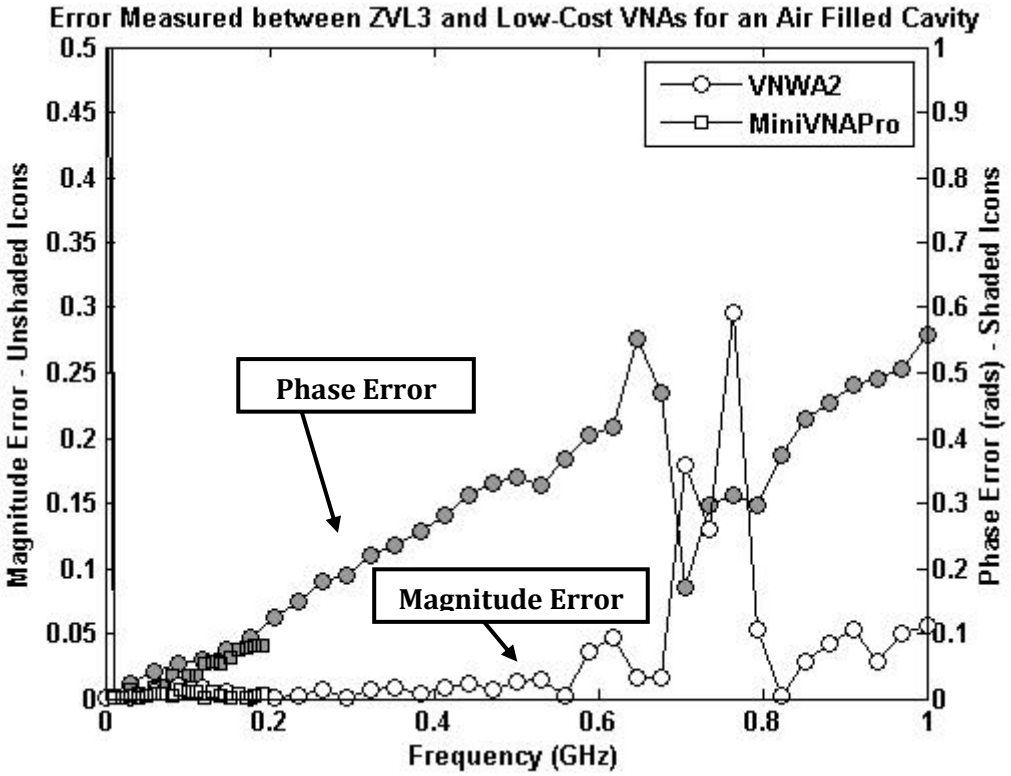

Figure 3-14: Error calculated between the low-cost VNAs and the laboratory-grade VNA for air measurements. Magnitude error (unshaded icons) is low until frequency exceeds 600 MHz, phase error (shaded icons) increases consistently.

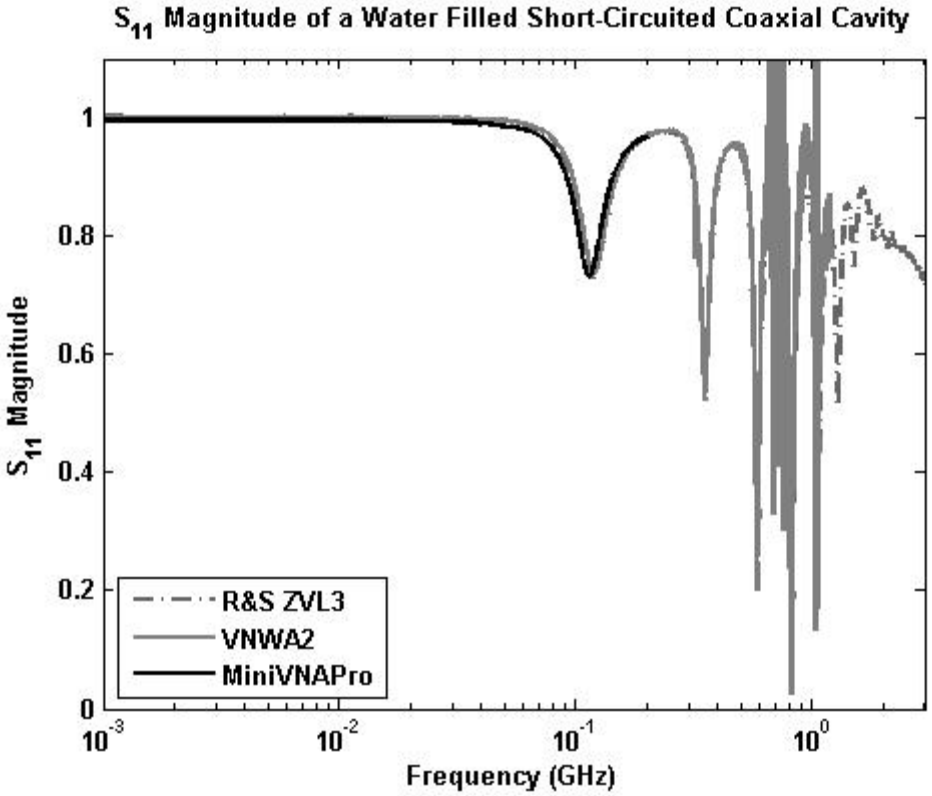

Figure 3-15: S_{11} magnitude for a short-circuited, water-filled, coaxial cavity measured using three VNAs.

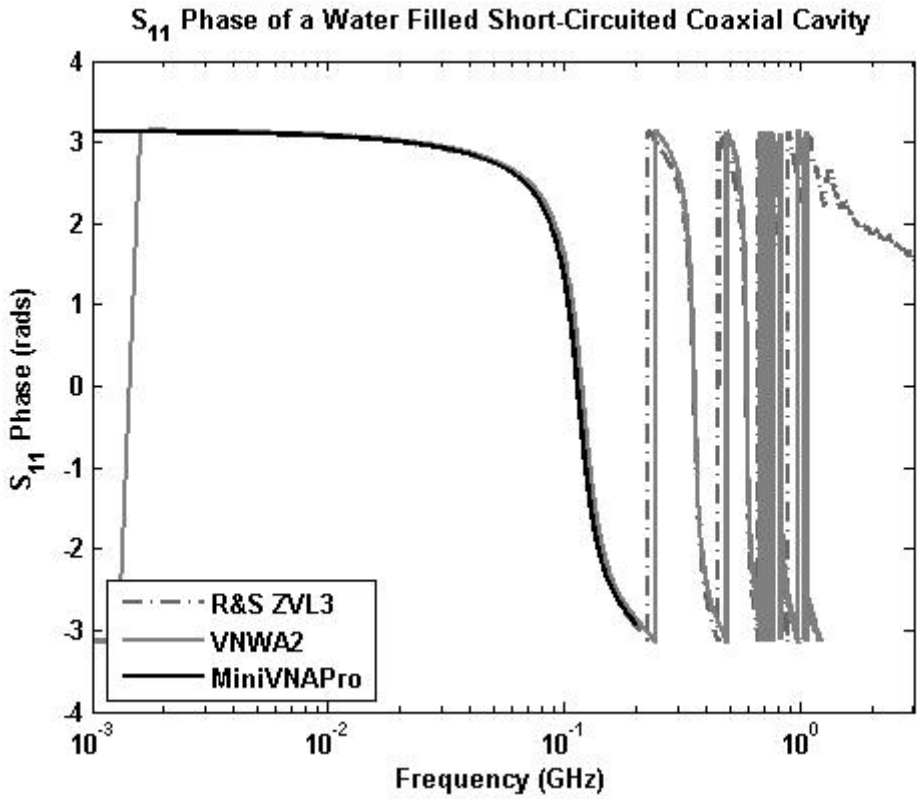

Figure 3-16: S11 phase for a short-circuited, water-filled, coaxial cavity measured using three VNAs.

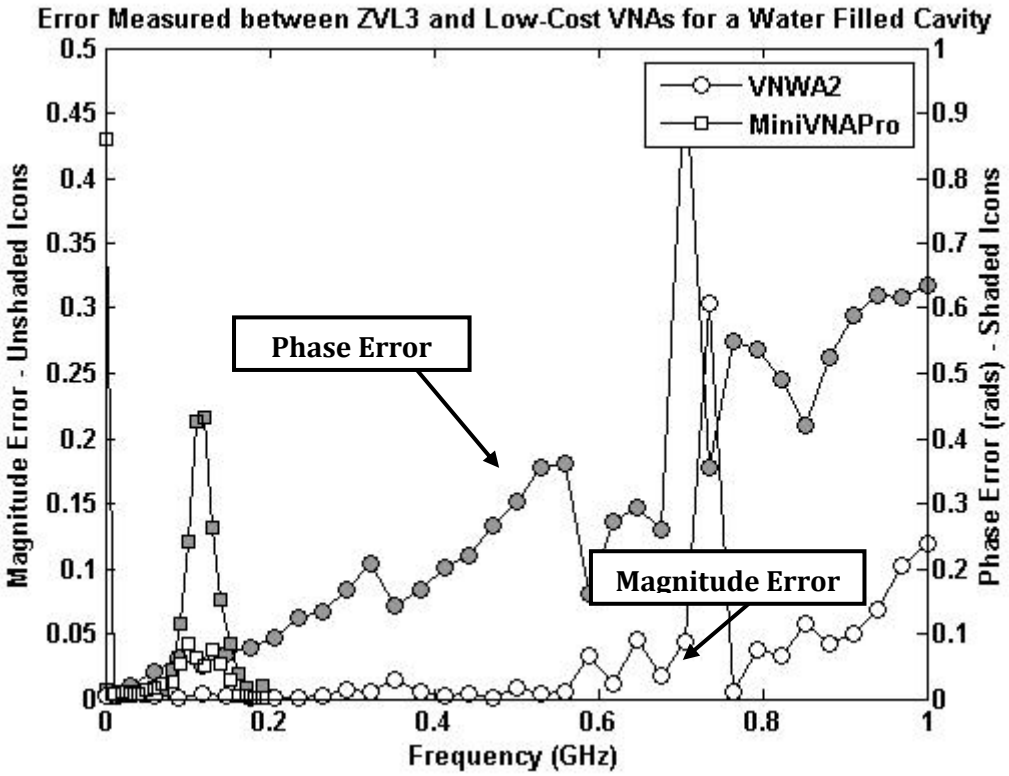

Figure 3-17: Error calculated between the low-cost VNAs and the laboratory VNA for measurements on a water-filled coaxial cavity. Magnitude error is denoted with unshaded icons, shaded icons denote phase. The MiniVNAPro exhibits much greater phase error than the VNWA2 where phase error increases consistently, similar to measurements on an air-filled coaxial cavity.

3.5.3 Two-Port Measurements

The two-port accuracy of the low-cost VNAs was tested using the two-port coaxial cavity described in section 3.4.1. As with the one-port measurements described above, the coaxial cavity was filled with air then tap-water and each VNA was used to measure the cavity response across its maximum frequency-range.

3.5.3.1 Results for Air-Filled Two-Port Coaxial Cavity

The magnitude and phase measurements for an air-filled coaxial cavity are shown in Figure 3-18 and Figure 3-19. Magnitude and phase show reasonable agreement for the S21 measurements, but the S11 measurement of the MiniVNAPro shows significant error. As this was not present during the one-port measurement the error must be due to the techniques used by the MiniVNAPro for simultaneously measuring S11 and S21. The error calculated by subtracting the low-cost VNA measurements from the interpolated results of the laboratory-grade VNA is shown in Figure 3-20 and Figure 3-21. Both low-cost VNAs show errors of around 10% of magnitude for

S21 measurements, and around 20% of magnitude for S11 measurements. Error in phase is calculated to be approximately 0.05 radians for both S21 measurements. S11 phase measured with the MiniVNAPro shows significant error (up to 0.5 rads), while S11 phase measured with the VNWA2 shows low error below 250 MHz (around 0.02 rads) then increases linearly whilst exhibiting the same region of error between 600 and 800 MHz that was shown in the one-port measurements.

3.5.3.2 Results for Water-Filled Two-Port Coaxial Cavity

The two-port measurements were repeated, with the coaxial cavity filled with tap-water. The measurements serve to illustrate the effectiveness of the low-cost VNAs for a high-attenuation measurement. Results are shown in Figure 3-22 - Figure 3-25.

Considering the MiniVNAPro; the magnitude measurements for both S11 and S21 were in good agreement with the laboratory-grade VNA. For the S11 measurement, maximum error was approximately 10% but was more typically 4%. The S21 measurement showed similar levels of error, and in both cases error was greater where magnitude was lower which fits with the relatively small dynamic range stated by the MiniVNAPro specification. S21 phase, measured by the MiniVNAPro was consistently within 0.2 rads of the results of laboratory-grade VNA. However, the phase of the S11 measurement appears completely erroneous.

The VNWA2 measurements show very little agreement with those of the laboratory-grade VNA, except for the S21 phase measurement which shows agreement above 300 MHz with relatively high error (up to 0.5 rads).

Neither low-cost VNA has the facility to calibrate using the seven standard calibration method (through, and open, short, load, on both ports) because port 2 cannot transmit. It is likely that a large proportion of the error reported here is due to the inability to fully calibrate for a two-port measurement. As a result of the high errors in the two-port measurements, the two-port inversion is included for completeness, rather than as a realistic method for use with low-cost VNAs.

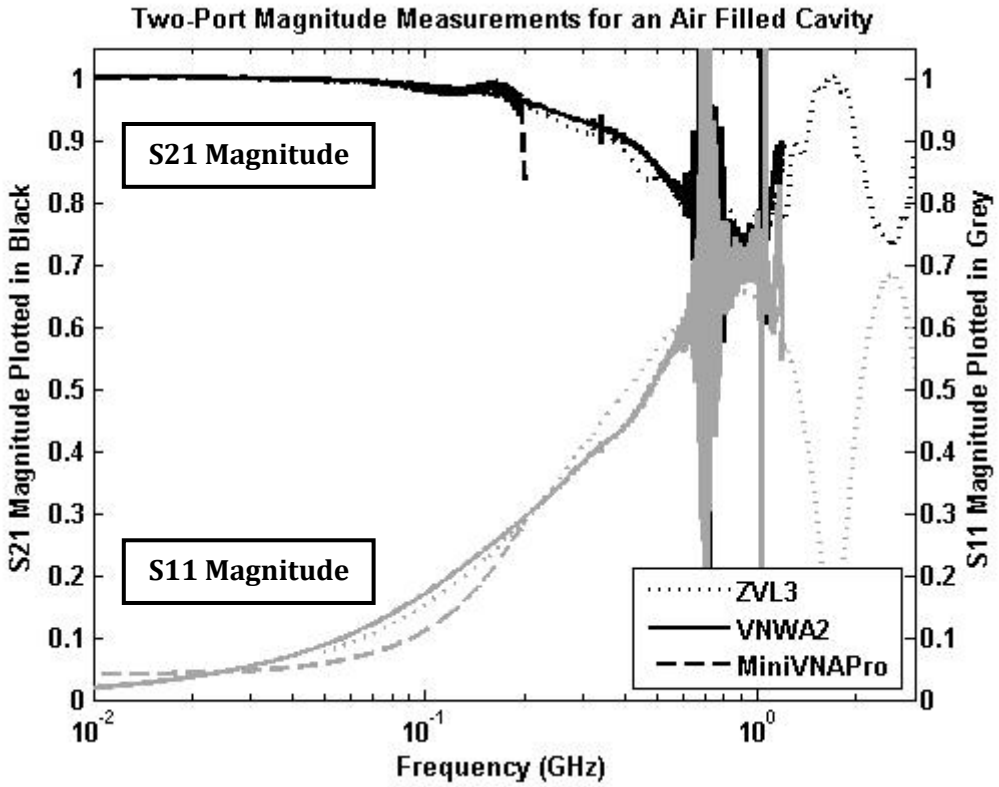

Figure 3-18: Two-port magnitude measurements, taken using three VNAs, for an air-filled coaxial cavity. S21 magnitude is shown in black, S11 magnitude is shown in grey.

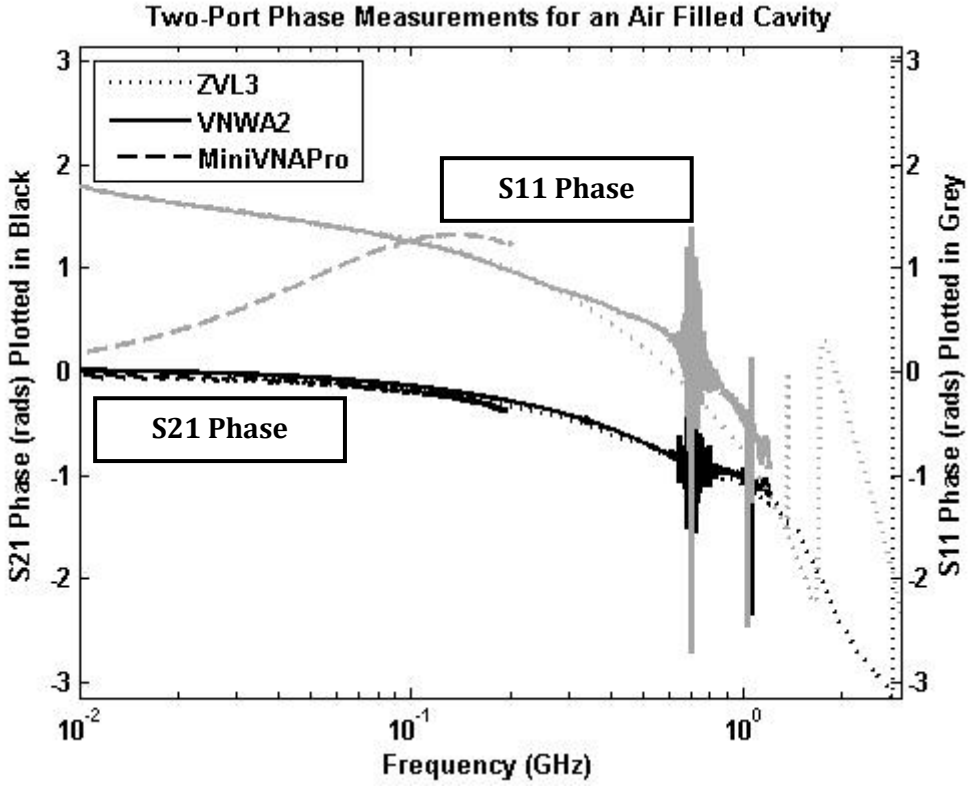

Figure 3-19: Two-port phase measurements, taken using three VNAs, for an air-filled coaxial cavity. S21 magnitude is shown in black, S11 magnitude is shown in grey.

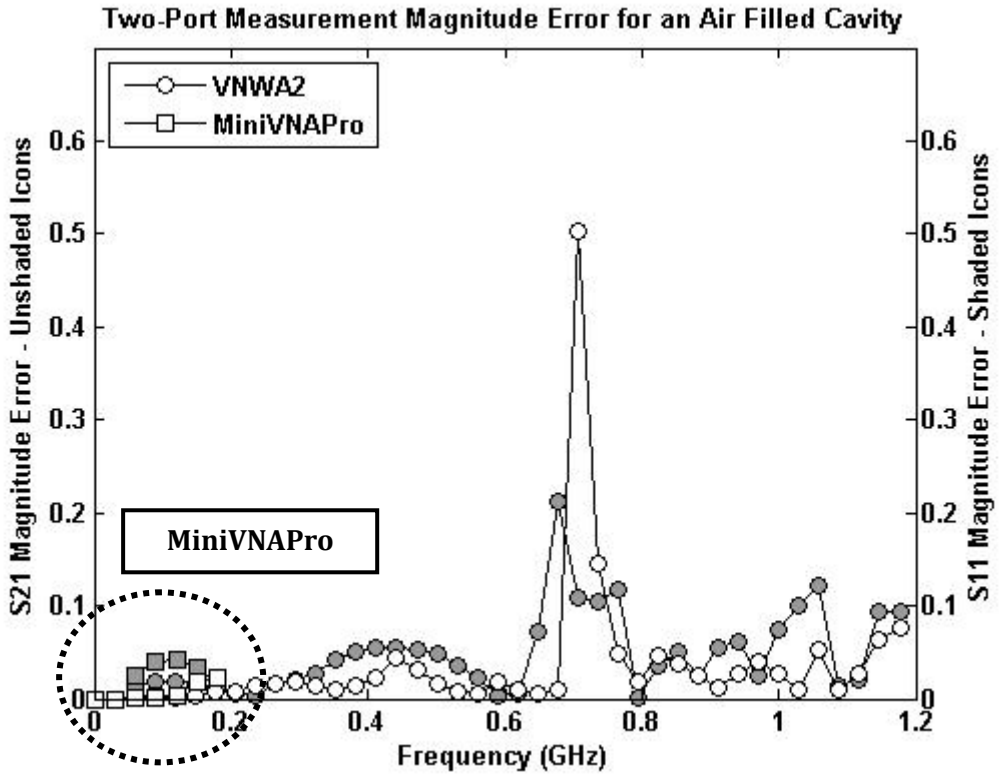

Figure 3-20: Magnitude error in two-port measurements of an air-filled coaxial cavity. Calculated by subtracting the low-cost VNA measurements from the laboratory-grade measurements. S21 is shown with unshaded icons, S11 shaded icons.

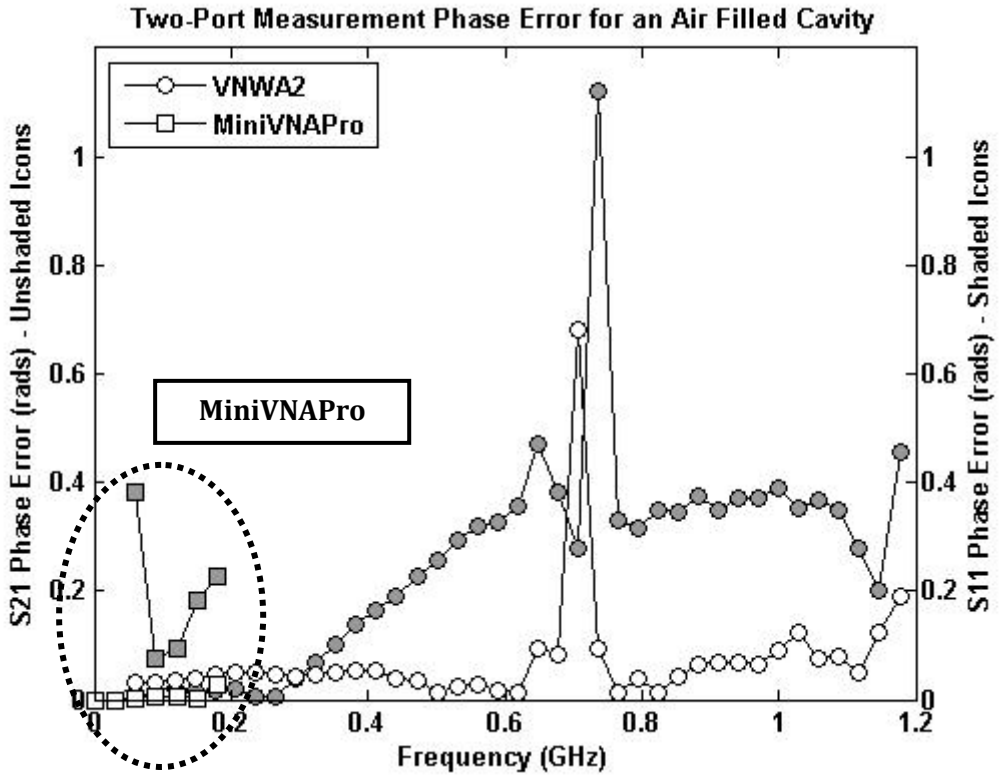

Figure 3-21: Phase error in two-port measurements of an air-filled coaxial cavity. Calculated by subtracting the low-cost VNA measurements from the laboratory-grade measurements. S21 is shown with unshaded icons, S11 shaded icons.

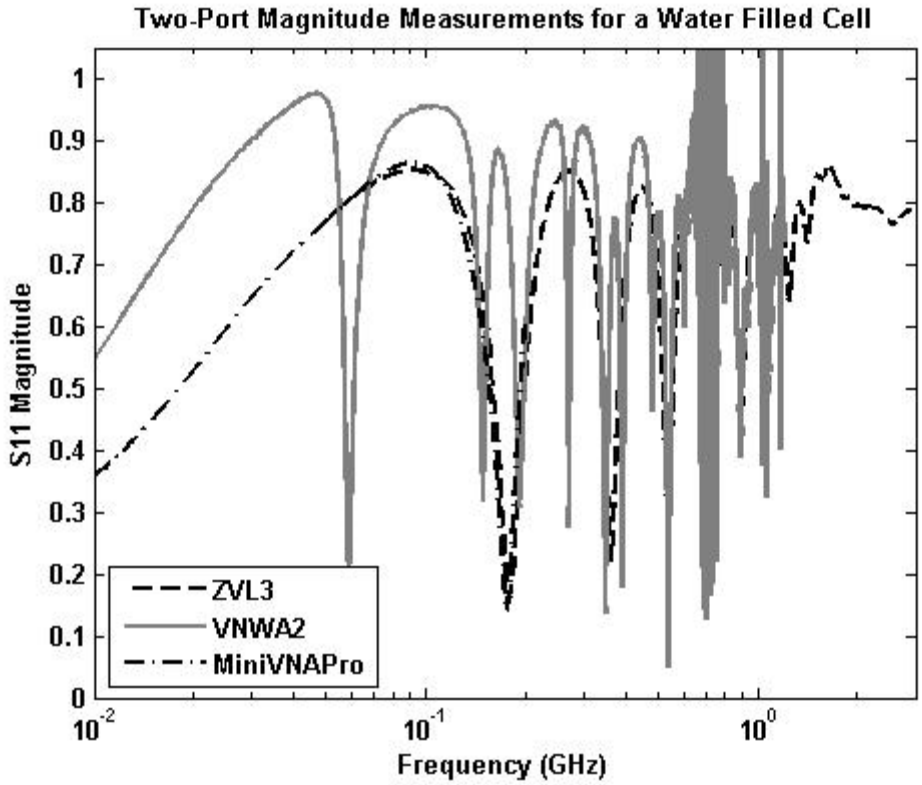

Figure 3-22: S11 magnitude of a two-port, water-filled, coaxial cavity. Measured using three different VNAs.

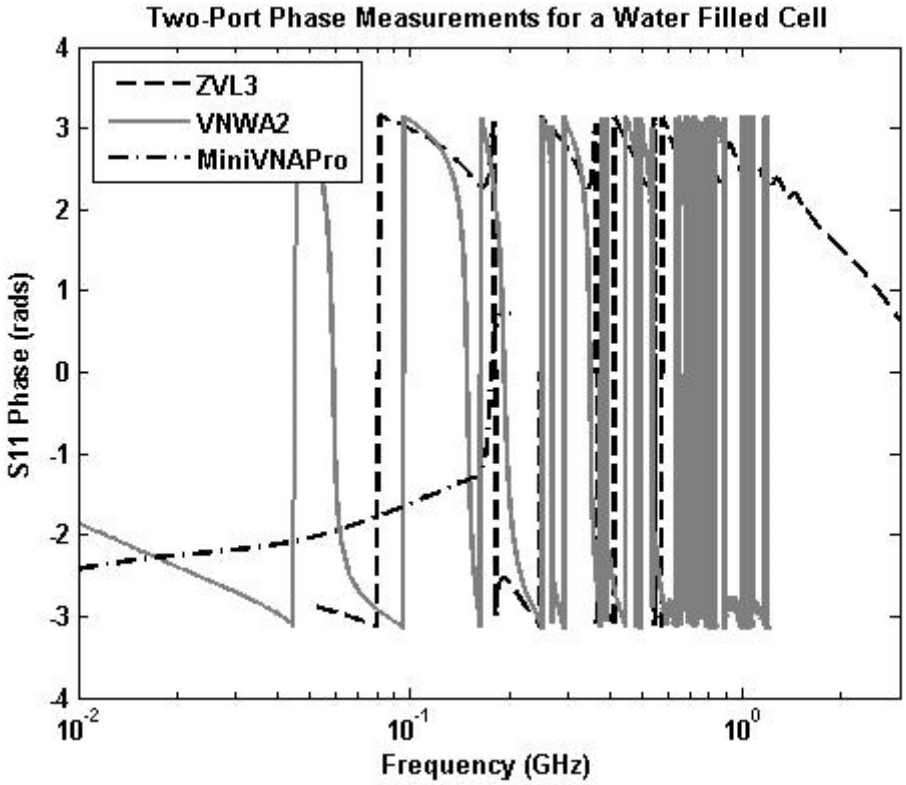

Figure 3-23: S11 phase of a two-port, water-filled, coaxial cavity. Measured using three different VNAs.

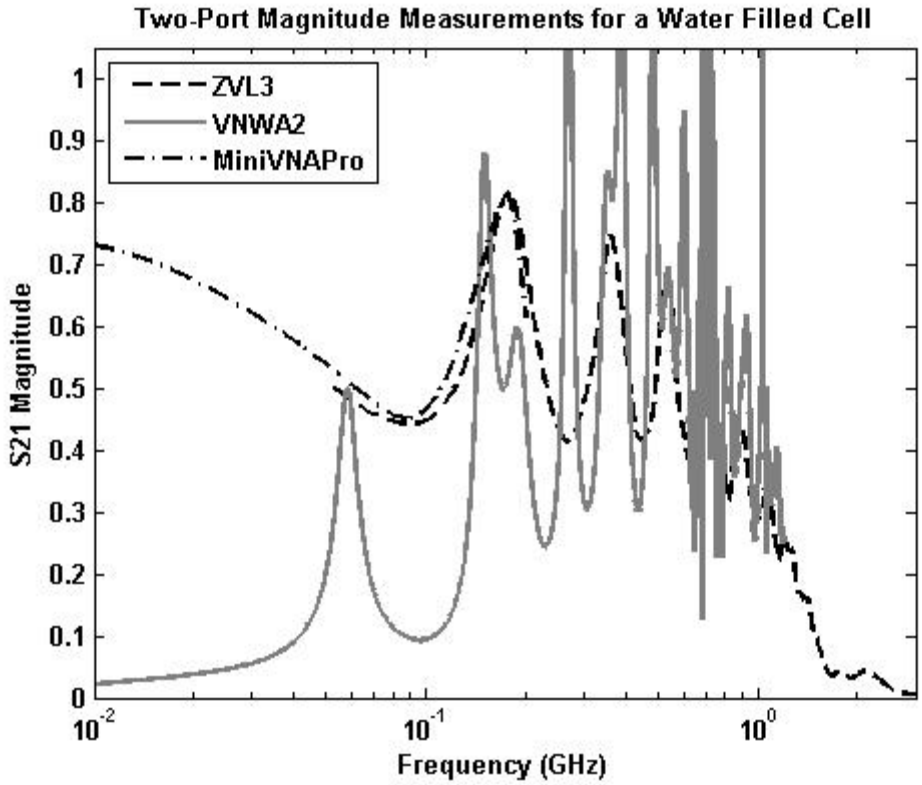

Figure 3-24: S21 magnitude of a two-port, water-filled, coaxial cavity. Measured using three different VNAs.

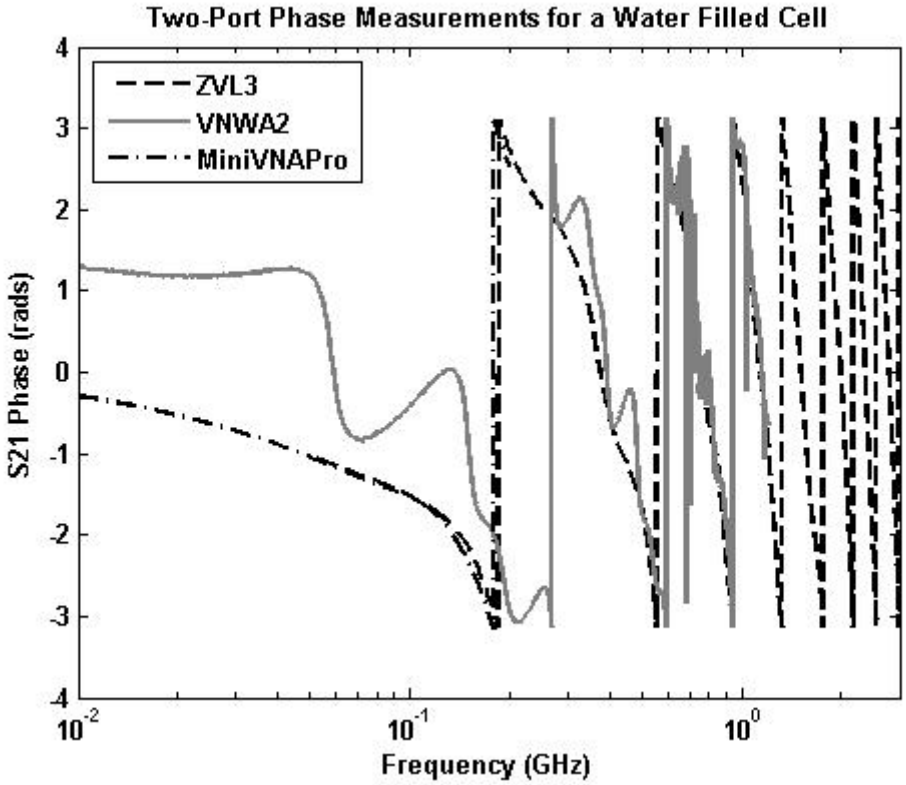

Figure 3-25: S21 phase of a two-port, water-filled, coaxial cavity. Measured using three different VNAs.

3.6 RESULTS

3.6.1 Calibration

This section presents results for the calculated scattering-parameters of the transition region. Comparing the results of the two different calibration methods goes some way to answering the question: Can a scattering matrix usefully describe the properties of a step-discontinuity in a coaxial transmission line?

3.6.1.1 Calibration from Three Short-Circuit Terminations

The calibration method outlined in section 3.4.3.1 was used with three different coaxial cavities of different lengths, by inserting brass discs into the cavities individually. It will be shown that some difference was observed between the transition regions of identically specified cavities. Despite these cavities being machined to within 0.1 mm of their specification, it is clear that small differences in geometry can result in measurable differences in calculated scattering-parameters. Figure 3-26 - Figure 3-31 show the calculated scattering-parameters for the transition regions.

Agreement is good between the 70 mm, 50 mm, and three cavity calibrations (mean difference between 70 mm and 50 mm cavities was 0.08 in magnitude and 0.30 rads in phase). However, the calibration for the 30 mm cavity exhibits oscillation of around 0.15 in magnitude and around 0.35 rads in phase. This is most likely due to the short length of the cavity reducing the measurable phase change and increasing error. The true measure of the effectiveness of these calibration results can only be established by comparison with a model, and by application to measurements of a coaxial cavity filled with a dielectric other than air.

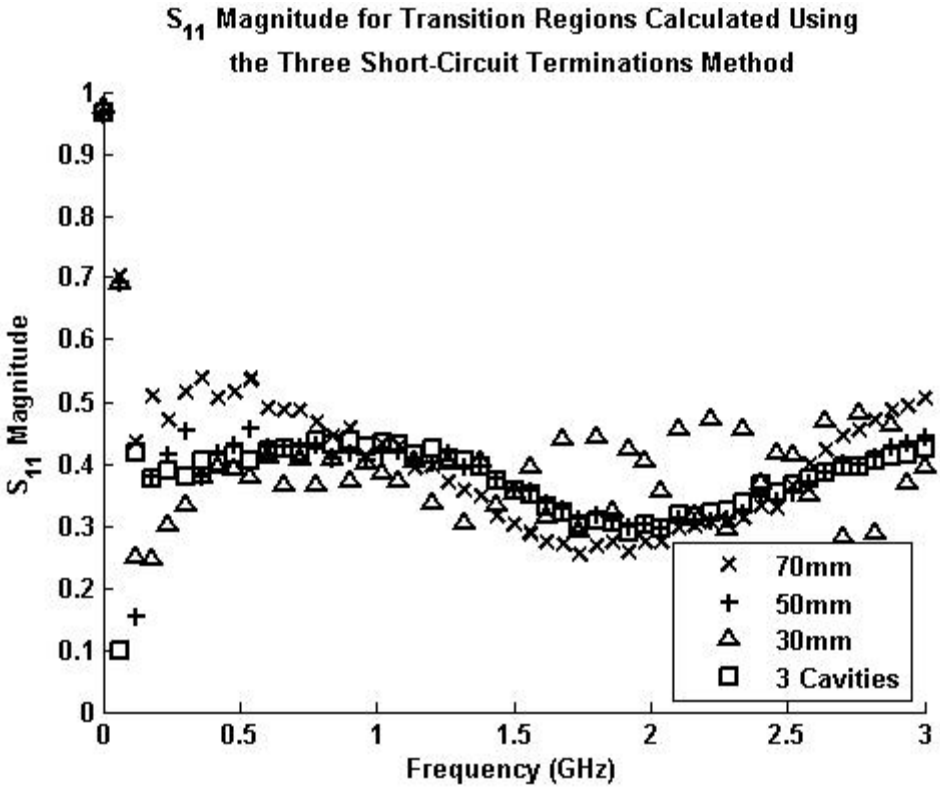

Figure 3-26: Transition Region S11 Magnitude calculated using 3 short-circuit terminations.

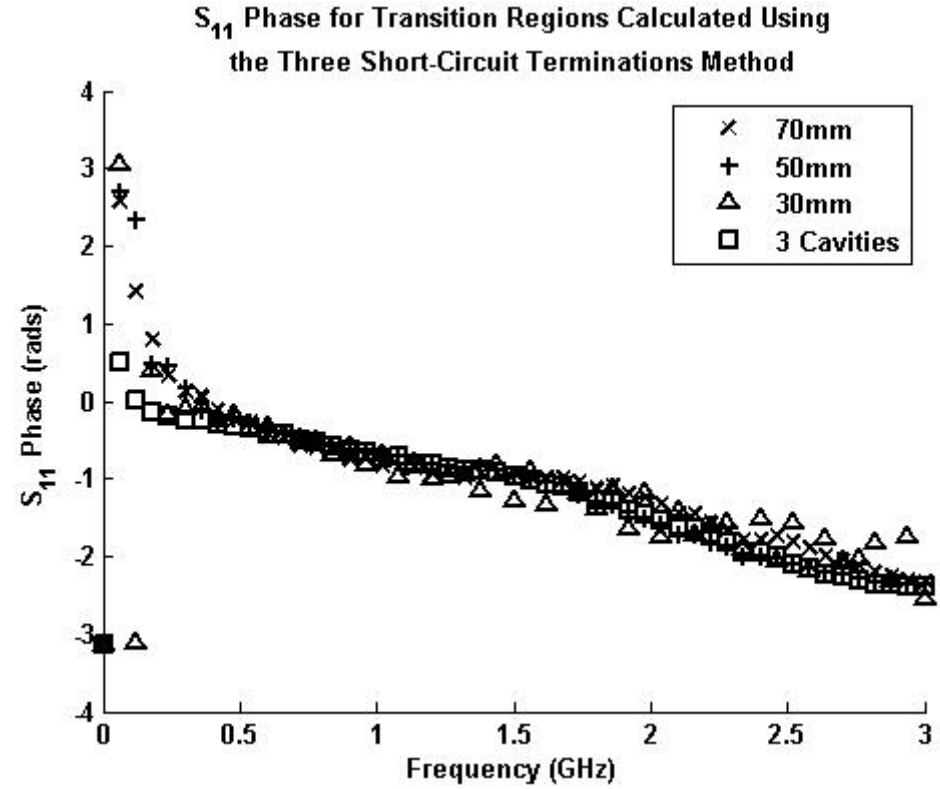

Figure 3-27: Transition Region S11 Phase calculated using 3 short-circuit terminations.

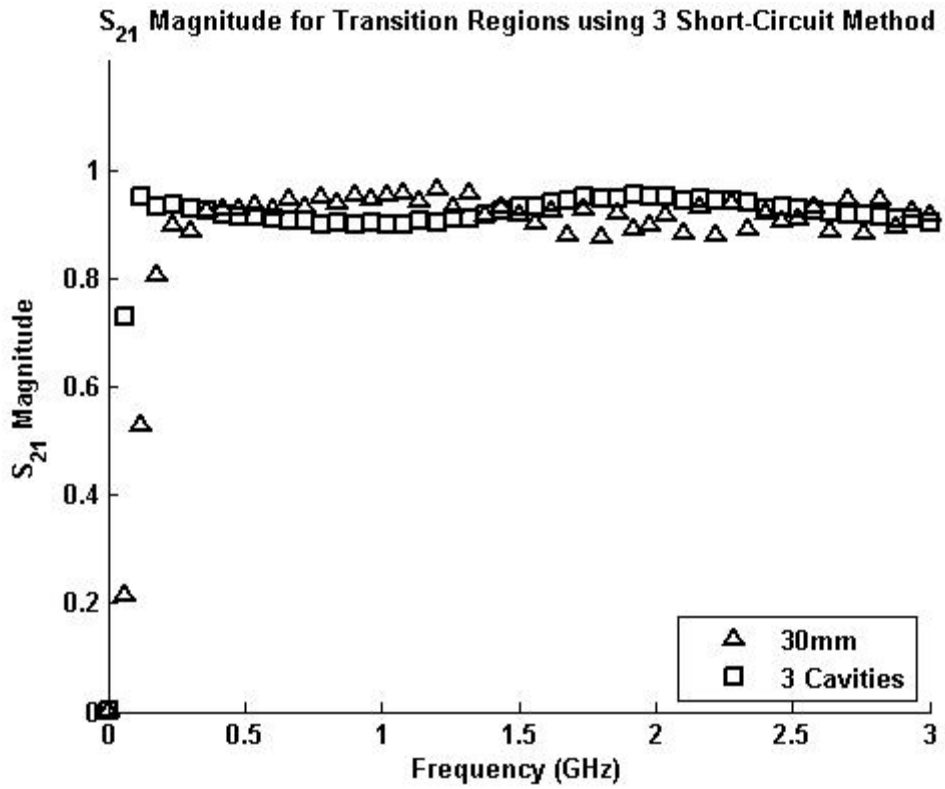

Figure 3-28: Transition Region S21 Magnitude calculated using 3 short-circuit terminations.

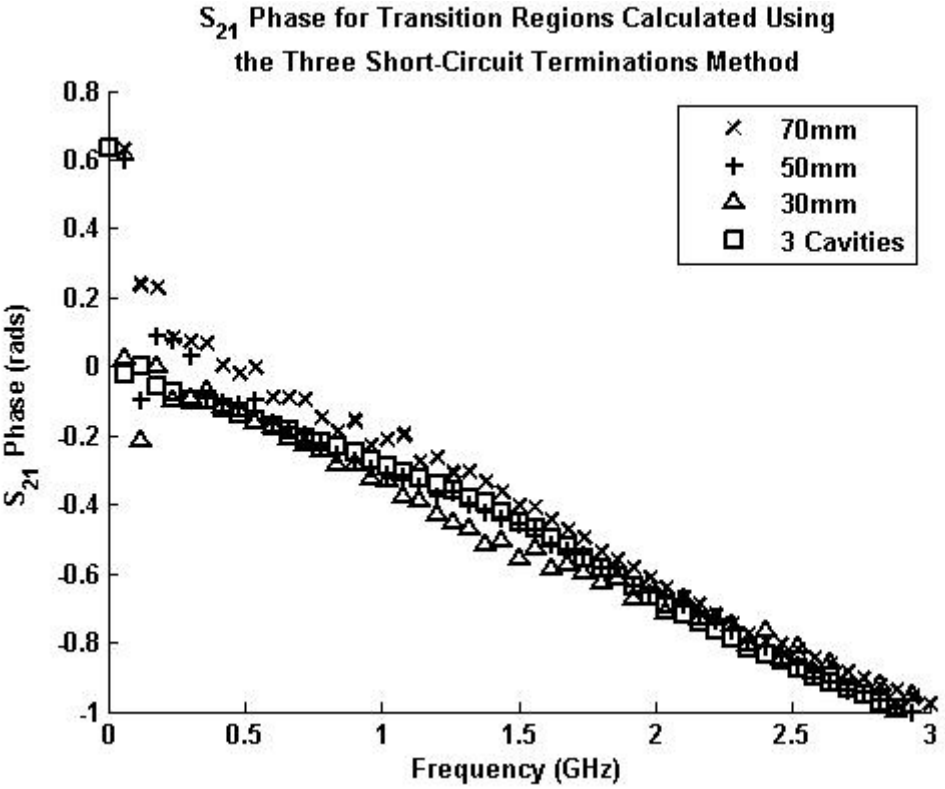

Figure 3-29: Transition Region S21 Phase calculated using 3 short-circuit terminations.

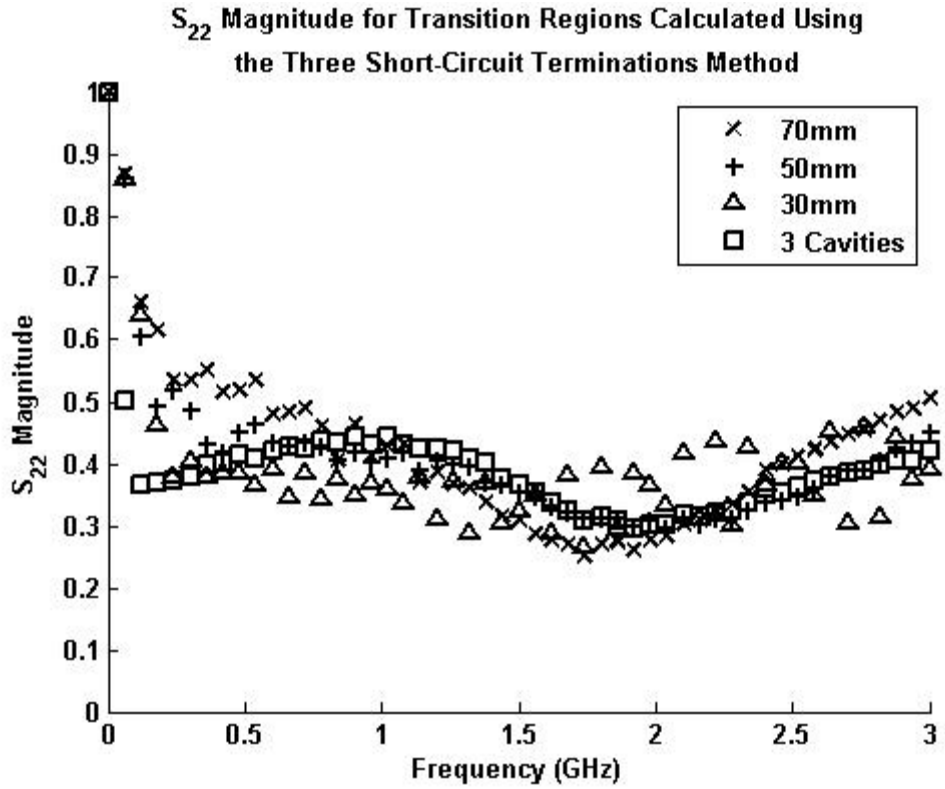

Figure 3-30: Transition Region S22 Magnitude calculated using 3 short-circuit terminations.

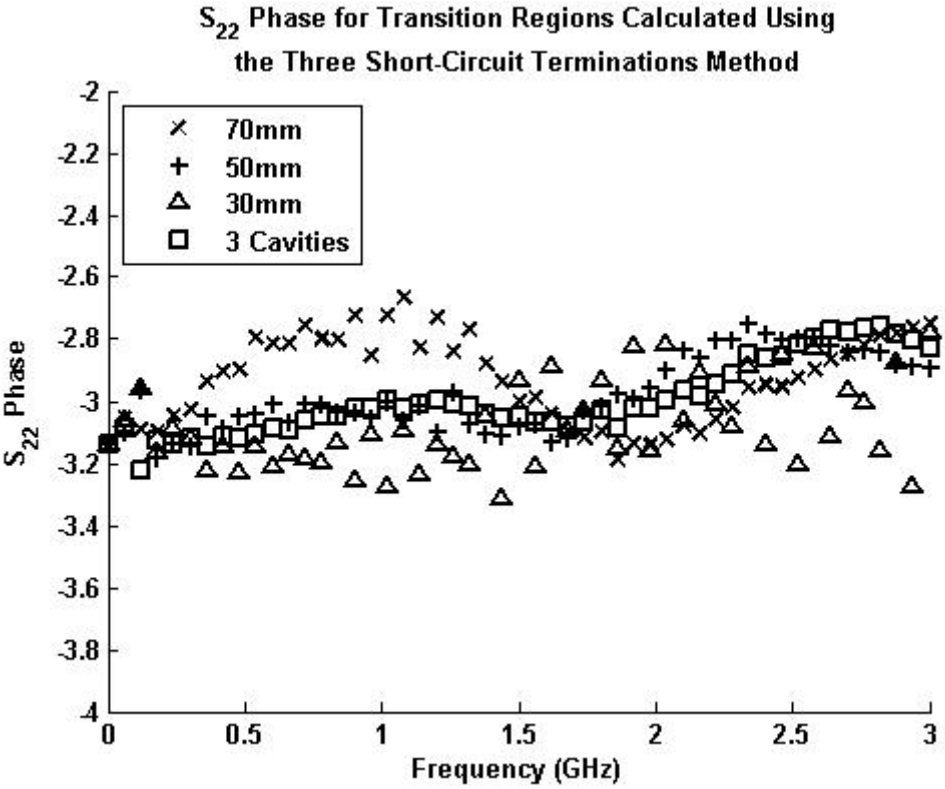

Figure 3-31: Transition Region S22 Phase calculated using 3 short-circuit terminations.

3.6.1.2 Calibration by Adjusting Model Parameters

Using the model outlined in section 3.4.3.2, model parameters were adjusted within defined bounds to increase the accuracy of the prediction. Two materials were used to test the model, air and tap-water. The minimisation was performed for the air measurement, the resulting values were used as the initial values for the minimisation using the tap-water measurement, and this was repeated for the air measurement. The parameters adjusted, with their upper and lower bounds, initial estimates and final values are given in Table 3-3. Measured and predicted S11 for air and tap-water measurements are shown in Figure 3-32 and Figure 3-33. Final calibration results for the transition region are shown in Figure 3-34, for comparison with Figure 3-26 to Figure 3-31.

It is clear that the prediction for air fits the measured results well but error increases with frequency. However, the error is much greater for tap-water. This is primarily due two factors: Firstly, tap-water is a medium which is not well characterised, predicted relative-permittivity is accurate only to within ±2 of real relative permittivity. This uncertainty could be reduced by using a material such as ethanol which is well characterised. However, for these experiments, measurements using ethanol and methanol suffered from evaporation during the measurements which meant results were unusable. The second factor is that the model assumes that the equivalent capacitance introduced due to the step discontinuity in the cavity is constant regardless of the media in the cavity. This assumption appears to be incorrect, and is discussed in greater detail in section 3.7.1.

Parameter	Original Estimate	Lower Bound	Upper Bound	Minimised Estimate
Cavity Inner Conductor Radius (mm)	2	1.5	2.5	2.063
Cavity Outer Conductor Radius (mm)	12	11	13	11.07
Cavity Length (mm)	70	67	73	69.49
Cable Inner Conductor Radius (mm)	0.6	0.05	1	0.4171
Cable Outer Conductor Radius (mm)	2	1	10	1.823
Transition Region Length (mm)	10	5	30	8.074
Relative-Permittivity of Cable Dielectric	2	1	5	3.727
Loss Tangent	0	0	1	2.45×10^{-10}

Table 3-3: Original and minimised model parameters from the calibration process.

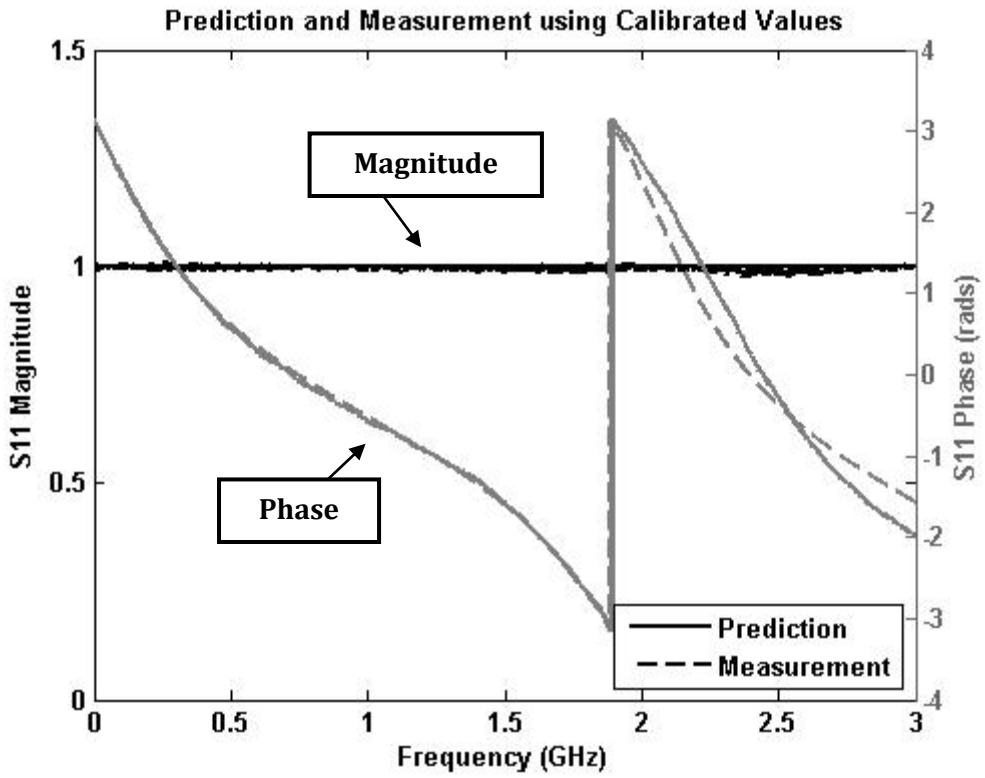

Figure 3-32: Minimised model and measured S11 for an air-filled coaxial cavity

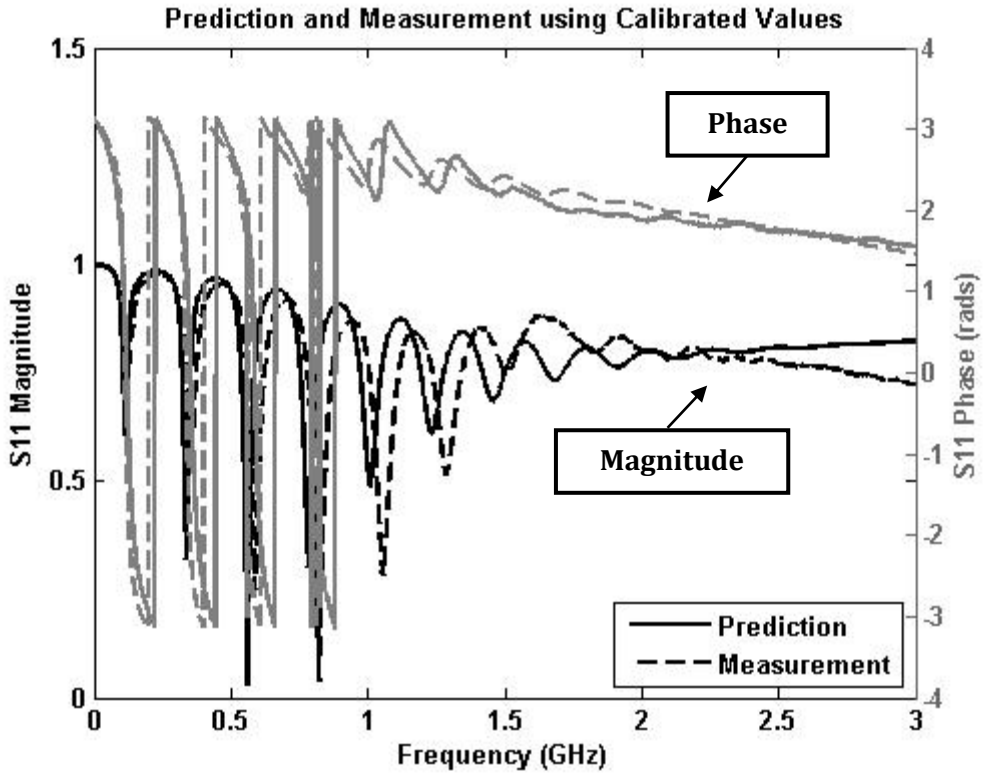

Figure 3-33: Minimised model and measured S11 for a water-filled coaxial cavity

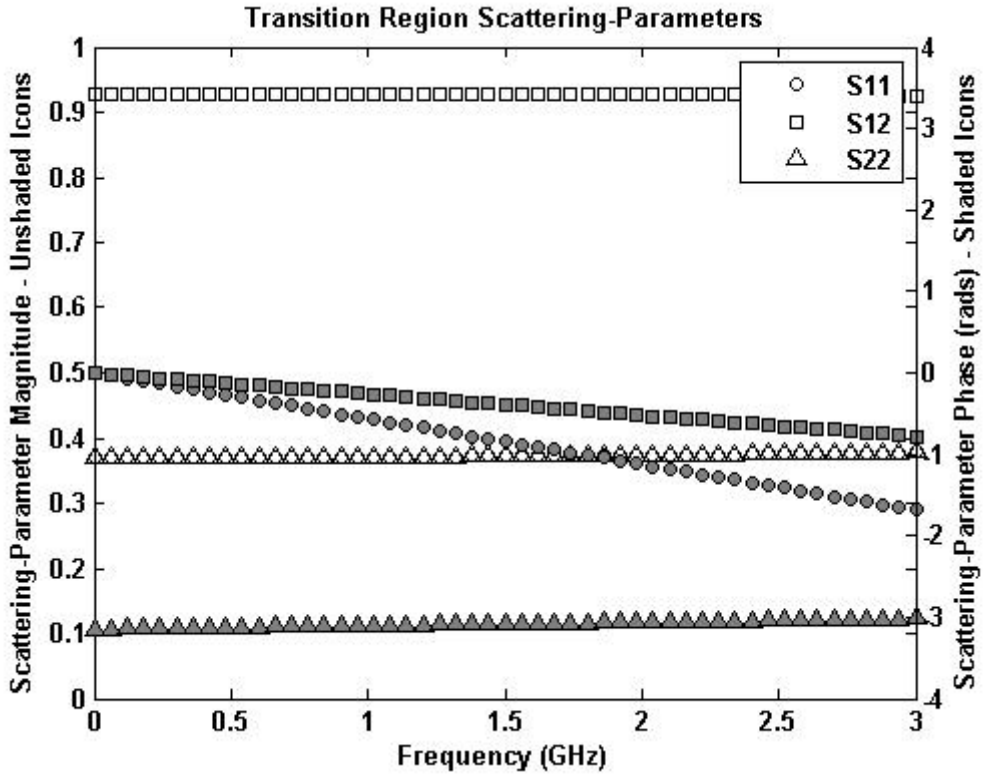

Figure 3-34: Transition region scattering-parameters derived using the Gorriti and Slob (2005b) calibration method. The unshaded markers denote magnitude and the shaded markers denote phase. Note S11 and S22 magnitude are approximately equal.

3.6.2 Uncertainty in Relative Permittivity Calculations

The results for relative permittivity calculations using the methods described above are shown in section 3.6.3. These results include uncertainty due to the uncertainty in the VNA measurements, determined using manufacturer specification for the laboratory-grade VNA, and using the values calculated in section 3.5 for the low-cost VNAs.

However, a significant uncertainty exists which is not readily quantified: The uncertainty due to error in calibration measurements taken to allow de-embedding of the coaxial cavity. Errors in the calibration measurements are a result of two primary sources: The first is the uncertainty in the VNA measurements which are used to calculate the scattering parameters of the transition region, these are easily quantified in the same way as the error for an individual measurement has been. The second source of error is due to the assumption that a calibration measurement taken using an air-filled cavity is valid for other materials measured. The scale of the error due to this assumption was unexpected. However, the results below will show that uncertainties not accounted for in the error analysis given in 3.4.4 dominate in some cases (see Figure 3-37, around 1.5 GHz for example).

The primary cause for these errors is believed to be the differing response in the fringing field, at the step discontinuity in the cavity, when the dielectric in the cavity is changed. Whilst the fringing field is well quantified in terms of an equivalent capacitance for an air filled cavity (Whinnery *et al.*, 1944; Somlo, 1967), no literature has been found which allows quantification of the difference in the cavity response due to a change in the dielectric at the discontinuity.

Figure 3-35 and Figure 3-36 are included to demonstrate the impact on the relative-permittivity calculation of errors in the calibration measurements. Both figures show considerable error introduced from relatively small errors in the calibration measurements. It is likely that errors increase as relative-permittivity of the dielectric increases due to increased change in the fringing field from the calibration measurement. Significant work is required to quantify the calibration errors due to the change in fringing field.

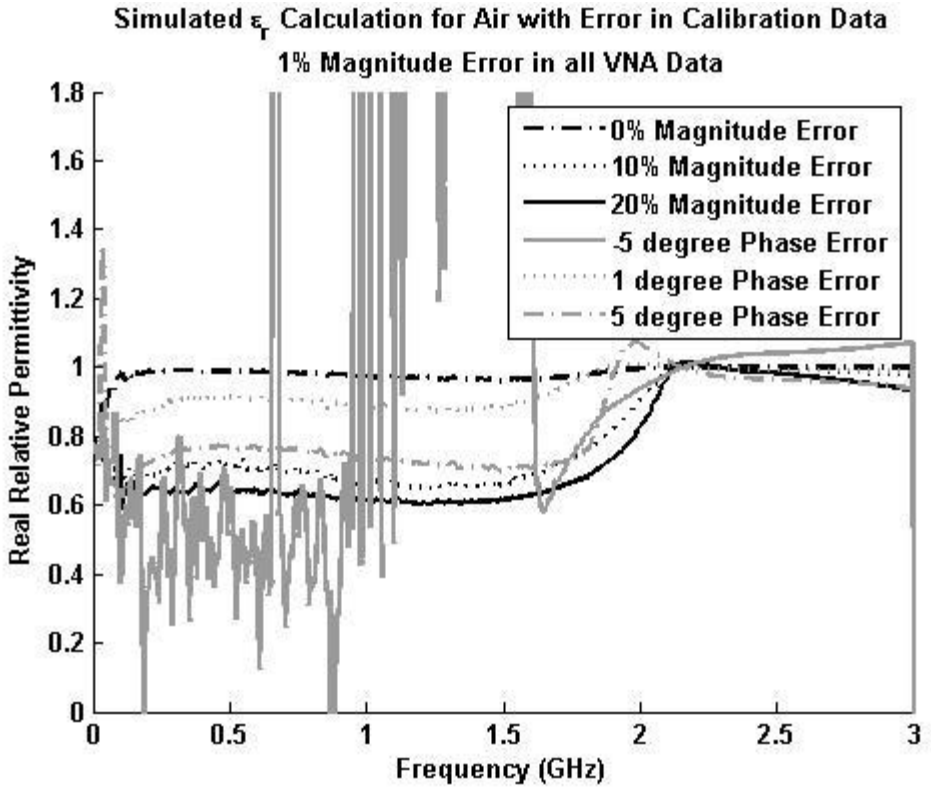

Figure 3-35: Error in the calculated relative-permittivity of air due to errors in the calibration measurements. Calculated using the methods described in section 3.4 with simulated data. Simulated data included a 1% magnitude error.

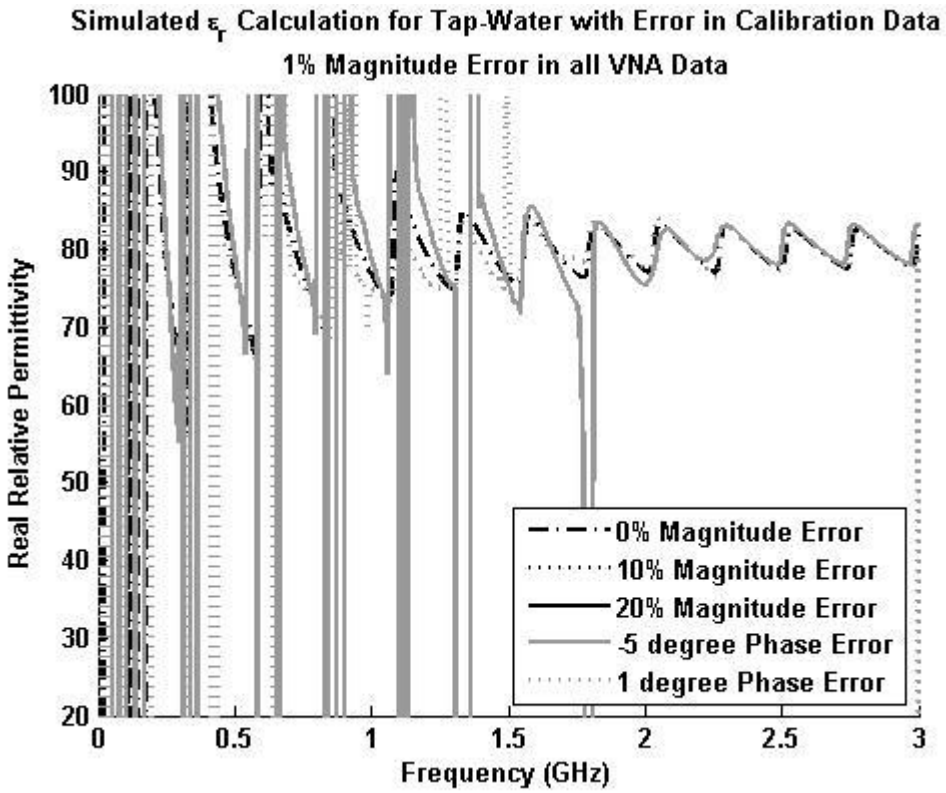

Figure 3-36: Error in the calculated relative-permittivity of tap-water (ε_r=80) due to errors in the calibration measurements. Calculated using the methods described in section 3.4 with simulated data. Simulated data included a 1% magnitude error.

3.6.3 One-Port Relative-Permittivity Calculation

The relative-permittivities of several different dielectrics were calculated using the different VNAs. However, the first results aim to show the most effective calibration mechanism using measurements taken with the laboratory-grade VNA. The uncertainties due to VNA error shown on the figures in this section were calculated using the method outlined in section 3.5.2, with the known error derived in section 3.5.

3.6.3.1 Calibration Comparison

The calculated relative-permittivity of air, using measurements of a 70 mm, one-port, coaxial cavity is shown in Figure 3-37. The result shown in Figure 3-37 used the parameter adjustment method for its calibration and gave a mean error of 0.052 (maximum 0.200). The equivalent measurement using the three short-circuit termination methodology is not shown because the air measurement is used in the calibration, and is computed to precisely match the expected result.

A better test of the calibration methods is to calculate the complex permittivity of a material which was not used in the calibration. The results of the calculated real-permittivity of dry sand are shown in Figure 3-38 and Figure 3-39. The results for the different calibration methods show good agreement. However, the three-short circuit termination method exhibits greater instability even after application of a low-pass filter. This is likely to be a result of small measurement errors at each frequency, for each of the three measurements, increasing uncertainty. The results calculated fit with the known relative permittivity of dry sand (Santamarina *et al.*, 2001) and show some dispersive behaviour.

The significant problem with the one-port method, from the perspective of this thesis and use of low-cost VNAs, is very high uncertainty at low-frequencies. The mean uncertainty, above 160 MHz for the result shown in Figure 3-39 is 3.8%, whereas the uncertainty below 160 MHz increases inversely as frequency decreases. Therefore, it is highly unlikely that this technique will provide usable measurements for relative-permittivity at very-low frequencies. However, as

discussed in Chapter 2, a large range applications exist for permittivity measurements between 200 MHz and 1 GHz.

3.6.3.2 Low-Cost VNA Measurements of Air

The measurements presented in this section show the calculated relative-permittivity of air, computed from measurements of short-circuit terminated coaxial cavities using low-cost VNAs. Figure 3-40 shows the calculated relative-permittivity from the VNWA2 measurement. The mean calculated relative-permittivity was 0.77 with a standard deviation of 0.24, between 2 MHz and 600 MHz. At frequencies above 600 MHz, the calculated relative-permittivity is highly erroneous and is only partially shown in Figure 3-40.

The uncertainty due to VNA error for the measurements using the low-cost VNAs, has been calculated by computing the relative-permittivity using the measured scattering-parameters, and the measured scattering-parameters plus or minus the error calculated in section 3.4.4. The use of this method, rather than the partial derivative method used with the laboratory-grade VNA (3-25) - (3-31), is due to the assumptions on which that method is based. It is assumed that the uncertainties of the input variables are small in comparison to the partial derivatives by which they are multiplied (Ku, 1969). This assumption cannot be maintained where high errors in the low-cost VNAs are present, and so the alternative methodology is used.

Figure 3-41 shows the calculated relative-permittivity from the MiniVNAPro measurement. Again, the result is reasonable with a mean relative-permittivity of 0.89 and a standard deviation of 0.11 above 2 MHz. The uncertainty due to VNA error is calculated using the same method as the VNWA2 results.

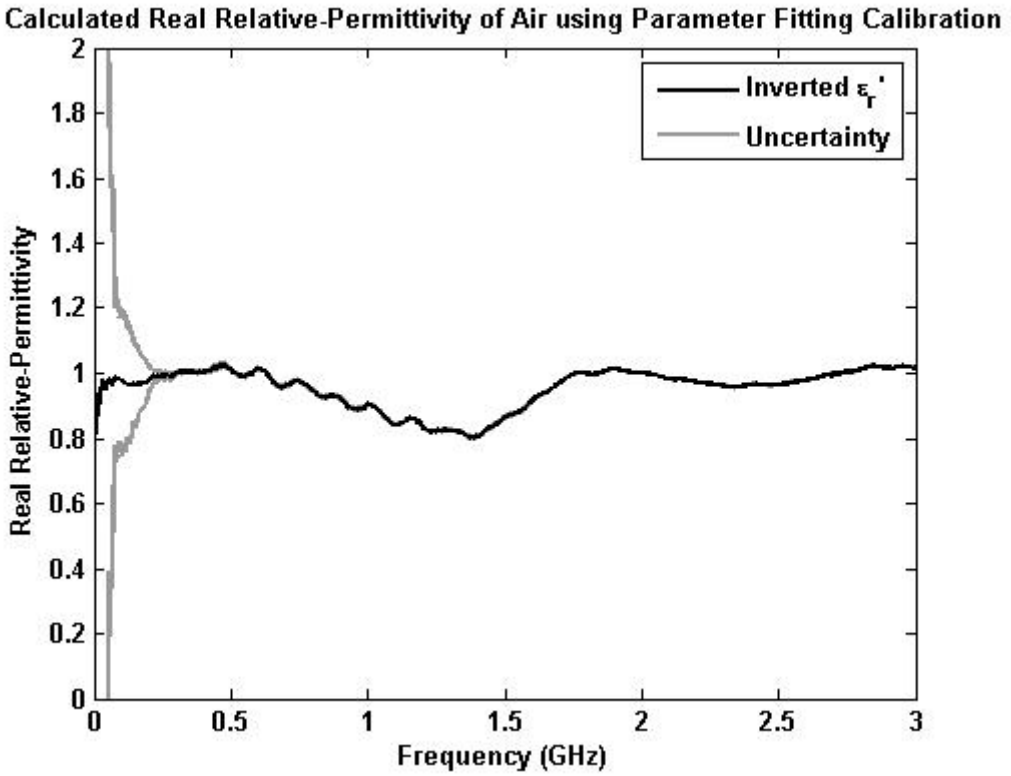

Figure 3-37: Real-permittivity calculated from measurement of a 70 mm coaxial cavity filled with air. Using calibration results from the parameter adjustment method. Uncertainty is calculated using partial derivatives based on the tolerances of the VNA as specified by the manufacturer, to 1 σ tolerance.

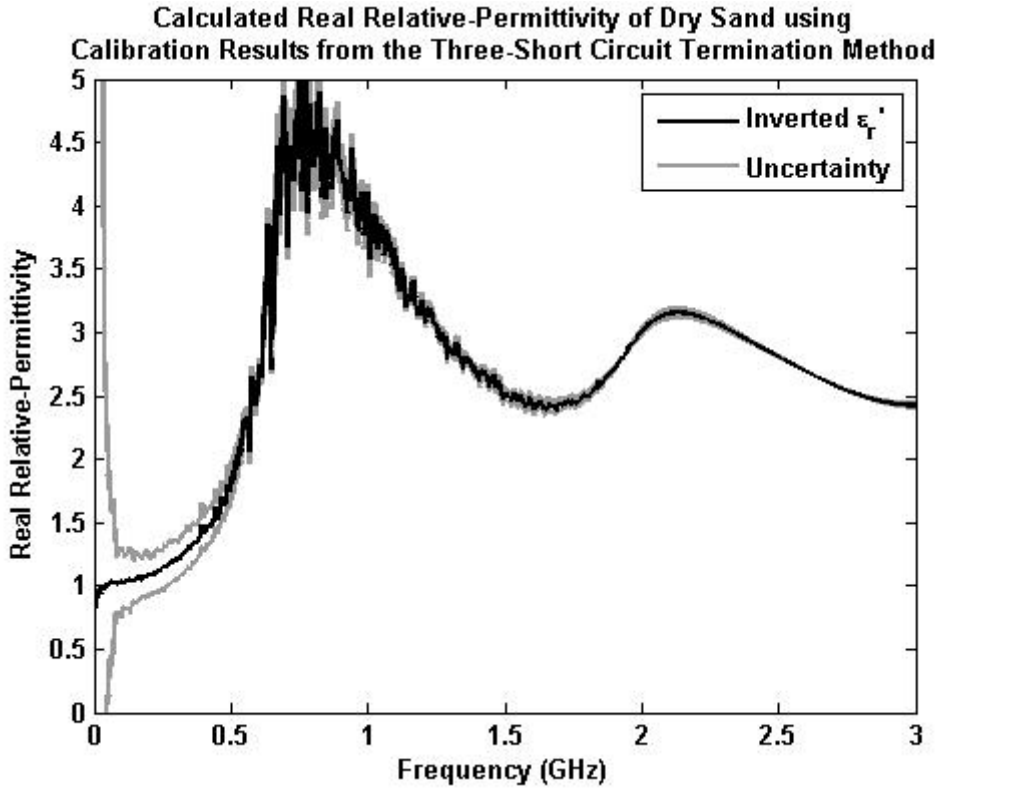

Figure 3-38: Real-permittivity calculated from measurement of a 70 mm coaxial cavity filled with dry sand. Using calibration results from the three short-circuit termination method. Uncertainty is calculated using partial derivatives based on the tolerances of the VNA as specified by the manufacture, to 1 σ tolerance.

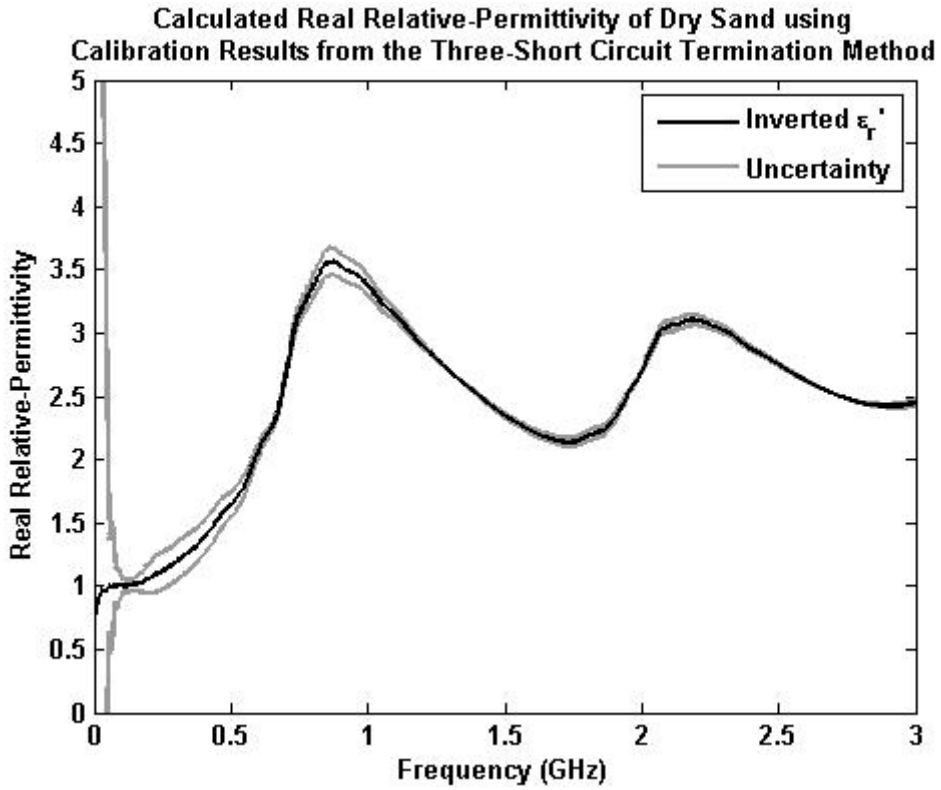

Figure 3-39: Real-permittivity calculated from measurement of a 70 mm coaxial cavity filled with dry sand. Using calibration results from the parameter adjustment method. Uncertainty is calculated using partial derivatives based on the tolerances of the VNA as specified by the manufacturer, to 1 σ tolerance.

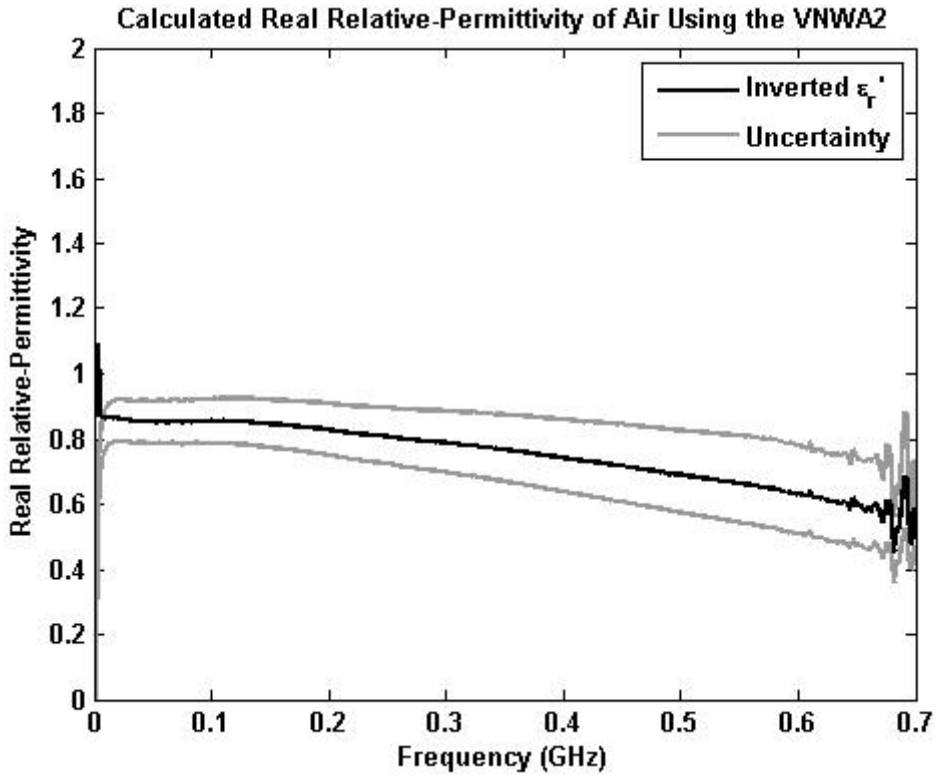

Figure 3-40: Calculated relative-permittivity of air using the VNWA2, from measurement of an air-filled, short-circuit terminated, coaxial cavity. The beginning of the erroneous region above 600 MHz is shown. Uncertainty is calculated using the measurement ± error shown in section 3.5.

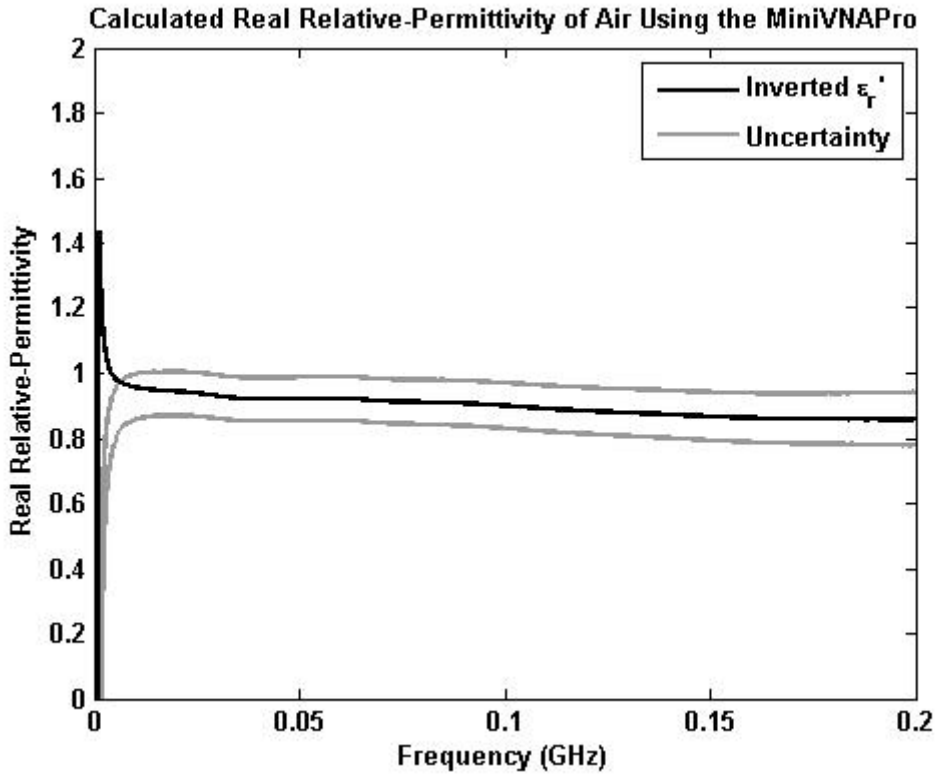

Figure 3-41: Calculated relative-permittivity of air using the MiniVNAPro, from measurement of an air-filled, short-circuit terminated, coaxial cavity. Uncertainty is calculated using the measurement ± error shown in section 3.5.

3.6.3.3 Low-Cost VNA Measurements of Dry Sand

The measurements were repeated for a coaxial cavity filled with dry sand. The calculated relative-permittivity from the VNWA2 and MiniVNAPro data are shown in Figure 3-42 and Figure 3-43, respectively. Both results show uncertainty calculated in the same way as the results presented for the relative-permittivity of air. However, the laboratory-grade results do not entirely fall within the stated uncertainty. This implies that the uncertainty must increase when the cavity contains dry sand. This is expected, given the increase in error with increased attenuation, and suggests that further work is needed to quantify the uncertainty in the low-cost VNA measurements for a range of dielectrics. Neither low-cost VNA has the frequency range to show the dispersive characteristics calculated using the laboratory-grade VNA (Figure 3-39).

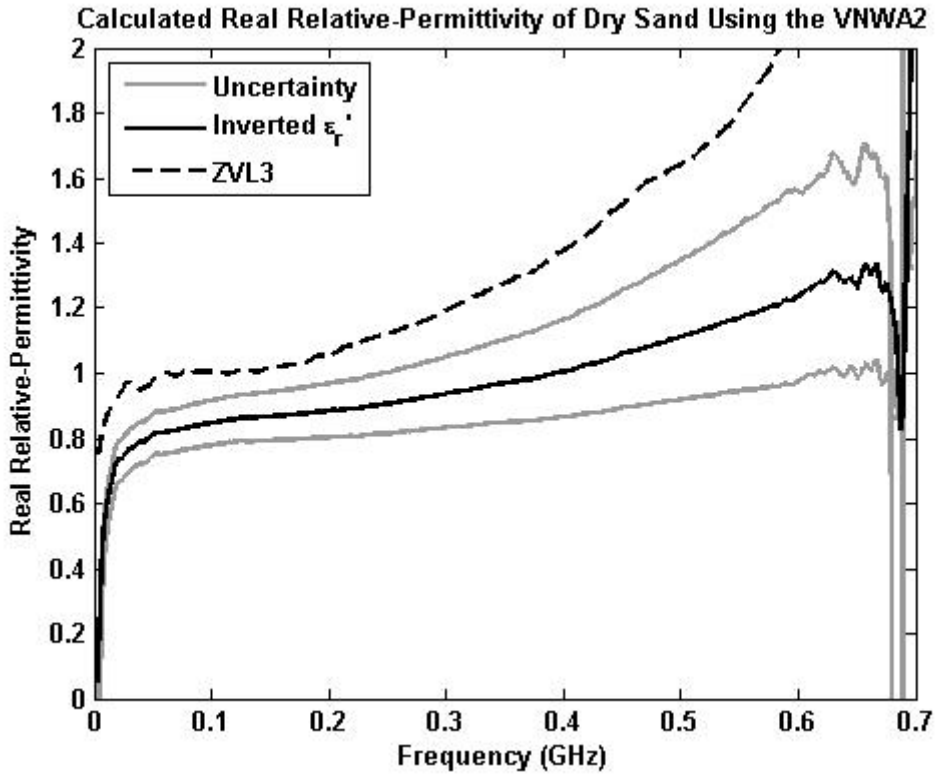

Figure 3-42: Calculated relative-permittivity from VNWA2 measurements of a sand-filled, short-circuit terminated, coaxial cavity. The equivalent result from the laboratory-grade VNA is shown for reference. Uncertainty is calculated using the measurement ± error shown in section 3.5.

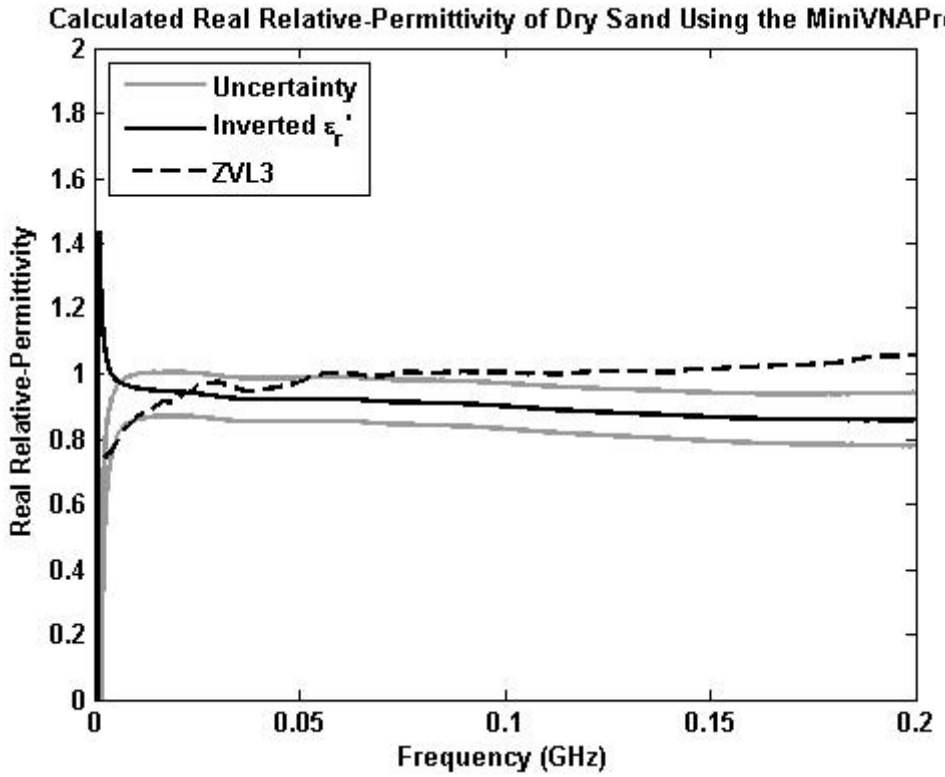

Figure 3-43: Calculated relative-permittivity from MiniVNAPro measurements of a sand-filled, short-circuit terminated, coaxial cavity. The equivalent result from the laboratory-grade VNA is shown for reference. Uncertainty is calculated using the measurement ± error shown in section 3.5.

Comparative results, showing the frequency-dependent relative permittivity of dry sand are difficult to obtain. It was shown by Kavian *et al.* (2010) that specific types of dry sand have relative permittivity between 2.5 and 3.6 in the frequency range up to 1 MHz. Whereas, Heimovaara *et al.* (1996) showed that the real relative permittivity of sand soil varies by around 20% at frequencies up to 1.5 GHz. Therefore, the results presented using the laboratory-grade VNA appear plausible, with the exception of the low-frequency region where relative permittivity is around 1, shown with large uncertainty.

3.6.4 Two-Port Relative-Permittivity Inversion

The low-cost VNAs reported very high error values for two-port measurements, which is most likely due to the inadequate calibration available when the second port cannot transmit. Therefore, it is not possible to produce useful results from the two-port methodology using low-cost VNAs. However, results are presented using a laboratory-grade VNA to provide results using a step-discontinuity coaxial cavity, which have not been reported before.

3.6.4.1 Calibration

The calibration methods presented have been shown to be effective for the one-port measurements. However, the calibration results for a two-port measurement are used for a more involved de-embedding process which will multiply any errors in the calibration. Therefore, it is important to show that the two-port coaxial cavity may be accurately predicted using the calibration data collected. Figure 3-44 - Figure 3-47 show the measured and predicted scattering-parameters for two-port coaxial cavity filled with air ($\varepsilon_r = 1, \sigma = 0\ Sm^{-1}$) and water ($\varepsilon_r = 79, \sigma = 0.04\ Sm^{-1}$). For both materials, there is significant error in the scattering-parameter magnitude, and increasing error in the scattering-parameter phase. For the measurement of an air-filled, two-port coaxial cavity, the maximum scattering-parameter magnitude error is 0.25 for both S11 and S21, while S11 phase error increases linearly to 0.8 rads and S21 phase error increases linearly to 4.6 rads. The increased attenuation for a water-filled cavity is predicted to increase the measured error and this is clearly shown to be the case.

3.6.4.2 Two-Port Calculation of Relative-Permittivity

Measurements taken using the laboratory-grade VNA were used to calculate relative-permittivity for air and dry-sand with the Boughriet method described in section 3.4.5. The de-embedding process was computed using data from the parameter-fitting calibration method. Results are shown in Figure 3-48 and Figure 3-49, which show inconsistent values for relative-permittivity with high uncertainty.

The inversion methodologies presented in this chapter all require a reliable model from which to calculate relative-permittivity. The differential equations for calculating uncertainty, (3-39) - (3-45), were used with the uncertainty measured on an air-filled coaxial cavity, to predict the best-case uncertainty for the two-port inversion techniques. It is expected that the measurement of an air-filled coaxial cavity represents the greatest achievable accuracy due to the increase in uncertainty due to increased losses.

Assuming $\Delta|S_{11}| = 0.25$, $\Delta\theta_{11} = 2.67 \times 10^{-10} \times f$, $\Delta|S_{21}| = 0.25$, and $\Delta\theta_{21} = 1.53 \times 10^{-9} \times f$, in the scenario that all other factors were precisely known, gave the uncertainty in relative-permittivity calculations shown in Figure 3-48 and Figure 3-49.

It is difficult to envisage usable results from this methodology without significant improvement in the calibration process.

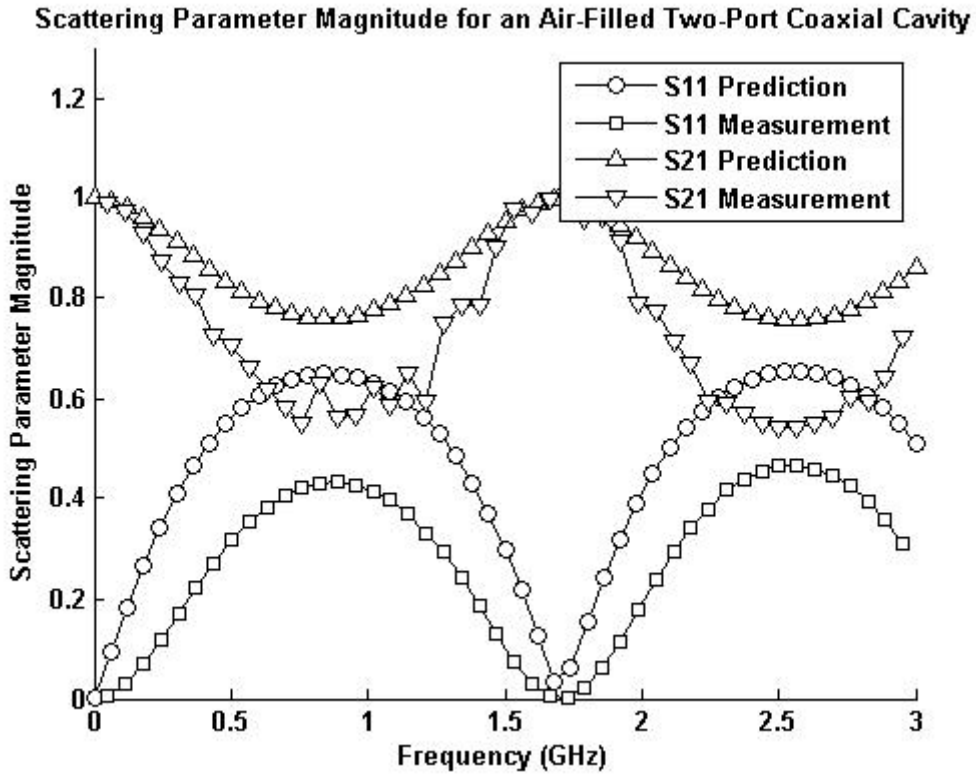

Figure 3-44: Measured and predicted scattering-parameter magnitude for a two-port coaxial cavity filled with air. Significant difference is shown between predicted and measured values due to imperfections in the calibration process.

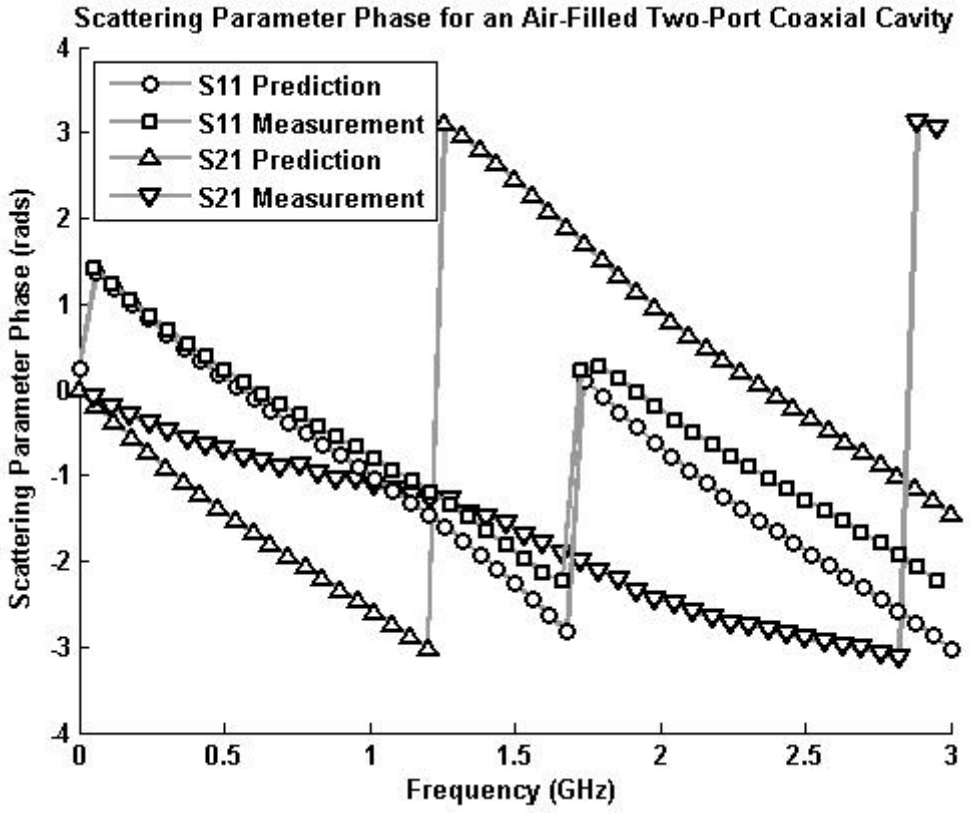

Figure 3-45: Measured and predicted scattering-parameter phase for a two-port coaxial cavity filled with air. Significant difference is shown between predicted and measured values due to imperfections in the calibration process.

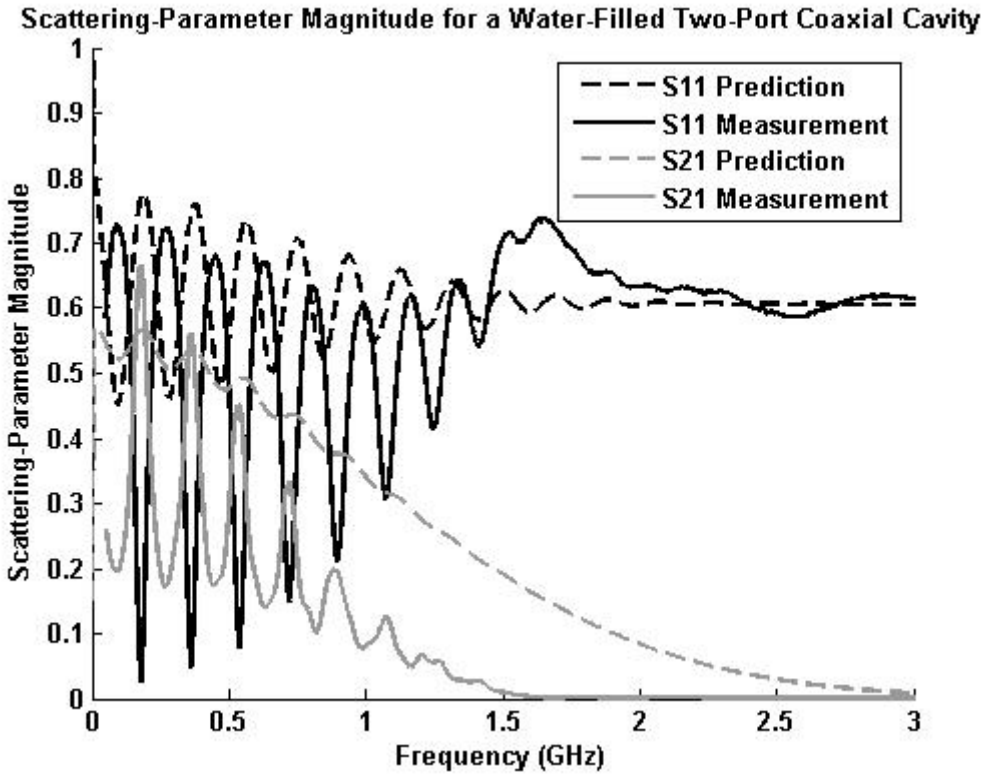

Figure 3-46: Measured and predicted scattering-parameter magnitude for a two-port coaxial cavity filled with tap-water $(\varepsilon_r = 79, \sigma = 0.04\ Sm^{-1})$. Significant difference is shown between predicted and measured values due to imperfections in the calibration process.

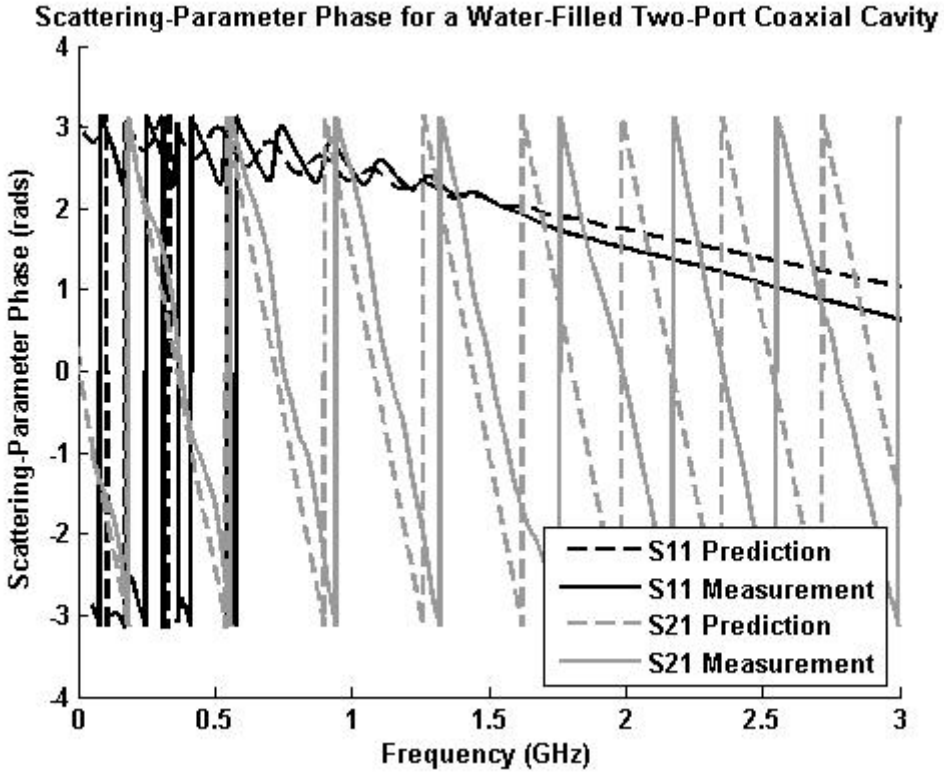

Figure 3-47: Measured and predicted scattering-parameter phase for a two-port coaxial cavity filled with tap-water $(\varepsilon_r = 79, \sigma = 0.04\ Sm^{-1})$. Significant difference is shown between predicted and measured values due to imperfections in the calibration process.

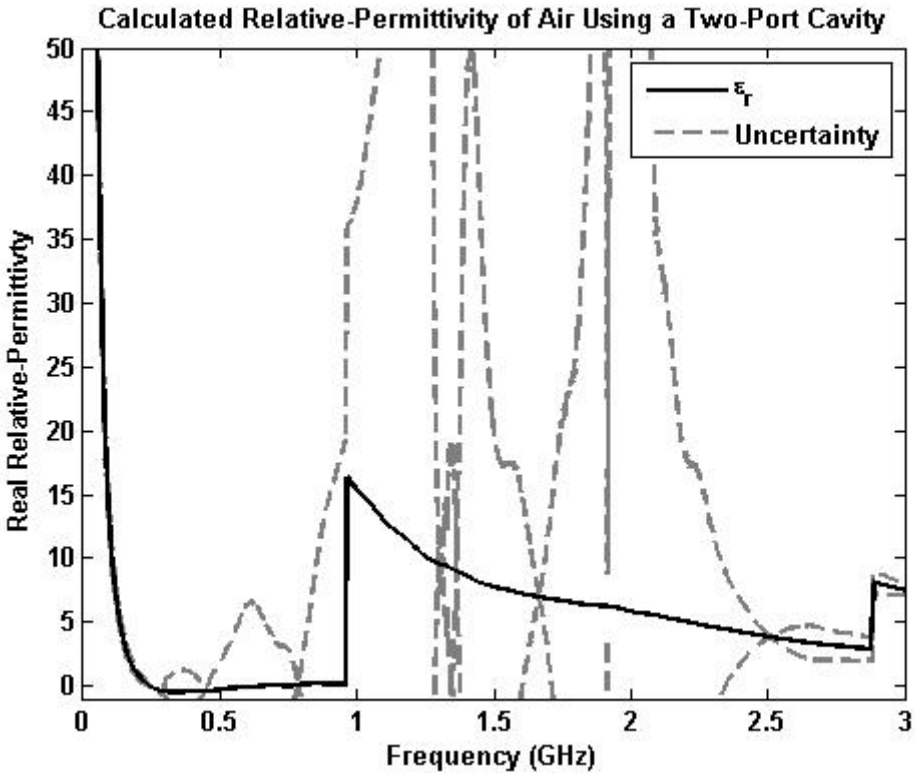

Figure 3-48: Real relative-permittivity of air calculated from measurements on a two-port coaxial cavity. High uncertainty and inconsistent results are shown due to imperfect calibration.

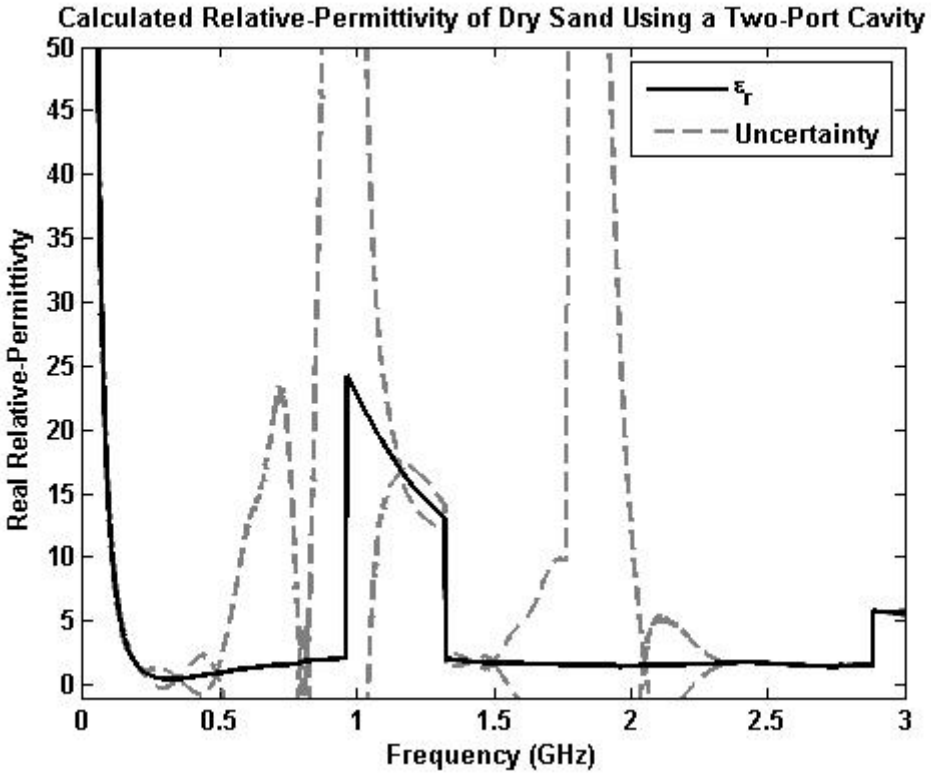

Figure 3-49: Real relative-permittivity of dry sand calculated from measurements on a two-port coaxial cavity. High uncertainty and inconsistent results are shown due to imperfect calibration.

3.7 DISCUSSION

3.7.1 Calibration Methods

Two calibration methods were used in this chapter. The first method used three short-circuit terminations at different positions in the transmission line to calculate the scattering-parameters of the transition-region. This method is well established, but has well documented failings in short transmission lines and at resonant frequencies (Shang *et al.*, 1999; Gorriti and Slob, 2005a). The second methodology adapted the method of Gorriti and Slob (2005b) who proposed adjusting model parameters to improve the accuracy of the model of the transmission line, which was then used to calculate the response of the dielectric-filled section. The proposed adaption was to include the equivalent capacitance of a step-discontinuity in the transmission line, using the modal analysis results presented by Whinnery *et al.* (1944) and Somlo (1967).

Both calibration methods allowed useful results for one-port measurements of air and sand, but the accuracy of both methods reduced when the cavity contained the high-loss dielectric (tap-water). Despite giving relatively similar results, the parameter-fitting method exhibited less local variation which was most likely due to requiring a single measurement to improve the model, rather than multiplying uncertainty from three measurements.

Neither calibration method was able to provide results which could de-embed a two-port measurement with sufficient accuracy to calculate the relative-permittivity with confidence. This questions the validity of attempting to quantify a step-discontinuity which is adjacent to the dielectric being characterised. A step-discontinuity results in fringing beyond the discontinuity which is then further affected by the relative-permittivity of the measured dielectric. A more sophisticated model for the discontinuity, such as those presented by Mahony (1988), or You and Abbas (2012), could have improved the calibration but would have resulted in significant complication to the inversion process. A better solution would have been to include a layer of a known dielectric beyond the discontinuity, large enough to entirely contain the fringing field.

This would result in a constant response from the transition region regardless of the dielectric within the cavity.

3.7.2 Error Analysis

Results for the calculation of relative-permittivity by one or two-port measurements were presented with values for uncertainty. For the laboratory-grade results, these values were calculated using the partial-derivative approach which quantified the calculation error from the known uncertainty of the inputs (Baker-Jarvis, 1990; Boughriet *et al.*, 1997). For the low-cost VNA results, these were calculated by repeating the calculation with measured scattering-parameters plus or minus the observed error in the low-cost VNAs.

The one-port methodology exhibited an increase in uncertainty proportional to $1/f$ at low frequencies which reduced its usable frequency range. However, it was shown that results have been obtained which typically fall within 10% of the laboratory-grade measurements. This shows that the one-port methodology, despite the calibration problems described, can produce useful results with low-cost VNAs.

Given the difficulties with the calibration process for the two-port measurements, it is difficult to draw any conclusions using the error-analysis of that method. However, from a literature survey it is felt that the Boughriet method (Boughriet *et al.*, 1997) has received relatively little attention. Boughriet *et al.* show their method as giving results comparable to the widely used Nicolson-Ross-Weir (NRW) method, but without the instability at half-wavelength frequencies. If this is the case, then the method ought to be widely adopted as an advance upon the NRW method.

3.7.3 VNA Comparison

The specifications of a number of VNAs were compared, and the low-cost VNAs were notable in their reduced dynamic range (up to 40 dB worse than a laboratory-grade VNA) but also their significantly lower cost. It would be misleading to suggest that the VNAs tested here represent anything other than a significant sacrifice in accuracy, frequency-range and usability, when

compared to a laboratory-grade VNA. However, there are situations where this compromise could be accepted. Applications which could tolerate larger errors include long-term monitoring where variation is more informative than absolute value or preliminary measurements where an indicative measurement with moderate confidence is sufficient.

Given the reported error for the one-port permittivity method presented here, it cannot be concluded that this method ought to be adopted for high precision measurements. However, despite the uncertainty range, the low-cost VNAs were used to calculate the relative-permittivity of air to within 0.11 (MiniVNAPro) and 0.23 (VNWA2) of the true value. Similarly, when measuring dry sand, both low-cost VNAs were used to present results which were close to the results of the laboratory-grade VNA (error of 0.3 rising to 0.9 for the VNWA2, and mean error of 0.2 for the MiniVNAPro). This suggests that, while the VNAs may not be useful for measurements requiring high-accuracy, approximate measurements can be made using the low-cost VNAs.

The comparison of two-port measurements did not provide results which would support the use of low-cost VNAs. Neither low-cost VNA measured results which compare to a laboratory-grade VNA, most probably due to the difficulties in calibration which were discussed. In order to use either low-cost VNA for two-port measurements a more robust two-port calibration process is required.

3.8 CHAPTER SUMMARY

The aim of this chapter was to investigate the application of low-cost VNAs to the measurement of the dielectric-properties of soil. Like-for-like comparison with a laboratory-grade VNA showed that low-cost VNAs can return one-port measurement results which correspond well to high-precision equipment, particularly for low-loss measurements. However, insufficient calibration mechanisms produce unreliable two-port measurement results using the low-cost VNAs.

The two methodologies used for calibration of a coaxial cavity - including step discontinuities - showed that the parameter-fitting method was slightly more stable than the three short-circuit termination method. However, neither method was sufficiently accurate to allow a two-port

measurement. The practical advantages of a step-discontinuity in the coaxial cavity include increased ease of sample preparation and reduced manufacturing cost. It is expected that the inclusion of a dielectric layer beyond the step-discontinuity could allow reliable calibration and enable researchers to realise the practical benefits of including a step-discontinuity, further research is required in this area.

Two existing methodologies were used to calculate relative-permittivity from the VNA measurements. The one-port methodology of Baker-Jarvis (1990) produced useful results with a laboratory-grade VNA but the uncertainty at low-frequencies limits its application with low-cost VNAs to approximate measurements. The two-port methodology by Boughriet *et al.* (1997) is a useful advance, but the limitations of the calibration procedures means it is not possible to comment on its efficacy.

CHAPTER 4: ELECTROMAGNETIC PROPAGATION IN LAYERED MEDIA

4.1 INTRODUCTION

4.1.1 Overview

This chapter demonstrates a new quasi-analytical method for calculating the electromagnetic (EM) field due to a vertical electric dipole (VED) in four-layered media. Consider a region in the shallow subsurface in which a water pipe is leaking, the simplest model applicable to this scenario is one with four layers: Air, unaffected soil near the surface, water-logged soil around the leaking pipe, and a bed-rock layer (Figure 4-1). A similar argument can be constructed when considering a large air-void, mineral deposit, or buried utility.

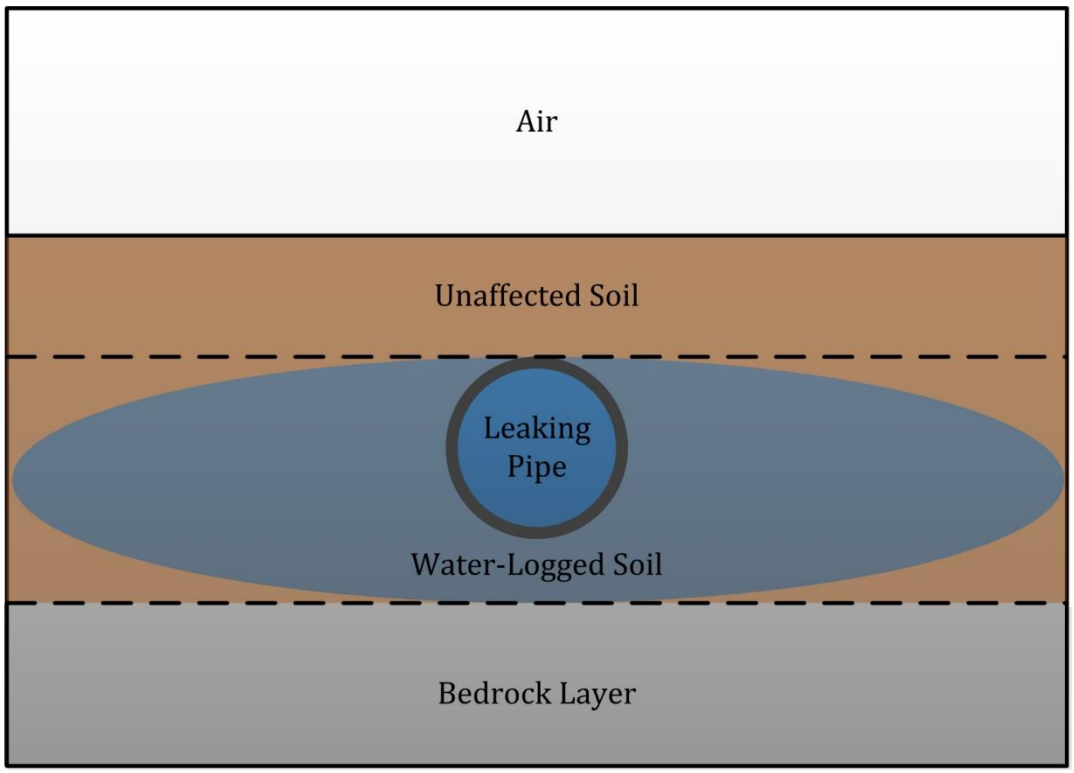

Figure 4-1: Geological profile of a leaking pipe. A four-layered model represents the simplest approximation of this geometry.

The reader might reasonably question the need for an analytical model, or why the analytical model requires an entire chapter. The analytical model is worth pursuing for several reasons: A numerical solution converges slowly due to the highly oscillatory nature of the integral equations describing the EM field in this geometry; a horizontal-electric dipole which could model an in-

pipe excitation is a logical extension of the VED case (Lu *et al.*, 2009); and when designing systems, it is useful to be able to quickly adjust model parameters – something that cannot be achieved with a slow numerical solution.

The work in this chapter will present a quasi-analytical solution to the above equation, but it will also show a number of flaws in previous publications. These flaws have made repeating earlier results exceedingly difficult and the requirement to correct previous errors makes this work quite involved.

4.1.2 Scope

This work considers the electromagnetic field in a four-layered media, due to a unit length vertical electric dipole in the air layer as shown in Figure 4-2. The derivations are limited to the methodology proposed by King and Sandler (1994), and developed by the works explored in the literature review.

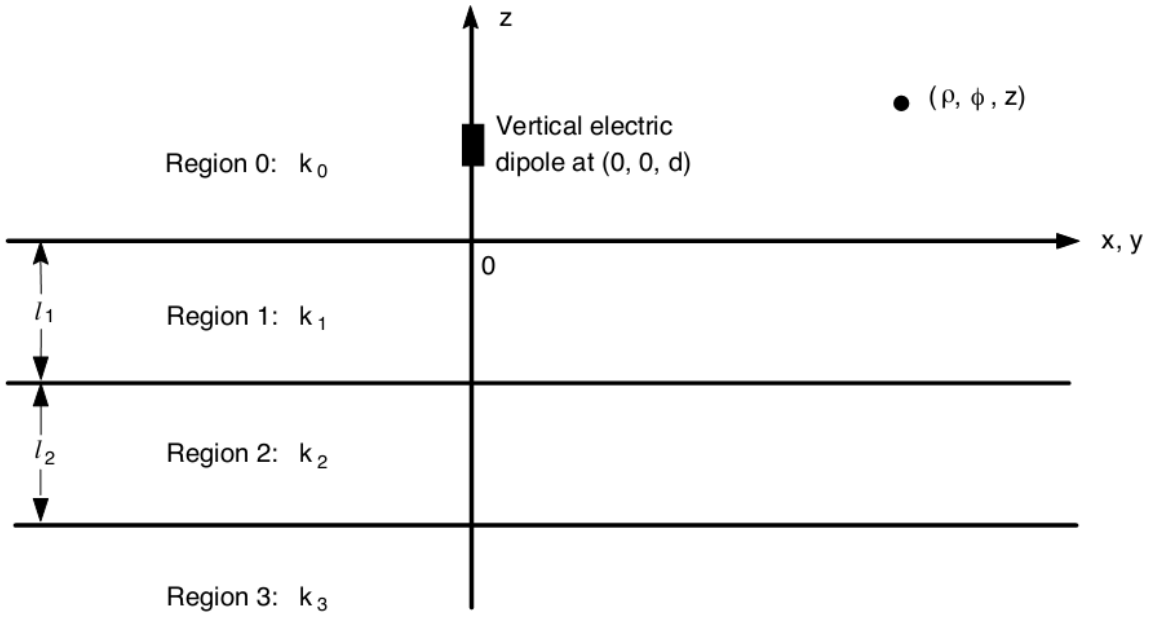

Figure 4-2 - System Geometry (after Xu *et al.*, 2008) © 2008 EMW Publishing

4.1.3 Assumptions

The following assumptions apply to this work, and are made for the example results given later in this chapter:

- The geometry adequately describes any physical system to which it is applied.
- The electromagnetic properties of each layer are correct across the homogenous, isotropic, linear bulk of the layer.
- The far-field assumption is valid at the observation point; at the frequencies used here this is correct, but this assumption is problematic when applying this work to the low-frequency region which the rest of this thesis considers.
- It is assumed that the lateral wave is dominated by the contribution of the first branch cut. In physical terms, the lateral wave in the layers below the first layer are assumed to be negligible. This allows single values for the wavenumber of the lateral wave, and an approximate value for the Hankel function.
- It is assumed that the Fresnel integral may be accurately approximated using the McLauren series expansion of the error-function.
- The boundary conditions outlined in section 4.3.2 are valid.

4.1.4 Chapter Structure

The first section presents a review of the specific literature which contributes directly to this chapter. The reader will appreciate that a sequence of publications, which followed two seminal works, have contributed to the state-of-the-art. Unfortunately, several publications are incomplete and include erroneous equations and results, these are highlighted. The underlying integral equations defining this situation were given by King *et al.* (1992) and utilised in the three-layer scenario by King and Sandler (1994) which created some controversy. The controversy is summarised and with the outcome showing that King and Sandler were correct but one of their assumptions was misleading (Zhang and Pan, 2002).

Following the literature review, the method of calculating the EM field due to a VED in a four-layered geometry is presented. The analysis is quite involved, and requires several steps, but it is hoped that the reader will be able to repeat the results – something lacking in much of the cited literature. The erroneous sections of the cited literature are then summarised, before new results are presented using the derived analysis. The results show that the trapped-surface wave cannot be neglected but does not come to dominate in the range considered, as in the three-layered geometry.

4.2 LITERATURE REVIEW

This section summarises the literature which directly informs the present work. The work by King *et al.* (King *et al.*, 1992; King and Sandler, 1994), provided the theoretical foundation for this chapter and was followed by a sequence of publications giving the electromagnetic field due to a VED in increasingly complex geometries (Zhang and Pan, 2002; Zhang *et al.*, 2004; Liu and Li, 2007; Xu *et al.*, 2008; Liu *et al.*, 2008). This work may be seen as the logical progression of that sequence of publications, which are summarised in Table 4-1.

The study of electromagnetic propagation in layered media has been ongoing for many years, the excellent review paper by Wait (1998a) is highly recommended for the reader interested in a full history of those developments, which is beyond the scope of this work. An appendix of the paper by Wait (1998a) also contains useful definitions of the various types of waves which propagate in layered media, this is most instructive as the terminology in this area is not consistent across sources.

The body of research, upon which this work is based, was triggered when Wait (1998b) published a comment on the work by King and Sandler (1994). King and Sandler (1994) had presented a paper in which they derived expressions for the electric field due to a VED in three-layered media in which one layer is air, one dielectric and one dielectric or a conductor.

Paper	Geometry	Dipole Type and Position	Observation Point	Exclusions
King and Sandler (1994)	Three layers	VED in air	All layers	$k_1 l \leq 0.6$ excluding the trapped surface wave
Zhang and Pan (2002)	Three layers, with a perfectly conductive third layer	VED in air	Air	
Zhang *et al.* (2004)	Three layers	VED in air	Air	
Liu and Li (2007)	Three layers over long range, in spherical coordinates	VED in air	Air	
Xu *et al.* (2008)	Four layers with a perfectly conductive fourth layer	VED in air	Air	
Liu *et al.* (2008)	Four layers with a perfectly conductive fourth layer	VED in second layer	Second layer	

Table 4-1: Summary of publications leading to this work

Wait's comment (Wait, 1998b) suggested that the earlier work (King and Sandler, 1994) had not correctly accounted for the presence of the trapped surface wave, and consequently presented incorrect results. This was justified by the absence of a range$^{-1/2}$ term, which is the defining characteristic of the trapped surface wave. In reply, King and Sandler (1998) refuted Wait's assertion, inviting him to complete a full derivation from first principles. The debate effectively concerned the efficient excitation of the trapped surface wave in the geometry in question, and whether it could be assumed to be negligible. Zhang and Pan (2002) set out to answer these questions with an analysis of the field due to a VED in a three-layered geometry, Zhang and Pan concluded that the results given by King and Sandler (1994) are correct if the thickness of the dielectric layer and the wave number in each medium conform to $k_1 l \leq 0.6$ and $k_1^2 \gg k_0^2$ (Zhang and Pan, 2002, p.13-7). Therefore, the paper by King and Sandler (1994) was correct, but the assumption the authors made for the thickness of the dielectric layer resulted in an apparently erroneous result which omitted the trapped surface wave. By neglecting the trapped surface

wave, King and Sandler caused their results to require significant amendment in the event that their assumptions were removed.

The extra calculations required to account for the trapped surface wave emerged in a series of papers with increasing complexity in the geometries: Zhang and Pan (2002) presented an investigation of the electric field from a VED in three-layered media, where the third layer is assumed perfectly conductive. Zhang *et al.* (2004) presented a similar analysis without the assumption of a perfectly conductive layer, making the geometry equivalent to the work of King and Sandler (1994). But, crucially, without the assumption of a thin second layer as seen in the paper by King and Sandler (1994). Following these papers, Liu and Li (2007) presented an interesting set of results calculated using the formulae of Zhang *et al.* (2004) which showed the electric fields due to a VED in a range of media and geometries. Liu and Li (2007) presented graphs showing the response of the field to changes in geometry and materials' dielectric properties, which have not been published elsewhere. Xu *et al.* (2008) presented an analysis of the four-layered scenario, which expanded the previous work, but used the assumption of a perfectly conductive fourth layer of the geometry. An extension to the work by Xu *et al.* (2008) was given by Liu *et al.* (2008) who calculated the electric field due placing the VED and observation point in the second layer of the geometry, rather than in air as calculated by Xu *et al.* (2008).

The reader will find that none of the papers published since that of King and Sandler (1994) fully explains the analysis which they are presenting or fully cite the prior work. Most neglect the derivation for the parameter Q which is fundamental to making an analysis of geometries different to those presented. Furthermore, only by picking apart the references made by these papers, and searching for further works, can the reader fully appreciate the successive steps which allowed the successful results to be presented. It is not suggested that there is any impropriety with the content of the work in either case, but a complete review of the literature and method is both useful and not found elsewhere.

4.3 PROCESS

This section defines the process required to calculate the field due to a VED in layered media, as used by the papers cited in Table 4-1. For the most part, publications have limited themselves to one of the three field components, (4-2) - (4-4), and made significant abbreviations to the derivation, which is understandable given the space constraints in publications. However, this chapter strives to give a complete derivation which may be easily followed without recourse to a number of other references.

4.3.1 Define the Geometry of the Medium

The system geometry is well defined in Figure 4-2 which shows the cylindrical and Cartesian coordinate systems in use *x, y, z, ρ, Φ*. The height *d* of the vertical electric dipole, the height *z* of the observation point, and the thicknesses l_1, l_2 of the two layers with non-infinite thickness are also shown.

The electromagnetic properties of the system rely on the system angular frequency ω $\left(\text{rad s}^{-1}\right)$, the permeability, and permittivity of free space μ_0, ε_0. The dielectric properties of the layers are described using the complex relative-permittivity of each layer ε_0, ε_1, ε_2, ε_3; all the layers are assumed non-magnetic and have a relative-permeability of 1. The value of *k*, (metres^{-1}) for each layer is derived from these three parameters and the subsequent evaluation is based upon this, and the geometric properties of the system.

$$k_j = \omega \sqrt{\mu_0 \left(\varepsilon_0 \varepsilon_j + {}^{i\sigma_j}/_{\omega} \right)} \tag{4-1}$$

4.3.2 Field Definitions

The field in this system is defined by (4-2) - (4-4) in the notation of King and Sandler (1994) and Zhang *et al.* (2004) which is a slight manipulation of that seen in chapter 11 of King *et al.* (1992).

$$B_{0\phi}(\rho, z) = \frac{i\mu_0}{4\pi} \int_0^\infty \left[e^{i\gamma_0 |z-d|} + e^{i\gamma_0 (z+d)} - (Q+1) e^{i\gamma_0 (z+d)} \right] \gamma_0^{-1} J_1(\lambda\rho) \lambda^2 d\lambda \tag{4-2}$$

$$E_{0\rho}(\rho,z)=\frac{i\omega\mu_0}{4\pi k_0^2}\int_0^\infty\left[\pm e^{i\gamma_0|z-d|}+e^{i\gamma_0(z+d)}-(Q+1)e^{i\gamma_0(z+d)}\right]J_1(\lambda\rho)\lambda^2 d\lambda \qquad (4\text{-}3)$$

$$E_{0z}(\rho,z)=\frac{-\omega\mu_0}{4\pi k_0^2}\int_0^\infty\left[e^{i\gamma_0|z-d|}+e^{i\gamma_0(z+d)}-(Q+1)e^{i\gamma_0(z+d)}\right]\gamma_0^{-1}J_0(\lambda\rho)\lambda^2 d\lambda \qquad (4\text{-}4)$$

Where:

$$\gamma_j=\sqrt{k_j^2-\lambda^2} \qquad (4\text{-}5)$$

Where γ_j is the propagation constant whose real component must be positive (King *et al.*, 1992), λ is the wavelength, ρ is the separation of the VED and the observation point, and J_n are the Bessel functions of the n^{th} kind, i denotes $\sqrt{-1}$.

The summation within integrals in (4-2) may be evaluated separately to describe the direct wave ($B_{0\phi}^{(1)}$), the ideal reflected wave ($B_{0\phi}^{(2)}$), and the trapped surface and lateral waves ($B_{0\phi}^{(3)}$); defined below (Wait, 1998a). With the equivalent separation made for the two electric-field components.

The solutions to integral equations (4-2) - (4-4) are the specific objective of this chapter. The inclusion of the Bessel functions should be noted, this is a result of the use of cylindrical coordinates and gives the solutions the highly oscillatory nature that makes a numerical solution slow to converge (Xu *et al.*, 2008).

Several implicit assumptions about the boundary conditions are made. Firstly, that Snell's law is applicable at the interfaces between layers, meaning that the field is only dependent on a continuous x component of the wavenumber, and k_z for each layer.

4.3.3 Direct and Ideal-Reflected Waves

The direct wave is the wave which propagates through air from the VED to the observation point, and the ideal-reflected wave is that way which propagates via a single reflection off the surface. The direct wave is independent of the properties of the layered media. Therefore, the solutions

to the above integrals, derived by King and Sandler (1994) and given explicitly by Zhang and Pan (2002), are valid. The terms for the direct waves are given by (4-6) - (4-8):

$$B_{0\phi}^{(1)} = -\frac{\mu_0}{4\pi} e^{ik_0 r_1} \left(\frac{\rho}{r_1}\right)\left(\frac{ik_0}{r_1} - \frac{1}{r_1^2}\right) \tag{4-6}$$

$$E_{0\rho}^{(1)} = -\frac{\omega\mu_0}{4\pi k_0} e^{ik_0 r_1} \left(\frac{\rho}{r_1}\right)\left(\frac{z-d}{r_1}\right)\left(\frac{ik_0}{r_1} - \frac{3}{r_1^2} - \frac{3i}{k_0 r_1^3}\right) \tag{4-7}$$

$$E_{0z}^{(1)} = \frac{\omega\mu_0}{4\pi k_0} e^{ik_0 r_1} \left[\frac{ik_0}{r_1} - \frac{1}{r_1^2} - \frac{i}{k_0 r_1^3} - \left(\frac{z-d}{r_1}\right)^2 \left(\frac{ik_0}{r_1} - \frac{3}{r_1^2} - \frac{3i}{k_0 r_1^3}\right)\right] \tag{4-8}$$

Similarly, the term for the ideal-reflected wave is insensitive to the composition of the layered media and the solutions derived by King and Sandler (1994), as restated by Zhang and Pan (2002), are used:

$$B_{0\phi}^{(2)} = -\frac{\mu_0}{4\pi} e^{ik_0 r_2} \left(\frac{\rho}{r_2}\right)\left(\frac{ik_0}{r_2} - \frac{1}{r_2^2}\right) \tag{4-9}$$

$$E_{0\rho}^{(2)} = -\frac{\omega\mu_0}{4\pi k_0} e^{ik_0 r_2} \left(\frac{\rho}{r_2}\right)\left(\frac{z+d}{r_2}\right)\left(\frac{ik_0}{r_2} - \frac{3}{r_2^2} - \frac{3i}{k_0 r_2^3}\right) \tag{4-10}$$

$$E_{0z}^{(2)} = \frac{\omega\mu_0}{4\pi k_0} e^{ik_0 r_2} \left[\frac{ik_0}{r_2} - \frac{1}{r_2^2} - \frac{i}{k_0 r_2^3} - \left(\frac{z+d}{r_2}\right)^2 \left(\frac{ik_0}{r_2} - \frac{3}{r_2^2} - \frac{3i}{k_0 r_2^3}\right)\right] \tag{4-11}$$

The value of r_1 and r_2, the cylindrical coordinate descriptions for the path lengths, are simply calculated using the normal conversion Cartesian to cylindrical coordinate (4-12), (4-13).

$$r_1 = \sqrt{\rho^2 + (z-d)^2} \tag{4-12}$$

$$r_2 = \sqrt{\rho^2 + (z+d)^2} \tag{4-13}$$

4.3.4 Integral Expression for the Trapped Surface and Lateral Waves

The trapped surface wave is the wave which propagates along the boundary between each layer, while the lateral wave is the wave which propagates through the dielectric in each layer (Wait, 1998a). The expressions for the trapped surface and lateral waves are extracted from (4-2) - (4-4):

$$B_{0\phi}^{(3)}(\rho,z)=\frac{i\mu_0}{4\pi}\int_0^{\infty}\left[-(Q+1)e^{i\gamma_0(z+d)}\right]\gamma_0^{-1}J_1(\lambda\rho)\lambda^2 d\lambda \tag{4-14}$$

$$E_{0\rho}^{(3)}(\rho,z)=\frac{i\omega\mu_0}{4\pi k_0^2}\int_0^{\infty}\left[-(Q+1)e^{i\gamma_0(z+d)}\right]J_1(\lambda\rho)\lambda^2 d\lambda \tag{4-15}$$

$$E_{0z}^{(3)}(\rho,z)=\frac{-\omega\mu_0}{4\pi k_0^2}\int_0^{\infty}\left[-(Q+1)e^{i\gamma_0(z+d)}\right]\gamma_0^{-1}J_0(\lambda\rho)\lambda^3 d\lambda \tag{4-16}$$

The solutions to the equations for direct and ideal-reflected wave components were derived by King *et al.* (1992). Therefore, the objective of this chapter has been refined to solving (4-14) - (4-16). Subsequent evaluations of equations (4-14) - (4-16) utilise Hankel functions in place of Bessel functions. This is required to extend the integral to ±∞ and results in a division by 2, see Kreyszig *et al.* (1999) for the relevant identities.

4.3.5 Derive and Simplify *Q* and *Q*+1

The term Q has been used throughout this section without definition. This section defines, and gives the derivation of this term. The Q term was first used by King *et al.* (1992) as a gathering of terms for a larger integral equation, consequently it does not have a physical definition. The term for an n-layered half space is defined as (4-17) (King *et al.*, 1992, p. 400).

$$-Q_n=\frac{\gamma_0-\frac{k_0^2}{\omega\mu_0}Z_{s0}(0)}{\gamma_0+\frac{k_0^2}{\omega\mu_0}Z_{s0}(0)} \tag{4-17}$$

Where n is the number of layers in the medium and $Z_{s0}(0)$ is the surface impedance, considering all the layers in the medium. The definition of the surface impedance, and the subsequent derivation of Q for a four-layered geometry is long-winded and somewhat tedious. Consequently, it is given in Appendix 3 which shows the derivation of $Z_{s0}(0)$, Q, and $Q+1$. The resulting update has not been published and is made by substituting $Q+1=iA(\lambda)/2q(\lambda)$ into (4-14) - (4-16):

$$B_{0\varphi}^{(3)}=\frac{\mu_0 k_0^2}{4\pi}\int_{-\infty}^{\infty}\frac{A(\lambda)}{q(\lambda)}\frac{\gamma_1 e^{i\gamma_0(z+d)}H_1^{(1)}(\lambda\rho)\lambda^2}{\gamma_0}d\lambda \tag{4-18}$$

$$E_{0\rho}^{(3)} = \frac{\omega\mu_0}{4\pi}\int_{-\infty}^{\infty}\frac{A(\lambda)}{q(\lambda)}\gamma_1 e^{i\gamma_0(z+d)}H_1^{(1)}(\lambda\rho)\lambda^2\,d\lambda \tag{4-19}$$

$$E_{0z}^{(3)} = \frac{i\omega\mu_0}{4\pi}\int_{-\infty}^{\infty}\frac{A(\lambda)}{q(\lambda)}\frac{\gamma_1 e^{i\gamma_0(z+d)}H_0^{(1)}(\lambda\rho)\lambda^3}{\gamma_0}\,d\lambda \tag{4-20}$$

Where:

$$A(\lambda) = -\frac{i\gamma_1\gamma_3k_2^2\tan(\gamma_1l_1)\tan(\gamma_2l_2)}{k_1^2} + i\gamma_2\gamma_3 + \frac{\gamma_2^2\,k_3^2\tan(\gamma_2l_2)}{k_2^2} + \frac{\gamma_1\gamma_2k_3^2\tan(\gamma_1l_1)}{k_1^2} \tag{4-21}$$

$$\begin{aligned} q(\lambda) = {} & \frac{\gamma_0\gamma_2^2k_1^2k_3^2\tan(\gamma_1l_1)\tan(\gamma_2l_2)}{k_2^2} - \gamma_0\gamma_1\gamma_2k_3^2 + i\gamma_0\gamma_2\gamma_3k_1^2\tan(\gamma_1l_1) \\ & + i\,\gamma_0\gamma_1\gamma_3k_2^2\tan(\gamma_2l_2) + \frac{\gamma_1^2\gamma_3k_0^2k_2^2\tan(\gamma_1l_1)\tan(\gamma_2l_2)}{k_1^2} \\ & - \gamma_1\gamma_2\gamma_3k_0^2 + \frac{i\gamma_1\gamma_2^2k_0^2k_3^2\tan(\gamma_2l_2)}{k_2^2} + \frac{i\gamma_1^2\gamma_2k_0^2k_3^2\tan(\gamma_1l_1)}{k_1^2} \end{aligned} \tag{4-22}$$

The number of terms make this derivation cumbersome, and considerable care must be taken to avoid propagating algebraic errors through to the solution.

4.3.6 Separation of the Trapped Surface and Lateral Waves

It was noted in the section 4.3.2 that both the trapped surface wave and lateral wave are defined by the third part of the expressions for each field ($B_{0\phi}^{(3)}$, $E_{0\rho}^{(3)}$, and $E_{0z}^{(3)}$). Complex analysis can be used to aid the solution to the integrals in (4-18) - (4-20) by restating the integral as the sum of its residues and a contour integral. This technique is used in the series of papers from that of Zhang and Pan (2002) to the work of Xu *et al.* (2008), and relies of the residue theorem and other tools from complex analysis. The reader is referred to Paliouras and Meadows (1990) for the relevant proofs. However, for this work it is simply stated that an integral from $-\infty$ to $+\infty$ may be solved be rearranging to the form:

$$B_{0\phi}^{(3)} = -\frac{ik_0^2\mu_0}{4\pi}\left\{2\pi i \times \sum_j Residues\left(\lambda_j^*\right) + \sum_k \int_{\Gamma_k} \frac{A(\lambda)}{q(\lambda)\gamma_0}\gamma_1 e^{i\gamma_0(z+d)}H_1^{(1)}(\lambda\rho)\lambda^2 d\lambda\right\} \tag{4-23}$$

Where λ_j^* refers to the poles within the integral expressions in (4-18) - (4-20) and Γ_k refers to the branch cuts in the complex plane, branch cuts denote points of discontinuity in the complex plane of a function, see Paliouras and Meadows (1990) for a complete definition.

The residues of a function are calculated using (4-24). A residue occurs at each pole, denoted z_0, in the function, and the evaluation of residues using (4-24) relies upon the assumptions that $f(z_0) \neq 0$ and "$g(z)$ has a zero of order 1 at z_0" (Paliouras and Meadows, 1990). The precise definition for the order of poles is beyond the scope of this work. However, (4-24) will return a pole in the case that the order of the pole at z_0 is greater than 1, ensuring that the assumption of the order of the pole is valid.

$$Res\left[\frac{f(z)}{g(z)}, z_0\right] = \frac{f(z_0)}{g'(z_0)} \tag{4-24}$$

It has been demonstrated that the trapped surface wave is determined by the sums of the residues in (4-23) and its equivalents, whilst the lateral wave is determined by the sums of the contour integrals around the branch cuts (Liu *et al.*, 2008). This separation is utilised in this chapter to allow easy subdivision of the calculation.

4.3.7 Evaluation of the Lateral Wave Component

It was argued by Zhang *et al.* (2004), when extending the work of Zhang and Pan (2002) to remove the perfectly conductive layer, that the lateral wave component in the lowest layer is negligible if it is slightly conductive. This argument is extended here, and allows the use of the solution to the lateral wave component derived by Xu *et al.* (2008). The expression relies on the Fresnel integral, which is approximated using the error-function and its McLauren series expansion (Kreyszig *et al.*, 1999). The lateral wave component is approximated by (Xu *et al.*, 2008):

$$B_{0\phi}^{(3L)} = -\frac{\mu_0 k_0^3}{2}\sqrt{\frac{1}{\pi k_0 \rho}}e^{ik_0 r_2}e^{-ip^*}F(p^*)\frac{\gamma_{10}\gamma_{20}\tan(\gamma_{20}l_2)+\frac{k_2^2}{k_1^2}\gamma_{10}^2\tan(\gamma_{10}l_1)}{\gamma_{10}k_2^2-\gamma_{20}k_1^2\tan(\gamma_{10}l_1)\tan(\gamma_{20}l_2)} \tag{4-25}$$

$$\begin{aligned} E_{0\rho}^{(3L)} = {} & \frac{\omega\mu_0 k_0^2}{2\pi}\sqrt{\frac{1}{\pi k_0\rho}}e^{ik_0 r_2}\frac{\gamma_{10}\gamma_{20}\tan(\gamma_{20}l_2)+\frac{k_2^2}{k_1^2}\gamma_{10}^2\tan(\gamma_{10}l_1)}{\gamma_{10}k_2^2-\gamma_{20}k_1^2\tan(\gamma_{10}l_1)\tan(\gamma_{20}l_2)} \\ & \cdot\left[\sqrt{\frac{\pi}{k_0\rho}}+\pi\frac{k_0\gamma_{10}}{k_1^2}e^{-ip^*}F(p^*)\cdot\frac{\gamma_{10}k_2^2\tan(\gamma_{10}l_1)+\gamma_{20}^2k_1^2\tan(\gamma_{20}l_2)}{\gamma_{10}k_2^2-\gamma_{20}k_1^2\tan(\gamma_{10}l_1)\tan(\gamma_{20}l_2)}\right] \end{aligned} \tag{4-26}$$

$$E_{0z}^{(3L)} = \frac{i\omega\mu_0 k_0^2}{2}\sqrt{\frac{1}{\pi k_0\rho}}e^{ik_0 r_2}e^{-ip^*}F(p^*)\frac{\gamma_{10}\gamma_{20}\tan(\gamma_{20}l_2)+\frac{k_2^2}{k_1^2}\gamma_{10}^2\tan(\gamma_{10}l_1)}{\gamma_{10}k_2^2-\gamma_{20}k_1^2\tan(\gamma_{10}l_1)\tan(\gamma_{20}l_2)} \tag{4-27}$$

Where *F(p*)* is the Fresnel integral:

$$F(p^*) = \frac{1}{2}(1+i) - \int_0^{p^*}\frac{e^{it}}{\sqrt{2\pi t}}dt \tag{4-28}$$

$$p^* = \frac{k_0\rho}{2}\left[\frac{z+d}{\rho}+i\frac{k_0}{k_1^2}\gamma_{10}\cdot\frac{\gamma_{10}k_2^2\tan(\gamma_{10}l_1)+\gamma_{20}k_1^2\tan(\gamma_{20}l_2)}{\gamma_{10}k_2^2-\gamma_{20}k_1^2\tan(\gamma_{10}l_1)\tan(\gamma_{20}l_2)}\right]^2 \tag{4-29}$$

With the far field assumption:

$$k_0\rho \gg 1 \text{ and } (z+d) \ll \rho \tag{4-30}$$

Which, when letting:

$$\lambda = k_0(1+i\tau^2) \tag{4-31}$$

Allowed the following approximations:

$$\gamma_0 \approx k_0 e^{i\frac{3}{4}\pi}\sqrt{2}\tau \tag{4-32}$$

$$\gamma_1 \approx \gamma_{10} = \sqrt{k_1^2-k_0^2} \tag{4-33}$$

$$\gamma_2 \approx \gamma_{20} = \sqrt{k_2^2-k_0^2} \tag{4-34}$$

$$H_1^{(1)}(\lambda\rho) \approx \sqrt{\frac{2}{\pi k_0\rho}}e^{i\left(k_0\rho-\frac{3}{4}\pi\right)}e^{-k_0\rho\tau^2} \tag{4-35}$$

4.3.8 Evaluation of the Trapped Surface Wave Component

The definition of a residue is given by (4-24), it is mathematically incomplete, but adequate for this work. To evaluate the residues of the integrands in equations (4-18) - (4-20), poles of the integrands are required. Therefore, to evaluate the trapped surface wave a list of the zeros in function $q(\lambda)$ must be found. This is obtained using a numerical simplex search, rather than the Newton-Raphson method suggested by Zhang *et al.* (2004) because it gave much greater stability.

Once the poles have been identified, (4-24) may be applied to the expressions for the lateral and trapped surface waves (4-18) - (4-20), to give the expression for the trapped surface wave:

$$B_{0\phi}^{(3T)} = 2\pi i \times -\frac{ik_0^2\mu_0}{4\pi}\sum_j \frac{A(\lambda_j^*)}{\frac{d}{d\lambda}[q(\lambda_j^*)]\gamma_0(\lambda_j^*)}\gamma_1 e^{i\gamma_0(z+d)}H_1^{(1)}\left((\lambda_j^*)\rho\right)(\lambda_j^*)^2 \tag{4-36}$$

$$E_{0\rho}^{(3T)} = 2\pi i \times -\frac{i\omega\mu_0}{4\pi}\sum_j \frac{A(\lambda_j^*)}{\frac{d}{d\lambda}[q(\lambda_j^*)]}\gamma_1 e^{i\gamma_0(z+d)}H_1^{(1)}\left((\lambda_j^*)\rho\right)(\lambda_j^*)^2 \tag{4-37}$$

$$E_{0z}^{(3T)} = 2\pi i \times \frac{\omega\mu_0}{4\pi}\sum_j \frac{A(\lambda_j^*)}{\frac{d}{d\lambda}[q(\lambda_j^*)]\gamma_0(\lambda_j^*)}\gamma_1 e^{i\gamma_0(z+d)}H_0^{(1)}\left((\lambda_j^*)\rho\right)(\lambda_j^*)^3 \tag{4-38}$$

The derivative of function $q(\lambda_j^*)$ is easily calculated using software such as Matlab or Mathematica, and is not stated here due to its length, but is given in Appendix 3.

4.4 Errors in the Literature

In the process of developing this work, a number of errors and omissions have been noted in the literature. None of these errors have been reported previously, and their publication represents new results. Many of these serve to obscure the best method for repeating previous measurements and some are highly misleading. In some cases a significant level of detail is required to show the source of the errors, in this case the supporting work is presented in Appendix 4. The errors are discussed in chronological order:

4.4.1 Roots of *q(λ)* Given by Zhang and Pan (2002) are Misleading

The equation for *q(λ)* in the three layered case, where the third layer is perfectly conductive, is given by Zhang and Pan (2002) as:

$$q(\lambda) = k_1^2\gamma_0 - ik_0^2\gamma_1 \tan(\gamma_1 l) \tag{4-39}$$

Zhang and Pan then note that if $k_0 \leq \lambda \leq k_1$ then γ_0 is a positive imaginary number while γ_1 is a positive real number. Manipulating (4-39) where $q(\lambda) = 0$ gives two functions which will be real where $k_0 \leq \lambda \leq k_1$:

$$f(\lambda) = \frac{k_1^2\gamma_0}{ik_0^2\gamma_1} \tag{4-40}$$

$$g(\lambda) = \tan(\gamma_1 l) \tag{4-41}$$

Zhang and Pan plot these functions, noting the roots of $q(\lambda)$ at the intersections (Figure 4-3). However, it will be seen that complex roots of $q(\lambda)$ exist and this method is impractical in that case. Zhang and Pan presented graphs showing the "first roots" of $q(\lambda)$ for increasing values of layer thickness, l. However, it is unhelpful to merely show the first roots of $q(\lambda)$ because evaluating the trapped surface wave requires all of the roots. Furthermore, it is seen when comparing the figures below that the "first root" plotted is not always the lowest in magnitude. This is evident when comparing the Figure 4-4, given by Zhang and Pan (2002) with Figure 4-5, which shows all of calculated the roots for the same geometry and dielectric properties. While the roots shown by Zhang and Pan (2002) are valid, they make repeating their results very difficult by neglecting the complete solution.

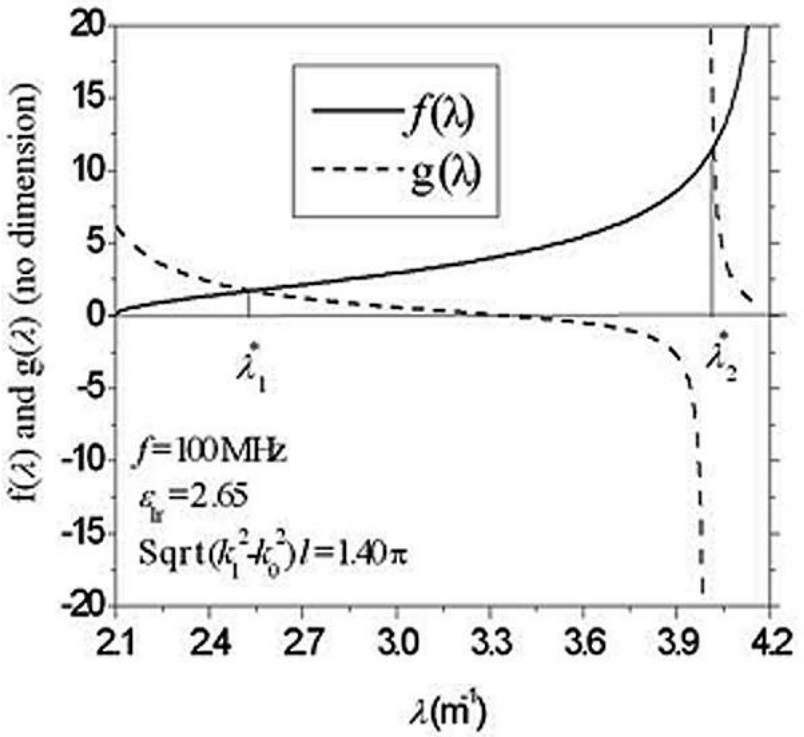

Figure 4-3: Roots of *q(λ)* by the method of assuming real *λ* and equating *f(λ)* and *g(λ)* (Zhang and Pan, 2002, Fig. 2) © 2002 by the American Geophysical Union

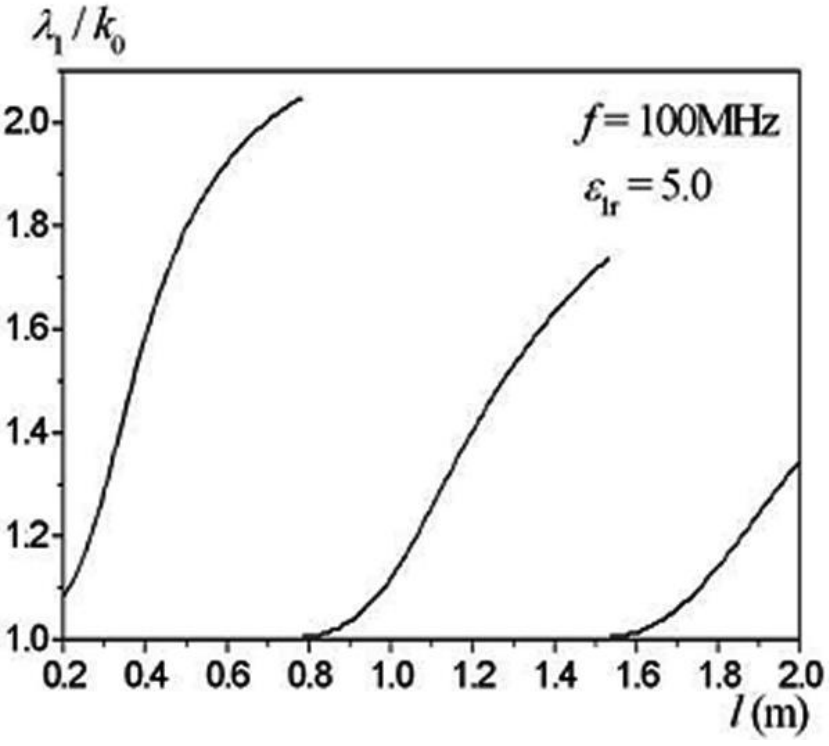

Figure 4-4: The first root of *q(λ)* with increasing layer thickness, *l*. When compared with Figure 4-5 this figure is seen to be incomplete and has not always selected the "first" root. (Zhang and Pan, 2002) © 2002 by the American Geophysical Union

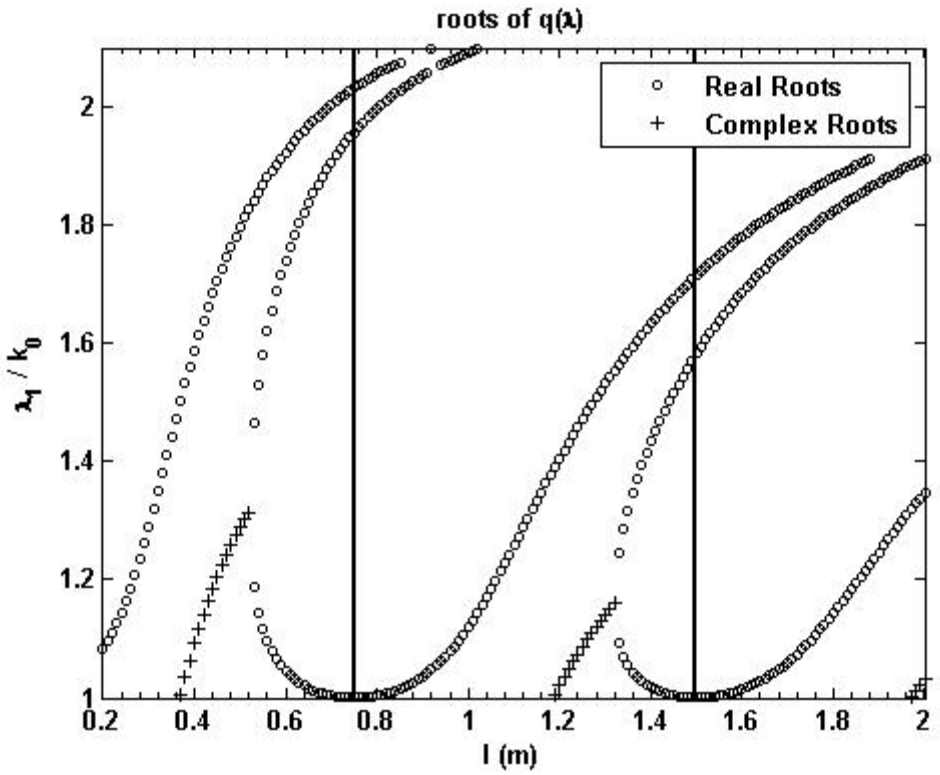

Figure 4-5: Roots of *q(λ)* with increasing layer thickness, repeating results shown in Figure 4-4. All roots are shown, including complex roots which do not feature in the explanation of Zhang and Pan (2002). Without showing all roots, it is difficult to use the results of Zhang and Pan (2002) to verify further research.

4.4.2 Sign Error in Zhang *et al.* (2004) Equations 9 – 11

It is difficult to follow the work of Zhang *et al.* because the authors do not give a citation for the term *Q*, or show the result of the derivation of *Q+1*. However, having repeated the derivation and inferred the value for *Q+1* from other equations, it is evident that a sign error exists in three of the equations given by Zhang *et al.* (2004).

Zhang *et al.* (2004) state that:

$$B_{0\varphi}^{(3)} = \frac{-i\mu_0}{4\pi} \int_{-\infty}^{\infty} \frac{A(\lambda)}{q(\lambda)} \frac{e^{i\gamma_0(z+d)} H_1^{(1)}(\lambda\rho)\lambda^2}{\gamma_0} d \tag{4-42}$$

This equation and its equivalents for the electric field components (Zhang *et al.*, 2004, eq. 9-11) exhibit a sign error. The derivation supporting this conclusion is shown fully in Appendix 4.

4.4.3 Graphs Showing Roots of $q(\lambda)$ vs. l by Zhang *et al.* (2004) are Erroneous

Zhang *et al.* (2004) present results for the first root of $q(\lambda)$ with varying values for the thickness of the dielectric layer (l). The difficulties in calculating the roots of an unstable, complex function are discussed above, but the graphs presented by Zhang *et al.* (2004) have been found to be incorrect. It is known that the real component of the propagation constant, γ, cannot be negative (King *et al.*, 1992). However, the only way to reproduce the results from Zhang *et al.* (2004) is to allow the propagation constant to be negative. The full set of roots, in both scenarios is given in Appendix 4.

4.4.4 Erroneous Plots for Roots of $q(\lambda)$ by Xu *et al.* (2008)

One of the most challenging parts of repeating the work published by previous authors is the determination of the zeros in $q(\lambda)$. Xu *et al.* (2008) give example results from their numerical methods but do not state the values found as part of their main results. Furthermore, Xu *et al.* (2008) present graphs for their function $q(\lambda)$ showing the zeros for two different geometries. It has been concluded, after repeating these graphs, that the graphs presented are erroneous and were computed using different input parameters to those stated. This conclusion is supported by comparing similar graphs in the work by Li (2009) whose results are very close to those found here but do not resemble the results from Xu *et al.* (2008). The results by Xu *et al.* are shown in Figure 4-6 while the correct results are shown in Figure 4-7.

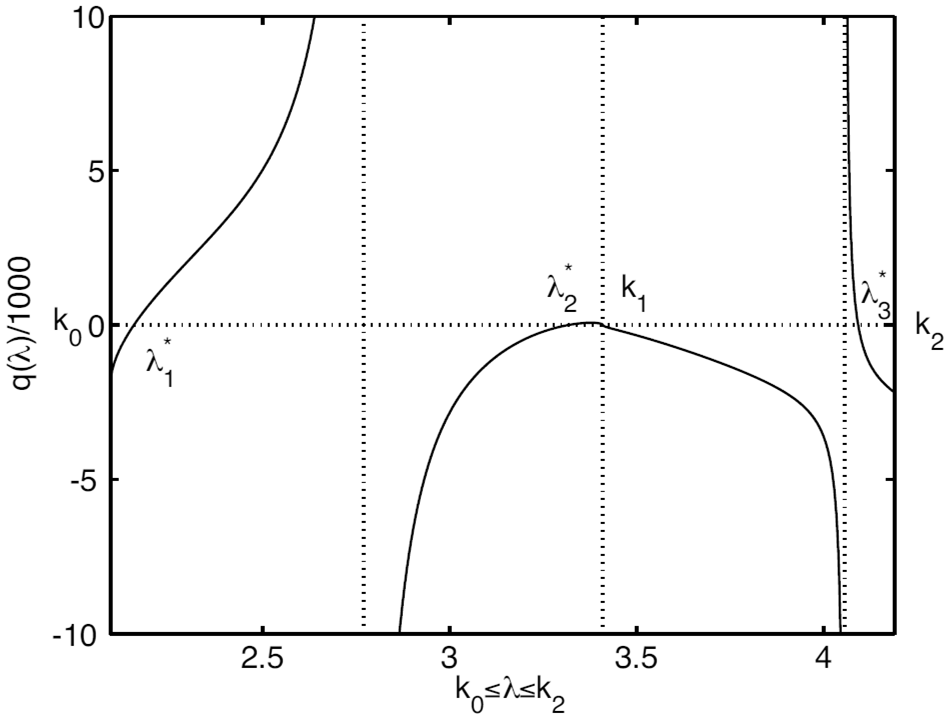

Figure 4-6: Erroneous graph showing function q(λ) (Xu *et al.*, 2008)

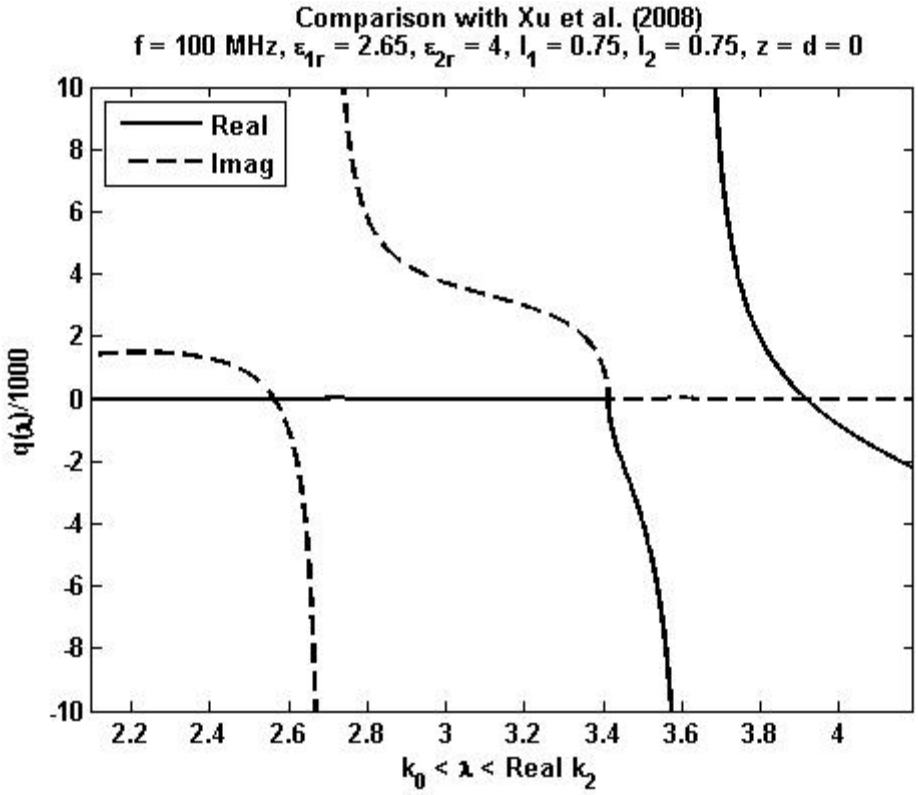

Figure 4-7: Correct representation of q(λ) calculated here and supported by a similar graph published by Li (2009).

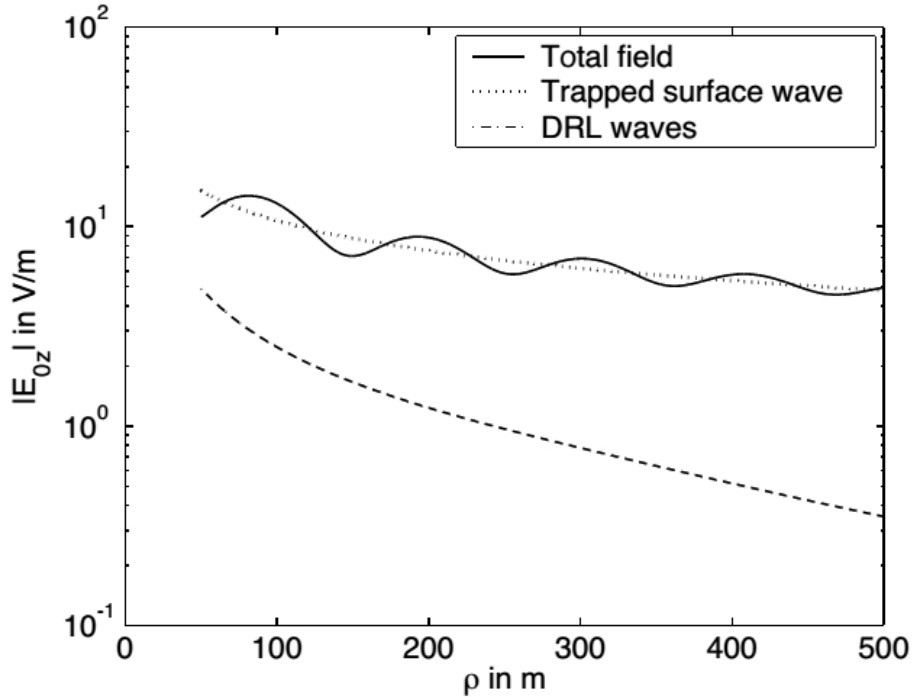

Figure 4-8: The total field calculated by Xu *et al.* (2008) in a four layered media with a perfectly conductive fourth layer. Where f = 100 MHz, ε_{1r}=2.65, ε_{2r} =2.65, $k_1l_1 = k_2l_2$=0.3, and z=d=0. (Xu *et al.*, 2008, Fig. 5)

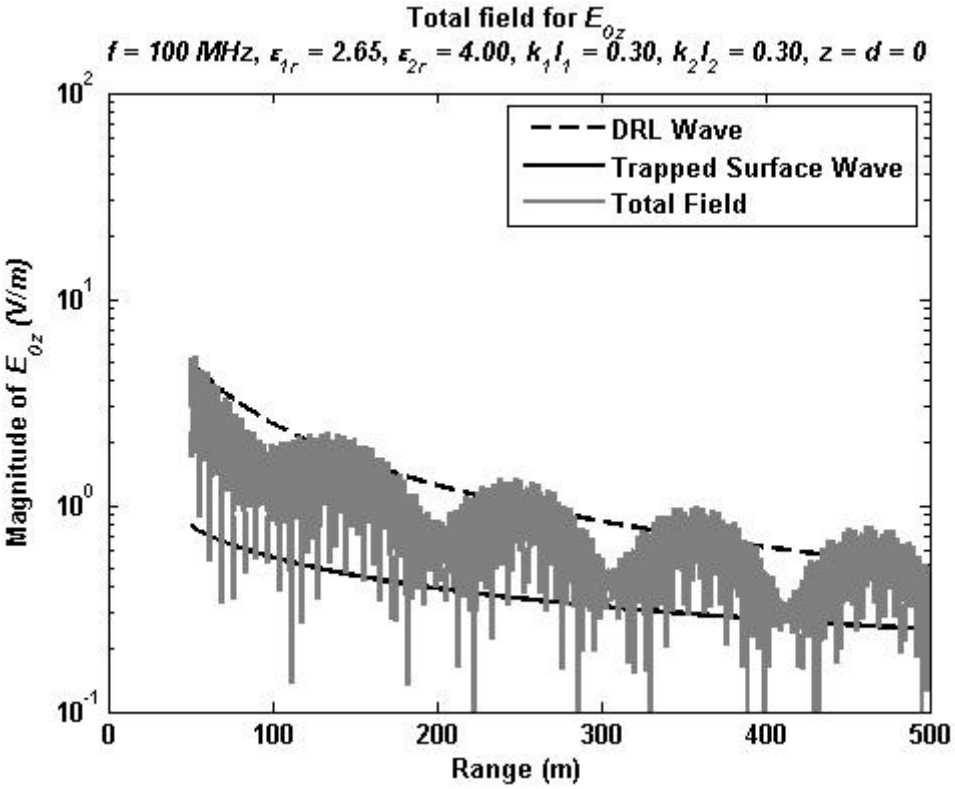

Figure 4-9: Results for the total field magnitude in a four layered geometry with perfectly conductive fourth layer, repeating results from Xu *et al.* (2008). Significant local variation is not shown by Xu *et al.* (2008).

4.4.5 EM Field Results Presented by Xu *et al.* (2008) are Overly Filtered

The results presented by Xu *et al.* (2008) for the total field cannot be replicated. The fields due to the direct, reflected, and lateral (DRL) waves and the trapped surface wave agree. However, the figures showing the total field magnitude for increasing range shows data which appears to have been smoothed to the point of being misleading. The graph presented by Xu *et al.* (2008) is shown in Figure 4-8 while the result computed for this thesis is shown in Figure 4-9.

4.5 Validation of the Model

In order to validate the methodology presented above, it is necessary to compare results with previous publications. However, no publications have been found which present comparable results. Therefore, the model has been validated mathematically, as far as possible, by showing that the equations derived in this chapter simplify to previously published equations where necessary assumptions are made. Appendix 5 demonstrates that the equations derived for this model reduce to those of Xu *et al.* (2008) when the fourth layer is assumed perfectly conductive; and reduce to those of Zhang *et al.* (2004) when a layer is assumed to have zero thickness.

4.6 New Results

This section presents the new results calculated as part of this work. In order to facilitate the easy repetition of this work, the first new result is shown in stages which follow those presented in section 4.3. The parameters of the geometries for which solutions are shown are given in Table 4-2.

Property	Geometry 1	Geometry 2	Geometry 3
Frequency	100 MHz	100 MHz	100 MHz
Layer 1 Material	Dry Sand	Dry Sand	Dry Sand
$\boldsymbol{\varepsilon_{1r}}$	4	4	4
$\boldsymbol{\sigma_1}$	0	0	0
Layer 2 Material	Water-Logged Sand	Corroded Steel	Air Void
$\boldsymbol{\varepsilon_{2r}}$	10	8.42+1.03i	1
$\boldsymbol{\sigma_2}$	0.04	Considered using complex ε_{2r}	0
Layer 3 Material	Dry Sand	Wet Soil	Wet Soil
$\boldsymbol{\varepsilon_{3r}}$	4	80	80
$\boldsymbol{\sigma_3}$	0	4	4
$\boldsymbol{l_1}$	1	1	1
$\boldsymbol{l_2}$	0.1	0.01	0.01
$\boldsymbol{\mu_1, \mu_2, \mu_3}$	1	1	1

Table 4-2: Properties of the new geometries studied modelled in this chapter.

4.6.1 Worked Example

The parameters given in Table 4-2 for geometry 1 are used to predict the electromagnetic field due to a VED in a four-layered medium which approximates that of a leaking pipe. In order to remain concise, the equations stated in section 4.3 are not repeated.

4.6.1.1 Direct and Ideal-Reflected Waves

Equations (4-6) - (4-8) describe the direct wave, while equations (4-9) - (4-11) describe the ideal reflected wave. These equations do not refer to the composition of the layered structure and are not different to any of the results presented by earlier authors.

4.6.1.2 Lateral Wave

The lateral wave equations for a four-layered media were derived by Xu *et al.* (2008) and restated in equations (4-25) - (4-35). These equations are used directly and present little difficulty to the researcher repeating these results.

4.6.1.3 Calculation of the Roots of q(λ) to Evaluate the Trapped Surface Wave

The function *q(λ)* is defined in (4-22), and contains too many terms for an analytical root-finding method. A numerical, simplex, search was employed which found roots at $\lambda = 4.9659 + 1.8750i$ and $\lambda = 2.9048 + 1.6585i$. These two values were used with equations (4-36) - (4-38) to evaluate the trapped surface wave.

4.6.1.4 Graphical Representation of Results

The field magnitude for the E_{0z} component of the solution given above is shown in Figure 4-10. This result shows that the trapped surface wave is not efficiently excited in the system described by geometry 1. Previous publications noted that a conductive base layer resulted in the most efficient excitation of the trapped surface wave so this result is unsurprising.

4.6.2 Additional Results

Equivalent results are shown for geometry 2, which approximates the situation where a metallic pipe has corroded. Poles of q(λ) were found at $\lambda = 4.0350 + 0.1046i$ and $\lambda = 1.0907 + 1.8947i$. The E_{0z} field component is shown in Figure 4-11. The scenario where there is an air void between the soil and water-logged base layer is described by geometry 3. The results for geometry 3 are shown in Figure 4-12 (poles at $\lambda = 4.0350 + 0.1046i$ and $\lambda = 1.0907 + 1.8947i$).

None of the results calculated show a significant contribution to the overall field from the trapped surface wave. Qualitatively, this can be explained by the dominant contribution being located at the deepest boundary where the field contribution must pass two other boundaries to contribute to the measured field. Based on these results, it seems likely that the contribution of the trapped surface wave will decrease as the number of layers increases, in the situation where the most conductive layer remains the deepest. This is notably different from the three-layered scenario (Zhang *et al.*, 2004) and field measurements could easily show the difference between three and four-layered situations by searching for the transition between the field dominated by DRL waves to dominated by the trapped surface wave.

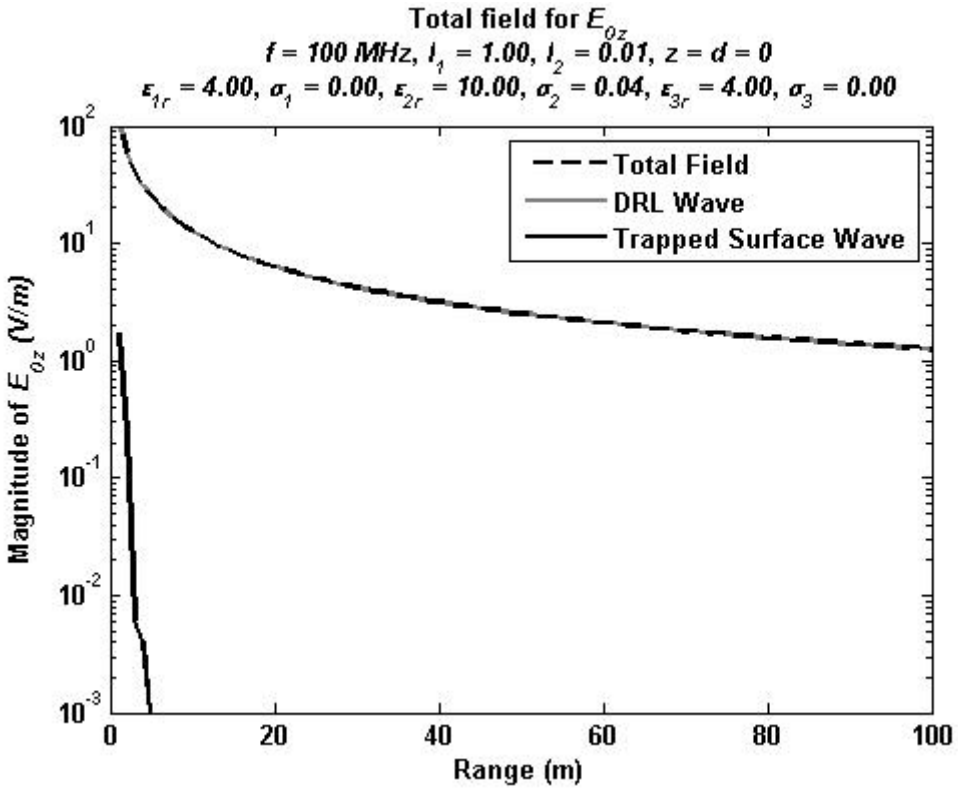

Figure 4-10: Magnitude E_{0z} field component of the electromagnetic field due to a VED in geometry 1. It is clear that the trapped surface wave is not efficiently excited, this fits with previous findings that the trapped surface wave requires a conductive layer to propagate efficiently.

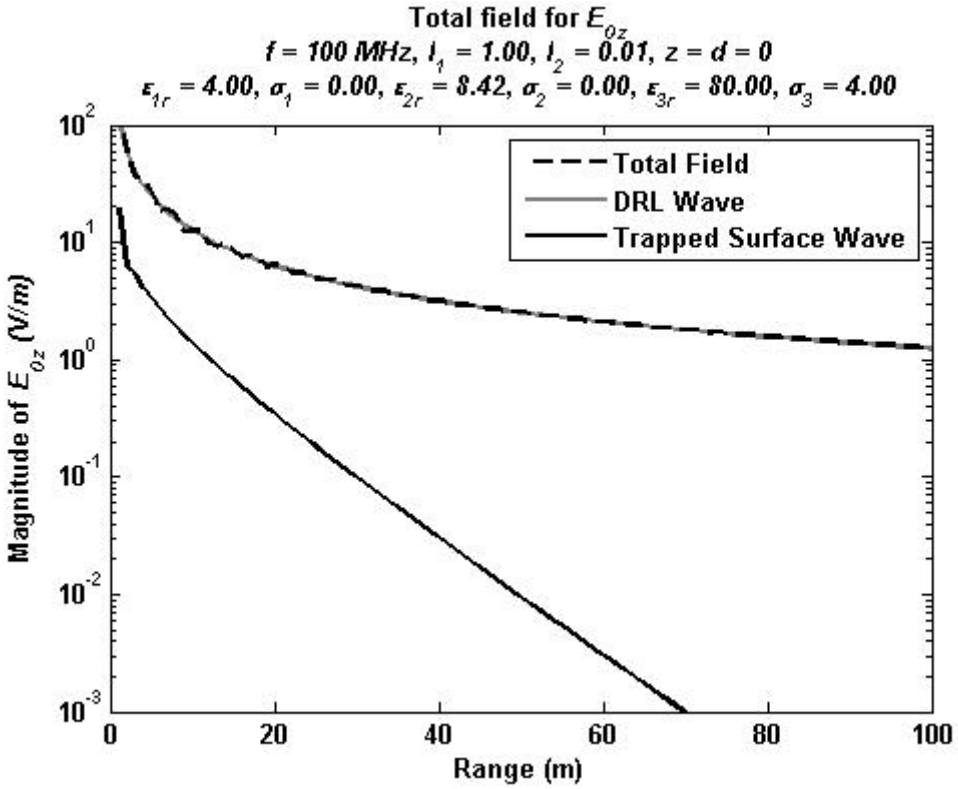

Figure 4-11: Magnitude of the E0z field component of the electromagnetic field due to a VED in geometry 2. The trapped surface wave is shown to be more efficiently excited than for geometry 1 but still contributes negligibly to the total field.

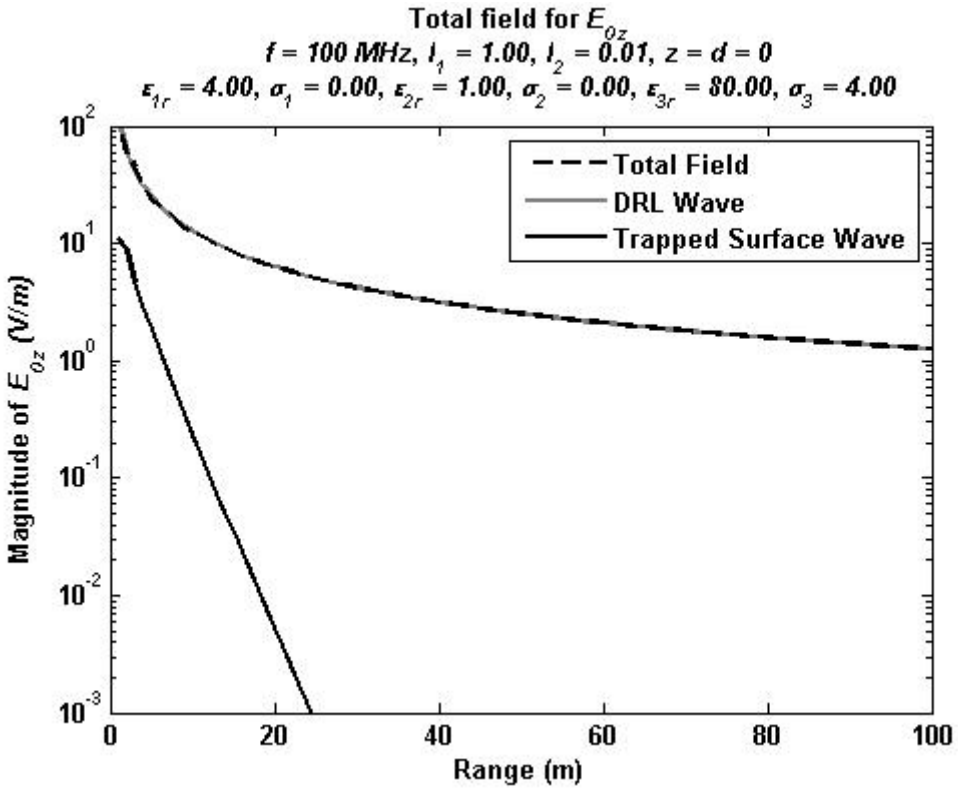

Figure 4-12: Magnitude of the E0z field component of the electromagnetic field due to a VED in geometry 3. The trapped surface wave is shown to be more efficiently excited than for geometry 1 but still contributes negligibly to the total field.

4.7 CHAPTER SUMMARY

The derivation of the electromagnetic field due to a vertical electric dipole in four layered geometries has been presented. The method for this derivation has been presented in a way which allows the reader to define their own geometries and gain results without reference to large numbers of other works.

Several errors in previously published works have been found and explained, these errors made repeating previous works extremely challenging. Errors included a sign error in an equation, graphs plotted with using parameters to those stated, and incomplete results presented in the derivation of the trapped surface wave.

The derivations required for these results are very unwieldy, and it is strongly recommended that any repeating work takes great care to guard against algebraic errors which are easily made and only found with great difficulty.

Three examples results have been presented, these results are illustrative of the power of a solution to the problem of the electromagnetic field due to a vertical electric dipole in a four-layered, when considering buried objects or leaking utilities. It has been shown that the trapped surface wave is negligible in the scenarios presented. In common with the findings for geometries with fewer layers, a layer of high conductivity increases the magnitude of the trapped surface wave. But these results suggest that an increase the number of layers in a geometry acts to reduce the measured field due to the trapped surface wave.

That the trapped surface wave is negligible for small range measurements is unsurprising. In the two and three layered case, it was shown that the trapped surface wave only dominates at greater range, once the direct and ideal reflected waves have attenuated. However, in the four-layered case the trapped surface wave is not excited with sufficient efficiency to have a non-negligible contribution to the overall field.

Results presented in Chapter 5 show evidence of multiple propagation paths. A comparison between the four-layered case, shown in this chapter, and the previously published three layered case, is used to make deductions about possible configurations of the soil which was measured. The case of a buried horizontal electric dipole, which closely matches the geometry used in Chapter 6 is not currently available.

CHAPTER 5: FIELD TRIALS MEASURING THE FEASIBILITY OF LOW-FREQUENCY DIRECTION OF ARRIVAL MEASUREMENTS IN SOIL

5.1 INTRODUCTION

The next two chapters describe the field work undertaken for this thesis, which explored the potential for using distributed in-pipe excitation, with low-frequency electromagnetic methods, to detect buried utilities. This chapter describes work which studies the feasibility of measuring the position of a pipe using distributed in-pipe excitation and direction of arrival (DoA) measurements with an array of sensors. This chapter is structured as follows: The principle of distributed in-pipe excitation is explained; the hypothesis being evaluated is then stated and justified; three field trials are then described, methods and results of each are given; finally, the chapter results are summarised.

5.1.1 Distributed In-Pipe Excitation

Figure 5-1 shows the principle of distributed in-pipe excitation including a sketch of the fundamental signal propagation. Note that the distributed in-pipe excitation occurs along the transmitter and is not a point source, as in a radio-sonde scheme.

Excitation from within the pipe has several advantages over exciting and receiving a signal at the surface:

- Propagation in one direction reduces the required propagation distance by a factor of two. In soil, signal attenuation is likely to be very high, and reduced propagation distance is invaluable for signal detection.
- Where a signal is excited at the surface, the measured reflected signal is dependent on the proportion of transmitted energy present at the target, and difference between the dielectric properties of the target and those of its surroundings. Where the signal is excited within the target, all of the transmitted energy is present at the target. However,

the dielectric properties of the target and soil may still cause significant attenuation at the target-soil interface.

- When the excitation takes place in the target, the first and strongest signal is likely to be due to the direct propagation path from the target. In a system where the transmission and reflection are co-located the strongest signal will be cross-talk between transmitter and receiver, or the direct wave along the surface of the ground. Furthermore, significant reflections may be measured from objects which are not the intended target. When excitation occurs within the target, the signal from any unintended targets will be reduced in magnitude by the imperfect reflection from that target.

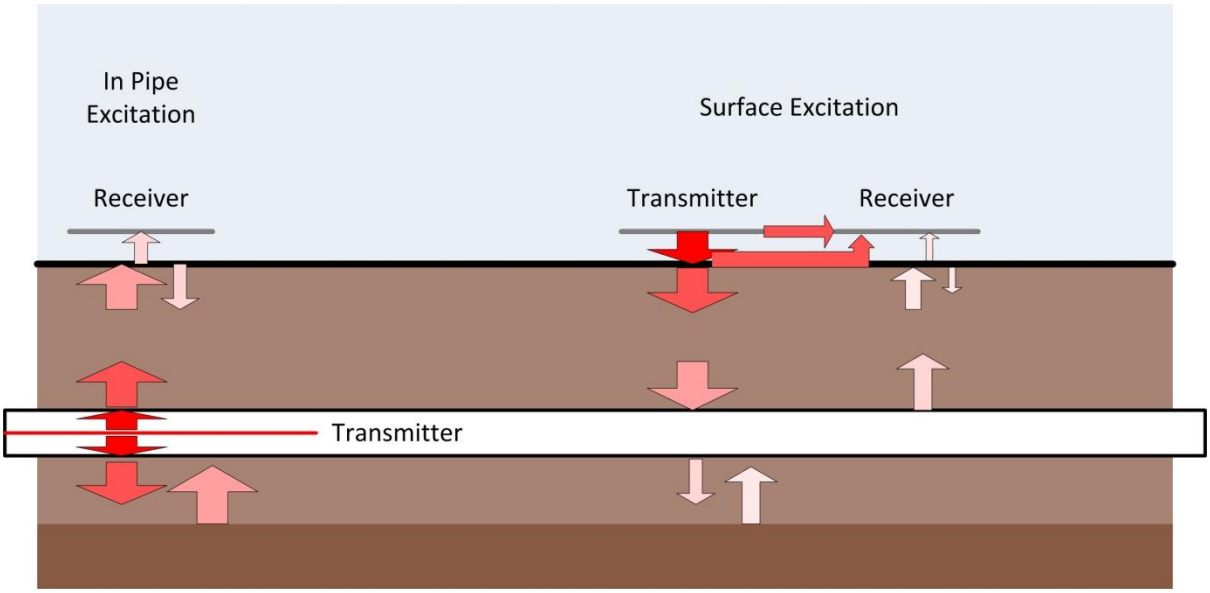

Figure 5-1: Overview of the concept of distributed in-pipe excitation. Selected propagating signals are shown as arrows, with size and colour indicating signal magnitude

In-pipe excitation is subject to a number of practical difficulties which surround the placing of any object within a live utility. There are stringent regulations surrounding working within live pipes, whether sewerage, clean water, or gas pipes (Great Britain, 1996). However, as the cost of damaged utilities rises, it may become cost effective to surmount these difficulties (McMahon *et al.*, 2005).

In this chapter a hypothesis is suggested, explored in the context of current research, and then tested with extensive field trials. It was considered to be a high-risk research objective, with

smaller chance of successful outcomes but significant prospect for novel development in the event of positive results. The second hypothesis, explored in the next chapter, was considered to have greater chance of success and – whilst still challenging – is a more incremental advance.

To the best of the author's knowledge, this type of experiment has not been previously reported. Various similar methods using acoustic technologies have been reported: A patent was issued in 1999 for a device which uses ultrasonic transducers to report on the condition of a pipe as it moves through it (Cook, 1999). Other methods involve exciting an acoustic wave on the pipe, for condition monitoring (Lowe *et al.*, 1998) and detection (Muggleton and Brennan, 2008).

5.2 HYPOTHESIS

The calculation of the direction of arrival (DoA) of a signal, measured on an array of sensors, is a mature research area with a range of proven methods. These methods typically rely on:

1. A signal-to-noise ratio which is high enough to detect the incoming signal.
2. Reliable phase measurements across an array of receiving sensors, with measurable phase change of less than a change in DoA of 5 degrees.
3. The far-field assumption where the incoming signal is assumed to be a plane-wave (phase is a function of the angle of arrival), or the near-field assumption where the incoming signal is assumed to be propagating spherically (phase is a function of the angle of arrival and the distance from the source).

If these assumptions are met, then an array of receiving sensors ought to be capable of determining the bearing of an EM field source within a pipe. Thus, as an EM field source is moved along a pipe, the receiving equipment could track the position of the field source, and determine the location of the pipe quickly and efficiently.

5.3 VALIDATING THE HYPOTHESIS

The literature review in Chapter 2 gives significant background in the methods for detecting a propagating wave and locating its source. This section uses those methods to show that the hypothesis being investigated was valid, in that the assumptions laid out could be met.

5.3.1 Expected Signal-to-Noise Ratio

This section considers the signal and noise separately, then combines to give an expected value for signal-to-noise ratio (SNR).

5.3.1.1 Signal

Modelling the propagation in layered media is complex, as shown in Chapter 4. The expected field magnitude, if the wave is a plane-wave propagating in homogenous media is now shown. Any lateral and surface wave components will reduce the expected SNR, as energy will propagate along multiple paths at different phase-velocities.

The signal magnitude of a plane-wave in a lossy medium decays exponentially, as follows (Paul and Nasar, 1987):

$$Normalised\ Signal\ Magnitude = \exp(-\alpha d) \tag{5-1}$$

$$\alpha = Real[\gamma] = Real[j\omega\mu(\sigma + j\omega\varepsilon)] \tag{5-2}$$

Where γ is the propagation constant, ω is the angular frequency, μ is the permeability of the medium, ε is the permittivity of the medium, and d is the propagation distance. The results of (5-1) and (5-2) are given in Figure 5-2 for a number of soils whose specifications are shown in Table 5-1. It is clear that soil type, and water content make a significant difference to the magnitude of the measured field.

Soil	ε_r	σ (Sm^{-1})	Volumetric Water Content	Observation Frequency	Source	Predicted Phase Velocity (ms^{-1})
Sandy Loam	1.8	0.002	0%	150 MHz	Robinson *et al.* (1999)	7.07×10^4
Sandy Loam	3	0.03	20%	70 MHz	Robinson *et al.* (1999)	1.83×10^4
Orleans Clay	42.6	$\varepsilon_r'' = 22$	~45%	100 MHz	Shang *et al.* (1999)	2.69×10^2
Berea Sandstone	10	0.01	-	0.1 MHz	Lesmes and Morgan (2001)	1.83×10^4
Berea Sandstone	10^7	0.01	-	0.1 Hz	Lesmes and Morgan (2001)	7.07×10^4

Table 5-1: Soil Properties and Expected Phase Velocity at 1 Hz

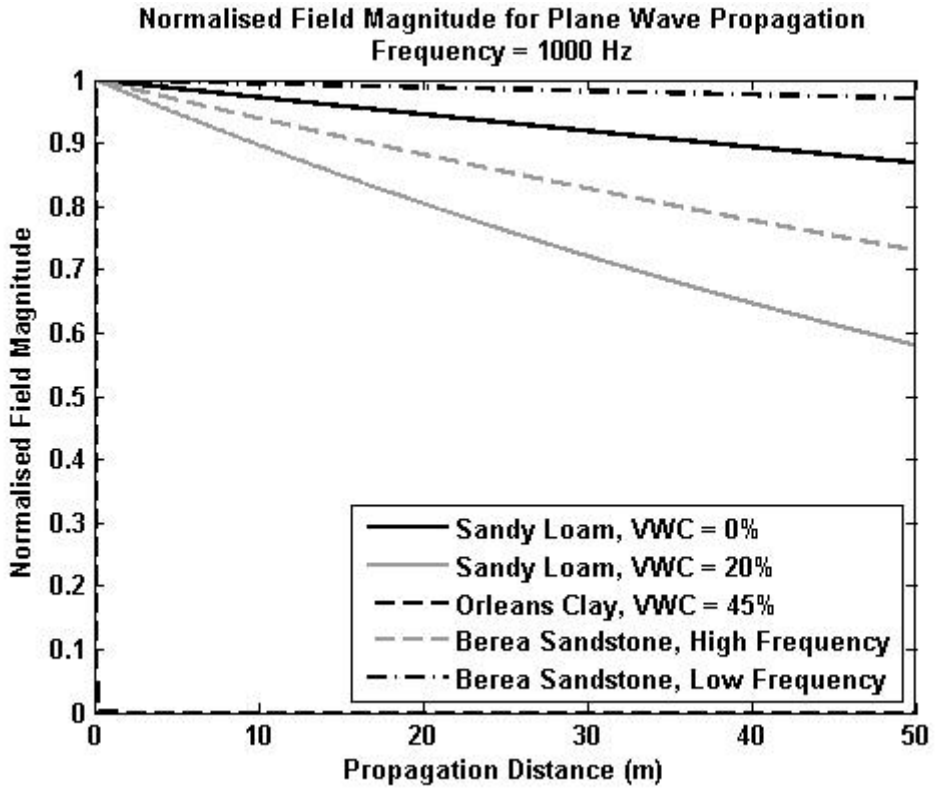

Figure 5-2: Normalised magnitude of a plane-wave propagating in homogenous soils - detailed in Table 5-1. Very large difference is shown between Orleans Clay and the less lossy soils.

Figure 5-3: Frequency dependent atmospheric electric field strength in urban environments (Skomal, 1978)

5.3.1.2 Noise

Specific measurements for electromagnetic noise at low-frequencies are hard to obtain. Fraser-Smith and Bowen (1992) and Surkov and Hayakawa (2007) both report magnetic fields in the ELF band. Surkov and Hayakawa (2007) show results of up to $1\text{mT}/\sqrt{\text{Hz}}$ at 10^{-3}Hz, corroborating a result of Lanzerotti *et al.* (1990) who took measurements at Arrival Heights, Antarctica and showed similar noise magnitudes (Volland, 1995). Human influence is also significant, Bowen *et al.* (1992) report that noise magnitudes in their urban measurement stations are an order of magnitude higher than that of their rural measurement stations. This is supported by the results of Skomal (1978) (Figure 5-3) who gave measurements for frequency dependent noise in a range of environments. The only reliable conclusion from the related literature is that there will be noise present in the ground, much of it man-made, but that the magnitude of that noise is highly dependent on the location in question. Noise figures will be reported for each field trial.

5.3.1.3 Signal-to-Noise Ratio

It has not been possible to calculate an expected SNR, due to the large number of dependant variables. The first task for the field trials conducted here, is to establish an SNR estimate.

5.3.2 Expected Wave Velocity of Low-Frequency Electromagnetic Waves in Soil

The propagation velocity for a plane-wave in a homogenous medium is derived from Maxwell's equations via the wave equations, giving the following results (Paul and Nasar, 1987):

$$\gamma = \sqrt{j\omega\mu(\sigma + j\omega\varepsilon)} \tag{5-3}$$

Where γ is the propagation constant, ω is the angular frequency, μ is the permeability of the medium, ε is the permittivity of the medium, and σ is the conductivity of the medium.

The attenuation constant, α, and the phase constant, β, are given by:

$$\gamma = \alpha + j\beta \tag{5-4}$$

The propagation velocity, c, is given in terms of the phase constant:

$$c = \frac{\omega}{\beta} \tag{5-5}$$

This relationship is shown graphically in Figure 5-4. The logarithmic relationship between permittivity and propagation velocity is only maintained when conductivity is negligible; otherwise conductivity dominates the relationship. The results of equations (5-3) - (5-5) are given for a number of soils in Table 5-1, computed for a frequency of 1 Hz.

It is clear from these examples that propagation velocities of the order of 10^4 ms^{-1} may be measured, but that not all results indicate this to be true. Figure 5-2 shows the results of (5-1) and (5-2) and by comparison with Figure 5-4 it can be seen that signals with low phase velocities also have increased attenuation. In the case of highly resistive soils (sandy loam, and Berea sandstone), loss may only be of the order of 3 dB. However, the more conductive Orleans clay exhibits loss of around 100 dB per meter.

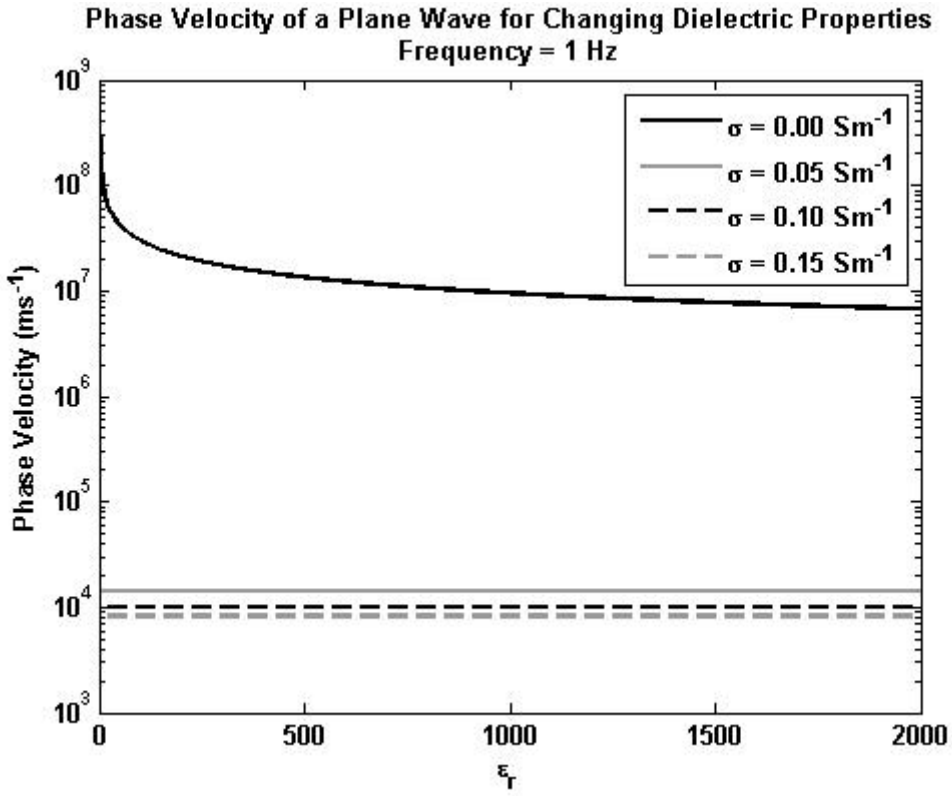

Figure 5-4: Theoretical propagation velocity of a plane-wave for increasing relative permittivity and conductivity.

5.3.3 Measurable Phase Change using an Array of Probes

Having established an approximate range for propagation velocity, it is now important to turn to the expected phase change between probes and assess whether that is measurable with the available SNR.

5.3.3.1 Expected Phase Change

The relationship between frequency, velocity and wavelength is well known as $c = f\lambda$. The phase change between two points on the array is determined by the ratio between the wavelength of the propagating wave and the distance between two probes in the direction of propagation (5-6):

$$\frac{\phi_{diff}}{2\pi} = \frac{d\cos\theta}{\lambda} = f\frac{d\cos\theta}{c} \tag{5-6}$$

Where ϕ_{diff} is the measured phase difference in radians, d is the array spacing, and θ is the angle between the array and the direction of propagation.

Taking an example propagation velocity of 10^5 ms^{-1} where the wave propagates parallel to the array, the expected phase change across the array is $6.28 \times 10^{-5} \times \mathrm{f} \times \mathrm{d}$ radians. Note, the proportional change with frequency and array spacing.

5.3.3.2 Phase Measurement Confidence

The methodology used to estimate the time-delay – or phase change – along the array is presented below. The method presented is the very widely used frequency-domain correlation method, chosen because the methodology is well documented, widely understood, with well-established error figures in the presence of noise. Furthermore, with high-speed Fourier transforms available the method is very simple to implement, and allows an increase in number of samples collected to correspond to increased signal-to-noise ratio (Bendat, 1978; Carter, 1987).

Having established the physical phase change which will exist if this wave propagates, it is crucial to calculate the tolerance of the phase measurement on an array of probes. To make this assessment, calculations are presented which follow the work of Bendat who shows (Bendat and Piersol, 1971; Bendat, 1978):

$$\hat{\gamma}_{xy}^2(f) = \frac{\left|\hat{S}_{xy}(f)\right|^2}{\hat{S}_{xx}(f)\hat{S}_{yy}(f)} \tag{5-7}$$

Where $\hat{\gamma}_{xy}^2(f)$ is the associated ordinary coherence estimate calculated at frequency f, known throughout this thesis as the cross-spectrum, $\hat{S}_{xy}(f)$ is the cross-spectral density function, and x and y denote two signals linked by transfer function $H_{xy}(f)$ with additive noise. The accent in $\hat{\gamma}$ and $\hat{S}$ denotes a smoothing by averaging the results from n_d measurements.

The phase error is calculated using (5-8):

$$\Delta\hat{\phi}_{xy} \approx \sin\Delta\hat{\phi}_{xy} \approx \varepsilon\left[\left|\hat{H}_{xy}(f)\right|\right] \tag{5-8}$$

Where $\Delta\hat{\phi}$ is the standard deviation of the phase measurement which is common for $\hat{H}_{xy}(f)$, $\hat{S}_{xy}(f)$, and $\hat{\gamma}_{xy}(f)$.

$\varepsilon\left[\left|\hat{H}_{xy}(f)\right|\right]$ denotes the random error formula:

$$\varepsilon\left[\left|\hat{H}_{xy}(f)\right|\right] = \frac{\sqrt{1-\gamma_{xy}^2(f)}}{\left|\gamma_{xy}(f)\right|\sqrt{2n_d}} \tag{5-9}$$

At this point SNR can be related to the error equations (Quazi, 1981, equation 11):

$$(SNR)^2 \approx \frac{S^2}{(S+N)^2}\Big/\left[1-\frac{S^2}{(S+N)^2}\right] = \frac{|\gamma(f)|^2}{1-|\gamma(f)|^2} \tag{5-10}$$

Combining (5-8), (5-9), and (5-10) gives the expression for the standard deviation of phase measurements as a function of SNR, and number of measurements:

$$\Delta\hat{\phi}_{xy} = \frac{1}{SNR\sqrt{2n_d}} \tag{5-11}$$

Throughout this work, a measurement accuracy of 3σ is expected, meaning that error bounds are shown at $\pm 3\Delta\hat{\phi}_{xy}$ with a 99.7% confidence.

5.3.3.3 Measurable Phase Change

Calculating the standard deviation of the phase measurement from an array of sensors allows the design of experiments which can measure phase with some certainty. An experiment may be designed which can examine whether waves propagate with low enough propagation velocity, and high enough SNR, to determine direction of arrival.

Without accurate SNR values, it is impossible to quantify the phase error; the results of the first field trials were used to quantify this factor. Table 5-2 shows the factors that are controlled in the following experiments, with the benefits of increasing or decreasing them. A compromise was reached in the effort to collect the most accurate data, by balancing these parameters to achieve measurement accuracy within the limitations of time, battery capacity, and technology.

Parameter Description	Result of Increase	Result of Decrease
TX Frequency (Hz)	Increased phase change between array elements	Possible increase effective permittivity of medium
Probe Spacing (m)	Increase phase change between array elements	Reduce far-field range. Increased practicality
Sampling Frequency	Reduced measurement time	Increased frequency resolution
Number of Samples	Increased frequency resolution	Reduced measurement time
Number of Measurement Slices	Increased SNR (number of samples must increase too)	Increased frequency resolution
Signal Voltage	Increased SNR, up to limit of equipment	

Table 5-2: Experimental Parameters and the Advantages of Increasing and Decreasing

5.3.4 The Far-Field Assumption

The, simple, range-independent, direction of arrival algorithms available are only valid where the far-field assumption can be made. The threshold distance for the far-field assumption is given by (Bienkowski and Trzaska, 2012):

$$R \geq \frac{2D^2}{\lambda} \tag{5-12}$$

Where R is the distance between transmitter and receiver, D is the size of the receiving array, and λ is the EM field wavelength.

The wavelength of the propagating field is related to the frequency by the propagation velocity. Acceptable values for R in defined soils, for an array equal in length to 10 wavelengths, and 10 metres in length, are shown in Table 5-3. Table 5-3 shows that the far-field assumption can be valid when a small array is positioned relatively close to a signal source, in some soils.

Soil	VWC	Frequency (Hz)	Wavelength (m)	Minimum R (m) (10m array)	Minimum R (m) (10λ array)
Sandy Loam	0%	1	7.07×10^4	0.0028 m	1.414×10^7
Sandy Loam	20%	1	1.83×10^4	0.0110 m	3.65×10^6
Orleans Clay	45%	1	2.69×10^2	0.7436 m	5.379×10^4
Berea Sandstone	-	1	3.08×10^4	0.0065 m	6.151×10^6
Sandy Loam	0%	100	7.07×10^2	0.28 m	1.414×10^5
Sandy Loam	20%	100	1.83×10^2	1.10 m	3.65×10^4
Orleans Clay	45%	100	2.69	74.36 m	5.379×10^2
Berea Sandstone	-	100	3.08×10^2	0.65 m	6.151×10^4

Table 5-3: Position of the far-field boundary, in a number of soils, at two frequencies. Soils with very low propagation velocity require a greater distance from the array before the far-field assumption is valid, but the increase in wavelength causes reduced phase change between array elements.

5.4 FIELD TRIAL METHODS AND RESULTS

The modelling which predicts that low-frequency electromagnetic techniques could be used for direction of arrival estimation is relatively simple. Despite this, no research has been found which aimed to take DoA measurements at low-frequencies in soil. The first question considered by these field trials is: Can the phase change of a propagating wave be measured in soil across an array of probes?

All field trials were conducted on earth dam sites, to ensure a water level was present in the soil. This ensures that multiple layers are available for the propagation of a wave, and that a region of moderate-to-high conductivity should be present.

5.4.1 Field Trial 1 – Small-Scale Test on a Dam in Birmingham

5.4.1.1 Aims

1. Measure the noise level in the subsurface at frequencies up to 1 kHz.
2. Observe any signals of opportunity and determine if a measureable phase change existed between the probes.

3. Test the laptops, data acquisition systems, and other equipment for use in outdoor field trials of this nature.

5.4.1.2 Physical Setup

The field trial took place on an earth dam, near the University of Birmingham. An aerial photo of the area is shown in Figure 5-5, and a photo of the measurement probes is shown in Figure 5-6. The physical setup of this experiment was very simple; an array of 5 regularly spaced probes was inserted in the dam and connected as shown in Figure 5-7. Voltages between the probes were measured using a 24-bit analogue-to-digital data acquisition system, controlled by a laptop computer (National Instruments, 2011; 2012). The spacing of the probes was varied between 20 cm and 300 cm.

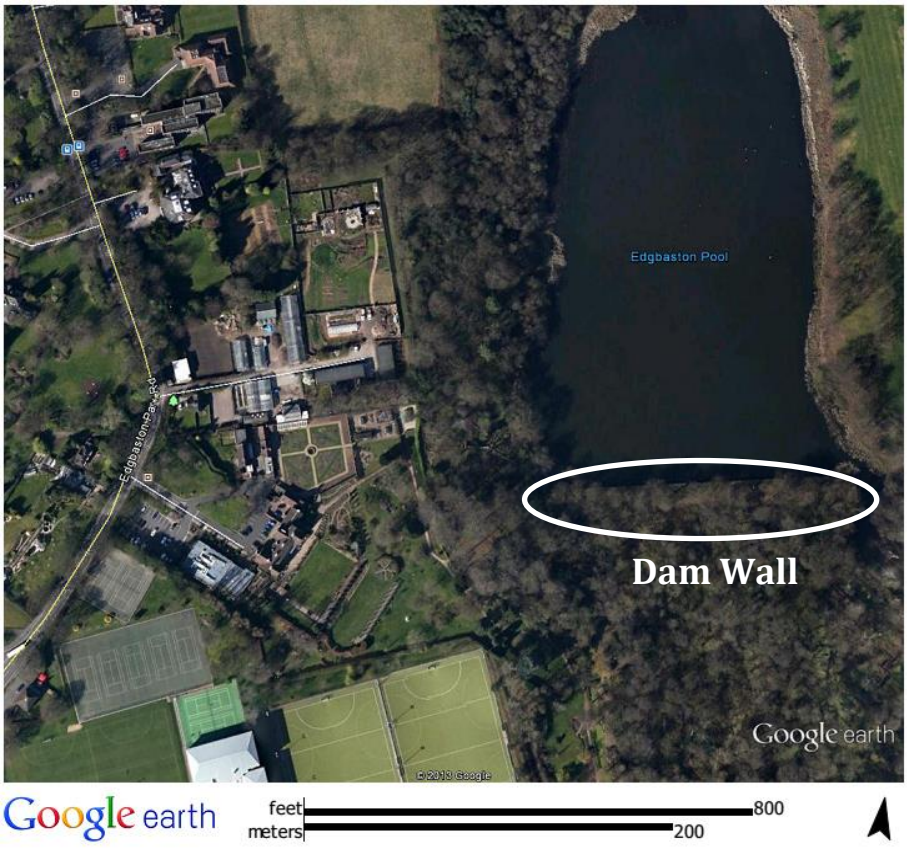

Figure 5-5: Aerial view of the test site, showing the reservoir, and the some of the University of Birmingham Campus (Google Earth, 2013b)

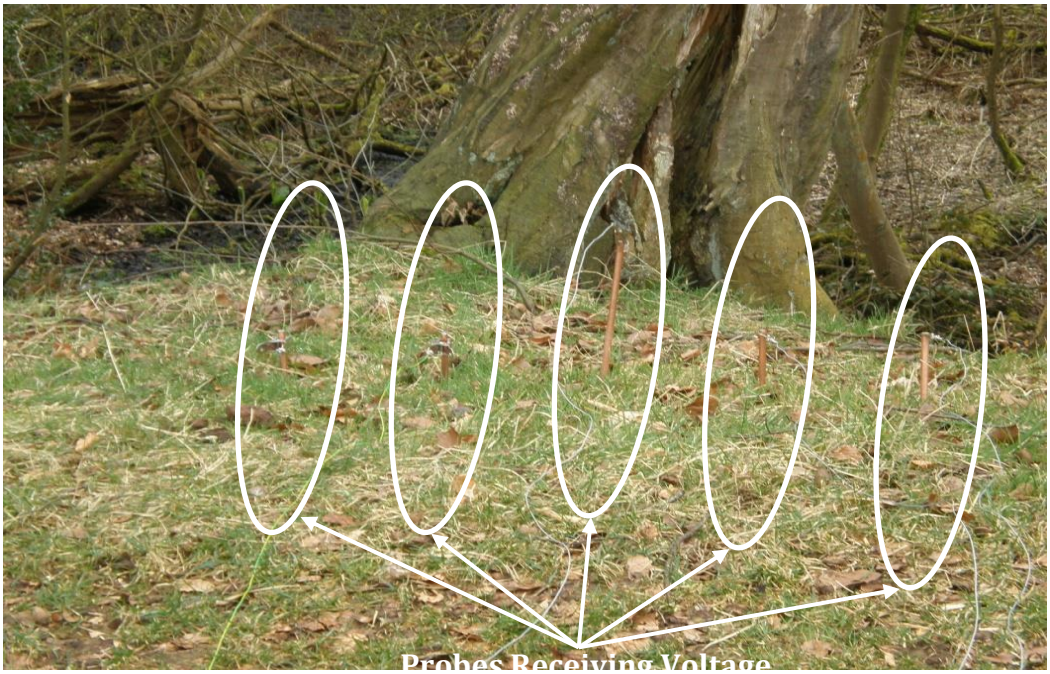

Figure 5-6: Probes placed in the earth dam at regular intervals

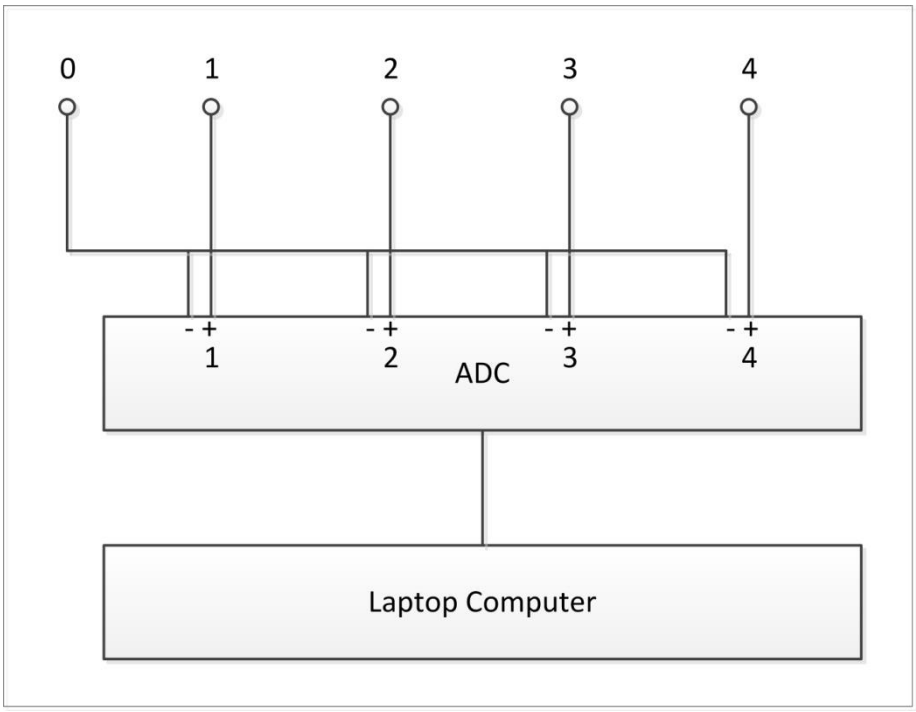

Figure 5-7: Probe connection to the data acquisition system

5.4.1.3 Measurement Setup

This field trial involved passive measurements; the only variables which could be controlled were the sampling frequency, number of samples per measurement, and the physical setup described above. Measurements were taken using the maximum sampling frequency available (50 kHz),

and each measurement collected 5 snapshots of 2^{22} measurements. This gave an acceptable compromise between number of measurements, available memory, and battery capacity. Each measurement took 7 minutes with an additional 2 minutes to store the data.

5.4.1.4 Results

The results are given in the same order as the field trial aims were stated:

Noise Level in the Subsurface in the ULF Band

To show the measured noise, it is instructive to consider both time and frequency-domain results. The following results are from channel 1, with probe spacing of 20 cm. Time-domain results (Figure 5-8) show all the snapshots and show a gradual change in all channels which is likely to be caused by electrode polarization. In addition, short transients are also evident. The source of these transients is unknown, but they could be a result of a glitch in the analogue-to-digital conversion. Other measurements exhibit similar glitches, but they are not at consistent times across measurements.

The frequency-domain result (Figure 5-9), is a fast-Fourier transform (FFT) of single snapshot of the same measurement. A flat-top window was applied, prior to the FFT. The frequency-domain result is dominated by 50 Hz and its odd harmonics, but a signal is also visible at 23.4 kHz. These signals are in addition to the random background noise, and demonstrate the importance of checking for interfering signals prior to measurement.

A more useful measurement than the frequency-domain data, is the measured electric field strength, in Volts per meter (Figure 5-10). The electric-field magnitude remains roughly constant at 10^{-7} $Vm^{-1}Hz^{-1}$, except where a signal is present such as at the harmonics of 50 Hz.

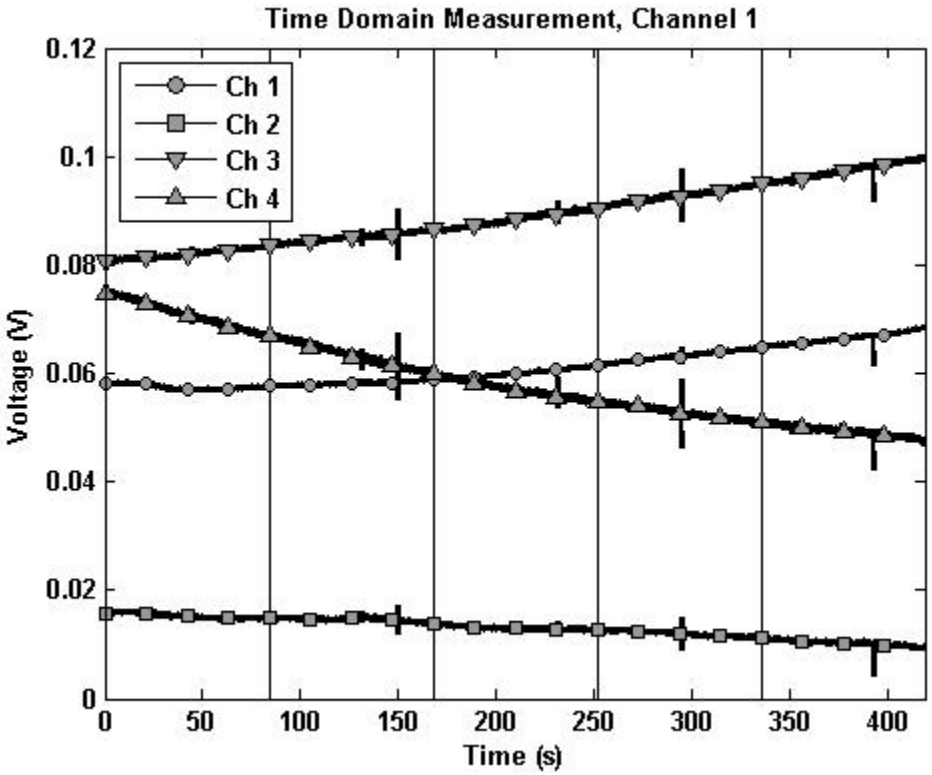

Figure 5-8: Time-domain measurements on channel 1, where probe spacing is 20 cm. Gradual change on all probes is evident, and is likely to be due to electrode polarization. Transients are also evident, shown which are likely to be buffer-overload on the sigma-delta ADC.

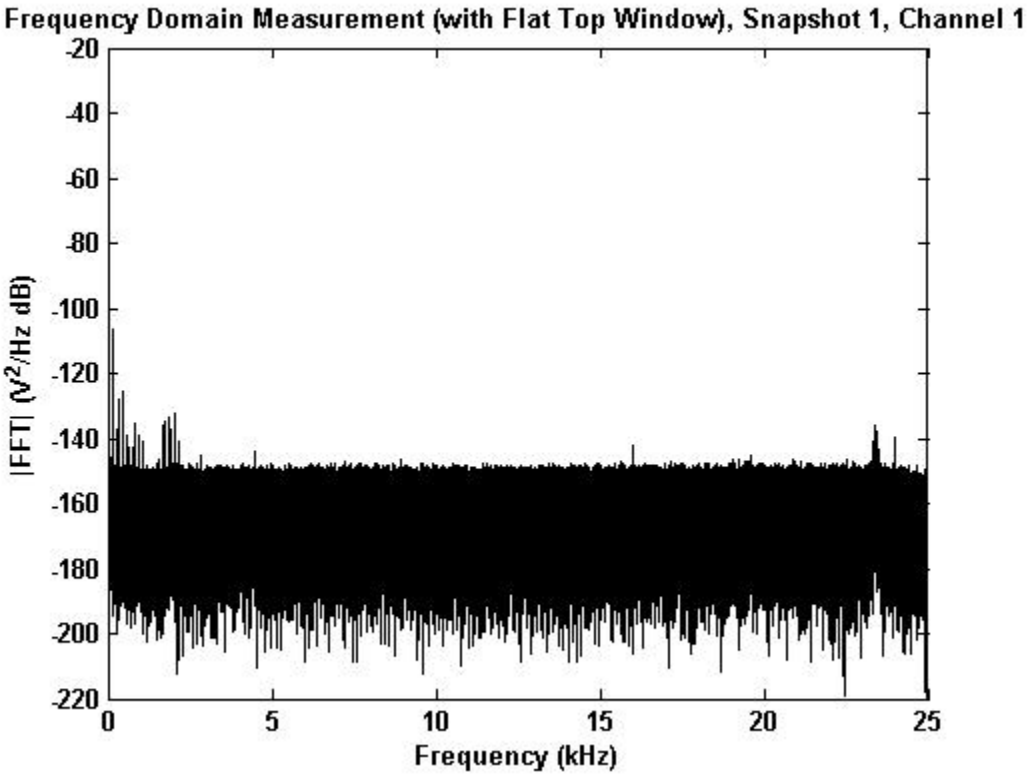

Figure 5-9: Frequency-domain measurements on channel 1, where probe spacing is 20 cm. Harmonics of 50 Hz are evident, a signal also is also present at around 24 kHz.

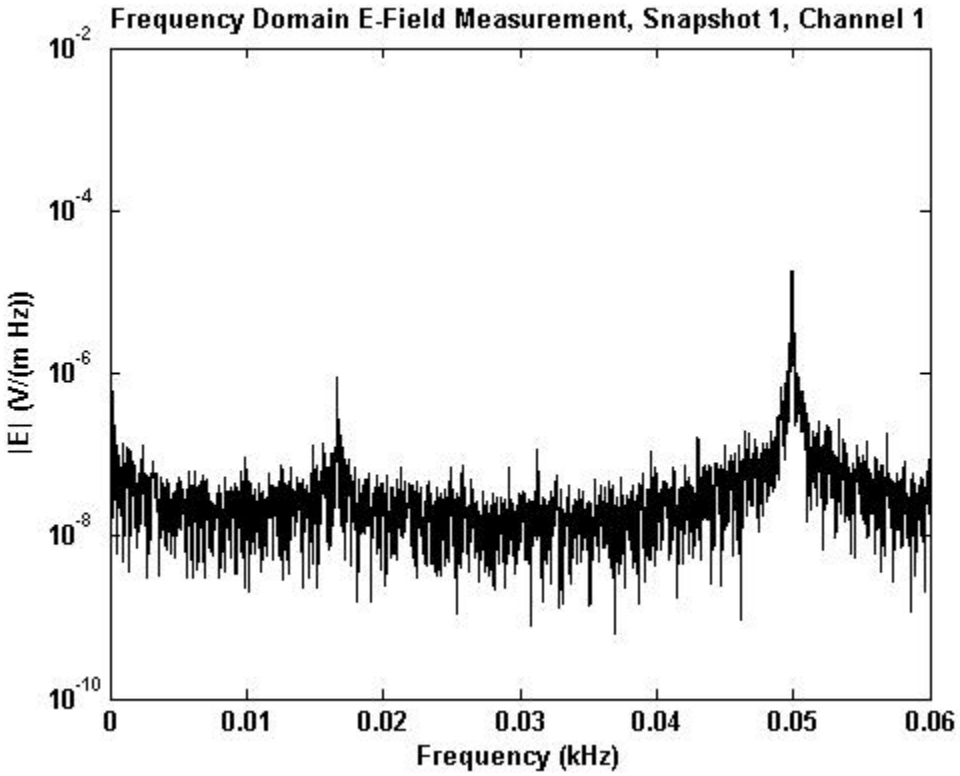

Figure 5-10: Electric-field magnitude in the frequency-domain, for the first snapshot of the measurement, probe spacing = 200 cm. This result was very similar to other measurements taken with different probe spacing.

Measurable Phase Change for Fields of Opportunity

The passive nature of this measurement means that fields of opportunity are the only way of considering phase change along the array.

The data was processed by applying a complex cross-spectrum to the measured signals, that is the frequency-domain equivalent of the cross-correlation function. The signals were correlated to the measurement taken on channel 1, and filtered so that only those with cross-spectrum magnitude ≥ 0.99 $\left(SNR \geq 17\ dB\right)$ are shown. The phase of the cross-spectrum is then plotted against the spacing of the array (Figure 5-11, Figure 5-12).

Using (5-10) and (5-11), SNR and $\Delta\phi$ were calculated. The 3σ tolerance was used for the error bounds, different frequencies show very different uncertainties. Measurement uncertainty is significantly greater than the measured phase change. This leads to the conclusion that signals of opportunity cannot prove high-enough SNR to measure phase change for the propagation velocities observed. This indicates a minimum propagation velocity for the observed signals of

opportunity shown in Table 5-4, calculated using (5-6) and by observing that phase change per meter is less than the measurement uncertainty. These results indicate that the signals of opportunity are not propagating at exceptionally low velocities, particularly for the high frequency signal of opportunity.

Signal Frequency (Hz)	**Measurement Uncertainty ($rads$)**	**Minimum Propagation Velocity (ms^{-1})**
50	0.018	1.75×10^4
150	0.0012	7.85×10^5
23407	0.034	4.32×10^6

Table 5-4: Signal of opportunity measurement uncertainty and corresponding minimum propagation velocities.

Test the Equipment for Field Trial Use

A number of practical lessons were learnt from this field trial:

- A system involving large numbers of wires requires a method of storing those wires to avoid very time consuming knots.
- Several minutes of battery life can be saved by hibernating, rather than shutting down, laptops prior to the trial with relevant software running.
- Crocodile clips make a convenient solution to connect wires to probes, but are prone to disconnecting themselves.
- If a field trial is set up in a public area, at least one measurement will be compromised by curious onlookers.

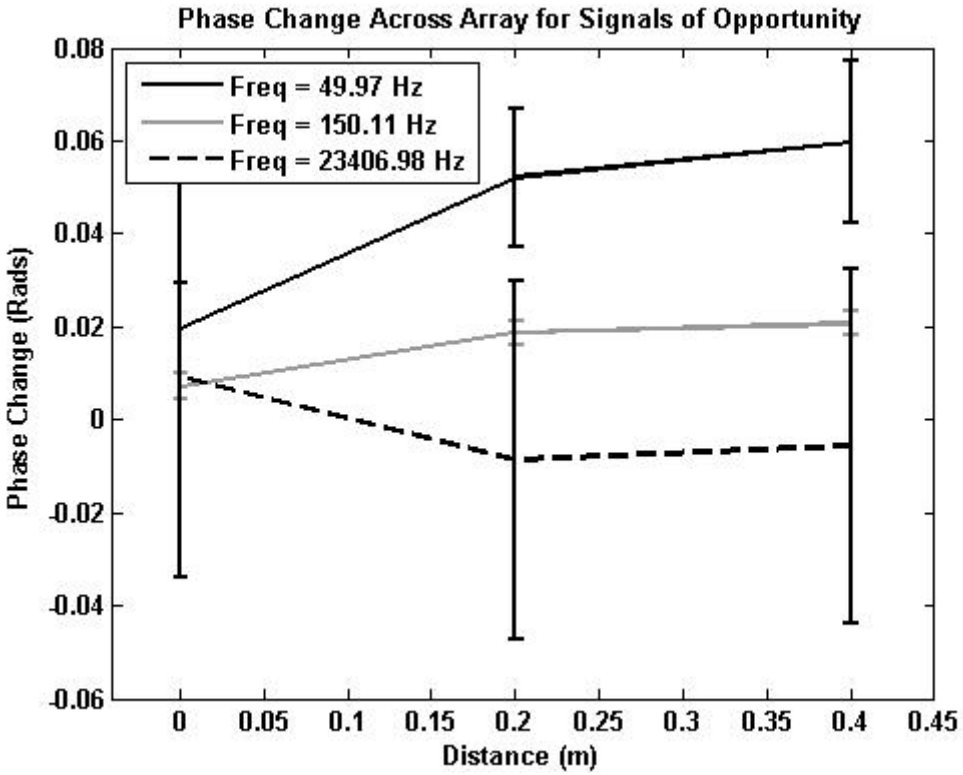

Figure 5-11: Phase change across a 20 cm spaced array for 3 signals of opportunity. The error bounds show significant variation.

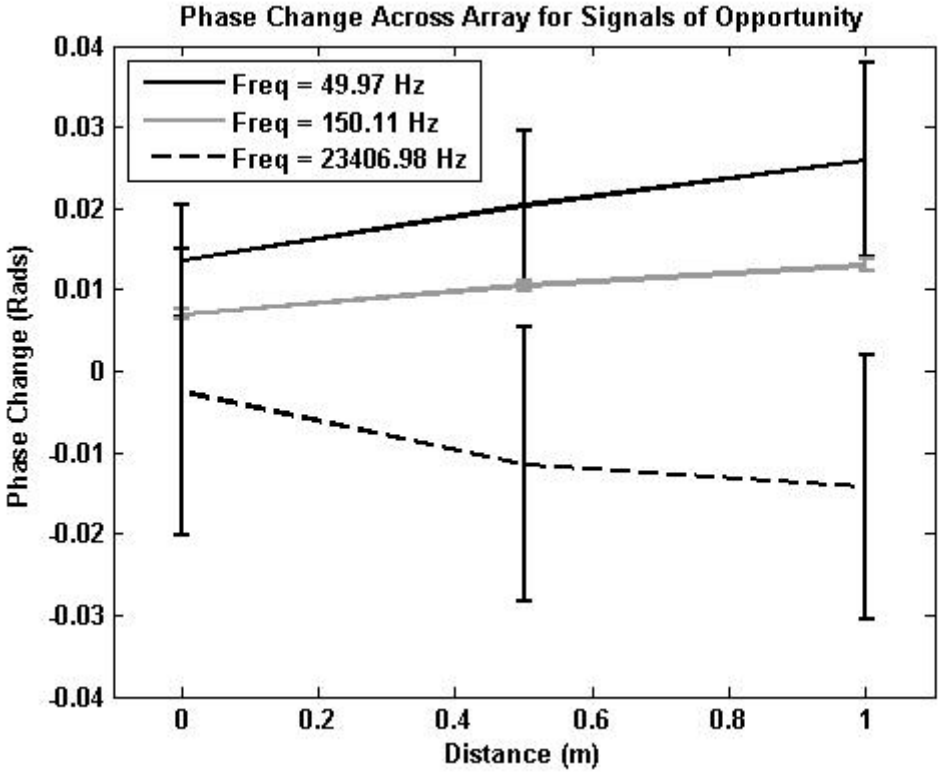

Figure 5-12: Phase change across a 50 cm spaced array for 3 signals of opportunity. The error bounds show significant variation.

5.4.2 Field Trial 2 – Larger Scale Test on a Dam in Birmingham with Excitation

5.4.2.1 Aims

1. Determine if excited signals can be detected, despite the attenuation of the soil.
2. Measure the SNR of the transmitted signals.
3. Determine if the phase of the excited signals is measurable with acceptable accuracy.
4. Examine if configuration is acceptable for measuring phase change along the array.

5.4.2.2 Physical Setup

The physical location of the field trial was the same as field trial 1 (Figure 5-5). The array of receive probes was also set up in the same configuration as field trial 1, but with 20 receive channels at 1 m spacing (Figure 5-7). The use of 20 channels was considered to give an acceptable compromise between maximising measurable phase change and ensuring the array size did not compromise either signal-detection or the far-field assumption. A pair of probes was inserted in a vertical configuration to excite a wave in the dam. This configuration is sketched in Figure 5-13.

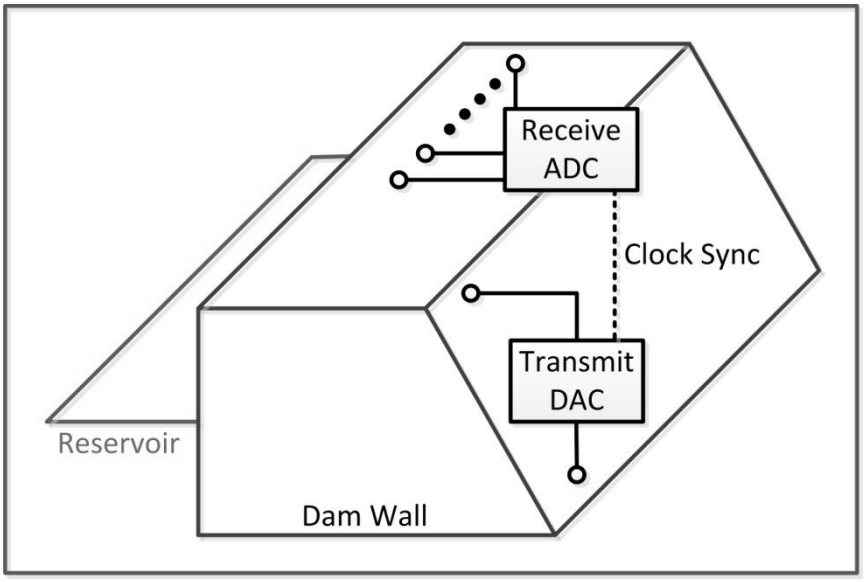

Figure 5-13: Block diagram representation of field trial with excitation of the dam.

5.4.2.3 Synchronisation of Two Measurement Chassis

The measurements were conducting using National Instruments data-acquisition chassis which have function-specific modules inserted (National Instruments, 2011). It was found that unacceptable levels of crosstalk occurred when using a digital-to-analogue (DAC) card to excite a wave in the dam, and the receive analogue-to-digital (ADC) cards in the same chassis. It was decided that significant physical separation between the transmit and receive hardware was required. The solution was to use two separate chassis, requiring synchronisation between the two chassis to ensure that the sampling rate was consistent.

Connectors are available on the measurement chassis to transmit and receive timing signals. The receive chassis was configured to transmit a timing pulse per sample which was used by the transmit chassis. At no point during testing or measurement was a sample missed using this method. However, when testing the output with a spectrum analyser, it was found that the actual frequencies in use were around 20% lower than intended. The cause of this is unknown, but it is likely that the length of the coaxial cable caused greater than intended impedance in the timing circuit. The software required to synchronise two chassis was not trivial, and the source code is included in Appendix 6 for reference.

The possibility of the coaxial cable acting as an unintended receive antenna was tested by surrounding the coaxial cable with a large wire coil which was energised using a signal generator. However, no difference was observed in measurements with this interference present.

5.4.2.4 Measurement Setup

The equipment was set up as shown in Figure 5-13, and one laptop computer controlled each chassis. The transmit frequency was varied from 0.1 Hz to 2 Hz in 0.1 Hz increments and then up to 45 Hz in 1 Hz increments. The sampling rate used was 2 kHz, taking measurements of 2^{17} samples meaning that each measurement took around 65 seconds.

5.4.2.5 Results

Results are presented in the same order as the aims of the field trial:

Determine if the excited signals can be detected, despite the attenuation of the soil

The first aim of this field trial was to demonstrate that signals could be transmitted and received through the dam. The first method applied to answering this question was to view the measured data in the frequency-domain. After applying a flat-top window, an FFT was taken and the results for 3 channels, at two different excitation frequencies, are shown in Figure 5-14 and Figure 5-15. In both cases, the excitation frequency was received on all three channels. However, signal amplitude was very low; lower than the ambient 50 Hz noise.

A more rigorous measurement, particularly when measuring phase, is taking the complex cross-spectrum. Figure 5-16 - Figure 5-19 show examples of the complex cross-spectrum magnitude calculated between the transmitted signal and the measured signals. These examples are typical, in that the signal is received with good correlation (complex cross-spectrum magnitude > 0.995, equivalent to SNR > 20 dB) at each frequency used, and on every channel of the array. It is clear that the transmitted signals are being measured at the receiving array.

Measure the SNR of the transmitted signals

It has been shown that to measure the direction of arrival (DoA) of a received signal, the phase measurement must be highly accurate. It has also been shown that the phase accuracy is dependent on the SNR, which is calculable from cross-spectrum magnitude. SNR was calculated for a selection of excitation frequencies, and is shown in Figure 5-20. The typical SNR is relatively consistent along the array. However, there is significant variation at some points along the array which can be explained by variation in probe contact with the ground, or imperfect contact between the probe and the ADC module. The highest SNR achieved was 20.4 dB at the 14 m probe where the transmit frequency was 24.1 Hz. More typical SNR was between 14 and 18 dB. It should be noted that a least-squares fit over many array elements reduces the required phase accuracy by approximately the square-root of the number of array elements (York, 1968; Kreyszig *et al.*, 1999).

Is This Configuration Acceptable for Measuring Phase Change along the Array?

Having calculated SNR, the next step is to calculate the phase error using (5-11). The 3σ confidence interval is shown in Figure 5-21. The expected phase error is relatively small; the typical confidence interval is around ±0.025 radians. However, if the wave is propagating at a velocity of 10^5 ms^{-1} endfire to the array, the calculations at the start of this chapter indicate an expected phase change of 0.0015 rads between array elements, reduced further if the wave was not propagating parallel to the array. Consequently, these results do not show the required accuracy for phase estimation unless the wave was propagating with much lower velocity than initially predicted.

For estimation of direction of arrival, the predicted accuracy for this configuration – using the MUSIC algorithm error analysis described in Chapter 2 – was 0.175 radians (10 degrees) for a 22 Hz signal, and 22.6 radians (1297 degrees) for a 2 Hz signal, propagating at 10^5 ms^{-1}, and increasing exponentially as the true direction of arrival approached broadside (90 degrees).

These results contribute to the aim of the next field trial, which is to devise a measurement system with sufficient SNR and large enough expected phase to make the desired phase measurements.

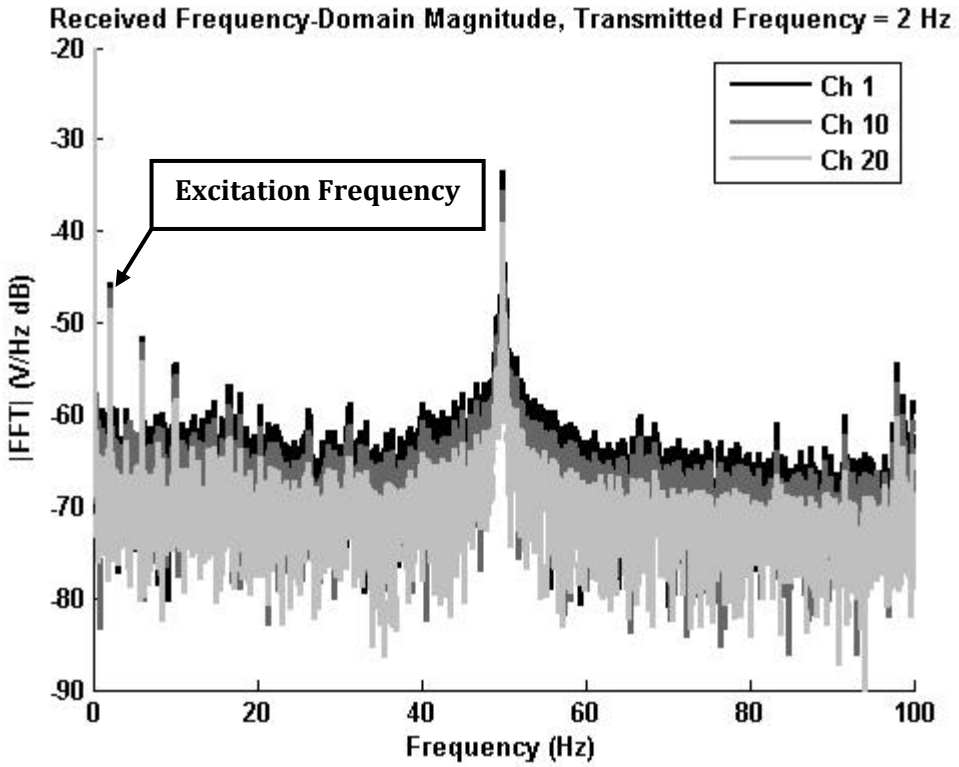

Figure 5-14: Magnitude of an FFT taken on 3 measurement channels, while excitation frequency = 2 Hz. The excitation frequency is visible, with its first two odd harmonics. 50 Hz ambient noise is also present.

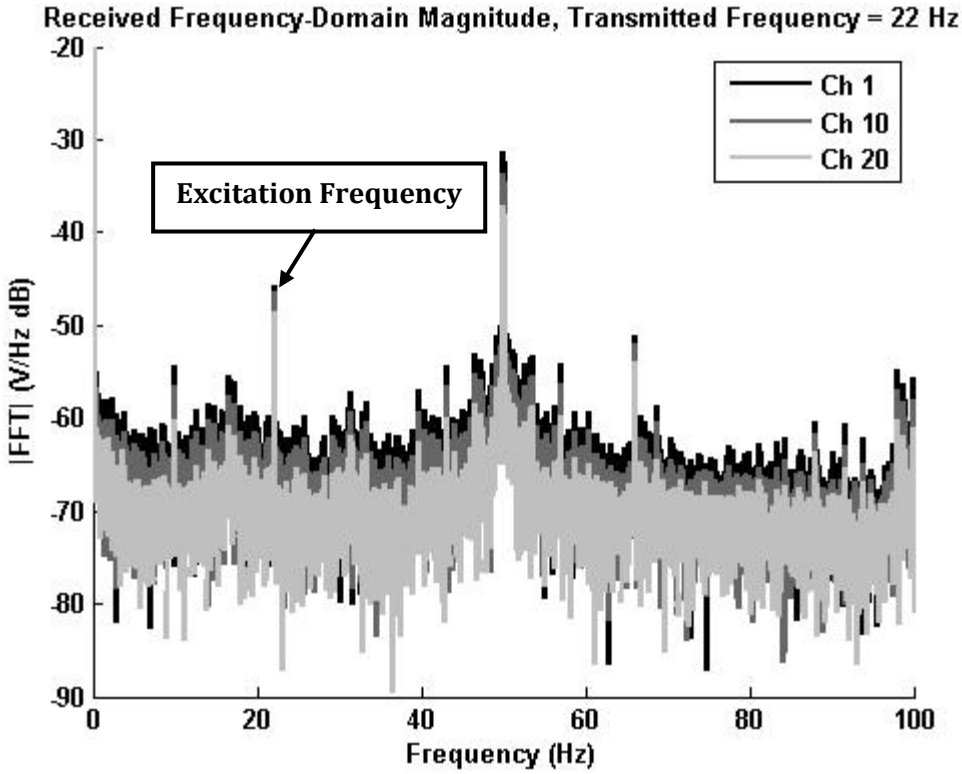

Figure 5-15: Magnitude of an FFT taken on 3 measurement channels, while excitation frequency = 22 Hz. The excitation frequency is visible, with its first odd harmonic. 50 Hz ambient noise is also present.

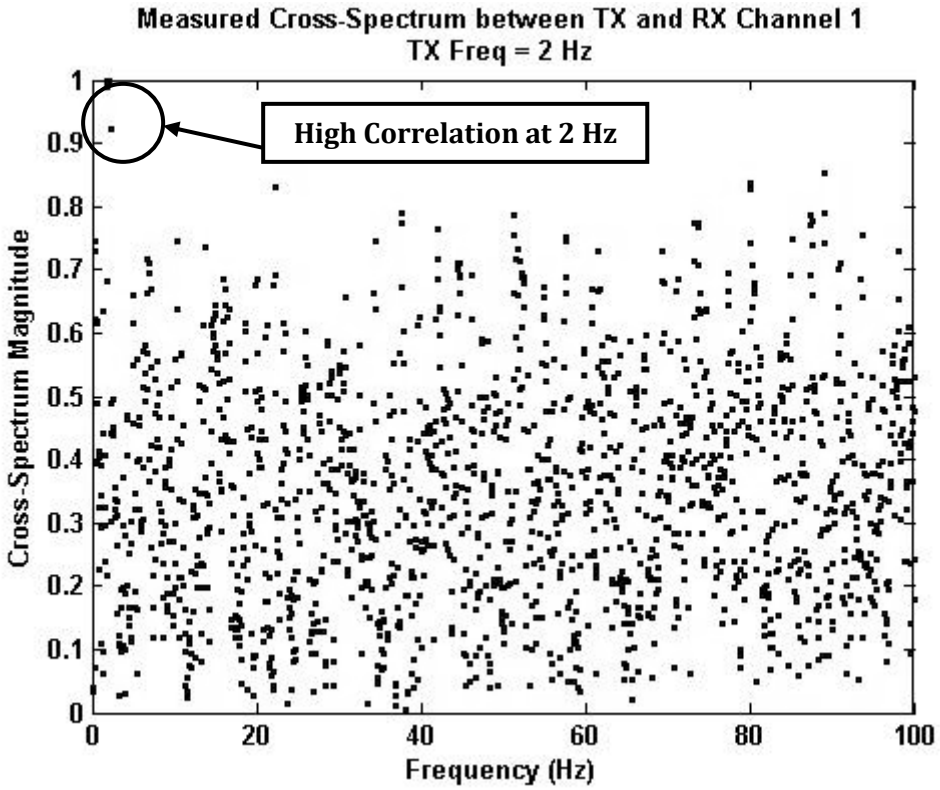

Figure 5-16: Cross-spectrum magnitude between 2 Hz transmitted signal and the measured signal on channel 1 of the array, high correlation is shown at 2 Hz.

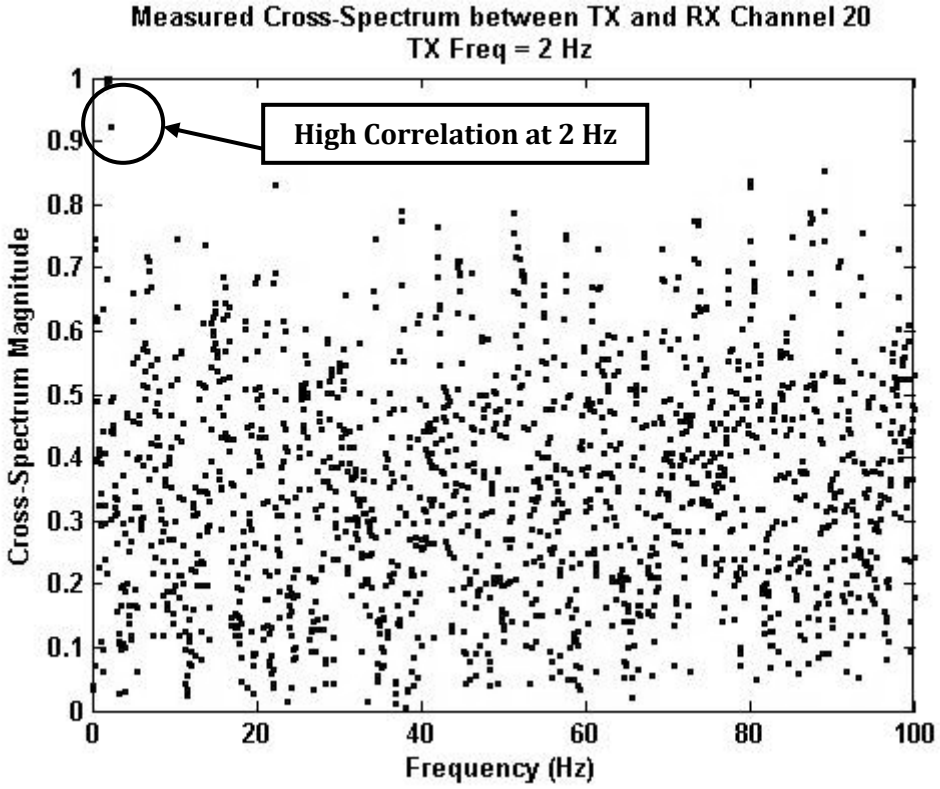

Figure 5-17: Cross-spectrum magnitude between 2 Hz transmitted signal and the measured signal on channel 20 of the array, high correlation is shown at 2 Hz.

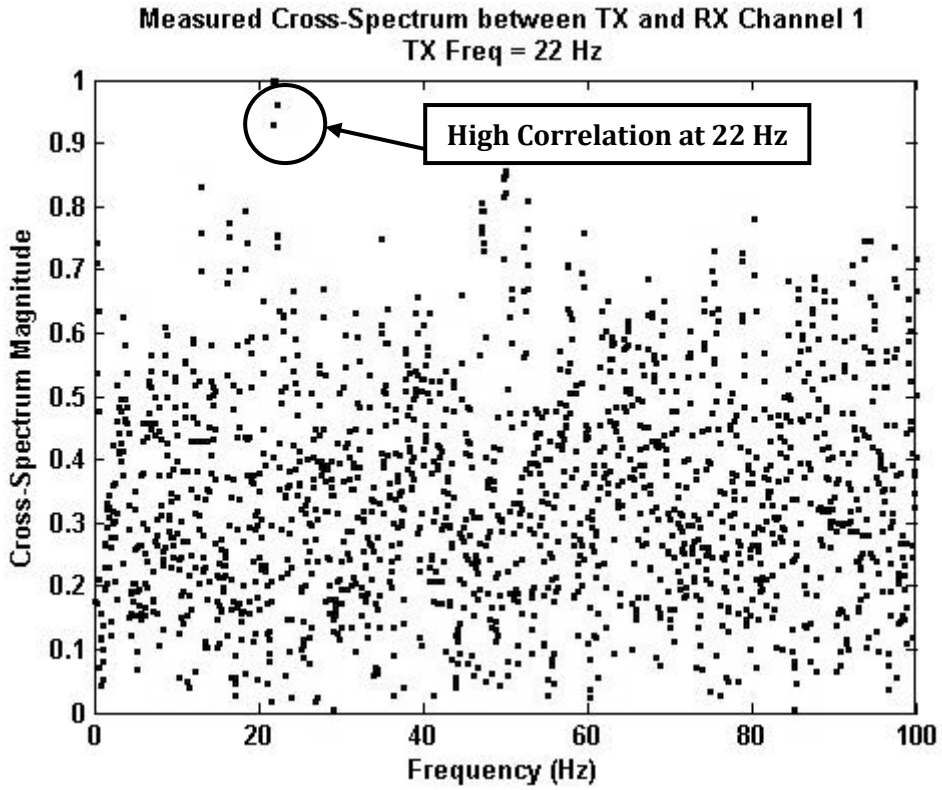

Figure 5-18: Cross-spectrum magnitude between 22 Hz transmitted signal and the measured signal on channel 1 of the array, high correlation is shown at 22 Hz.

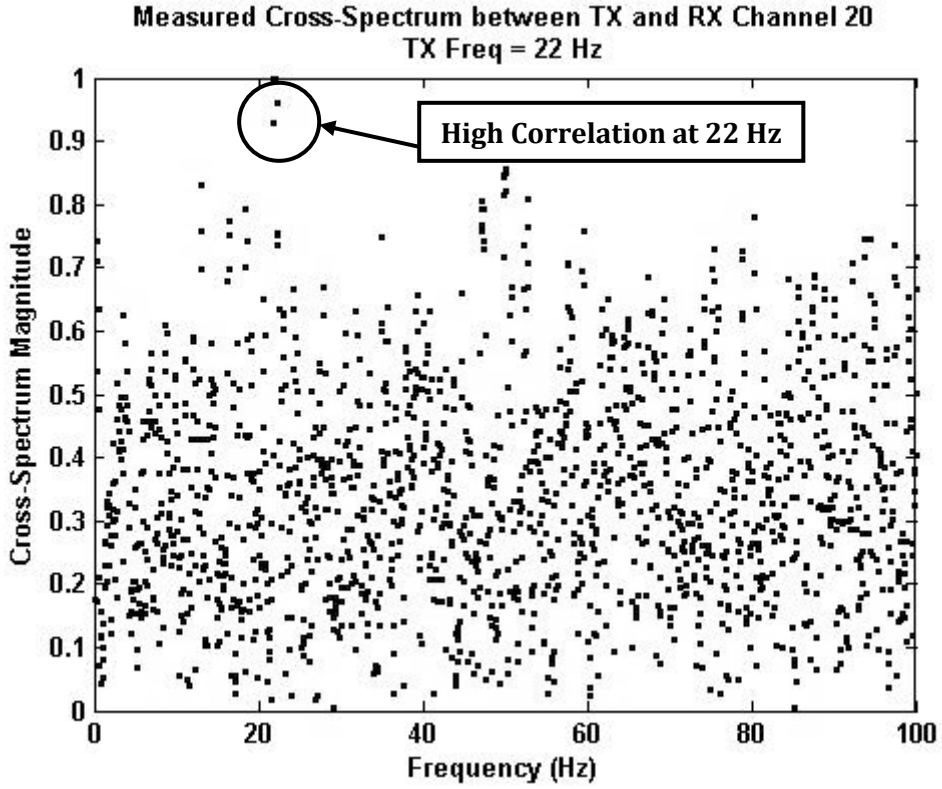

Figure 5-19: Cross-spectrum magnitude between 22 Hz transmitted signal and the measured signal on channel 20 of the array, high correlation is shown at 22 Hz.

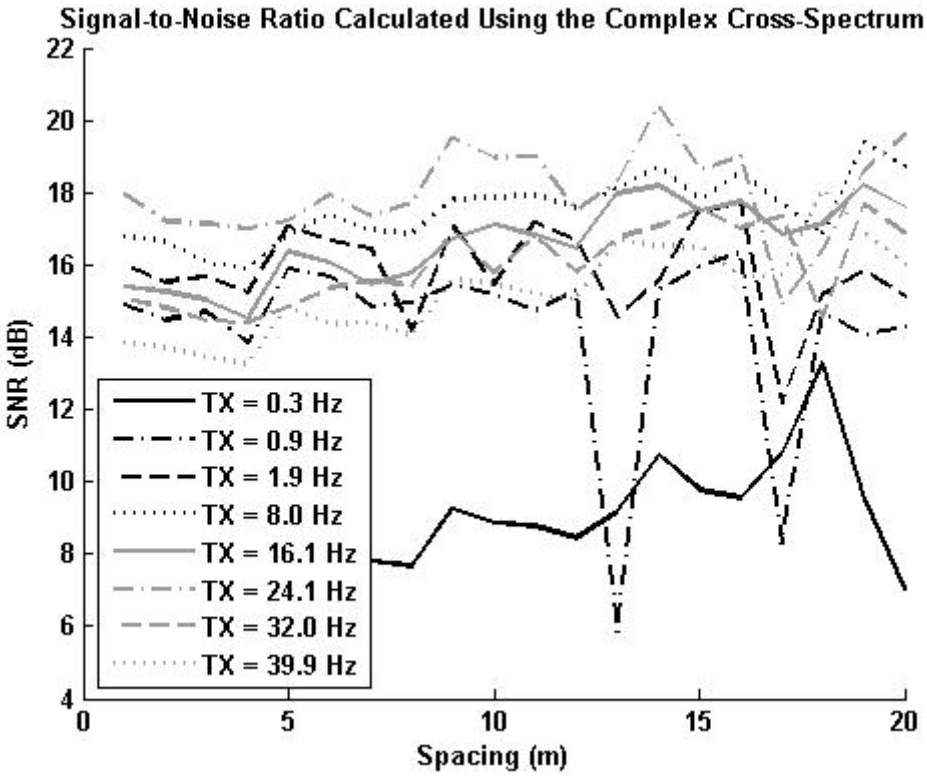

Figure 5-20: SNR calculated at each point on the receive array from measured complex cross-spectrum. Change in SNR along the array is relatively small.

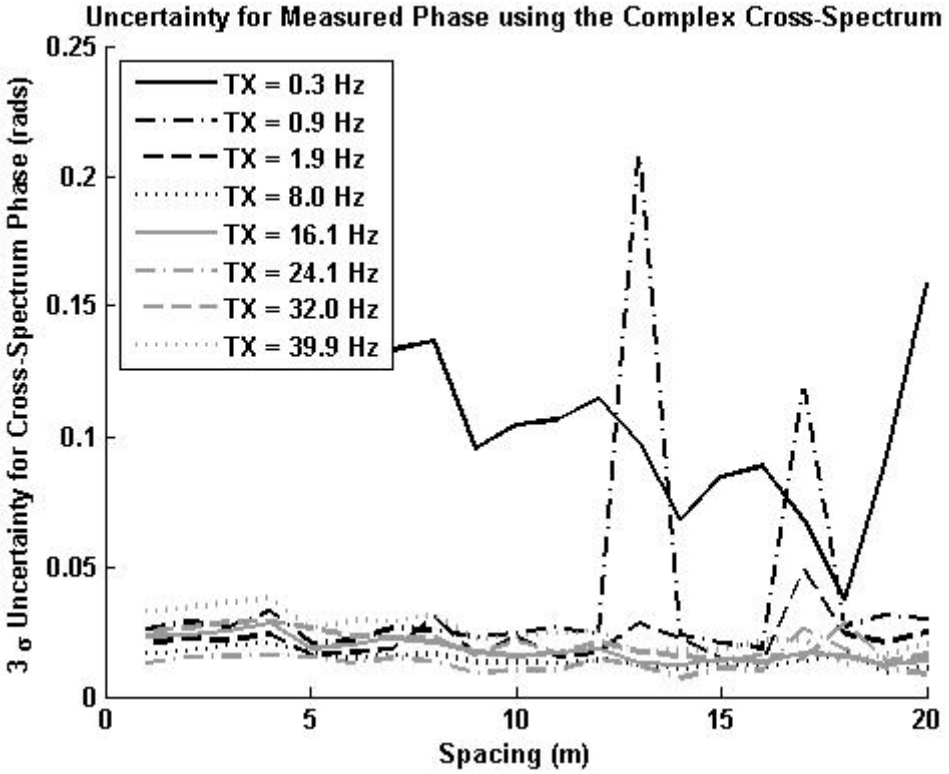

Figure 5-21: Phase error magnitude, calculated from SNR, using a 3σ confidence interval. The calculated error is too large for accurate DoA estimation.

5.4.3 Field Trial 3 – Larger Scale Test on a Dam in Bristol with Excitation

This field trial represents the final attempt to measure a wave propagating slowly though soil, to validate the idea of a utility detection method based on the use of a DoA algorithm on received low-frequency electromagnetic signals.

5.4.3.1 Aims

The aims of this field trial were as follows:

1. Measure SNR in a rural location
2. Determine if a measurable phase change occurred across the array when using the most sensitive, feasible, measurement set up.
3. Conclude whether DoA measurements are possible in soil, using low-frequency electromagnetic fields.

5.4.3.2 Physical Setup

This field trial was conducted on a test site near Bristol. A week-long field trial for the Mapping the Underworld project allowed equipment to be in place for a week, giving ideal opportunity for measurements of extended duration. An aerial image of the test-site is shown in Figure 5-22.

The physical positioning of the probes was very similar to field trial 2, and is shown in Figure 5-13. The separation of the receive probes was 2 metres, the reason for this is discussed, with the other measurement parameters in the next section. In this field trial, the means of connection between the measurement equipment and the probes was changed from crocodile clips to banana plugs. This gave greater consistency in the electrical connection between the probes and the chassis.

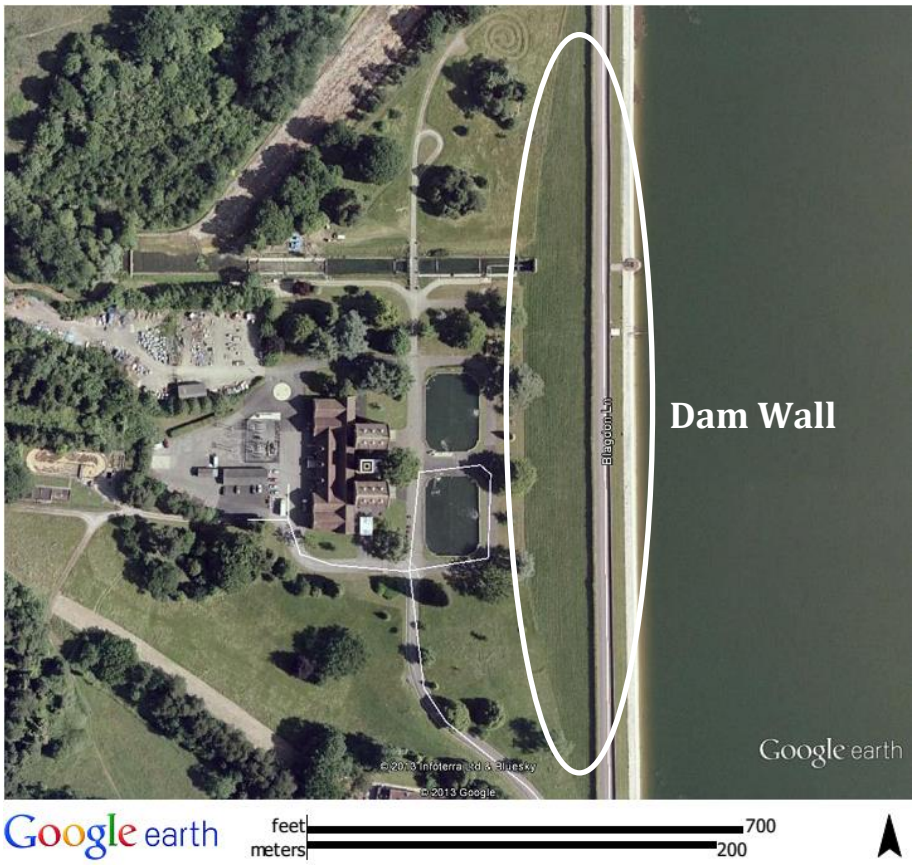

Figure 5-22: Aerial view of the test site outside Bristol (Google Earth, 2013a)

5.4.3.3 Measurement Setup

The equipment was connected in the same manner as field trial 2 (Figure 5-13), and synchronisation of the transmit and receive chassis was achieved in the same manner. In an effort to maximise the probability of measuring the phase change along the receive array, the following values were calculated:

Step 1: Required Phase Resolution

Assuming a signal propagating at $10^5\ ms^{-1}$ along (end-fire to) the array, the phase change between two array probes is calculated as:

$$\phi_{diff} = 2\pi f \frac{d\cos\theta}{c} = 6.2832 \times 10^{-5} \times f \times d \qquad (5\text{-}13)$$

Step 2: SNR Based Limit to Phase Resolution

Taking the typical SNR measured in field trial 2, (5-11) allows the calculation of the phase error:

$$SNR_{previous} \approx 16dB = 39.8 \tag{5-14}$$

$$\Delta\hat{\phi}_{xy} = \frac{1}{SNR}\frac{1}{\sqrt{2n_d}} = 0.025\frac{1}{\sqrt{2n_d}} \tag{5-15}$$

Step 3: Use Frequency, Spacing, and Number of Slices to Equate the Two

Before determining measurement parameters for the field trial, several other limitations will be given:

- Measurement duration cannot exceed the battery capacity of a laptop battery.
- Increasing the array size is limited by practicality and the increased attenuation it causes.
- Increasing frequency increases the signal attenuation, and moves the measurement out of the exceptionally high permittivity region.

It was decided to operate with transmit frequencies of the order of 330 Hz, taking 8 snapshots of 2^{21} samples per measurement, with array spacing of 2 metres. This updates equations (5-13) - (5-15) as follows:

$$\phi_{diff} = 6.2832 \times 10^{-5} \times 330 \times 2 = 0.0415\, rads \tag{5-16}$$

$$\Delta\hat{\phi}_{xy} = \frac{1}{SNR}\frac{1}{\sqrt{2n_d}} = 0.0011 \tag{5-17}$$

The expected phase difference along the array is now less than the expected phase tolerance. Even when considering 3σ precision, expected tolerance is a factor of 6 greater than expected phase change. However, in order to achieve an estimate for direction of arrival, the measurement must be able to distinguish between the phase change of the wave propagating parallel to the array and the smaller phase changes of a wave propagating at an angle to the array.

This experiment was performed at the maximum level of precision: Averaging the cross-spectrum with slices of 2^{17} samples gave 248 averages, whilst measurements required 27 minutes to collect and store, using all of the available memory in the receiving laptop. An array of 21 probes, at 2 metre spacing, resulted in a 40 metre array, giving a high likelihood of reduced

SNR at the furthest probes (reduced signal magnitude of 3 dB over similar distances is shown in Figure 5-2).

5.4.3.4 Results

The results are presented in the same order as the aims of the field-trial.

Measure SNR in a rural location

In common with previous field trials, the frequency-domain measurements for a number of channels are presented in Figure 5-23. The transmitted wave is measured at all channels, with a magnitude similar that of to the adjacent harmonics of 50 Hz. The more rigorous cross-spectrum method is shown in Figure 5-24 and Figure 5-25 for two channels, the correlation at the transmitted frequency is much greater than any other frequency.

Using (5-10), the SNR can be calculated for each transmitted frequency at each measurement probe on the array. These results are shown in Figure 5-26, it can be seen that the SNR is lower than previous field trials, even with the extended measurement time. This can easily be attributed to increased soil attenuation.

Determine if a measurable phase change occurred across the array

The method for calculating the error in the calculated phase change, given above, is applied here. The phase measured along the array is plotted in Figure 5-27, with error values calculated using (5-11) . The error reported is approximately 0.15 rads, which represents a reduction in accuracy compared to field trial 2, this is expected considering the reduced SNR.

Considering Figure 5-27, it appears that the phase change occurs in two distinct regions – between 2 and 12 metres, and between 14 and 40 meters, indicating a change in the dominant propagation path. When considering the wave propagation in layered media, the results of Chapter 4 – and its supporting work – are relevant (King *et al.*, 1992; King and Sandler, 1994; Zhang and Pan, 2002). Consider the example results shown in Figure 5-28, the dominant wave changes from the direct, reflected, and lateral (DRL) component, to the trapped surface wave. It

has been shown that the trapped surface wave propagates with a wavenumber between the wavenumbers of the materials on either side of the relevant boundary (Wait, 1962). Consequently, after the change of the dominant wave path, the wave is expected to propagate at a different propagation velocity.

However, the straight line fit which provides an estimate for propagation velocity, in both of these regions will be shown to have considerable error. The final result presented in this chapter, is calculated by fitting linear curves to the two regions identified, to give an estimate for the propagation velocity of the wave in each section. A linear fit was made using a weighted least-squares regression, and the values calculated are shown in Table 5-5. The graphical representation of this fit is shown in Figure 5-29.

Region	Propagation velocity	Lower Bound	Upper Bound
2 to 12 metres	4.97×10^4 ms^{-1}	2.62×10^4 ms^{-1}	4.91×10^5 ms^{-1}
14 to 40 metres	1.03×10^6 ms^{-1}	5.49×10^5 ms^{-1}	8.29×10^6 ms^{-1}

Table 5-5: Propagation velocity measurements

These results suggest that the dominant propagation path between 2 and 12 meters, likely to be a lateral wave, propagates more slowly than the dominant wave beyond 12 meters, which is likely to be a trapped surface wave. This implies that the soil is composed of at least two layers with a more conductive layer above a less conductive layer, assuming that conductivity dominates the calculation of propagation velocity. This seems counter-intuitive, but the construction of the earth dam or the cold weather conditions during the field trial could both have caused these ground conditions.

Field trial three has shown that phase measurements, for the purposes of estimating propagation velocity, can be achieved in soil with low-frequency electromagnetic waves. This field trial has also provided results which appear to give support to qualitative expectations of the mathematical methods discussed in Chapter 4.

Is This Configuration Useful for Direction of Arrival Estimation?

Finally, the error in a DoA estimate made using this measurement configuration is calculated. Assuming a SNR of -1 dB (Figure 5-26) and the propagation velocities calculated above, the error for this configuration is shown in Figure 5-30. It can be seen that where propagation velocity is 5×10^5 ms^{-1} the error DoA estimate remains below 5 degrees where true DoA is below 39.5 degrees and the lower velocity wave dominates. This indicates that under certain conditions this configuration could be used for DoA estimation. However, where propagation velocity is 1×10^6 ms^{-1} usable DoA estimates are not possible. It is therefore vital to ensure that propagation velocity is known before utilising this configuration for a DoA estimate.

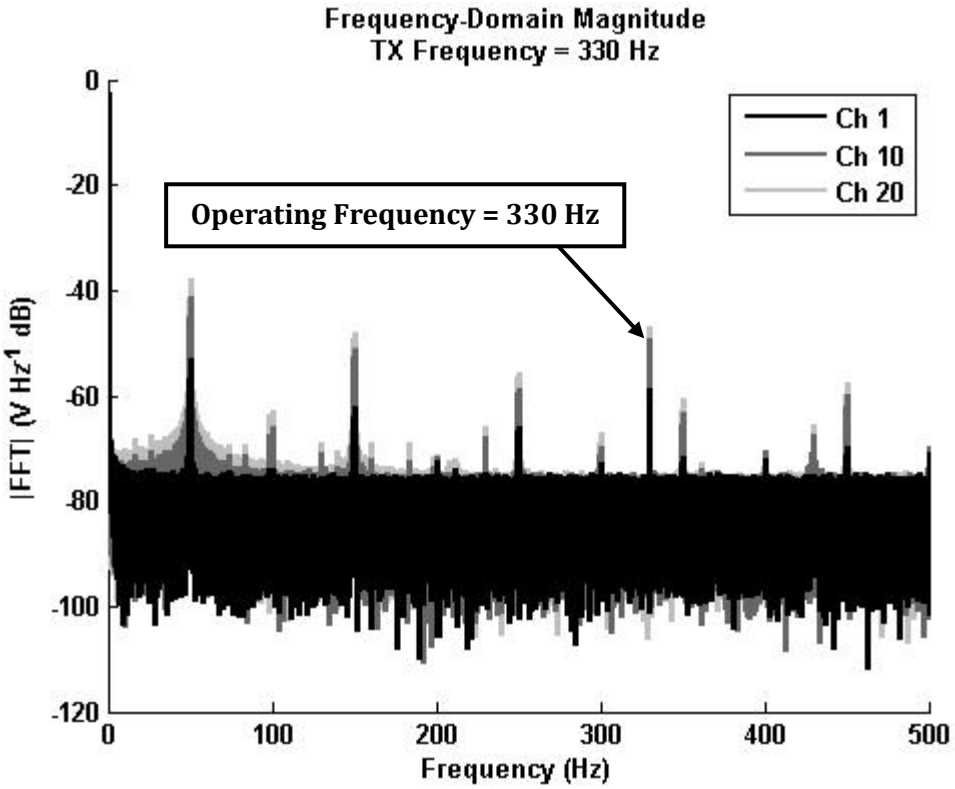

Figure 5-23: Frequency-domain measurements at Bristol test site. The

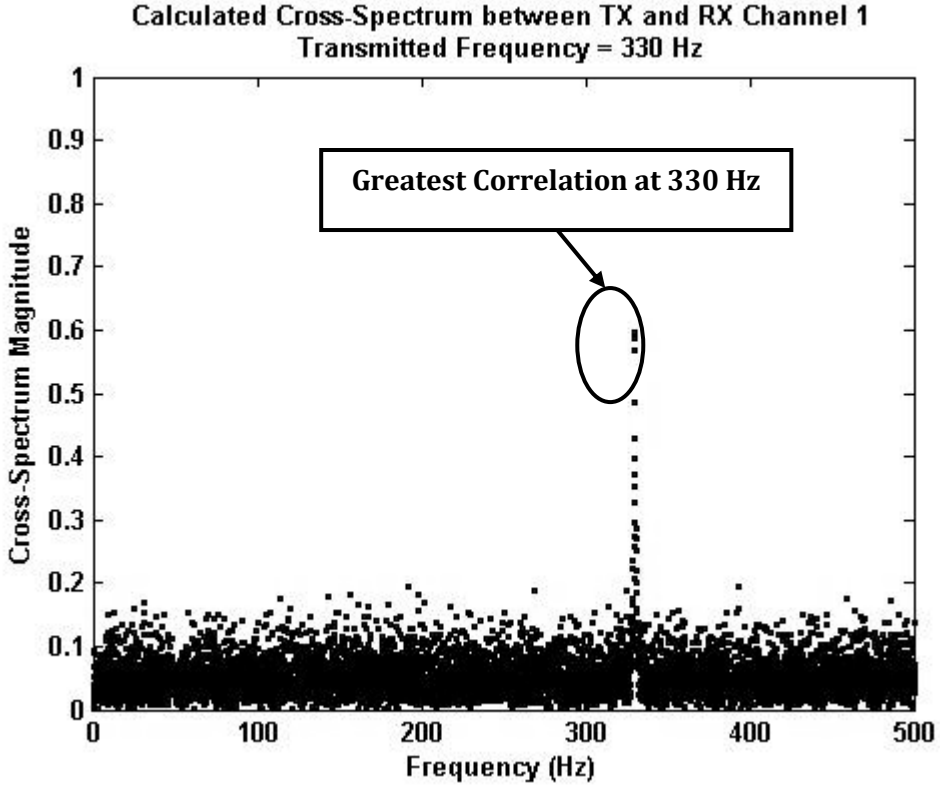

330

Figure 5-24: Cross-spectrum magnitude between the transmitted and received signal on channel 1 of the receive array. Good correlation is shown at the transmit frequency.

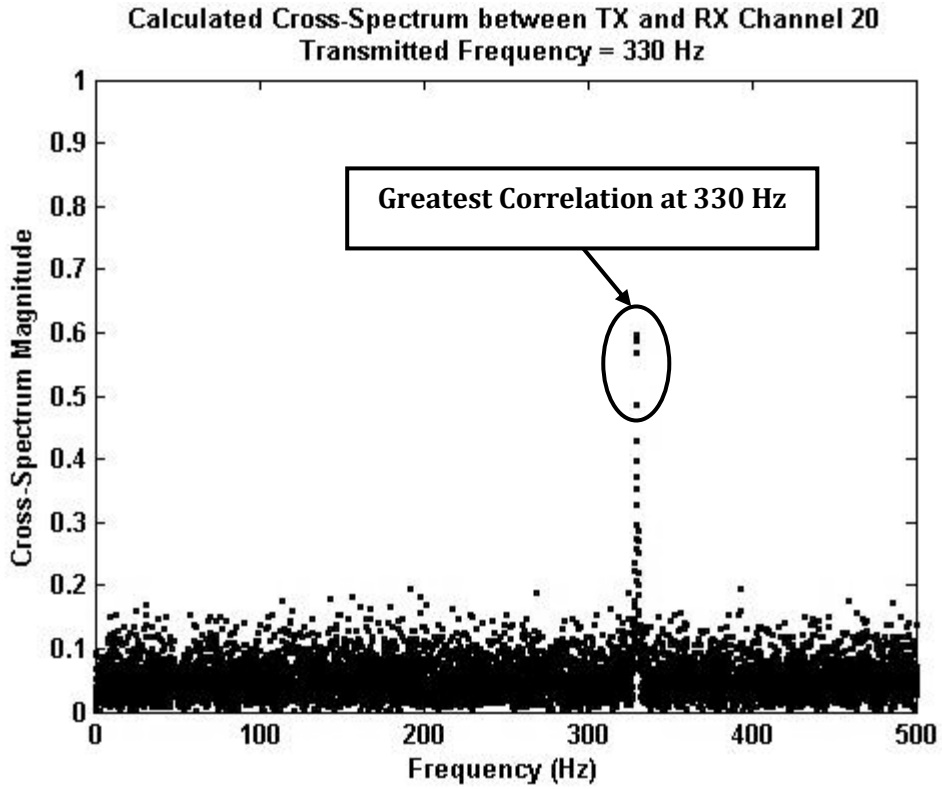

Figure 5-25: Cross-spectrum magnitude between the transmitted and received signal on channel 20 of the receive array. Good correlation is shown at the transmit frequency.

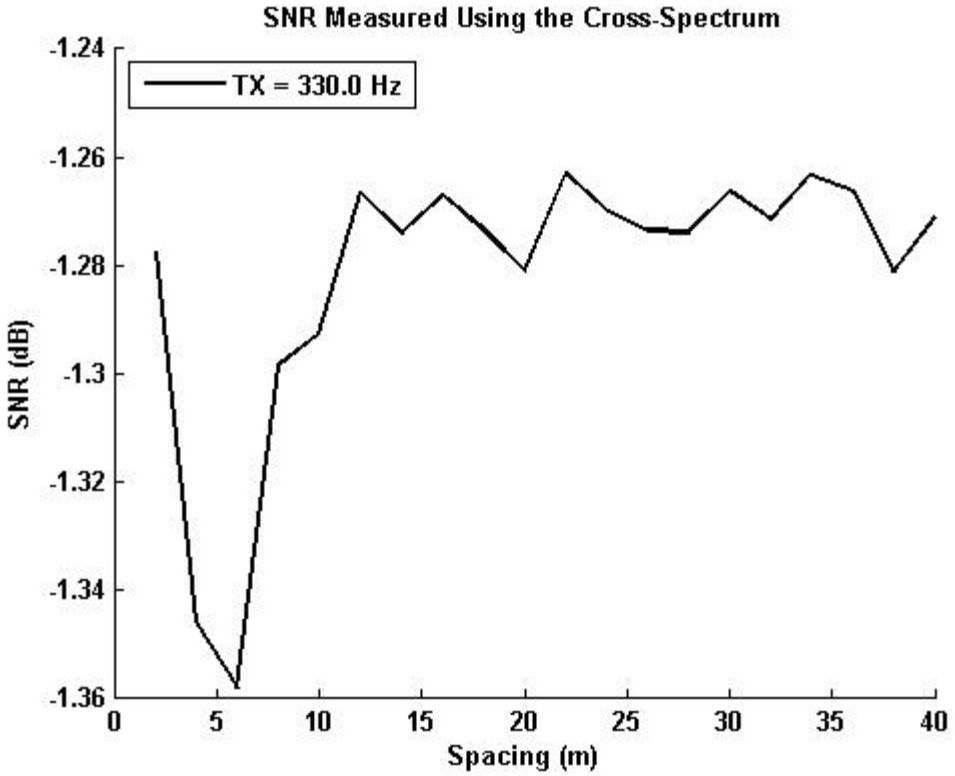

Figure 5-26: Measured SNR along the array, where transmit frequency = 330 Hz. The SNR is higher than in previous field trials, and is consistent at different receive channels.

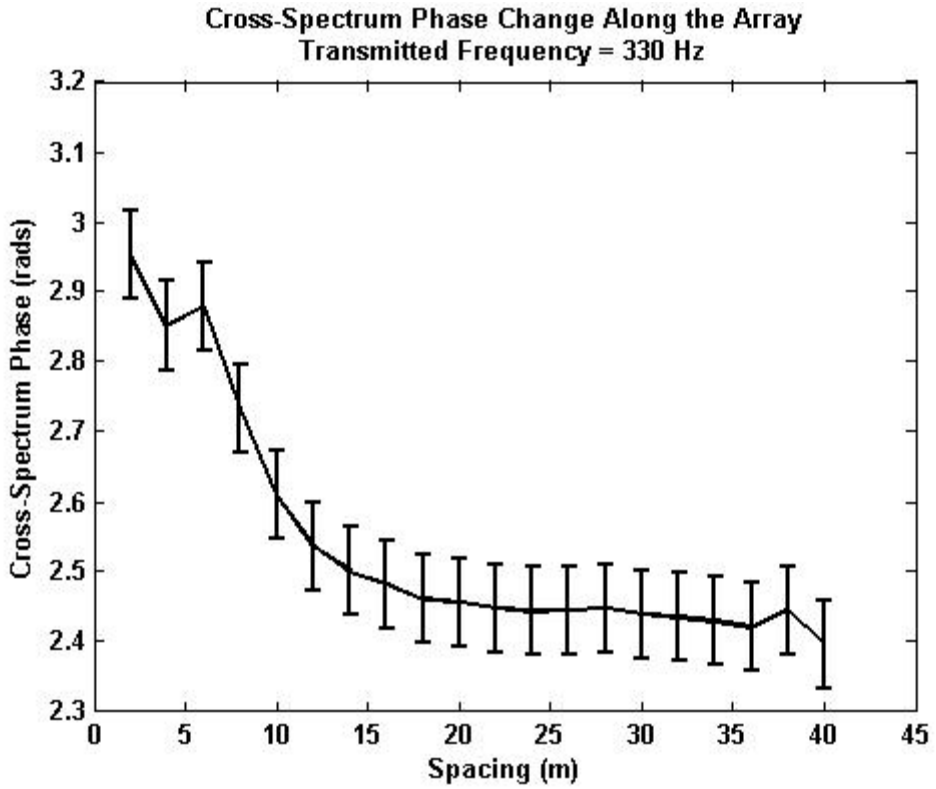

Figure 5-27: Measured phase along the receive array, where TX frequency = 330 Hz. The phase error is still too large for meaningful direction of arrival estimates.

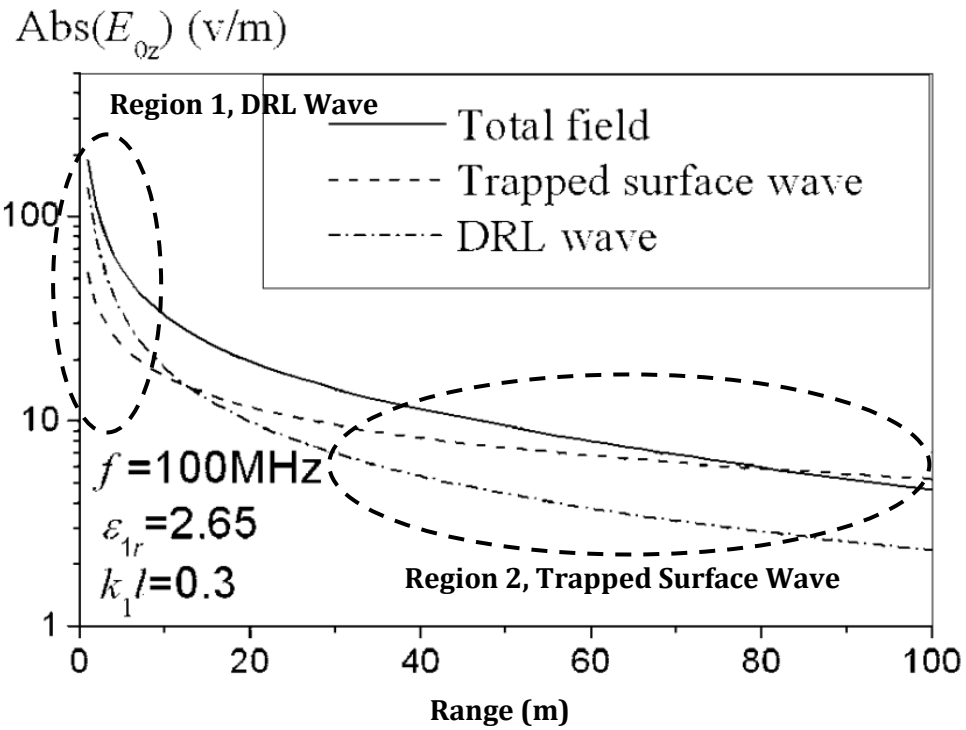

Figure 5-28: Electric field magnitude as a function of distance for a three layered media. The dominance of the trapped surface wave over the DRL wave at greater distances is clear (after Zhang and Pan, 2002) © 2002 by the American Geophysical Union

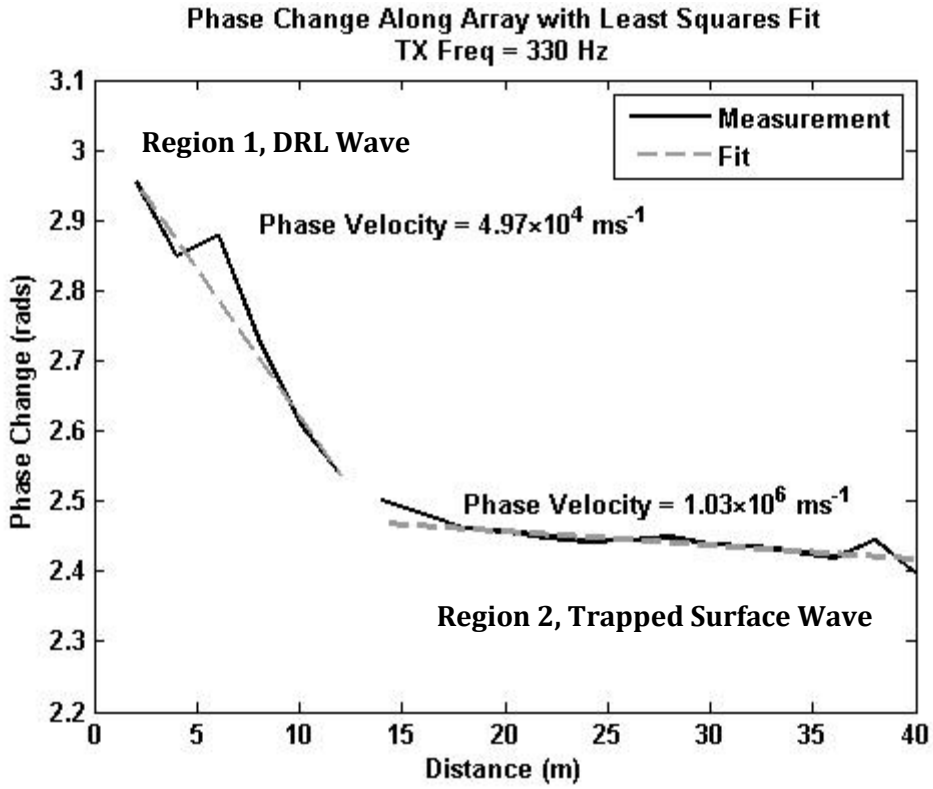

Figure 5-29: Phase change along the measurement array, where TX Freq = 330 Hz. A linear fit has been applied to the two distinct sections of the results.

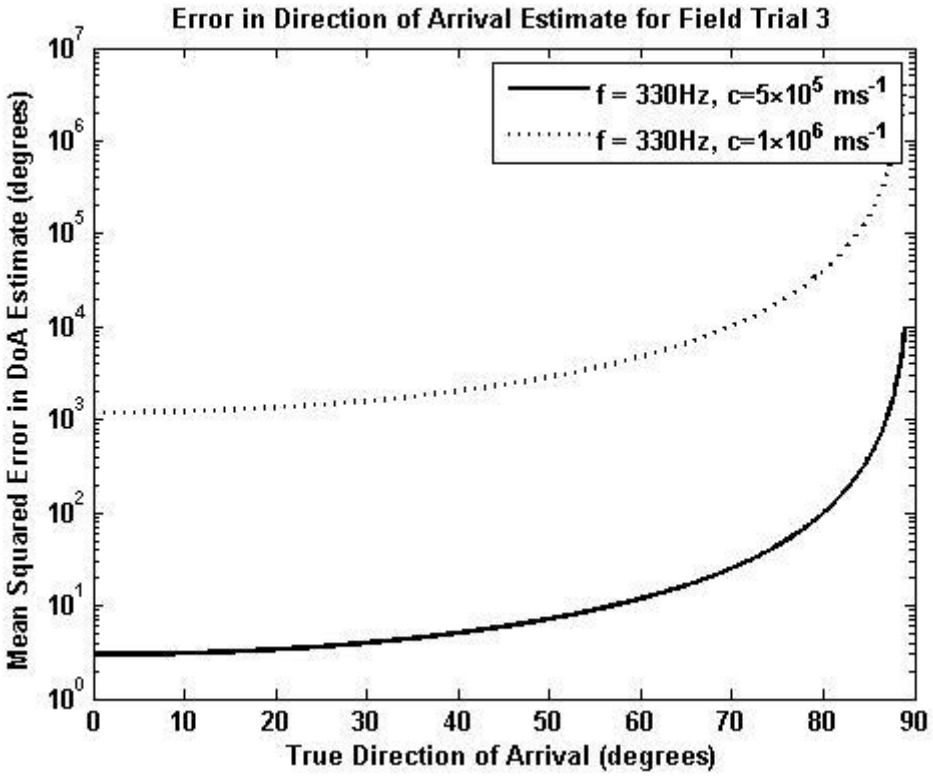

Figure 5-30: Direction of arrival estimate error, for the configuration used in field trial 3. Where propagation velocity = 5×10^5 ms^{-1} the expected error remains below 5 degrees up to a true DoA of 39.5 degrees.

5.5 CHAPTER SUMMARY

This chapter presented the results of three field trials, which attempted to record evidence of electromagnetic waves propagating at velocities low enough to allow measurement of their propagation velocity and direction of arrival.

Field trial 1 recorded passive measurements on a dam wall near Birmingham, UK. This measurement showed that signals of opportunity were present in the dam, but that measurement accuracy was insufficient to measure signal phase. An electric field value for the ambient noise was measured which informed the later field trials.

Field trial 2 recorded the results of low-frequency excitation within the dam wall. The field trial showed that the excited signal could be received at every point along the measurement array, with field magnitude being comparable to the ambient 50 Hz noise. Typical SNR values of 16 dB were recorded. This SNR was shown to be insufficient for measuring phase change or direction of arrival between array probes, for phase velocities of the order of 10^5 ms^{-1}.

Field trial 3 used the SNR information from field trial 2 and the formulae for phase change and measurement accuracy to devise the most sensitive configuration practicable. This configuration took measurements with very long duration, around 30 minutes per measurement. The transmission frequency was also increased to increase the expected phase change between array elements. Furthermore, it was hoped that the rural location would reduce ambient noise levels. The results strongly indicated propagation by multiple paths, as predicted by the theory of propagation in layered media, detailed in Chapter 4. The calculation for DoA error in this configuration indicated that it could be possible to make useful calculations (error < 5 degrees) where DoA is less than 40 degrees, and where the lower of the two propagation velocities dominates. Given the difficulty in validating these conditions, it is unlikely that this method will lead to useful results in a more realistic field trial.

These field trials have shown that low-frequency electromagnetic fields in soil can be excited and detected across a dam. Results which indicate that the waves were propagating via a number of

paths were reported in field trial 3; where the propagation velocity showed two distinct regions, conforming to the prediction made in Chapter 4 when considering a wave propagating in layered media. Phase accuracy is shown to be sufficient for a direction of arrival estimate under certain conditions. However, the difficulty in confirming these conditions makes the method unrealistic for measurements without the facility to rigorously measure the propagation velocity.

CHAPTER 6: MEASURING PIPE LOCATION USING IN-PIPE EXCITATION

6.1 INTRODUCTION

This chapter describes the second part of the field-work undertaken for this thesis. The work described here sought to explore the potential for using in-pipe excitation at low-frequencies to detect buried utilities by measuring the resulting electric-field magnitude. A detailed hypothesis is given below.

The work undertaken in Chapter 5 showed that low-frequency signals can be detected at distances of up to 40 metres from an excitation source. However, Chapter 5 also showed that accurate phase information cannot be readily recovered from signals propagating in the ground. By focussing on the magnitude of the electric field, at different spatial positions, it was hoped that the position of the pipe could be determined.

This chapter is structured as follows: The hypothesis under investigation is stated, followed by a review of the state-of-the-art as it relates to this work. Simulation results are then presented which inform the design of the experiment. The experimental design is then given, with sufficient detail to repeat the measurements, measurement results are then presented and discussed.

6.2 HYPOTHESIS

If phase measurements are not practical then an in-pipe excitation may be detected at the surface using magnitude measurements. The largest field magnitude would be present directly above the pipe, showing the location of the buried utility. This method relies on:

1. Reliable detection of the electromagnetic field at the surface.
2. The signal propagating most efficiently to the closest point at the surface.
3. A measurement technique which allows fast enough measurement that a test-site can be measured over a short time period. Therefore, soil conditions will not change so radically as to alter the results, and a measurement will be practical to undertake.
4. Sufficient spatial resolution to discern the pipe location from measurement results.

A block diagram of the expected measurement configuration is given in Figure 6-1.

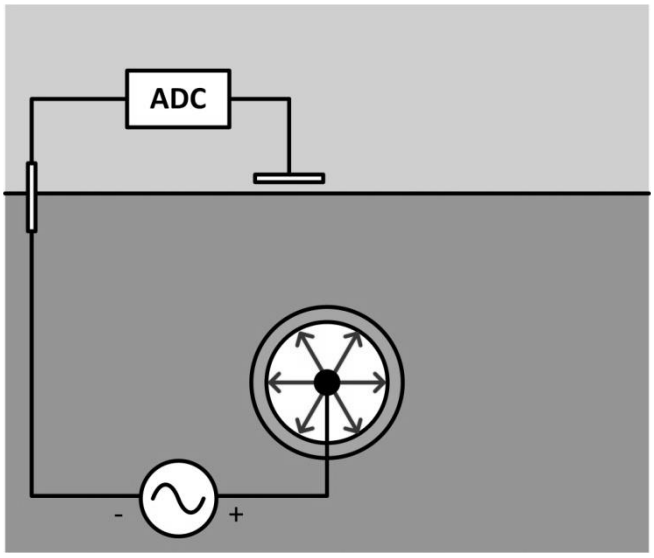

Figure 6-1: Sketch of the measurement configuration

6.3 FACILITATING SCIENCE

This section describes the science relevant to the field trial being undertaken. It is split into sections concerning the signal excitation, and signal propagation. The required background concerning measurement equipment was given in Chapter 2.

6.3.1 Signal Excitation

6.3.1.1 Theoretical Basis

The techniques for exciting electromagnetic waves at radio-frequencies have been extensively researched in the form of antenna theory. Good introductions to this subject can be found in a large number of text books (King and Smith, 1981; Kraus, 1988). However, in the low frequency-range studied here much of the complexity is removed by the electrostatic approximation. The electrostatic approximation relies on negligible variation with time which removes the interdependence between electric and magnetic fields; reducing Faraday's Law to (6-1) (Paul and Nasar, 1987):

$$\nabla \times \boldsymbol{E} = 0 \qquad (6\text{-}1)$$

The fields excited during this work had frequency greater than 0 Hz, so had a time-dependence. However, a quasi-static assumption can still be applied and, within limitations, gives good results. An appropriate example of this technique is given by Grcev and Grceva (2009), who calculated the current induced on two buried wires using the method of moments. Citing the classic works by Wait (1989) and Harrington (1993), Grcev and Grceva (2009) state the limitations of the quasi-static approximation as:

$$|k_1 r_1| \ll 1 \tag{6-2}$$

$$r_1 < \frac{\lambda}{10} \tag{6-3}$$

Where k_1 is the wavenumber of the material and r_1 is the range Equation (6-2) is often described as:

$$|k_1 r_1| \leq 0.1 \tag{6-4}$$

The range dependence in (6-2) - (6-4) is present due to the assumption in the quasi-static approximation that the system is in equilibrium at all times. This equilibrium is only possible if changes in the system can be assumed to occur instantaneously. Therefore, the assumption is invalidated by long ranges over which this cannot be true (Zangwill, 2013).

These limitations are illustrated graphically, for typical values of ground conductivity in Figure 6-2. Grcev and Grceva (2009) also showed results for the induced current on buried cables with good agreement between a quasi-static solution and a full-field solution at 100 kHz. These results give strong support to the use of a quasi-static model to predict the measured field. It will be noted that the two limitations described are subtly different, this is due to the increased tolerance required for analyses such as the method-of-moments. This increased tolerance has caused researchers to move from the fundamental limitation given by (6-2) to the slightly altered form given by (6-3) (Grcev and Grceva, 2009).

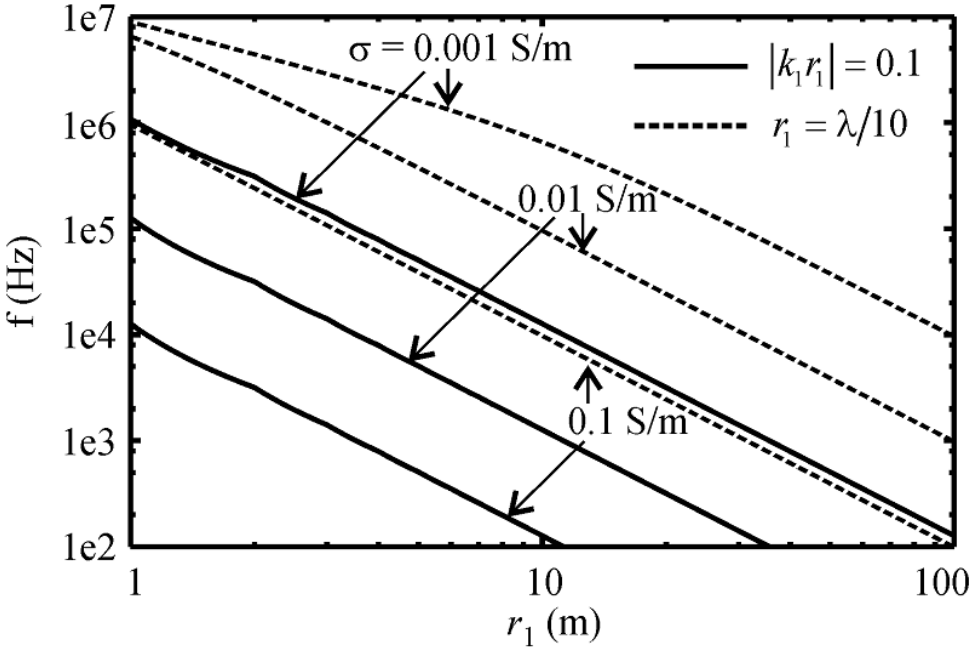

Figure 6-2: Limits of the quasi-static assumption for different ground conductivities (after Grcev and Grceva, 2009) © 2009 IEEE

6.3.1.2 Predicted Field

The electric-field excited by a voltage applied to a cable in the centre of a hollow, air-filled pipe with grounded walls, is easily predicted using the electrostatic approximation. The more complex situation where the ground point is offset is considered in the following section. Following Paul and Nasar (1987):

$$E = \frac{V}{r \ln\left(\frac{b}{a}\right)} \tag{6-5}$$

Where V is the voltage between the source and the grounded outer conductor, r is the radial distance from the centre axis, a and b represent the radial position of the inner and outer conductors, respectively.

6.3.1.3 Practicalities

The process of exciting a low-frequency electromagnetic wave from within a pipe has a number of associated practical difficulties. Physical access to the pipe must be obtained, this has been achieved by using pipes at test-sites, but for live sub-surface utilities would represent a logistical challenge: A cable must be inserted into the pipe, the cable must have enough stiffness to be

confident that it is moving along the pipe, but be flexible enough to enter and follow the pipe. Finally, it is impossible to know the exact radial position of the conductor, although when considering the unknown properties of the surrounding soil this does not significantly add to the measurement uncertainty.

6.3.2 Signal Propagation

Having excited an electric field within the pipe, it is crucial to understand the mechanisms which allow it to propagate to the receiving equipment.

6.3.2.1 Analytical Methods

Consider a cylindrical, hollow, air-filled, pipe with grounded walls and a line of charge at its centre. Considering Gauss' Law, and the constitutive equation where polarization is neglected (Paul and Nasar, 1987):

$$\nabla \cdot \vec{E} = \rho/\varepsilon \tag{6-6}$$

By defining the boundary conditions, this model can be extended to one where the pipe walls, and a homogenous soil are included, particularly if the geometry is considered cylindrical, with a grounded outer radius. However, when taking a measurement relative to single distant point with a flat surface plane, the cylindrical assumption becomes impractical. Consequently, the predicted field results were generated using finite-element modelling software which made use of the electrostatic approximation (COMSOL, 2013).

The final analytically derived point to consider is the difference between a measured point-voltage and a measured dipole-voltage due to an electric field, predicted using the quasi-static approximation. Expressions are easily derived which show that the measured voltage using a dipole is proportional to $1/r^3$ whereas a point voltage has a dependence on $1/r^2$ (Paul and Nasar, 1987, pp. 103-104). When making field measurements, a dipole method will suffer significantly greater field-magnitude degradation, with increased distance, than a point voltage.

6.3.2.2 Numerical Methods

The expected field is predicted by making use of the electrostatic approximation. An analytical solution is possible, given the cylindrical nature of the excitation. However, the following figures have been produced using the COMSOL finite-element modelling software package (COMSOL, 2013). This has the advantage of being able to model a multitude of different scenarios quickly, presenting the results in different graphical representations, without relying on the cylindrical coordinate system.

The following results demonstrate a qualitative expectation of the measurable field due to in-pipe excitation, but the uncertainty in the soil conditions means that the magnitude cannot be reasonably predicted. Furthermore, the inhomogeneity of the soil mean that localised variation of soil-conditions will change the field properties for small areas of the measurement.

Two scenarios have been computed and are shown in the figures below. Both results are shown as plan views of a 3D simulation, therefore field lines at different depths are overlaid. The first scenario (Figure 6-3) is that the ground is a perfect dielectric; the electric field lines are plotted radially from the 0 V reference point expanding to become linear near the excitation within the pipe. The second scenario (Figure 6-4) is that the ground is sufficiently conductive to negate the position of the 0 Volt reference point; this scenario is modelled by letting the edges of the simulation, parallel to the pipe, become a 0 Volt reference to simulate an infinite geometry. In this scenario, the electric field lines are plotted parallel to the in-pipe excitation. The true field will be a superposition of these two scenarios, with the relative weighting determined by the attenuation of the soil between the in-pipe excitation and the 0 Volt reference point. Given the non-stationary, unpredictable, nature of soil that was outlined in Chapter 2, a reliable simulation has not been possible.

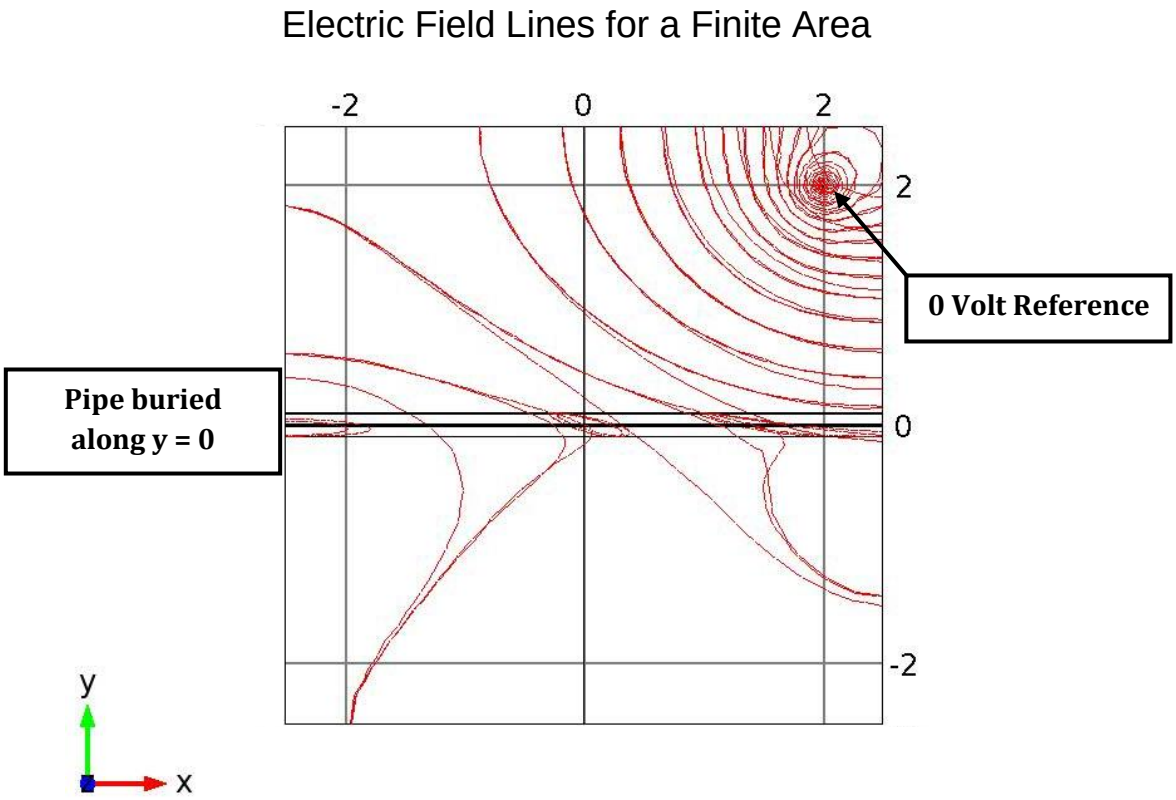

Figure 6-3: Plan view of electric field lines (in red) in a 3D simulation. An antenna is present in a buried pipe at y = 0 with a 0 V reference point present on the surface at x = 2, y = 2. The field lines are seen converging radially on the 0 V reference, becoming more linear towards the in-pipe excitation.

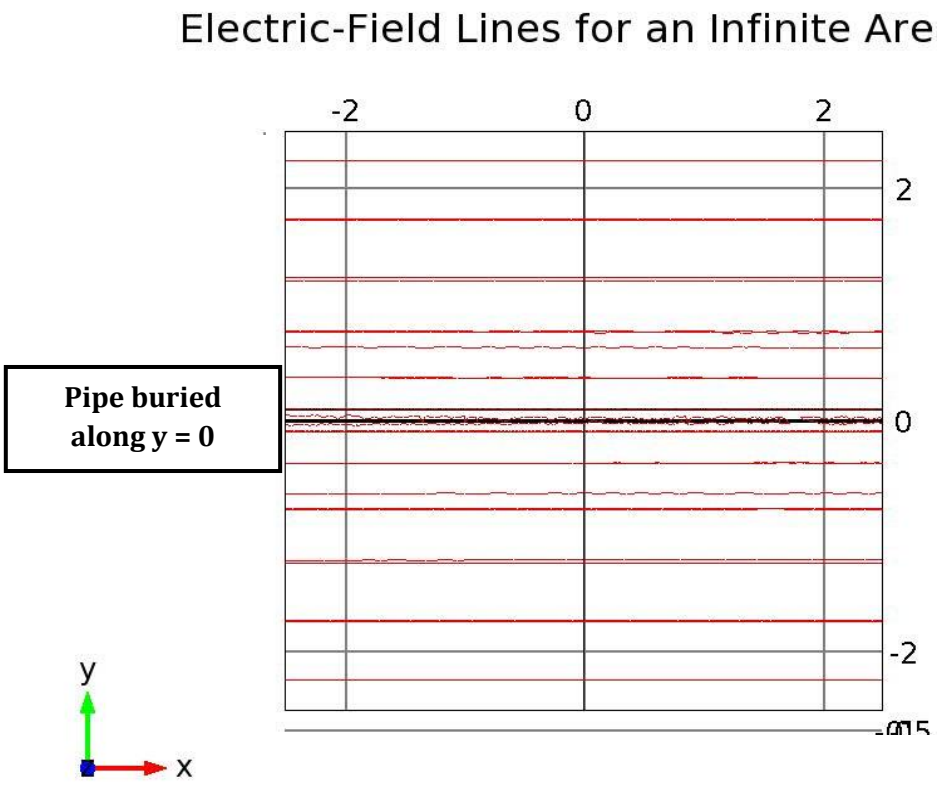

Figure 6-4: Plan view of electric field lines (in red) in a 3D simulation. An antenna is present in a buried pipe at y = 0 and the electric field lines radiate linearly from this pipe. In this simulation the 0 V reference point is the upper and lower edges of the geometry to simulate a 0 V reference being neglected by highly attenuating soil.

6.3.3 Signal Measurement

It was decided that capacitively-coupled probes were the best method for measuring signals during this field-trial. This allowed a significant reduction in the time required for equipment set up, and ensured that measurements were possible on hard surfaces. Capactively-coupled sensors have been used for low-frequency measurements in the past. A good review was given by Kuras *et al.* (2006) who derived the theoretical basis for a four-pole resistivity measurement using capacitive-plates, and experimentally verified the results. This method has since been used for resistivity surveys, Foo *et al.* (2010) showed results from a resistivity survey using capacitive-plate sensors, and showed that coherent results were possible at frequencies which are not harmonics of 50 Hz.

6.4 Field Trial Method

6.4.1 Field Trial Location and Physical Configuration

The field trial was conducted on a test-site in the north-west of England. The site consists of a number of buried utilities, in a variety of configurations and at varying depths, including pipes into which cables may be inserted. The results presented below were taken on a portion of the test-site with a single pipe buried at a depth of approximately 30 cm, with a grassy surface. The soil surrounding the pipe is separated into three bays with clay, granular, and rubble based soil. Due to commercial confidentiality, it is not possible to reproduce maps showing ground truth at the test-site; a sketch is given in Figure 6-5 which indicates the layout sufficiently well. Note that the excitation cable was inserted to a point 6 metres from the edge of the measurement area, this allowed examination of the field at the end of the excitation.

Figure 6-6 shows a measurement in progress, within a measured grid, and the transmitting equipment in the background, connected via the 0 V connection which was not allowed to touch the ground. Similarly, Figure 6-7 shows a measurement in progress on the grassed section of the test-site, the Mapping the Underworld acoustic sensor is also being tested.

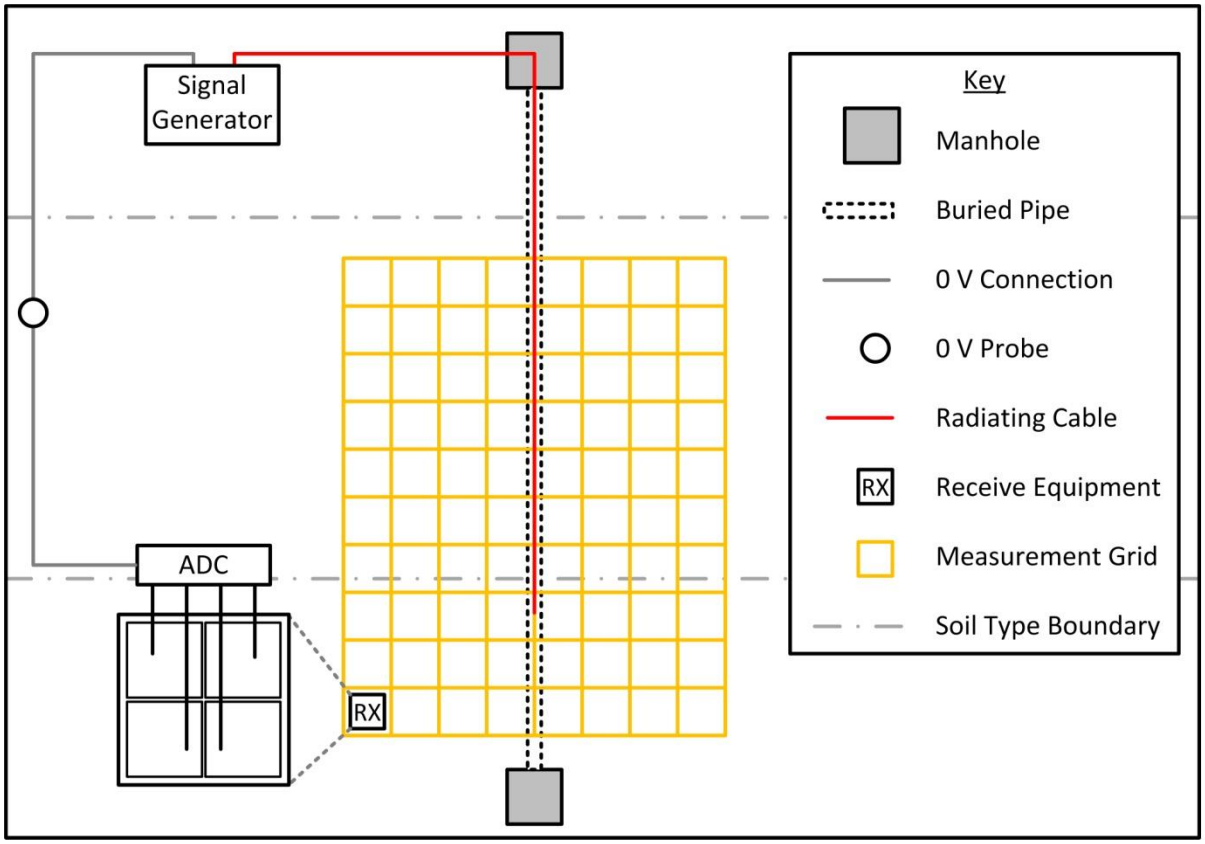

Figure 6-5: Sketch of the physical layout of the test-site.

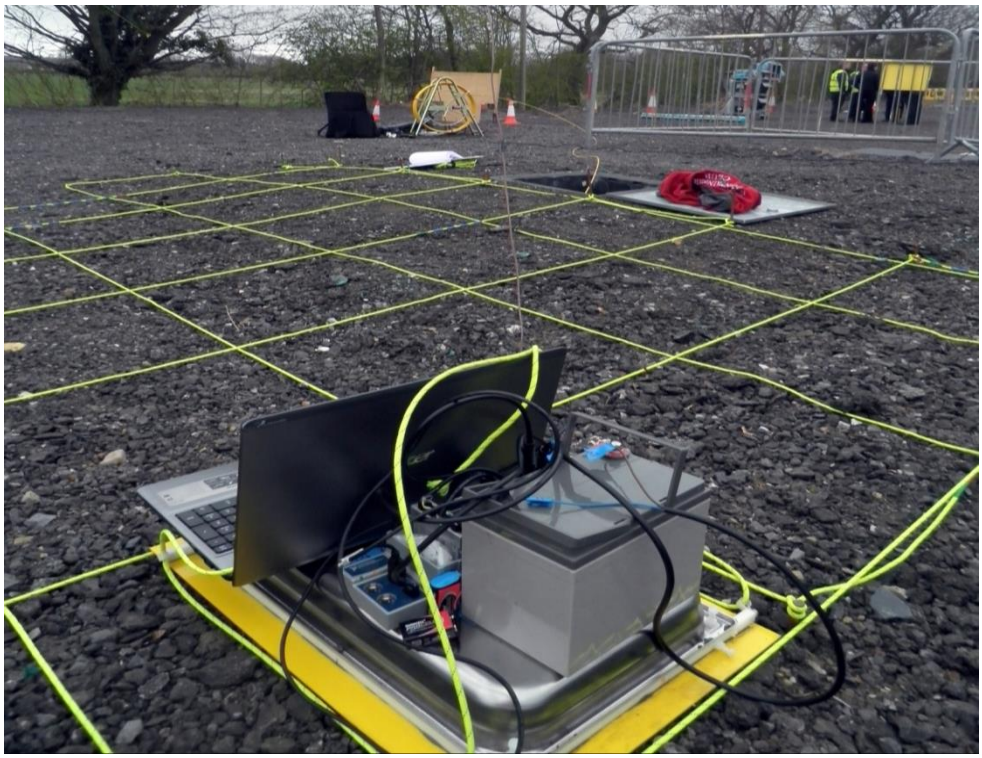

Figure 6-6: Field trial equipment. The controlling laptop, ADC with its battery, and the earth-shielded capacitive-plates are in the foreground, on the marked grid. The connecting earth wire can be seen, with the exciting cable shown entering the manhole, and the transmitting equipment in the background.

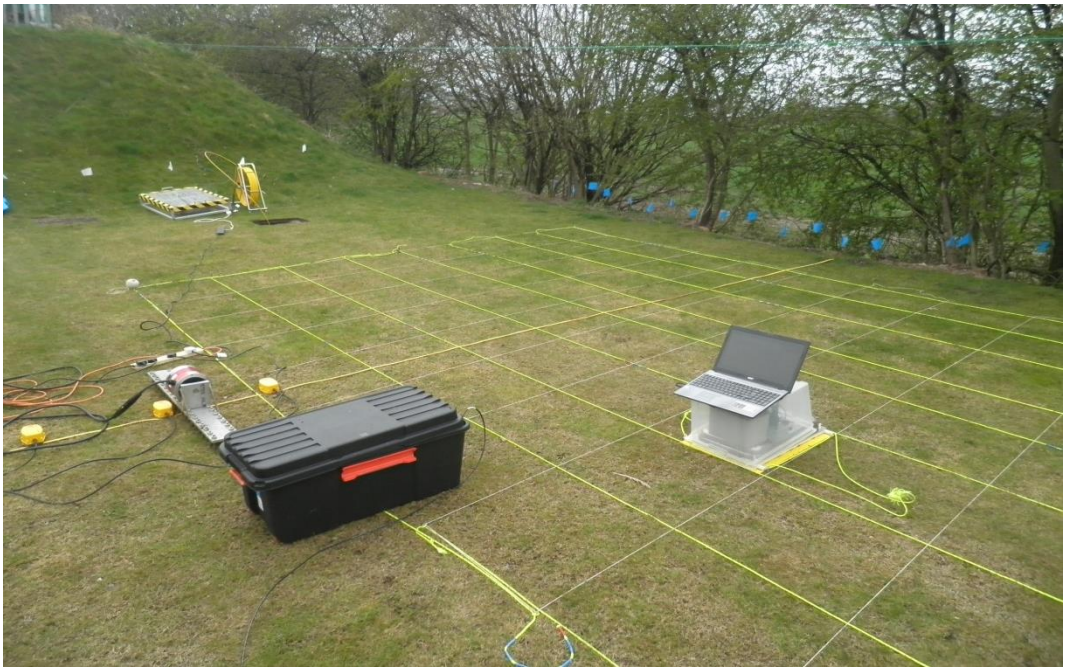

Figure 6-7: Measurement under way on the grassed section of the test-site, the measurement grid is visible, with the transmitting equipment in the background.

6.4.2 Measurement Equipment

In order to measure voltage at a large number of spatial locations it was decided to use capacitively coupled sensors rather than buried probes. This decision results in lower certainty in spatial position, and requires additional amplification, but allows faster movement around the test site and gives more consistent contact with the ground. A block diagram showing the measurement setup is shown in Figure 6-8.

Four capacitive sensors were used to measure voltage at each spatial position. Each capacitive-plate was connected, via a high-impedance charge amplifier (Texas Instruments OPA129), to a 24-bit analogue-to-digital converter (ADC). The ADC used was a National Instruments NI9239 (National Instruments, 2012) 24-bit, four channel module, running at a sampling rate of 50kHz. The ADC module was mounted in a National Instruments NI9178 chassis connected to the controlling laptop via USB 2.0 (National Instruments, 2011). The capacitive-plates were mounted on a single sheet of acrylic to give consistent relative-permittivity and spacing between the plates and the ground. An earthed metal shield was also mounted around the capacitive-plates and charge amplifiers, to reduce interference. The 0 V reference was provided by a probe inserted

into the ground at a distance from the measurement site, the following connections were made to that 0 V reference:

- Earthed shield surrounding capacitive-plates and charge amplifiers.
- Negative terminal of each ADC channel.
- 0 V terminal of the battery powering the ADC module.
- 0 V terminals of the charge amplifier circuits.
- Negative terminal of the signal generator providing the in-pipe excitation.

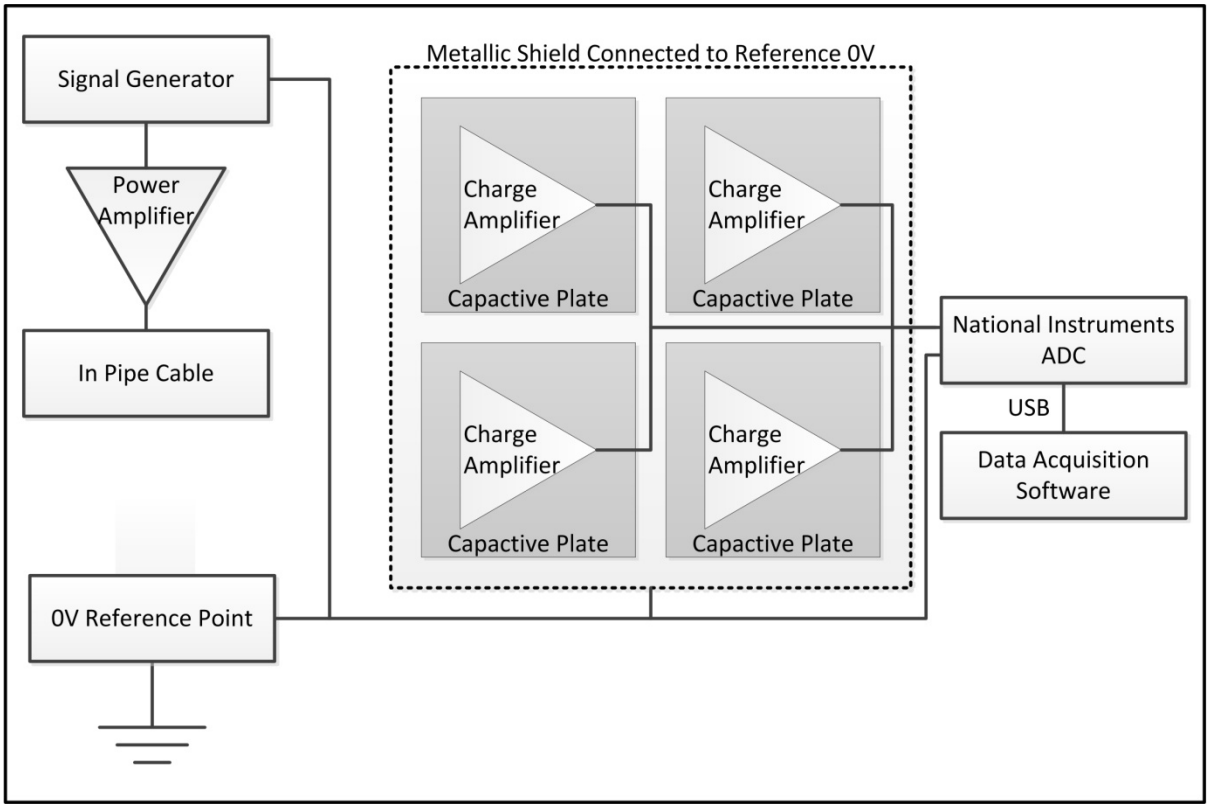

Figure 6-8: Block diagram of the measurement system used to measure electric field magnitude due to in-pipe excitation.

A number of options exist for controlling data-acquisition using these National Instruments modules. In these trials, bespoke software was written in C# using the Microsoft .NET Framework. The bespoke software controlled the National Instruments equipment, and wrote the acquired data to text files with a small amount of additional information including spatial position, time, and transmit frequency. The software interface used is shown in Figure 6-9.

The following configuration was used for each measurement:

- 50 kHz sampling rate.
- 2^{16} samples per measurement, giving a measurement time of 1.31 s.
- 24-bit measurements with a range of ± 10 V, giving a maximum resolution of 1.2 μV.

6.4.3 In-Pipe Excitation

The in-pipe excitation was accomplished using a plastic rod with a twisted pair of cables inside. This was the best solution found to overcome the physical challenges outlined above, and its entrance to the pipe is shown in Figure 6-10.

It was decided to apply a sinusoidal signal to the cable, given the required number of spatial measurements, a stepped-frequency approach was deemed to require a prohibitive amount of time. Furthermore, by utilising a single frequency it was possible to select a frequency with minimal interference by measuring the electric-field prior at the start of the field-trial.

A previous field trial on this site had shown that in the frequency range up to 20 kHz, the measured signal magnitude increased with frequency, this fits with the circuit theory view of the pipe wall as a purely capacitive element in the propagation path. Consequently the frequency transmitted was chosen to be around 16 kHz, with the specific frequency chosen to avoid interfering signals. This was chosen to coincide with the highest frequency with approximately 0 dB gain in the ADC receiver circuitry (National Instruments, 2012).

A laboratory-grade signal-generator was used to generate the sinusoidal signal, this was connected through an audio-band power amplifier which increased the signal voltage from ±10 V to around ±25 V and gave greater capacity for delivering current.

Using (6-2) and (6-3) it is possible to confirm that the quasi-static approximation is valid in this case.

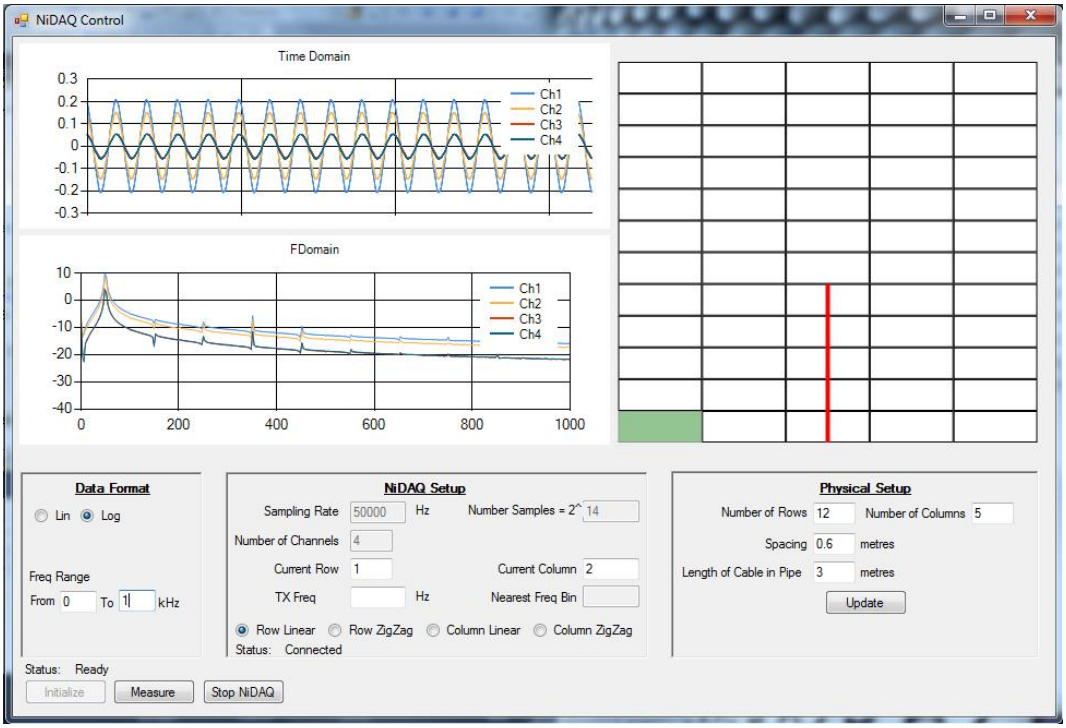

Figure 6-9: Control interface used in the in-pipe excitation field trials, in this test the 50 Hz ambient noise is clearly visible in time and frequency-domains.

Figure 6-10: Excitation cable entering the buried pipe, a tight corner required a flexible cable, but roughness within the pipe required a degree of rigidity. The blue valve controlled access to the pipe.

6.5 FIELD TRIAL RESULTS

6.5.1 Calibration

Once the field trials were complete, calibration measurements were taken to ensure the gain in the signal path was equal for all channels, at the measurement frequency. The measurement equipment was placed on a large metallic sheet, which extended at least 1 metre in all directions from the measurement equipment. The metal sheet was excited with a sinusoidal signal at the field-trial transmission frequency, with peak-to-peak voltage of 20 Volts. The resulting measurement was used to calculate a gain factor that was applied to each channel before the remaining results were calculated.

6.5.2 Single-Channel Results

The measurements described above resulted in four channels of time-domain data, for each spatial location. The first stage of analysis was to plot the frequency-domain magnitude, at the transmitted-frequency, for each spatial position. A flat-top window function was applied to the time-domain data, and an FFT was then computed. The frequency-domain magnitude at the transmitted-frequency is plotted, the validity of the frequency plotted was tested by ensuring it represented a local maximum. Results are shown in Figure 6-11 to Figure 6-14. There is an indication in some of the data presented in Figure 6-11 to Figure 6-14 of a linear peak which corresponds to the pipe position. However, the low spatial-resolution makes this conclusion difficult to support.

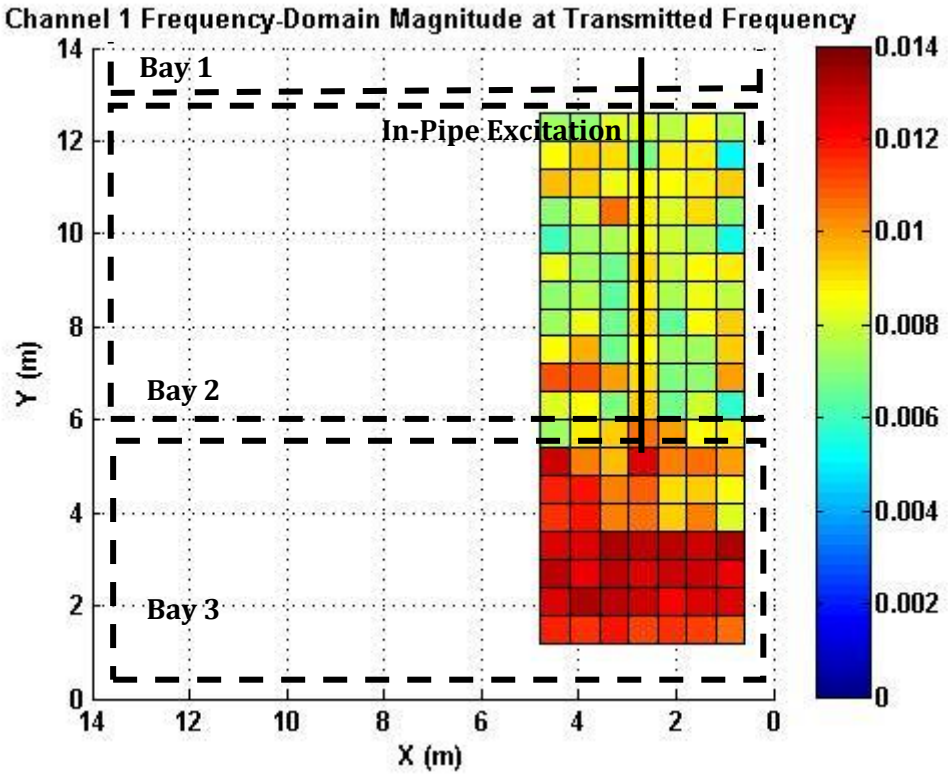

Figure 6-11: Frequency-domain magnitude on channel 1 at the transmitted frequency, calculated using an FFT of windowed time-domain data. A sketch of the ground truth is overlaid.

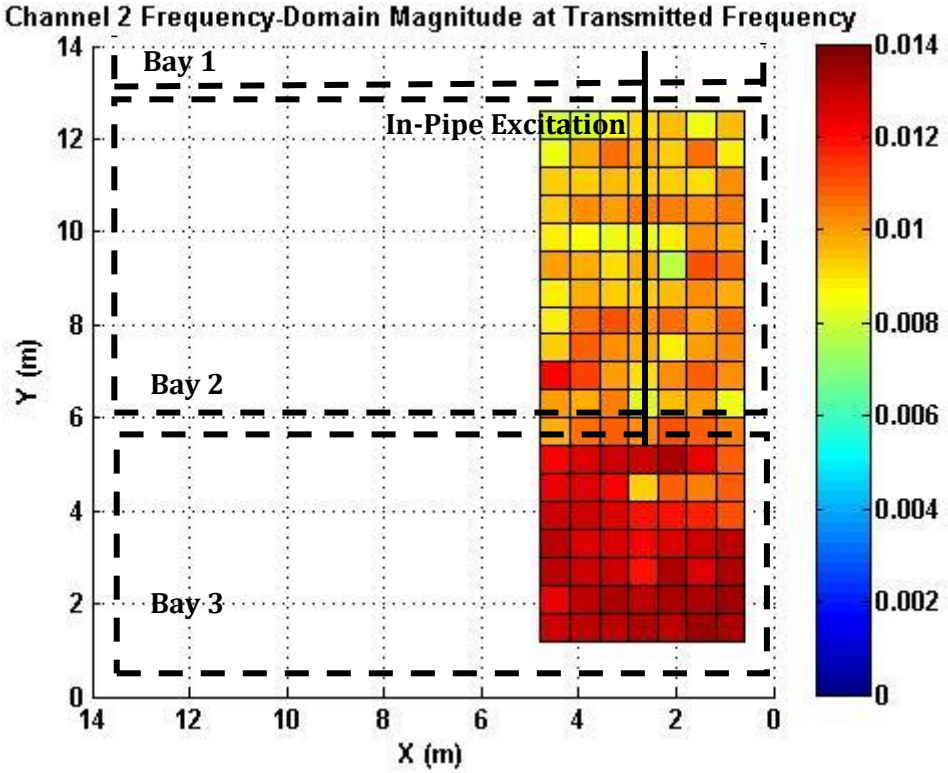

Figure 6-12: Frequency-domain magnitude on channel 2 at the transmitted frequency, calculated using an FFT of windowed time-domain data. A sketch of the ground truth is overlaid.

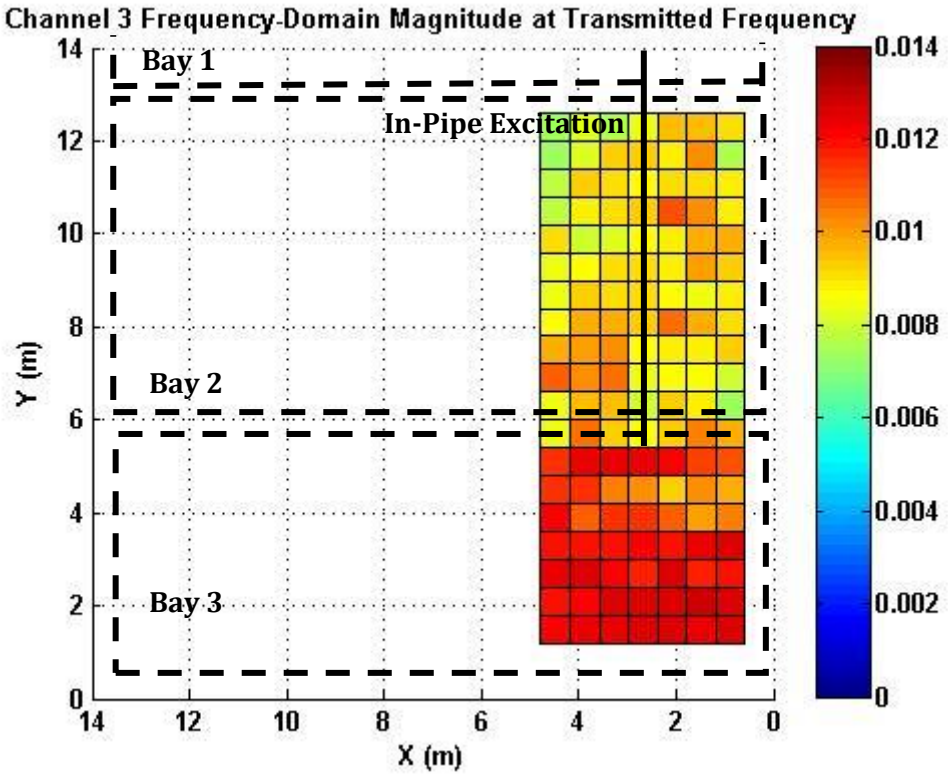

Figure 6-13: Frequency-domain magnitude on channel 3 at the transmitted frequency, calculated using an FFT of windowed time-domain data. A sketch of the ground truth is overlaid.

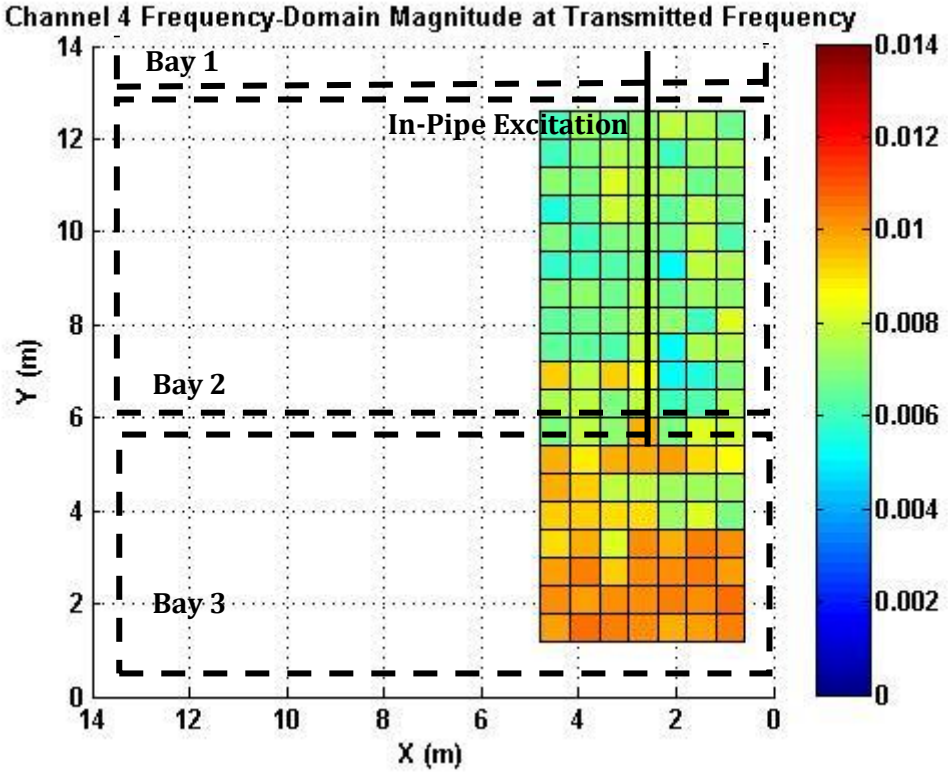

Figure 6-14: Frequency-domain magnitude on channel 4 at the transmitted frequency, calculated using an FFT of windowed time-domain data. A sketch of the ground truth is overlaid.

6.5.3 Spatially-Filtered Single-Channel Results

In order to increase the precision of the results, it was decided spatially interpolate the results shown in Figure 6-11 - Figure 6-14. To achieve this filtering, each element in the result matrices - shown in Figure 6-11 - Figure 6-14 - was replaced with a 4×4 matrix whose values were the same as that of the original element. A two dimensional, 16-point moving average filter was then applied – implemented using the common convolution method (Smith, 2003).

Results are shown in Figure 6-15 to Figure 6-19. Figure 6-15 to Figure 6-18 are shown on the same scale to ease comparison. However, this masks the results in the case of channel 4, which is reproduced with a more appropriate colour scale in Figure 6-19.

The data for channel 1 and channel 4 show a noticeable peak which corresponds well to the pipe position; this is not well supported by channels 2 and 3. Several regions of high signal magnitude are shown in a number of figures. The origin of these, apparently erroneous, results is discussed in section 6.5.6. In all cases, the 0 V reference point was located at Y = 6 m, X = 12 m.

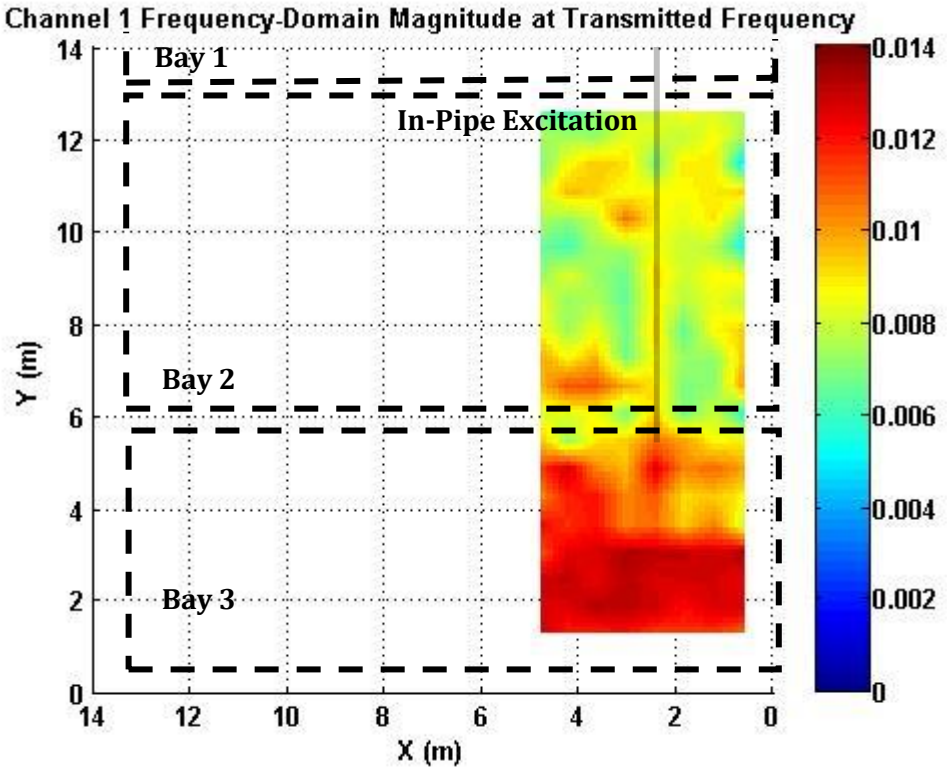

Figure 6-15: Frequency-domain magnitude for channel 1, calculated in the same way as Figure 6-11 but with a moving average filter applied to spatially-oversampled data. A peak is shown consistent with the pipe location. A sketch of the ground truth is overlaid.

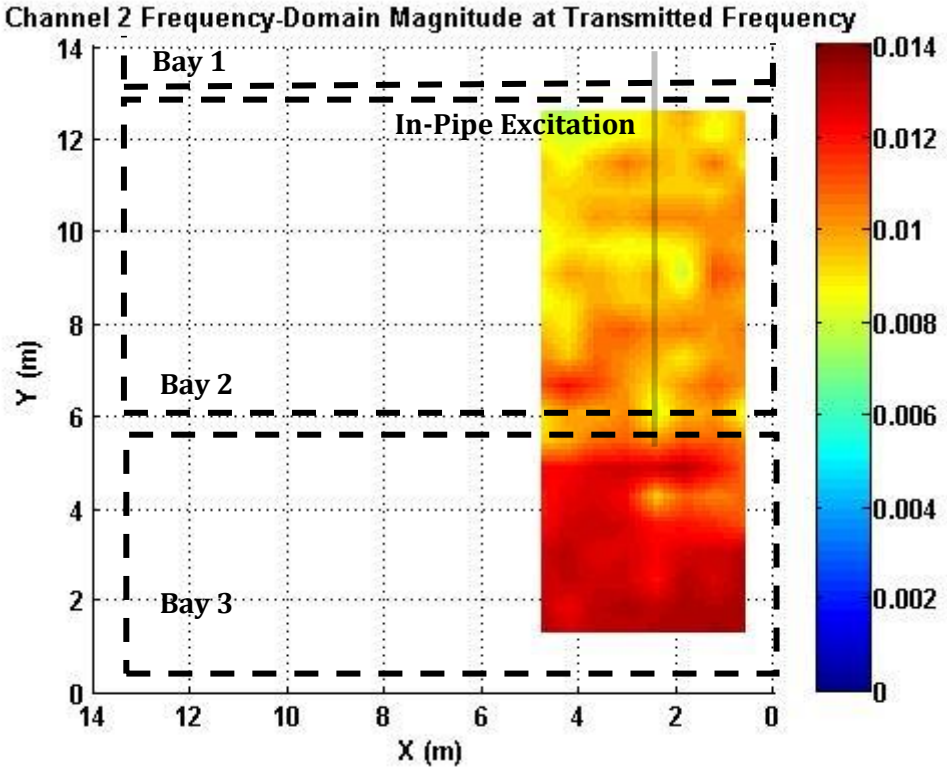

Figure 6-16: Frequency-domain magnitude for channel 2, calculated in the same way as Figure 6-12 but with a moving-average filter applied to oversampled data. The field is not consistent with the known pipe location. A sketch of the ground truth is overlaid.

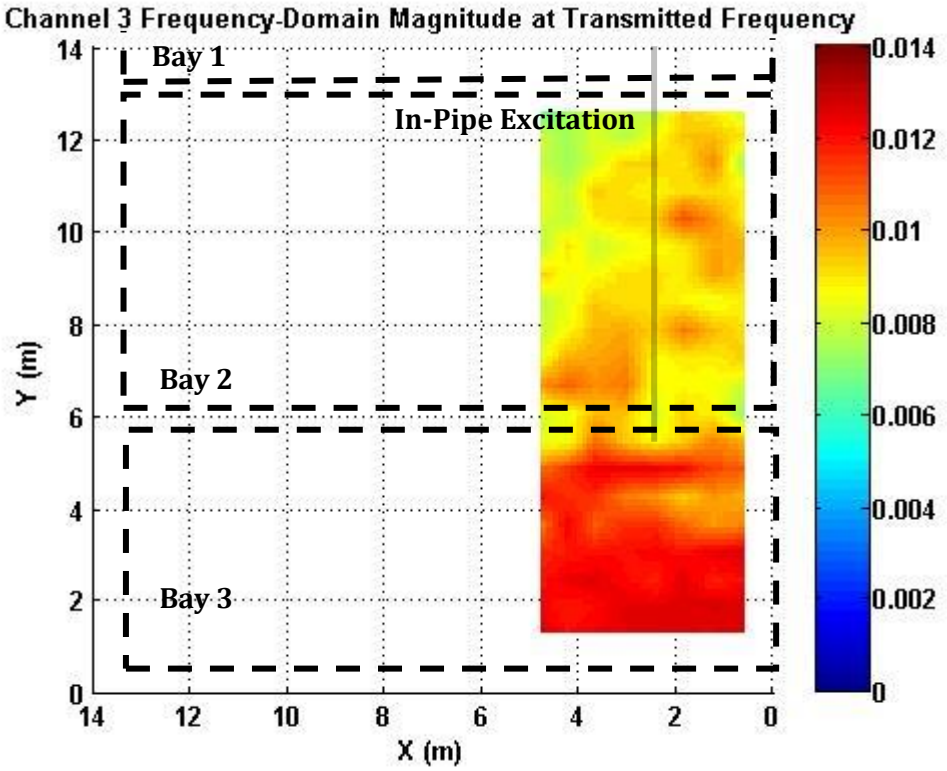

Figure 6-17: Frequency-domain magnitude for channel 3, calculated in the same way as Figure 6-13 but with a moving-average filter applied to oversampled data. The field is not consistent with the known pipe location. A sketch of the ground truth is overlaid.

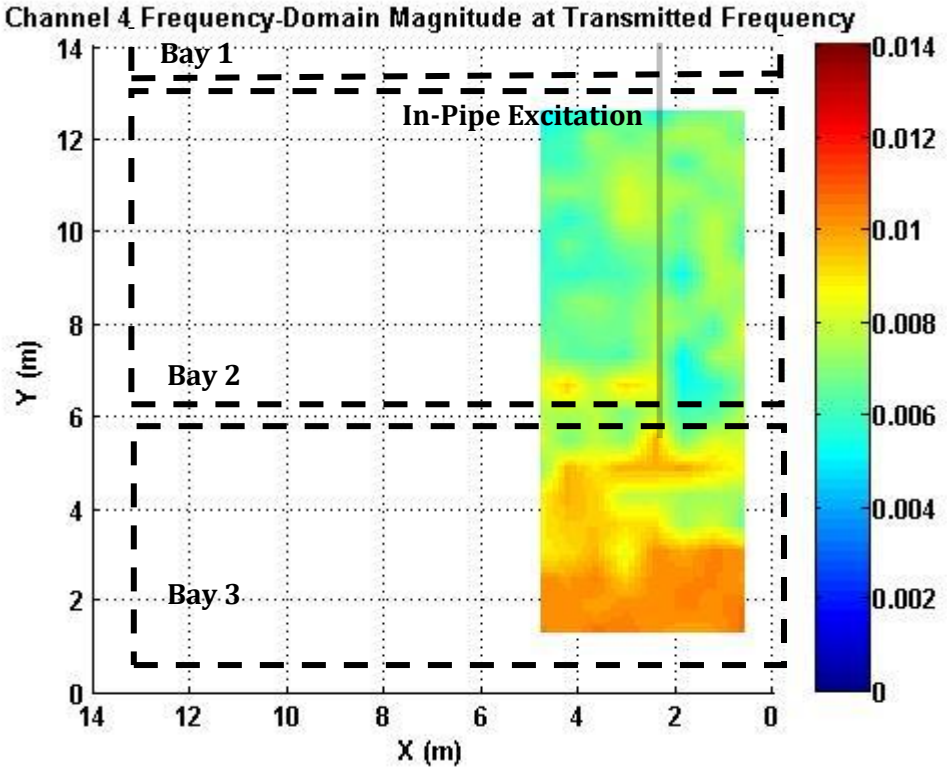

Figure 6-18: Frequency-domain magnitude for channel 4, calculated in the same way as Figure 6-14 but with a moving-average filter applied to oversampled data. The field is consistent with the known pipe location at some points. A sketch of the ground truth is overlaid.

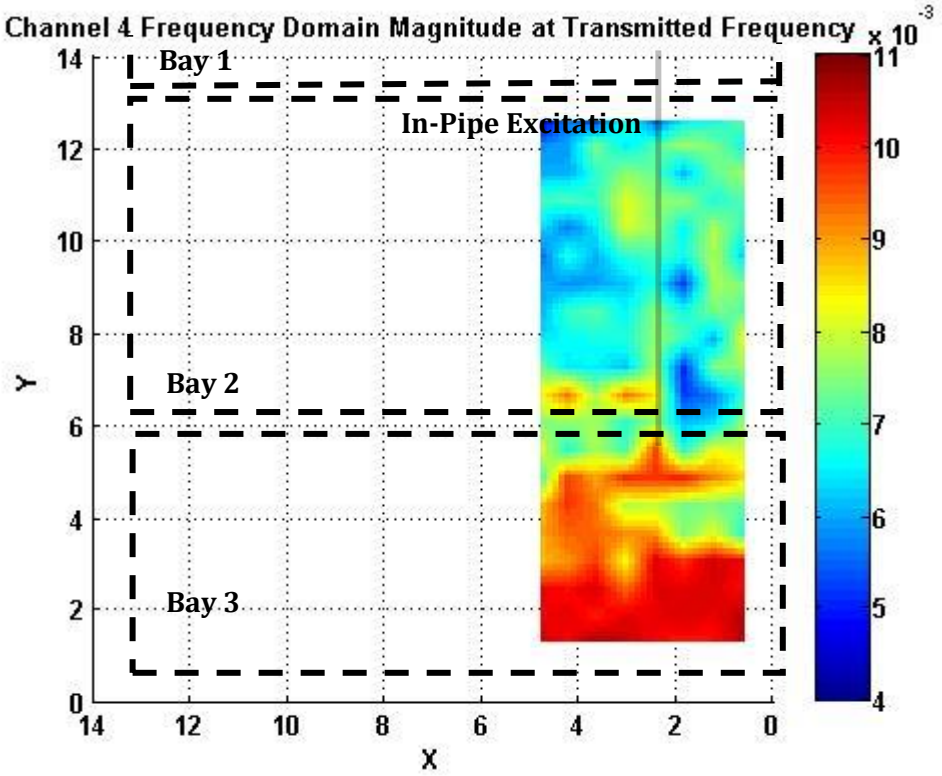

Figure 6-19: Frequency-domain magnitude for channel 4, showing the same data as Figure 6-18 but with the colour scale modified to better fit the data. The field is consistent with the known pipe location at some points. A sketch of the ground truth is overlaid.

6.5.4 Differential Results

The predicted field was expected to be orientated approximately perpendicular to the excitation cable with peak-magnitude at the closest point. At the end of the excitation cable, it was expected that the field would curl around the end of the cable, giving a component parallel to it. For this reason, four probes were included which were used to measure the field parallel and perpendicular to the excitation cable. The following results shown the measured voltage between each pair of probes, the expectation was that the field would be evident parallel to the field. Results were processed in the same way as above, an FFT was taken on windowed time-domain data, results were spatially-oversampled and a moving average filter applied.

The results are presented in Figure 6-20 - Figure 6-23. However, the results only indicate the clear presence of an in-pipe excitation in one of the two perpendicular cases, while a less clear indication is also given in one of the parallel cases. The explanation for this is evident when considering the measured range across the individual channels. If the system calibration was

perfect, then the measured frequency-domain magnitude would be comparable across the four channels. In this case, it appears that the gain on each channel is not uniform. Consequently, the differential results are presented with low confidence. Furthermore, the electrostatic approximation predicts an increased order of magnitude in the range dependency when measuring differential voltage compared to a single point, reducing the expected signal-magnitude greatly.

The remainder of this chapter will discuss the single channel data, which are compared to the change in soil conditions and GPR results.

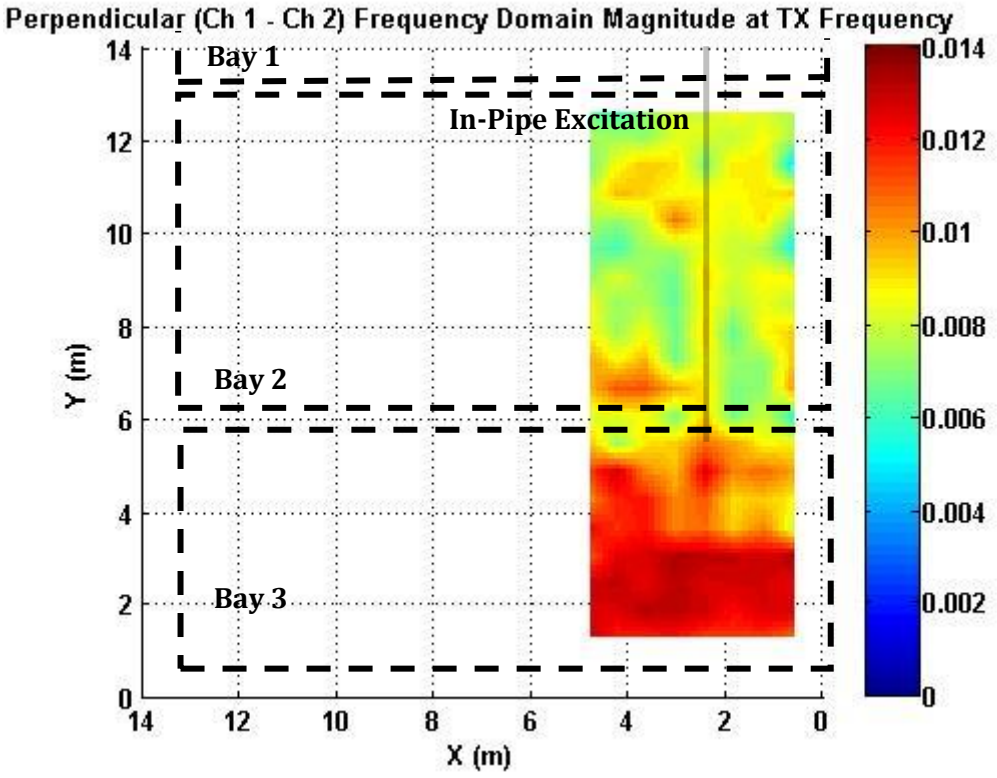

Figure 6-20: Perpendicular frequency-domain magnitude at the transmitted frequency, measured between channels 1 and 2. A sketch of the ground truth is overlaid.

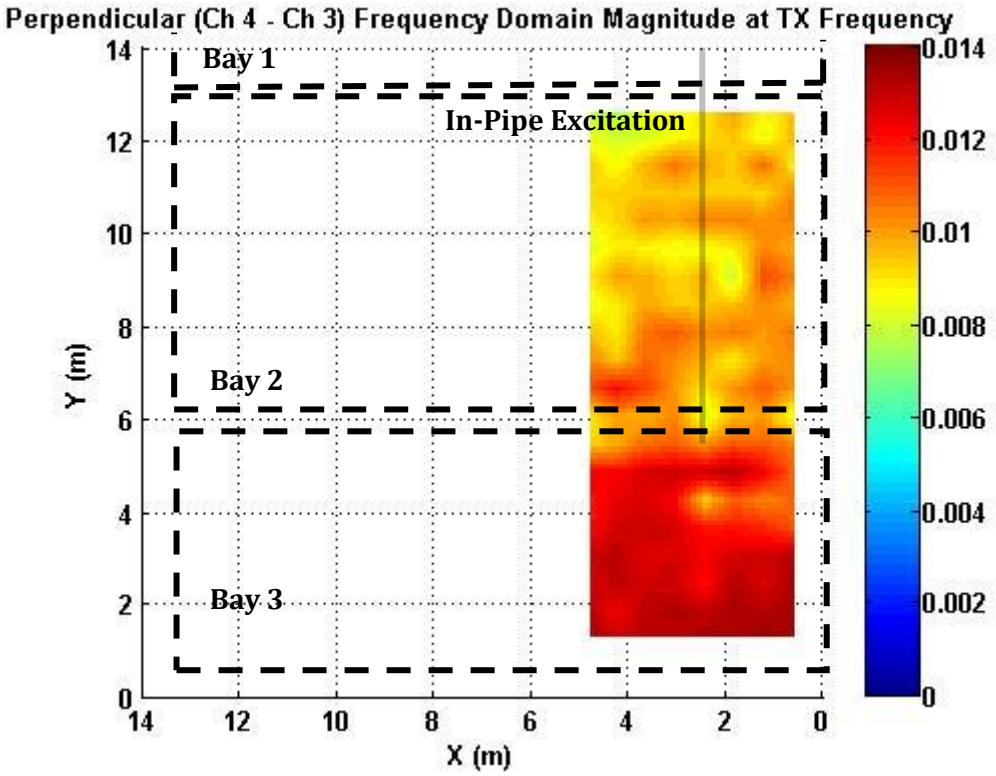

Figure 6-21: Perpendicular frequency-domain magnitude at the transmitted frequency, measured between channels 4 and 3. A sketch of the ground truth is overlaid.

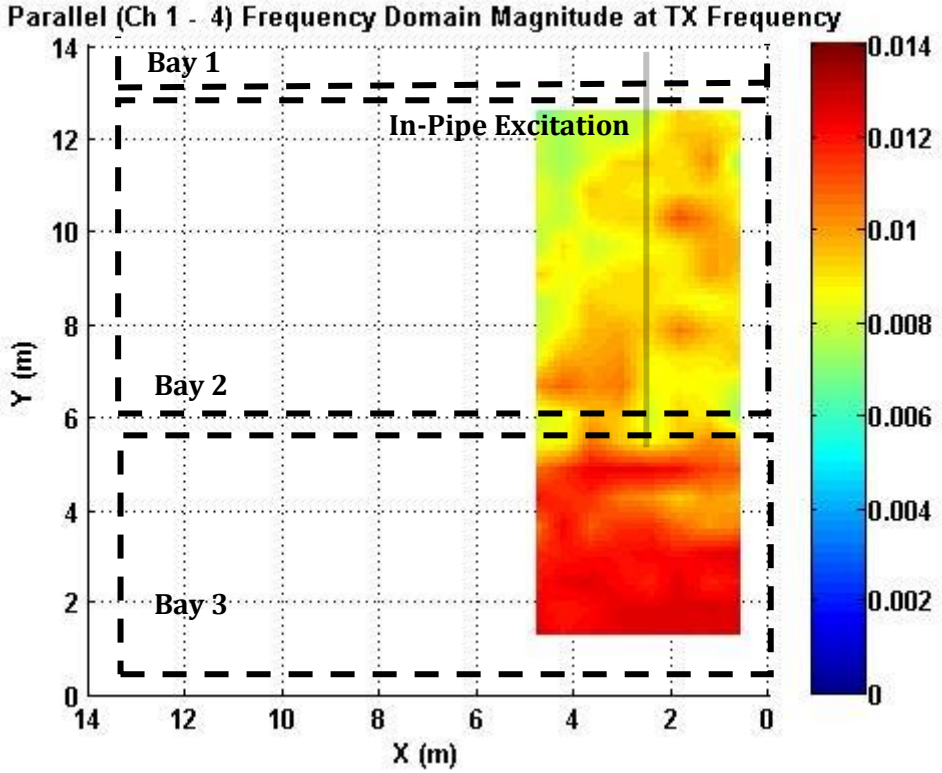

Figure 6-22: Parallel frequency-domain magnitude at the transmitted frequency, measured between channels 1 and 4. A sketch of the ground truth is overlaid.

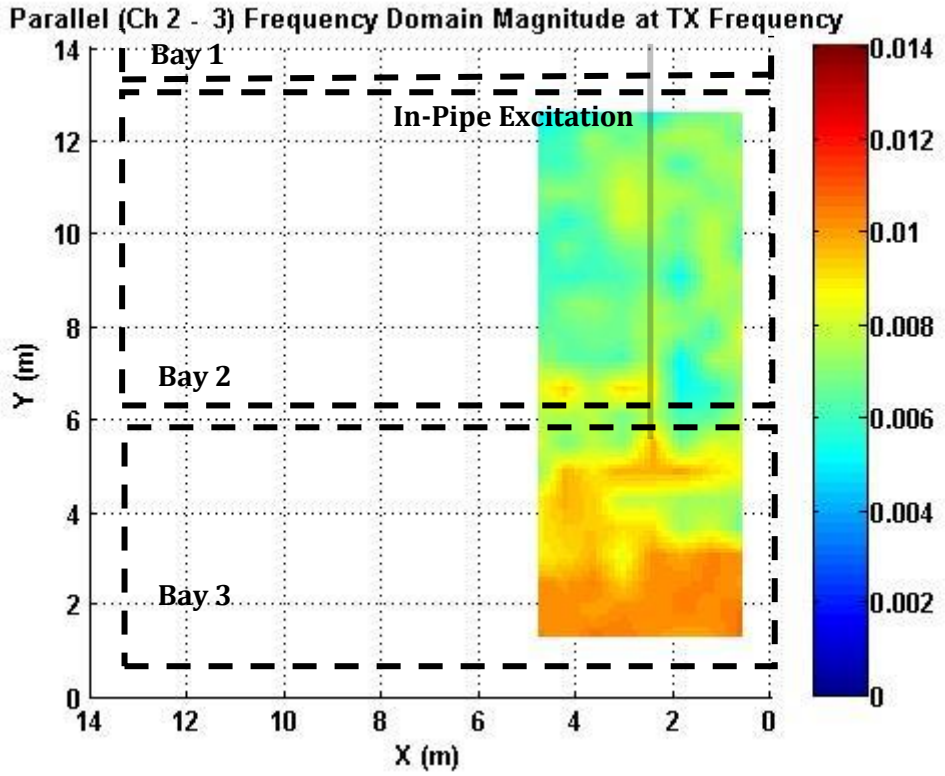

Figure 6-23: Parallel frequency-domain magnitude at the transmitted frequency, measured between channels 2 and 3. A sketch of the ground truth is overlaid.

6.5.5 Spatial Location of the Results

A researcher working on a separate part of the Mapping the Underworld project undertook a GPR survey of the test-site, using commercial GPR equipment. The GPR data was used for two reasons: To identify the location of the changes in soil type across the test-site; and to compare anomalous results in the measurements presented here with the GPR survey of that location.

The data presented here has all been located using x-y coordinates relative to the marked out grid on the test-site. The GPR data is presented as reflections for a length of measurement, with different data files corresponding to different directions and starting points on the test-site. Therefore, spatial information was required to accurately co-locate the data in a way which allowed comparison. Spatial position was found using a total station by Leica-Geosystems (Leica-Geosystems, 2013). The position of the grids used for GPR and measurements of the in-pipe excitation are plotted in Figure 6-24.

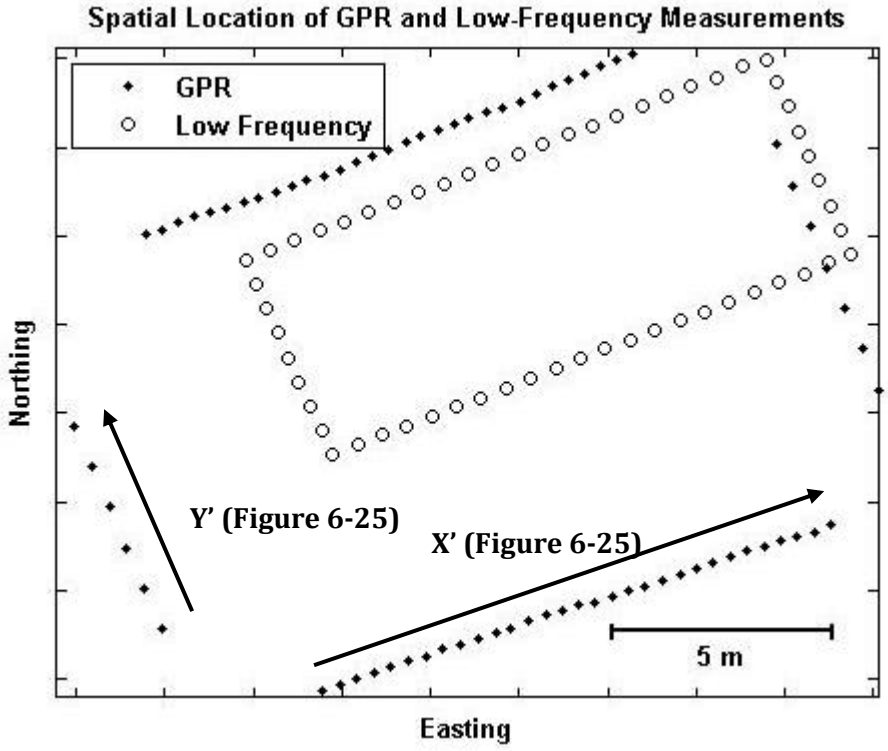

Figure 6-24: Location of grids for GPR and low-frequency measurements using the total-station measurement equipment. Arrows denoting axis labels for Figure 6-25 are shown.

6.5.6 Comparison with GPR Data

6.5.6.1 Change in Soil Type

GPR is an excellent tool for locating changes in soil conditions, the differences in measured reflections can often be seen clearly on a raw "b-scan". However, in this case another MTU researcher produced results similar to Figure 6-25 which shows positive, negative, and zero reflections for the GPR measurements across the test-site. By comparing a number of these figures, it is possible to identify the boundaries in the soil conditions, at X' = 5.8 m, and X' = 12.3 m. Using the spatial co-location method outlined above, these bay edges can be projected onto the results measured with in-pipe excitation, without changing the coordinate system in use. Only one boundary was present in the field-trial area, and that is shown in Figure 6-26, which is an update to Figure 6-15.

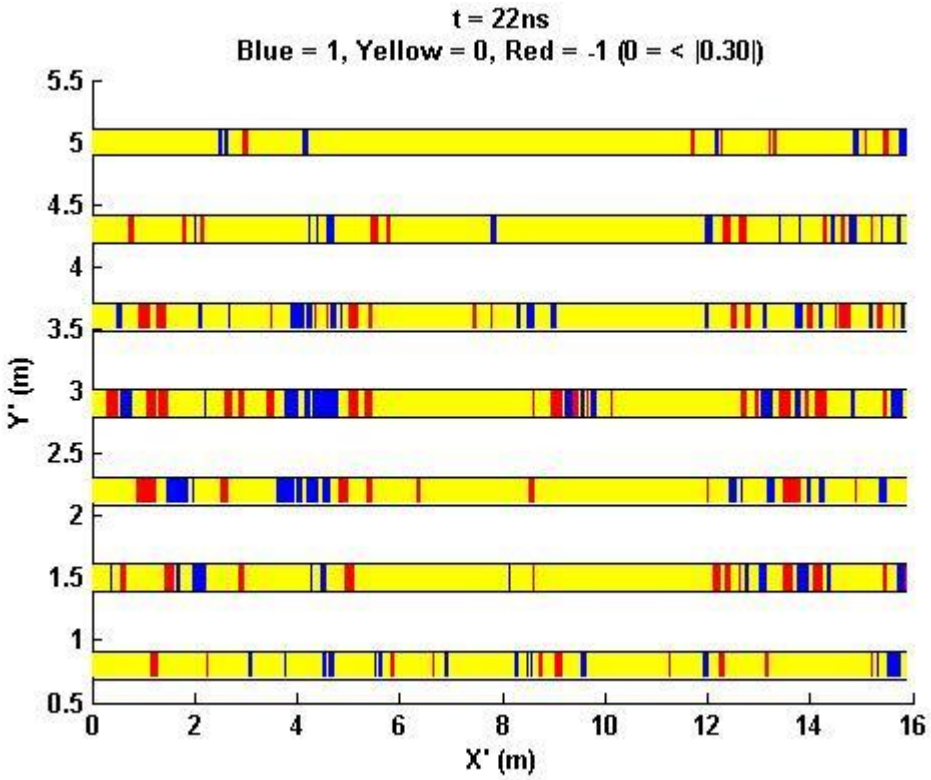

Figure 6-25: Sample GPR results, the polarity of the measured GPR reflection at a depth corresponding to a 22 ns travel time is shown. The significant change in reflection due to a change in soil results in relatively obvious changes across the measurement area, evident at X' = 5.8 m and X' = 12.3 m.

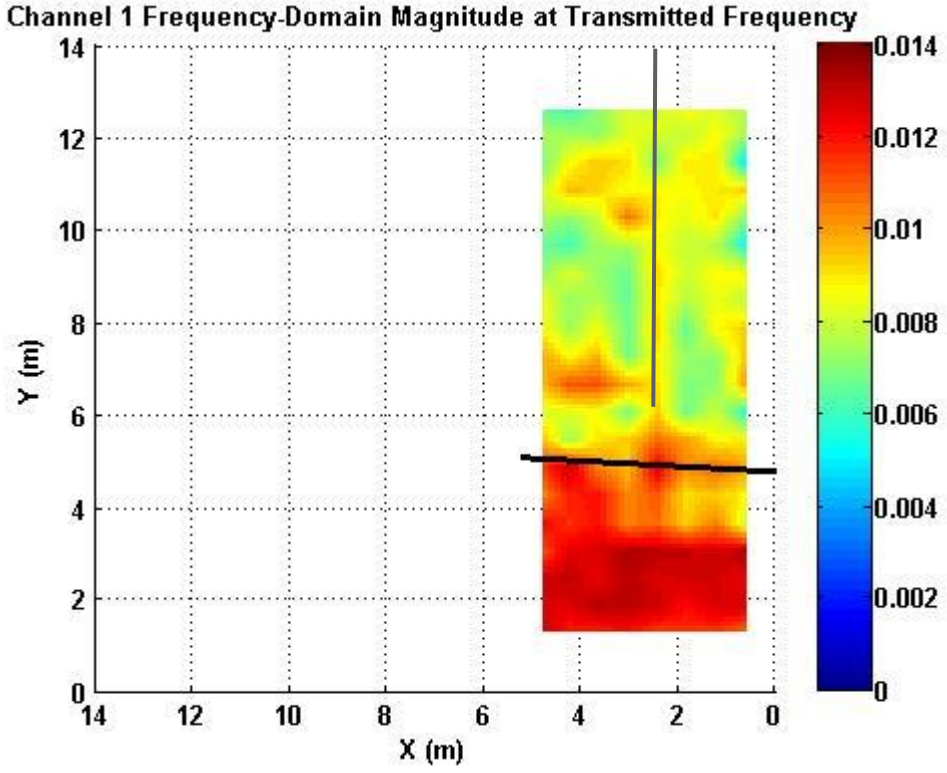

Figure 6-26: Magnitude of received signal at the transmitted frequency, smoothed to increase resolution. The signal source is 30 cm below the surface in the centre of the plot at x = 3 m, between y = 13 m and y = 6 m. Change in soil type shown with a black line, while the in-pipe excitation is shown with a grey line.

It is evident, when considering Figure 6-26, that a significant change occurs at the transition to a clay-based soil. It is most unfortunate that this transition obscures the effects of the end of the excitation cable which occurs at the same point. It seems illogical that the area in which there is no signal-excitation could have measurements so much stronger that region in which excitation occurred. Several possible explanations for this are offered in the discussion section.

6.5.6.2 Comparison of Anomalous Results

Several areas show high field-magnitude where there is no mapped source. These can be explored using GPR data taken on the same site. For a guide to reading GPR waveforms, the reader is referred to the work by Cassidy (2009). The GPR measurements are presented as b-scans, which show the magnitude of the reflected signal as a function of time – which corresponds to reflection depth – and distance along a measurement pass in the X' direction. Therefore, targets are observed as hyperbolae indicating a reflection from a point whose range changes spherically as the GPR passes over the stationary target.

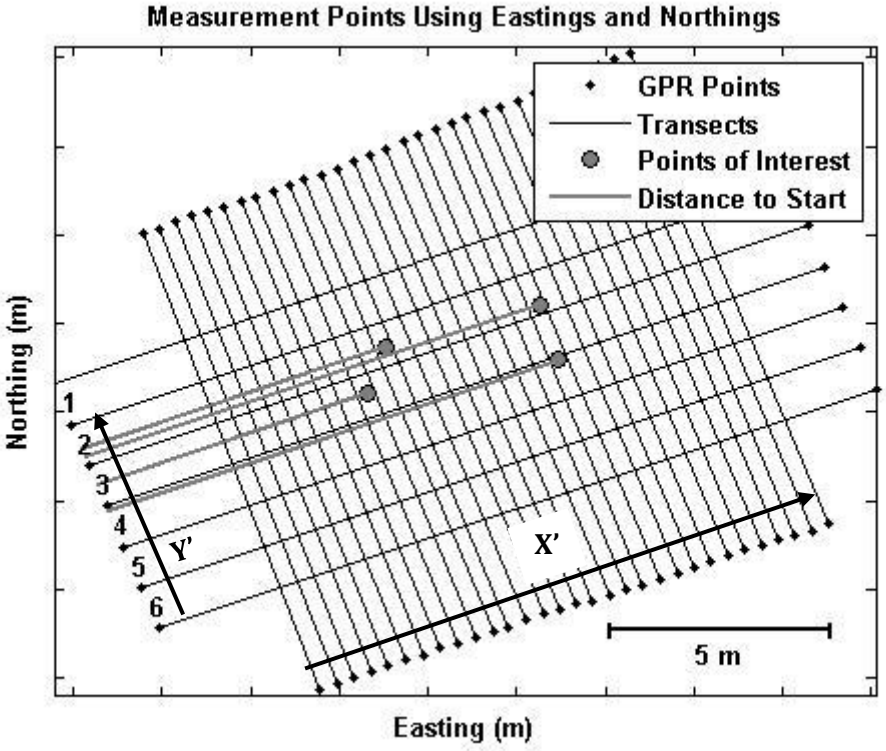

Figure 6-27: GPR data transects, showing points-of-interest with their distances from the beginning of the GPR sweep. The X' axis is used in the GPR data plotted in Figure 6-27 - Figure 6-31.

Several points are identified on Figure 6-26: The region y < 5 m; the area between x = 5 m, y = 7 m and x = 3 m, y = 7 m; a point x = 3 m, y = 10 m; and a point at x = 4 m, y = 11 m. The GPR data was taken from the long transects and the points of interest are identified by determining the distance into the transect at which the relevant point is located. It should be noted that the spatial resolution of the results presented here was originally 60 cm, while the spatial positional accuracy of the GPR results is increasingly degraded along a transect by uneven ground and the difficulty of travelling in a perfectly straight line. The process of identifying the appropriate transect, and the position within it, is graphically illustrated in Figure 6-27 but cannot be expected to determine matching spatial positions, to accuracy of the order of centimetres.

6.5.6.3 Area where y < 5

There is no indication in the GPR data of sub-surface targets causing the high field-magnitude measured in the area where y < 5 m. It is more likely that an increase in ion-mobility due to the clay based soil composition (Santamarina *et al.*, 2001) caused increased field-magnitude, despite the excitation being distant from the majority of this area. It is unfortunate that the end of the excitation cable coincided with this boundary, and further measurements are required to investigate this unexpected result.

6.5.6.4 Area between x = 5 m, y = 7 m and x = 3 m, y = 7 m

Two GPR results are presented in Figure 6-28 and Figure 6-29, representing data for either end of the area in question. There are indications of a shallow target at around X' = 10 metres on both GPR measurements, within 70 cm of the centre of the anomalous area. However, this does not correspond exactly to the position of the anomalous result.

6.5.6.5 Point at x = 3 m, y = 10 m

A single GPR measurement is presented in Figure 6-30, with an obvious shallow target present within 50 cm of the corresponding anomaly. The target appears at X' = 7.7 m, while the anomalous result is at approximately X' = 7.2 m. The shallow nature of the target could indicate a rock or similar imperfection in the soil.

6.5.6.6 Point at x = 4 m, y = 11 m

A single GPR measurement is presented in Figure 6-31 which shows a strong target at X' = 5 m, and what appears to be an echo at X' = 6 m in the region of the anomaly. This does not indicate the presence of a target in the anomalous area.

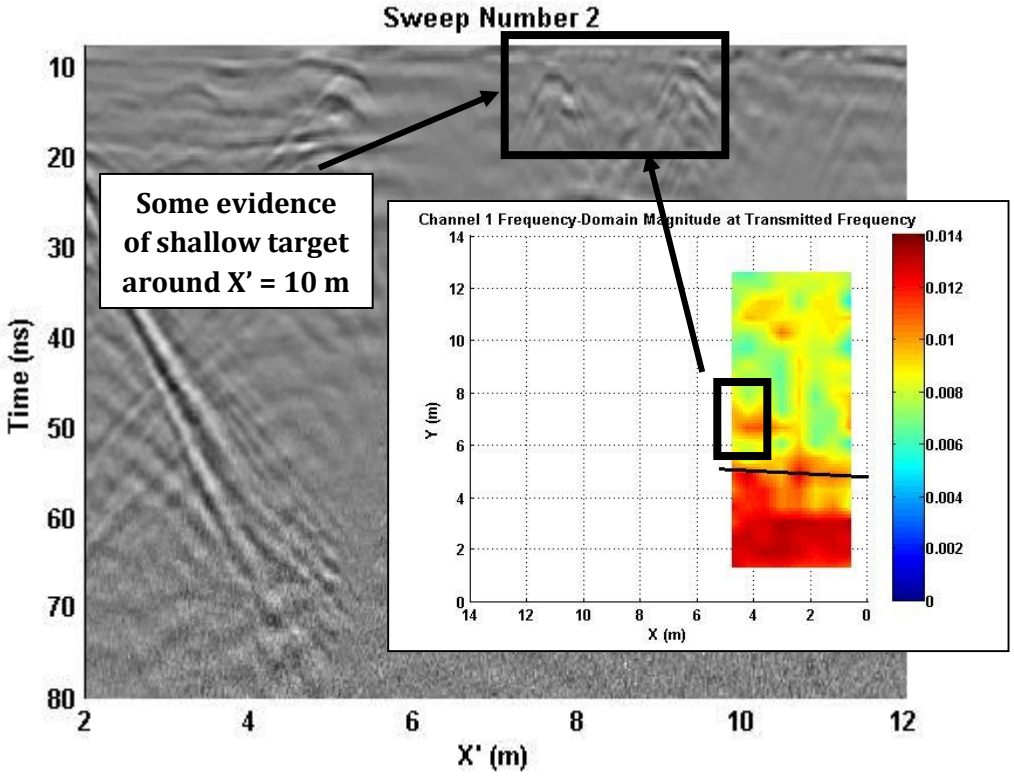

Figure 6-28: GPR measurement corresponding to the area between x = 5 m, y = 7 m, and x = 3 m, y = 7 m, which is at D = 10.7 m here. There are indications of a shallow target at around D = 10 m. Figure 6-26 inset for comparison.

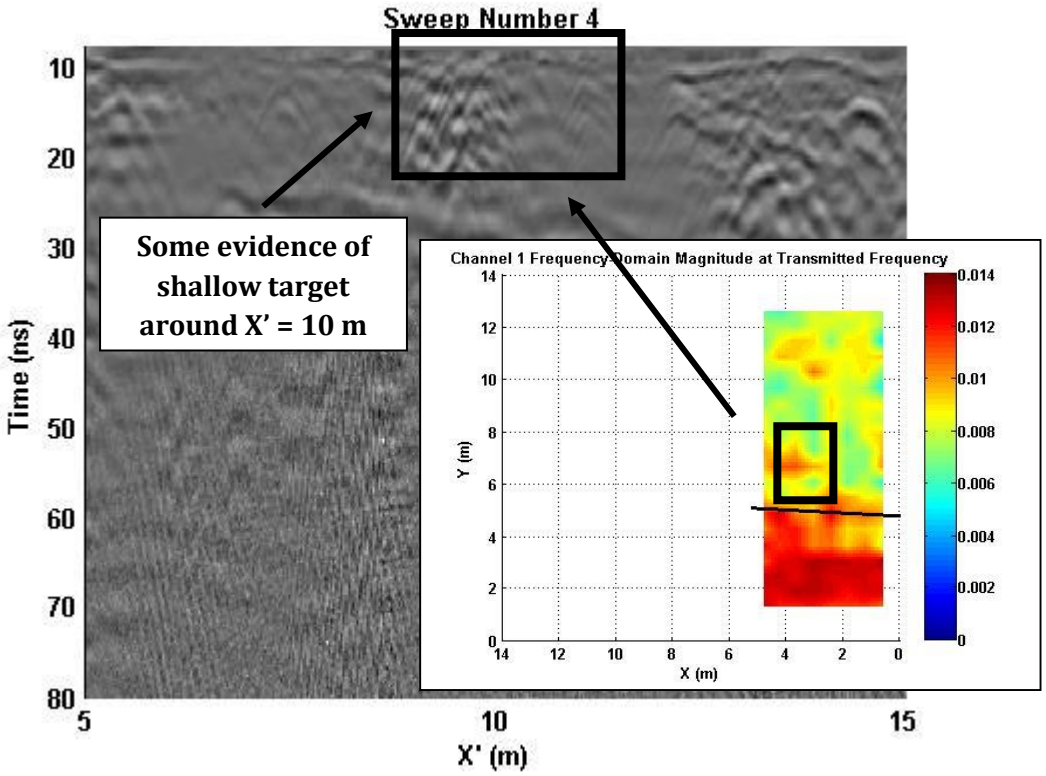

Figure 6-29: GPR measurement corresponding to the area between x = 5 m, y = 7 m, and x = 3 m, y = 7 m, which is at D = 10.7 m here. There are indications of a shallow target at around D = 10 m. Figure 6-26 inset for comparison.

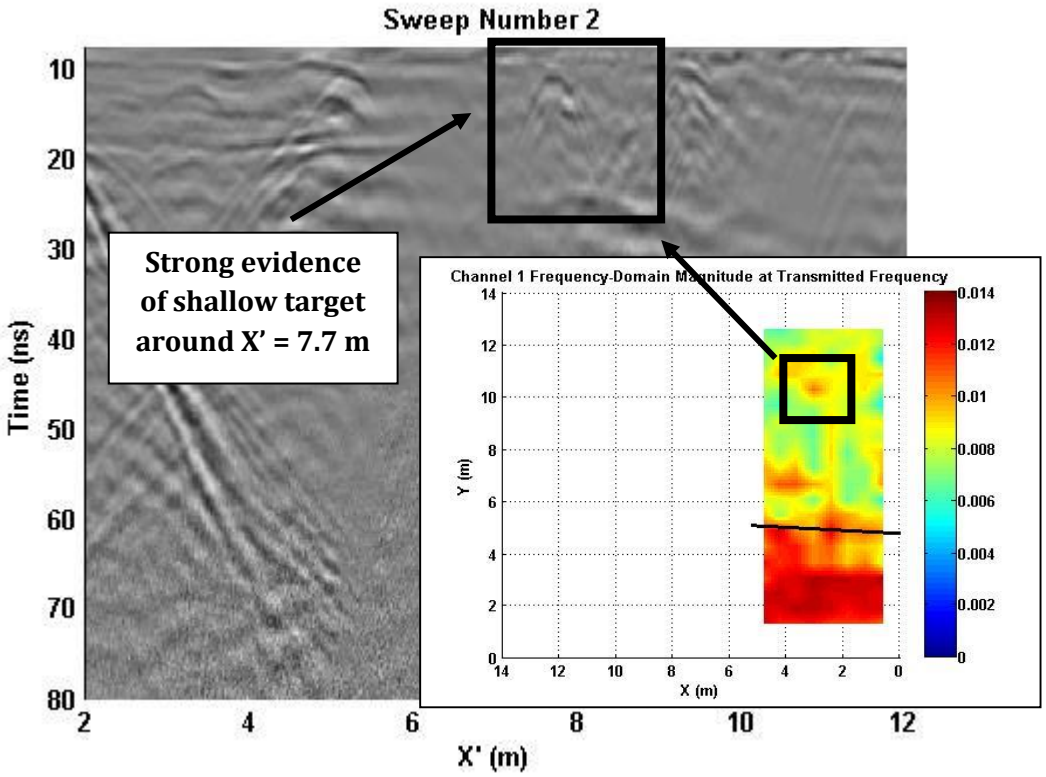

Figure 6-30: GPR measurement corresponding to a point at x = 3 m, y = 10 m, which is at D = 7.2 m here. There are clear indications of a shallow target at D = 7.7 m. Figure 6-26 inset for comparison.

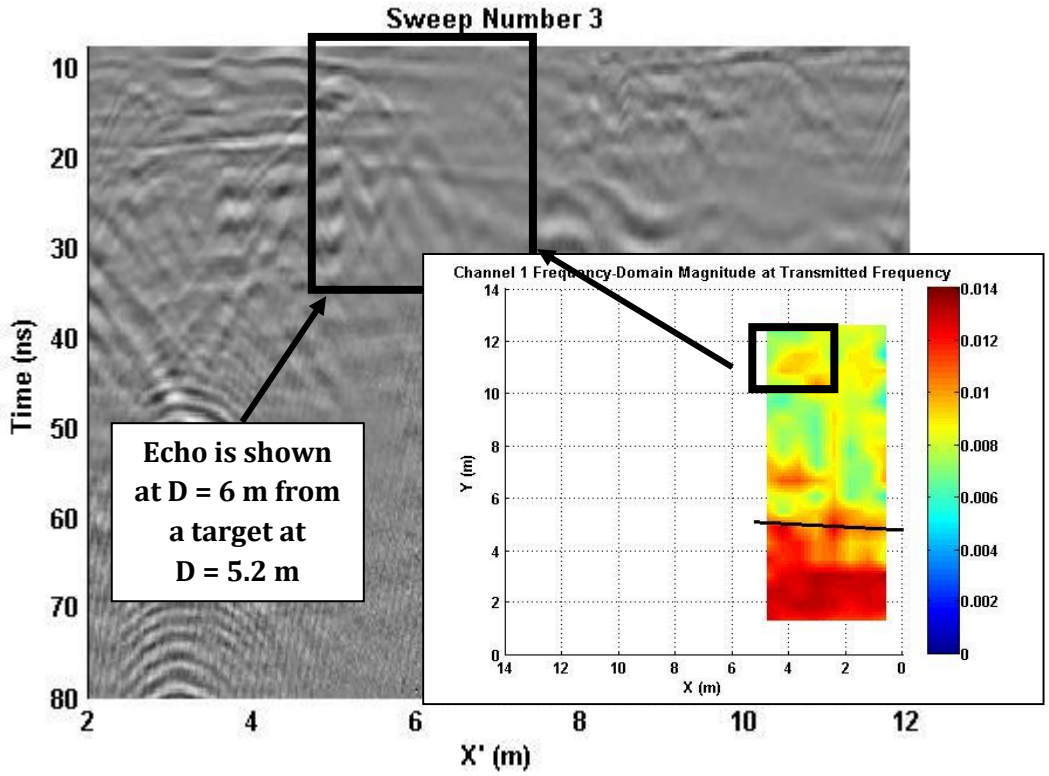

Figure 6-31: GPR measurement corresponding to a point at x = 4 m, y = 11 m, which is at D = 6.5 m here. A faint target is apparent at D = 6 m but it looks to be an echo from a stronger target at D ≈ 5 m. Figure 6-26 inset for comparison.

6.6 CHAPTER SUMMARY

This chapter has described field-trials undertaken to examine the use of in-pipe excitation, with low-frequency electromagnetic fields, to locate buried pipes. The experiment described used capacitively coupled sensors to measure the voltage at different positions on a test-site, these were then spatially-oversampled, and filtered to show field-magnitude at different locations. Some results showed very good agreement with the known location of the in-pipe excitation.

The observed peak in field-magnitude occupied a very small spatial position, which fitted with the prediction of conductive ground heavily attenuating the transmitted signals. It was hoped that the field direction could have been calculated by measuring orthogonal voltages between known points. However, this did not produce meaningful results; measuring the signals differentially increases the effective signal attenuation to r^{-3} and it is likely that this made the measurement unusable.

It is noticeable that only two of the four measurement channels showed results supporting the above conclusion. This demonstrates the difficulty in taking measurements of this nature, and there are several factors that can reduce measurement reliability. These include surface roughness or user-error causing insufficient or inconsistent coupling to the ground; highly attenuating localised ground conditions; or the highly sensitive amplifier circuits performing below expected levels.

It is believed that these are the first results published which show that low-frequency electromagnetic in-pipe excitation can be used to locate buried pipes. These field-trials were undertaken under controlled conditions, with well-known ground-truth, and considerable scope remains for further investigation of the method.

CHAPTER 7: CONCLUSIONS AND RECOMMENDATIONS

This thesis considered the use of low-frequency electromagnetic fields, excited within a pipe, to detect buried-utilities. It has been shown that low-frequency signals can be excited in the shallow-subsurface, and detected at distances of 30 metres. Furthermore, signals excited from within a buried-pipe have been used to determine the location of that pipe.

The specific conclusions of this thesis are summarised below.

7.1 CONCLUSIONS

Low-cost vector network analysers were shown to present usable results for reflection-only measurements, when compared to equivalent laboratory-grade equipment. However, reflection and transmission measurements were not found to be reliable, most likely due to problems with the calibration procedure. The inclusion of a step-discontinuity in a coaxial cavity for measuring the relative-permittivity of a material was not shown to give reliable results, despite the practical advantages for sample preparation. The step-discontinuity was shown to result in scattering-parameters of the transition regions which varied with the dielectric in the cavity. It was suggested that the inclusion of a known dielectric layer could overcome this obstacle.

A new methodology was presented for calculating the electromagnetic field in a four-layered medium due to a vertical electric dipole. This methodology was used to compute example results, including the scenarios of a leaking pipe, and a large void, in the sub-surface. The results showed that the trapped surface wave contributed negligibly in the chosen scenarios. However, the contribution was shown to increase with a more conductive fourth layer, as expected from previous works. A number of errors and omissions in previous publications were observed and discussed. These errors made repetition of previous work exceedingly challenging, and it is hoped that their inclusion will reduce this problem in future.

Field trial measurements observed the propagation of low-frequency electromagnetic fields with relatively low velocities of propagation (10^4 ms^{-1} to 10^6 ms^{-1}). This is consistent with the effects

of the known conductivity of soil at low-frequencies. However, it was not possible to determine whether exceedingly high values of permittivity, which have been reported in soils at low-frequencies, are measurable over the bulk of the soil. It was shown that for one measurement configuration a useful direction of arrival measurement would be possible. However, the required propagation velocity, array size, signal and noise characteristics make confirming this measurement configuration difficult for practical measurements.

Measurements of the electric field magnitude at different spatial positions were used to detect signals excited from within a buried-pipe. Furthermore, it was demonstrated that this measurement can be used to locate the buried-pipe. The results presented included a number of anomalous increases in measured field magnitude, and it was shown that some of these anomalies coincided with shallow targets, of unknown origin, on a ground-penetrating radar survey. Significant work remains to determine the accuracy and limitations of this technique for the detection of buried utilities.

7.2 RECOMMENDATIONS

This thesis leads to a number of recommendations for further work:

Low-cost vector network analyser technology is applicable to existing methods for measuring the dielectric properties of soils. These methods include short-circuit terminated coaxial cavities; open ended coaxial waveguides, or time-domain reflectometry probes. By utilising low-cost vector network analysers, these methods may be used a greater range of field work, giving potential for new in-situ measurements in environments where this was not previously possibly.

Coaxial cavities, incorporating a step-change discontinuity, were used in this thesis to improve the ease of sample preparation, and reduce the manufacturing cost for measurement of the relative-permittivity of soils. It was shown that calibrating such a cavity is exceedingly challenging. Further measurements, which include a layer of known dielectric between the discontinuity and the sample, may allow use of this technique by evaluating the reliability of calibration for this type of cavity.

A method of calculating the electric field, due to a vertical electric dipole, in four layered media was presented. It has been shown that the case of a buried horizontal dipole is an extension of the same analysis (King *et al.*, 1992; Lu *et al.*, 2009). The buried horizontal dipole lends itself well to the situation of in-pipe excitation, and it would be interesting to apply the results of such an analysis to measurements studying in-pipe excitation.

The field trial results presented support the use of low-frequency electromagnetic fields, excited within a pipe, for the location of buried pipes. There are few practical difficulties for repeating these experiments, and there remains considerable scope for evaluating the limitations of the technique in terms of different soil conditions, utility depth, and spatial accuracy.

The results shown in Chapter 6 also suggested that measurements using in-pipe excitation could indicate the presence of anomalies in the vicinity of the pipe. The most obvious application of this technique is to attempt to detect utilities buried in the area around the buried pipe; a similar suggestion was made by Pennock and Redfern (2007) for ground-penetrating radar measurements. Repetition of the measurements presented in Chapter 6, in areas with known, co-located, utilities would be exceedingly interesting.

APPENDIX 1

LINK BETWEEN SCATTERING-PARAMETERS AND TRANSMISSION LINE CALCULATIONS

This appendix uses the well-known definitions of scattering-parameters, in conjunction with transition-matrices to show that a coaxial cavity can be defined using scattering-parameters in a method which is equivalent to the transmission line method.

TRANSMISSION LINE

The impedance of a terminated transmission line may be evaluated from its component values using the well-known equation (Pozar, 1990, p. 81):

$$Z_{in} = \frac{Z_{load} + Z_{char} \tanh(\gamma d)}{Z_{char} + Z_{load} \tanh(\gamma d)} \tag{A1-1}$$

Where

$$\gamma = \sqrt{(R + j\omega L)(G + j\omega C)} \tag{A1-2}$$

$$Z_{char} = \sqrt{(R + j\omega L)/(G + j\omega C)} \tag{A1-3}$$

R, L, *G*, and *C* refer to the electrical properties of the transmission line, *d* is the length of the transmission line, and Z_{load} is the termination impedance. It is possible, therefore, to determine the impedance and reflection-coefficient of a sequence of transmission lines using this equation and iterating from the load towards the source.

The value for reflection coefficient from a terminated coaxial cavity has been known for many years (Clarkson *et al.*, 1977). Following the work of Giese and Tiemann (1975), Clarkson *et al.* (1977) gave equations for a coaxial cavity with short, open and matched terminations. The short-circuit case is given:

$$S_{11}|_{short\ circuit} = \frac{\rho - \exp[-2\gamma l]}{1 - \rho \exp[-2\gamma l]} \tag{A1-4}$$

Where ρ is the reflection coefficient between the coaxial line of standard impedance and an air filled coaxial cavity with the same properties as that being used, but of infinite length; l is the length of the coaxial cavity; $\gamma = -j\omega/c_0$.

SCATTERING-PARAMETERS

It will now be shown that specified scattering matrices equate to the values given for a short circuit terminated coaxial line given by Clarkson *et al.* (1977) (A1-4). Scattering-parameters are defined for a two port network as (Pozar, 1990):

$$\begin{bmatrix} b_1 \\ b_2 \end{bmatrix} = \begin{bmatrix} S_{11} & S_{12} \\ S_{21} & S_{22} \end{bmatrix} \begin{bmatrix} a_1 \\ a_2 \end{bmatrix} \tag{A1-5}$$

Where a_n is the signal input to port *n* and b_n is the signal output at port *n*.

Coaxial Cavity

When considering the coaxial cavity filled with a lossless dielectric, and with perfectly matched termination, no reflection occurs at either terminal, this is all accounted for in the properties of the transition region. The change to the signal within the cavity is accounted for as a phase shift determined by the length of the cavity, and the propagation speed of the wave.

$$S_{cell} = \begin{bmatrix} 0 & \exp(-j\theta_c) \\ \exp(-j\theta_c) & 0 \end{bmatrix} \tag{A1-6}$$

Where $\theta_c = \omega L_{cell}/c$, and c is the wave velocity in the dielectric.

The expression for the resulting phase shift in the coaxial cavity is widely available, examples include Baker-Jarvis *et al.* (1990) and Gorriti and Slob (2005b), this assumes that the cavity is connected to transmission lines which are of matched impedance. This is clearly untrue, so the components either side of the cavity must account for the mismatch.

Transition Regions

The scattering matrix for the transition between coaxial cable and the cavity is slightly more difficult to define, physically it consists of the effect of the impedance mismatch between the two

regions; the effect of the length of the transition region on the phase; and the effect of the step discontinuity.

Impedance Mismatch

Clarkson *et al.* (1977) define ρ as the reflection coefficient between the cable and an open, infinite coaxial cavity, which accounts for the impedance mismatch this may be used as the value for S11 of the transition region.

$$\rho = \frac{Z_0 - Z_C}{Z_0 + Z_C} \tag{A1-7}$$

Where Z_0 is the characteristic impedance of the coaxial line, and Z_C is the characteristic impedance of the air filled cavity. Both are evaluated using the well known equation for the characteristic impedance of a coaxial line (Pozar, 1990 p. 76):

$$Z_0 = \sqrt{\frac{\mu}{\varepsilon}} \frac{\ln\left(b/a\right)}{2\pi} \tag{A1-8}$$

Where μ and ε are the permeability and permittivity of the dielectric in the coaxial line; and b and a are the outer and inner radii of the coaxial line, respectively.

If it is assumed that the transition between the coaxial cable and cavity is infinitely small in length, then no phase change is applied by the S21 parameter, which is therefore would be assumed to be $\sqrt{1-\rho^2}$ representing the power not reflected (Baker-Jarvis *et al.*, 1992). Similarly, S22 can be thought of as the reflection coefficient from the air-filled cavity to a coaxial line with impedance Z_0, which is $-\rho$. This leads to the final element of the scattering matrix, S21 which is $\sqrt{1-\rho^2}$.

Phase Change due to Transition Region Length

The assumption that the transition region is infinitely small in length is clearly invalid. Furthermore, the transition region has been defined as the region between the calibration plane and the start of the sample, and so includes the region of the cavity before the sample begins. Therefore, a parameter has been included into S21 and S12 which accounts for the non-zero length. The non-zero length is represented as a phase shift in the same way the idealised cavity

is represented by a phase shift (A1-6). The scattering matrix may then be represented as the combination of the impedance mismatch and the non-zero transition region length:

$$S_{coaxial-cell} = \begin{bmatrix} \rho & \exp(-j\theta_{trans})\sqrt{1-\rho^2} \\ \exp(-j\theta_{trans})\sqrt{1-(-\rho)^2} & -\rho \end{bmatrix} \quad \text{(A1-9)}$$

It is shown below, that the scattering matrix for the transition region (A1-9), in conjunction with the ideal scattering matrix for the coaxial cavity (A1-6), reduces to an expression for the input impedance equivalent to that given by Clarkson *et al.* (1977) and here in (A1-4).

Step Discontinuity in the Transmission Line

The effects of a step discontinuity in the transmission line are documented in the main body of this thesis. The possibility of a step discontinuity in the transmission line was not considered by Clarkson *et al.* (1977) and is not useful for this comparison.

TRANSITION-PARAMETERS

Having defined the scattering-parameters for the different elements of the system in (A1-6) and (A1-9), it will now be shown that (A1-12) may be used to convert to transition-parameters, and define the system as a whole, in agreement with the results of Clarkson *et al.* Transition matrices are calculated as:

$$T_{cell} = \begin{bmatrix} \exp\left(-\frac{j\omega L}{c}\right) & 0 \\ 0 & \exp\left(\frac{j\omega L}{c}\right) \end{bmatrix} \quad \text{(A1-10)}$$

$$T_{coaxial-cell} = \begin{bmatrix} \frac{\exp(-j\theta_{trans})}{\sqrt{1-\rho^2}} & \frac{\rho\exp(-j\theta_{trans})}{\sqrt{1-\rho^2}} \\ \frac{\rho\exp(j\theta_{trans})}{\sqrt{1-\rho^2}} & \frac{\exp(j\theta_{trans})}{\sqrt{1-\rho^2}} \end{bmatrix} \quad \text{(A1-11)}$$

Where the link between scattering and transition matrices is given by (Pozar, 1990):

$$\begin{bmatrix} T_{11} & T_{12} \\ T_{21} & T_{22} \end{bmatrix} = \begin{bmatrix} -\dfrac{\det(S)}{S_{21}} & \dfrac{S_{11}}{S_{21}} \\ -\dfrac{S_{22}}{S_{21}} & \dfrac{1}{S_{21}} \end{bmatrix} \tag{A1-12}$$

$$\begin{bmatrix} S_{11} & S_{12} \\ S_{21} & S_{22} \end{bmatrix} = \begin{bmatrix} \dfrac{T_{12}}{T_{22}} & \dfrac{\det(T)}{T_{22}} \\ \dfrac{1}{T_{22}} & -\dfrac{T_{21}}{T_{22}} \end{bmatrix} \tag{A1-13}$$

Leading to a definition of the system as:

$$\begin{aligned} T_{system} &= T_{coaxial-cell} \times T_{cell} \\ &= \frac{1}{\sqrt{1-\rho^2}} \begin{bmatrix} \exp(-j\theta_c)\exp(-j\theta_{trans}) & \rho\exp(j\theta_c)\exp(-j\theta_{trans}) \\ \rho\exp(-j\theta_c)\exp(j\theta_{trans}) & \exp(j\theta_c)\exp(j\theta_{trans}) \end{bmatrix} \end{aligned} \tag{A1-14}$$

Considering the definition of the transition matrices, and that for a short-circuit termination $a_2 = -b_2$, it is easily seen that the solution to b_1/a_1 for the above transition matrix is equal to (A1-6). Equation (A1-15) is equivalent to (A1-6) - derived by Clarkson *et al.* (1977) – with the addition of a phase shift, represented by the multiplication $\exp(-j\theta_{trans})$, due to the distance between the calibration plane of the VNA and the beginning of the sample.

$$S_{11}|_{short\ circuit} = \exp(-j\theta_{trans})\frac{\rho - \exp(-j2\theta_c)}{1 - \rho\exp(-j2\theta_c)} \tag{A1-15}$$

APPENDIX 2

N-TYPE CONNECTOR TECHNICAL DRAWING

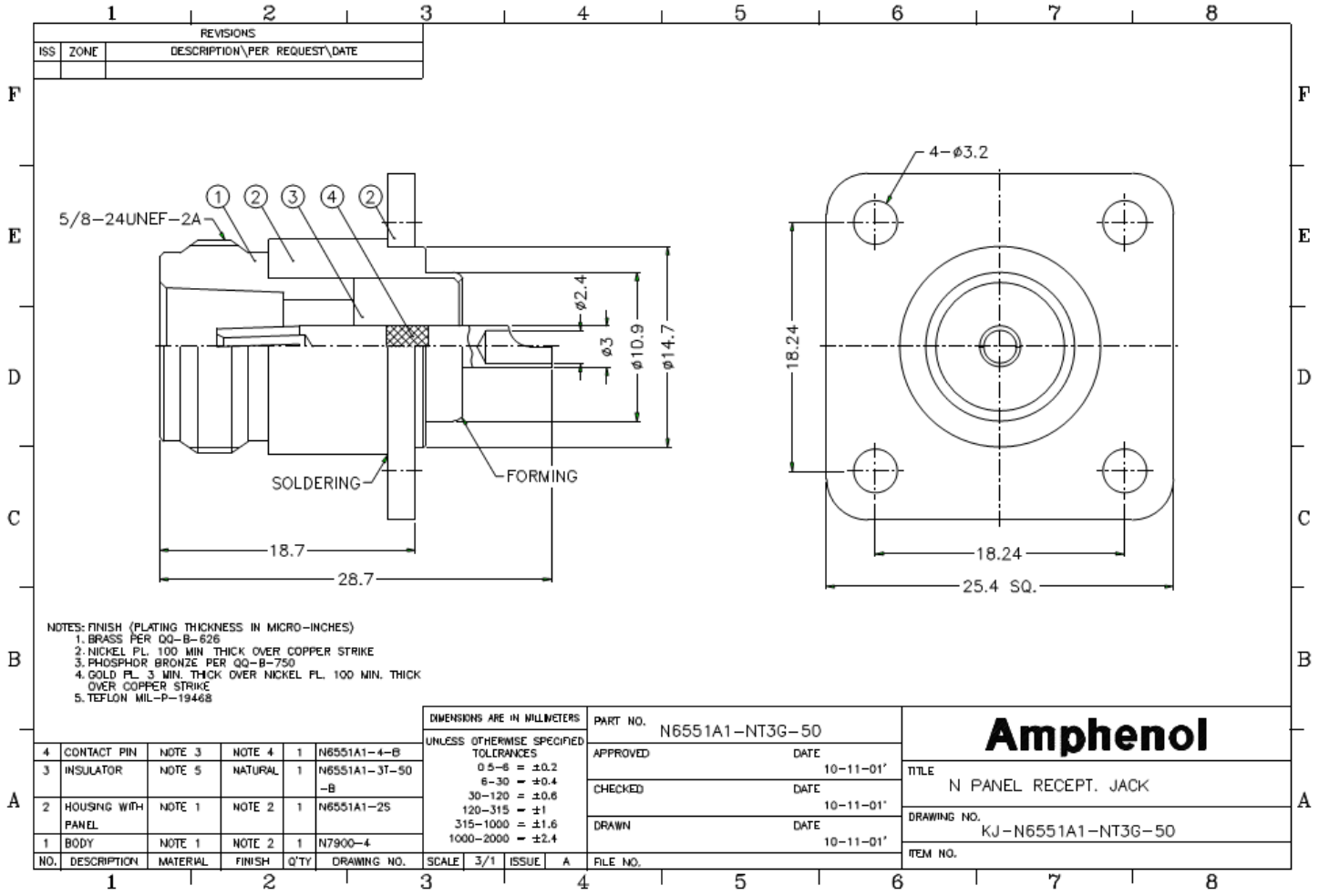

APPENDIX 3

DERIVATION OF Z_{S0}, Q, AND Q+1

King *et al.* (1992) equation 11.3.19, expression for surface impedance of a n-layered structure:

$$Z_{s0}(z_0') = \frac{\omega\mu_0\gamma_1}{k_1^2}\tanh\left\{-i\gamma_1 l_1 + \tanh^{-1}\left[\left(\frac{\gamma_2 k_1^2}{\gamma_1 k_2^2}\right)\tanh[-i\gamma_2 l_2 + \tanh^{-1}\left[\left(\frac{\gamma_3 k_2^2}{\gamma_2 k_3^2}\right)\tanh[-i\gamma_3 l_3 + \tanh^{-1}\left[\left(\frac{\gamma_n k_{n-1}^2}{\gamma_{n-1} k_n^2}\right)\tanh[-i\gamma_n l_n + \tanh^{-1}\left(\frac{\gamma_{n+1} k_n^2}{\gamma_n k_{n+1}^2}\right)\right]\right]\ldots\right]\right]\right\} \quad \text{(A3-1)}$$

Simplified for a four layer region:

$$Z_{s0}(z_0') = \frac{\omega\mu_0\gamma_1}{k_1^2}\tanh\left[-i\gamma_1 l_1 + \tanh^{-1}\left[\left(\frac{\gamma_2 k_1^2}{\gamma_1 k_2^2}\right)\tanh\left[-i\gamma_2 l_2 + \tanh^{-1}\left(\frac{\gamma_3 k_2^2}{\gamma_2 k_3^2}\right)\right]\right]\right] \quad \text{(A3-2)}$$

Using trigonometric identities the hyperbolic tangents may be removed:

$$Z_{s0}(z_0') = \frac{\omega\mu_0\gamma_1}{k_1^2}\frac{i\tan(-\gamma_1 l_1) + \left(\frac{\gamma_2 k_1^2}{\gamma_1 k_2^2}\right)\frac{i\tan(-\gamma_2 l_2) + \left(\frac{\gamma_3 k_2^2}{\gamma_2 k_3^2}\right)}{1 + i\tan(-\gamma_2 l_2)\left(\frac{\gamma_3 k_2^2}{\gamma_2 k_3^2}\right)}}{1 + i\tan(-\gamma_1 l_1)\left(\frac{\gamma_2 k_1^2}{\gamma_1 k_2^2}\right)\frac{i\tan(-\gamma_2 l_2) + \left(\frac{\gamma_3 k_2^2}{\gamma_2 k_3^2}\right)}{1 + i\tan(-\gamma_2 l_2)\left(\frac{\gamma_3 k_2^2}{\gamma_2 k_3^2}\right)}} \quad \text{(A3-3)}$$

Which may be reduced to:

$$Z_{s0}(z_0') = \frac{\omega\mu_0\gamma_1}{k_1^2}\frac{\tan(\gamma_1 l_1)\tan(\gamma_2 l_2)\,\gamma_1\gamma_3 k_2^4 - \gamma_2\gamma_3 k_1^2 k_2^2 + i\gamma_2^2 k_1^2\,k_3^2\tan(\gamma_2 l_2) + i\tan(\gamma_1 l_1)\,\gamma_1\gamma_2 k_2^2 k_3^2}{\gamma_2^2 k_1^2 k_3^2\tan(\gamma_1 l_1)\tan(\gamma_2 l_2) - \gamma_1\gamma_2 k_2^2 k_3^2 + i\tan(\gamma_1 l_1)\,\gamma_2\gamma_3 k_1^2 k_2^2 + i\tan(\gamma_2 l_2)\,\gamma_1\gamma_3 k_2^4} \quad \text{(A3-4)}$$

Finally, considering equation 11.3.20 from King *et al.* (1992):

$$-Q_n = \frac{\gamma_0 - \frac{k_0^2}{\omega\mu_0}Z_{s0}(0)}{\gamma_0 + \frac{k_0^2}{\omega\mu_0}Z_{s0}(0)} \quad \text{(A3-5)}$$

Gives an expression for Q:

$$-Q = \frac{\gamma_0 - \frac{k_0^2\gamma_1}{k_1^2}\frac{\tan(\gamma_1 l_1)\tan(\gamma_2 l_2)\,\gamma_1\gamma_3 k_2^4 - \gamma_2\gamma_3 k_1^2 k_2^2 + i\gamma_2^2 k_1^2\,k_3^2\tan(\gamma_2 l_2) + i\tan(\gamma_1 l_1)\,\gamma_1\gamma_2 k_2^2 k_3^2}{\gamma_2^2 k_1^2 k_3^2\tan(\gamma_1 l_1)\tan(\gamma_2 l_2) - \gamma_1\gamma_2 k_2^2 k_3^2 + i\tan(\gamma_1 l_1)\,\gamma_2\gamma_3 k_1^2 k_2^2 + i\tan(\gamma_2 l_2)\,\gamma_1\gamma_3 k_2^4}}{\gamma_0 + \frac{k_0^2\gamma_1}{k_1^2}\frac{\tan(\gamma_1 l_1)\tan(\gamma_2 l_2)\,\gamma_1\gamma_3 k_2^4 - \gamma_2\gamma_3 k_1^2 k_2^2 + i\gamma_2^2 k_1^2\,k_3^2\tan(\gamma_2 l_2) + i\tan(\gamma_1 l_1)\,\gamma_1\gamma_2 k_2^2 k_3^2}{\gamma_2^2 k_1^2 k_3^2\tan(\gamma_2 l_2)\tan(\gamma_1 l_1) - \gamma_1\gamma_2 k_2^2 k_3^2 + i\tan(\gamma_1 l_1)\,\gamma_2\gamma_3 k_1^2 k_2^2 + i\tan(\gamma_2 l_2)\,\gamma_1\gamma_3 k_2^4}} \quad \text{(A3-6)}$$

The expression for *Q+1* is then found by algebraic manipulation:

$$Q+1 = \frac{\begin{aligned}&\text{-}2ik_0^2\gamma_1(i\tan(\gamma_1 l_1)\tan(\gamma_2 l_2)\,\gamma_1\gamma_3 k_2^4 - i\gamma_2\gamma_3 k_1^2 k_2^2 - \gamma_2^2 k_1^2\,k_3^2\tan(\gamma_2 l_2) - \\ &\tan(\gamma_1 l_1)\,\gamma_1\gamma_2 k_2^2 k_3^2)\end{aligned}}{\begin{aligned}&\gamma_0\gamma_2^2 k_1^4 k_3^2\tan(\gamma_2 l_2)\tan(\gamma_1 l_1) - \gamma_0\gamma_1\gamma_2 k_1^2 k_2^2 k_3^2 + i\gamma_0\gamma_2\gamma_3 k_1^4 k_2^2\tan(\gamma_1 l_1) \\ &+ i\,\gamma_0\gamma_1\gamma_3 k_1^2 k_2^4\tan(\gamma_2 l_2) + \gamma_1^2\gamma_3 k_0^2 k_2^4\tan(\gamma_1 l_1)\tan(\gamma_2 l_2) \\ &- \gamma_1\gamma_2\gamma_3 k_0^2 k_1^2 k_2^2 \\ &+ i\gamma_1\gamma_2^2 k_0^2 k_1^2\,k_3^2\tan(\gamma_2 l_2) + i\gamma_1^2\gamma_2 k_0^2 k_2^2 k_3^2\tan(\gamma_1 l_1)\end{aligned}} \quad \text{(A3-7)}$$

Which may also be expressed as:

$$Q+1 = \frac{2ik_0^2\gamma_1 A(\lambda)}{q(\lambda)} \quad \text{(A3-8)}$$

Where, having multiplied numerator and denominator by $1/k_1^2k_2^2$:

$$A(\lambda) = -\frac{i\gamma_1\gamma_3 k_2^2\tan(\gamma_1 l_1)\tan(\gamma_2 l_2)}{k_1^2} + i\gamma_2\gamma_3 + \frac{\gamma_2^2\,k_3^2\tan(\gamma_2 l_2)}{k_2^2} + \frac{\gamma_1\gamma_2 k_3^2\tan(\gamma_1 l_1)}{k_1^2} \quad \text{(A3-9)}$$

$$q(\lambda) = \frac{\gamma_0\gamma_2^2k_1^2k_3^2\tan(\gamma_1 l_1)\tan(\gamma_2 l_2)}{k_2^2} - \gamma_0\gamma_1\gamma_2k_3^2 + i\gamma_0\gamma_2\gamma_3k_1^2\tan(\gamma_1 l_1)$$

$$+ i\,\gamma_0\gamma_1\gamma_3k_2^2\tan(\gamma_2 l_2) + \frac{\gamma_1^2\gamma_3k_0^2k_2^2\tan(\gamma_1 l_1)\tan(\gamma_2 l_2)}{k_1^2} - \gamma_1\gamma_2\gamma_3k_0^2 \qquad \text{(A3-10)}$$

$$+ \frac{i\gamma_1\gamma_2^2k_0^2k_3^2\tan(\gamma_2 l_2)}{k_2^2} + \frac{i\gamma_1^2\gamma_2k_0^2k_3^2\tan(\gamma_1 l_1)}{k_1^2}$$

This is then substituted into the equations for the field due to vertical electric dipole as follows:

$$B_{0\phi}^{(3)}(\rho,z) = \frac{1}{2}\frac{i\mu_0}{4\pi}\int_{-\infty}^{\infty}\left[-(Q+1)e^{i\gamma_0(z+d)}\right]\gamma_0^{-1}H_1^{(1)}(\lambda\rho)\lambda^2 d\lambda \qquad \text{(A3-11)}$$

Substituting (A3-8) into (A3-11):

$$B_{0\phi}^{(3)}(\rho,z) = \frac{1}{2}\frac{i\mu_0}{4\pi}\int_{-\infty}^{\infty}\left[-\left(\frac{2ik_0^2\gamma_1A(\lambda)}{q(\lambda)}\right)e^{i\gamma_0(z+d)}\right]\gamma_0^{-1}H_1^{(1)}(\lambda\rho)\lambda^2 d\lambda \qquad \text{(A3-12)}$$

After making minor simplifications:

$$B_{0\phi}^{(3)}(\rho,z) = \frac{k_0^2\mu_0}{4\pi}\int_{-\infty}^{\infty}\left[\left(\frac{A(\lambda)}{q(\lambda)}\right)\gamma_1e^{i\gamma_0(z+d)}\right]\gamma_0^{-1}H_1^{(1)}(\lambda\rho)\lambda^2 d\lambda \qquad \text{(A3-13)}$$

Similarly:

$$E_{0\rho}^{(3)}(\rho,z) = \frac{\omega\mu_0}{4\pi}\int_{-\infty}^{\infty}\left[\left(\frac{A(\lambda)}{q(\lambda)}\right)\gamma_1e^{i\gamma_0(z+d)}\right]H_1^{(1)}(\lambda\rho)\lambda^2 d\lambda \qquad \text{(A3-14)}$$

$$E_{0z}^{(3)}(\rho,z) = \frac{i\omega\mu_0}{4\pi}\int_{0}^{\infty}\left[\left(\frac{A(\lambda)}{q(\lambda)}\right)\gamma_1e^{i\gamma_0(z+d)}\right]\gamma_0^{-1}H_0^{(1)}(\lambda\rho)\lambda^3 d\lambda \qquad \text{(A3-15)}$$

APPENDIX 4

SUPPORTING EVIDENCE FOR ERRORS IN THE LITERATURE DISCUSSING PROPAGATION IN LAYERED MEDIA

This appendix provides the supporting derivations, and figures, for the errors which have been found in the literature relating to the propagation of electromagnetic fields in layered media. The errors which have been found are stated in section 4.4.

SIGN ERROR IN ZHANG ET AL. (2004) EQUATIONS 9 – 11

This section demonstrates the sign error in 3 equations by Zhang *et al.* (2004).

Zhang *et al.* (2004) equation (4):

$$Q = -\frac{\frac{\gamma_0}{k_0^2} - \frac{\gamma_2}{k_2^2} - i\left(\frac{\gamma_0}{k_0^2}\frac{\gamma_2}{k_2^2}\frac{k_1^2}{\gamma_1} - \frac{\gamma_1}{k_1^2}\right)\tan(\gamma_1 l_1)}{\frac{\gamma_0}{k_0^2} + \frac{\gamma_2}{k_2^2} - i\left(\frac{\gamma_0}{k_0^2}\frac{\gamma_2}{k_2^2}\frac{k_1^2}{\gamma_1} + \frac{\gamma_1}{k_1^2}\right)\tan(\gamma_1 l_1)} \tag{A4-16}$$

Adding one with a common denominator:

$$Q + 1 = \frac{-\frac{\gamma_0}{k_0^2} + \frac{\gamma_2}{k_2^2} + i\left(\frac{\gamma_0}{k_0^2}\frac{\gamma_2}{k_2^2}\frac{k_1^2}{\gamma_1} - \frac{\gamma_1}{k_1^2}\right)\tan(\gamma_1 l_1) + \frac{\gamma_0}{k_0^2} + \frac{\gamma_2}{k_2^2} - i\left(\frac{\gamma_0}{k_0^2}\frac{\gamma_2}{k_2^2}\frac{k_1^2}{\gamma_1} + \frac{\gamma_1}{k_1^2}\right)\tan(\gamma_1 l_1)}{\frac{\gamma_0}{k_0^2} + \frac{\gamma_2}{k_2^2} - i\left(\frac{\gamma_0}{k_0^2}\frac{\gamma_2}{k_2^2}\frac{k_1^2}{\gamma_1} + \frac{\gamma_1}{k_1^2}\right)\tan(\gamma_1 l_1)} \tag{A4-17}$$

Eliminating common terms:

$$Q + 1 = \frac{2\frac{\gamma_2}{k_2^2} + i\left(\frac{\gamma_0}{k_0^2}\frac{\gamma_2}{k_2^2}\frac{k_1^2}{\gamma_1} - \frac{\gamma_1}{k_1^2}\right)\tan(\gamma_1 l_1) - i\left(\frac{\gamma_0}{k_0^2}\frac{\gamma_2}{k_2^2}\frac{k_1^2}{\gamma_1} + \frac{\gamma_1}{k_1^2}\right)\tan(\gamma_1 l_1)}{\frac{\gamma_0}{k_0^2} + \frac{\gamma_2}{k_2^2} - i\left(\frac{\gamma_0}{k_0^2}\frac{\gamma_2}{k_2^2}\frac{k_1^2}{\gamma_1} + \frac{\gamma_1}{k_1^2}\right)\tan(\gamma_1 l_1)} \tag{A4-18}$$

Simplifies to:

$$Q+1=-2\frac{-\frac{\gamma_2}{k_2^2}+i\left(\frac{\gamma_1}{k_1^2}\right)\tan(\gamma_1 l_1)}{\frac{\gamma_0}{k_0^2}+\frac{\gamma_2}{k_2^2}-i\left(\frac{\gamma_0}{k_0^2}\frac{\gamma_2}{k_2^2}\frac{k_1^2}{\gamma_1}+\frac{\gamma_1}{k_1^2}\right)\tan(\gamma_1 l_1)} \tag{A4-19}$$

Taking the equation for magnetic field (Zhang *et al.*, 2004, equation 1):

$$B_{0\varphi}^{(3)}=\frac{i\mu_0}{4\pi}\int_0^\infty\left[-(Q+1)e^{i\gamma_0(z+d)}\right]\gamma_0^{-1}J_1(\lambda\rho)\lambda^2 d\lambda \tag{A4-20}$$

Changing to the Hankel function:

$$B_{0\varphi}^{(3)}=\frac{i\mu_0}{4\pi}\int_{-\infty}^\infty\left[-(Q+1)e^{i\gamma_0(z+d)}\right]\gamma_0^{-1}\frac{H_1^{(1)}}{2}(\lambda\rho)\lambda^2 d\lambda \tag{A4-21}$$

Substitute in *Q+1* and eliminate the multiple of 2 in the numerator and denominator:

$$B_{0\varphi}^{(3)}=\frac{i\mu_0}{4\pi}\int_{-\infty}^\infty-\left[-\frac{-\frac{\gamma_2}{k_2^2}+i\left(\frac{\gamma_1}{k_1^2}\right)\tan(\gamma_1 l_1)}{\frac{\gamma_0}{k_0^2}+\frac{\gamma_2}{k_2^2}-i\left(\frac{\gamma_0}{k_0^2}\frac{\gamma_2}{k_2^2}\frac{k_1^2}{\gamma_1}+\frac{\gamma_1}{k_1^2}\right)\tan(\gamma_1 l_1)}\right]\frac{e^{i\gamma_0(z+d)}H_1^{(1)}(\lambda\rho)\lambda^2}{\gamma_0}d\lambda \tag{A4-22}$$

Gathering terms for ease of expression, and eliminating two negatives:

$$B_{0\varphi}^{(3)}=\frac{i\mu_0}{4\pi}\int_{-\infty}^\infty\frac{A(\lambda)}{q(\lambda)}\frac{e^{i\gamma_0(z+d)}H_1^{(1)}(\lambda\rho)\lambda^2}{\gamma_0}d\lambda \tag{A4-23}$$

Where:

$$A(\lambda)=-\frac{\gamma_2}{k_2^2}+i\frac{\gamma_1}{k_1^2}\tan(\gamma_1 l_1) \tag{A4-24}$$

$$q(\lambda)=\frac{\gamma_0}{k_0^2}+\frac{\gamma_2}{k_2^2}-i\left(\frac{\gamma_0}{k_0^2}\frac{\gamma_2}{k_2^2}\frac{k_1^2}{\gamma_1}+\frac{\gamma_1}{k_1^2}\right)\tan(\gamma_1 l_1) \tag{A4-25}$$

Comparing equations (A4-23) - (A4-25) with the equivalent expressions by Zhang *et al.* (2004) reveals a sign error between (A4-23) and its equivalent. The derivation above is entirely based on the equations given by Zhang *et al.* (2004). Therefore, it must be concluded that a sign error exists in equations 9 – 11 of Zhang *et al.* (2004).

PLOTS SHOWING ROOTS OF Q(Λ) VS. L BY ZHANG ET AL. (2004) ARE ERRONEOUS

Zhang *et al.* (2004) present roots of $q(\lambda)$ for increasing values of thickness of the dielectric layer, *l*. The similar figures presented by Zhang and Pan (2002) are criticised above for creating difficulty in repeating their results by neglecting to state all of the roots are required to evaluate the trapped surface wave. The same criticism can be made of the plots presented by Zhang *et al.* (2004). However, the plots by Zhang *et al.* (2004) not only contain omissions, but are erroneous.

Figure A4-1 and Figure A4-2 give the results presented by Zhang *et al.* (2004), these were found using a Newton-Raphson iteration method, see Mathews (1992) for further explanation. Attempts were made to reproduce the results shown in Figure A4-1 and Figure A4-2, using a simplex search implemented in Matlab (Lagarias *et al.*, 1998). The simplex search was used to find two sets of results, the real component propagation constant was constrained to be positive (Figure A4-3; Figure A4-4), and the propagation constant was allowed to be positive or negative in the second set (Figure A4-5; Figure A4-6).

Figure A4-1: Real component of the first root of $q(\lambda)$ vs thickness of the dielectric layer, *l*. (Zhang *et al.*, 2004, Fig. 3)

Figure A4-2: Real component of the first root of $q(\lambda)$ vs thickness of the dielectric layer, *l*. (Zhang *et al.*, 2004, Fig. 4) © 2004 Taylor & Francis

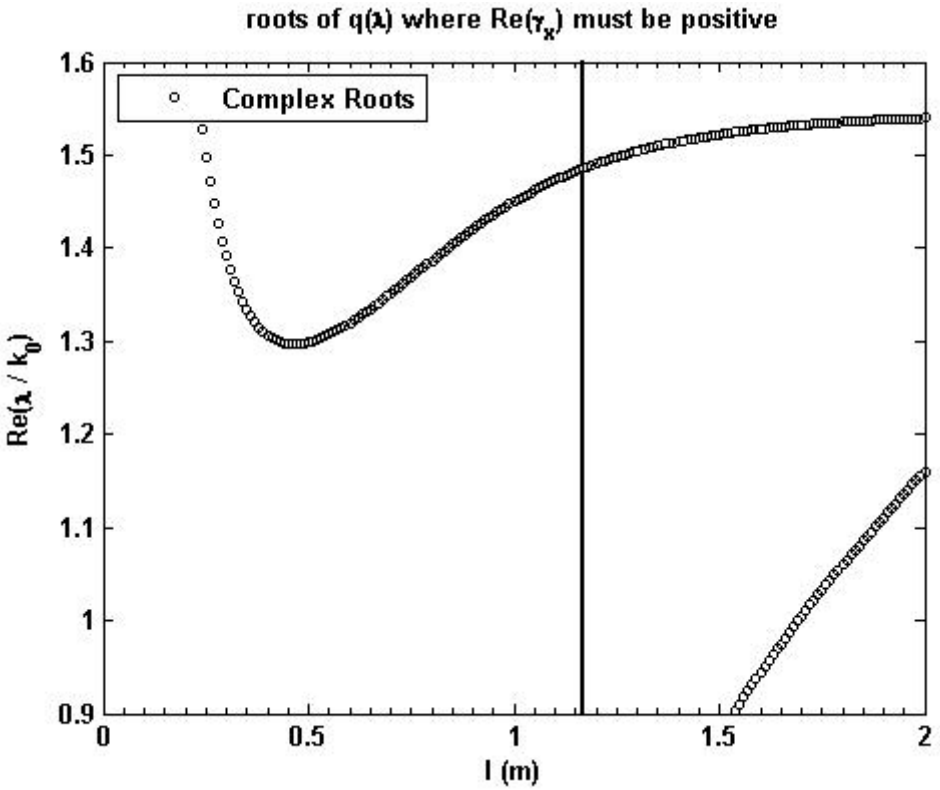

Figure A4-3: Real component of the roots of $q(\lambda)$ vs thickness of the dielectric layer, *l*. The real component of the propagation constant must be positive.

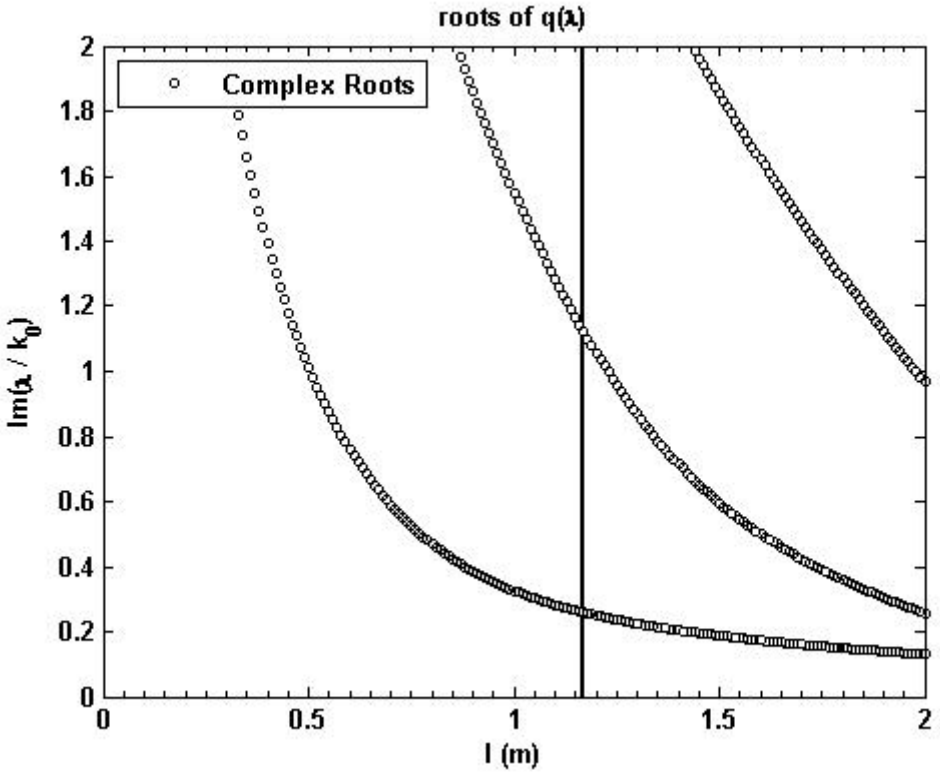

Figure A4-4: Imaginary component of the roots of $q(\lambda)$ vs thickness of the dielectric layer, *l*. The real component of the propagation constant must be positive.

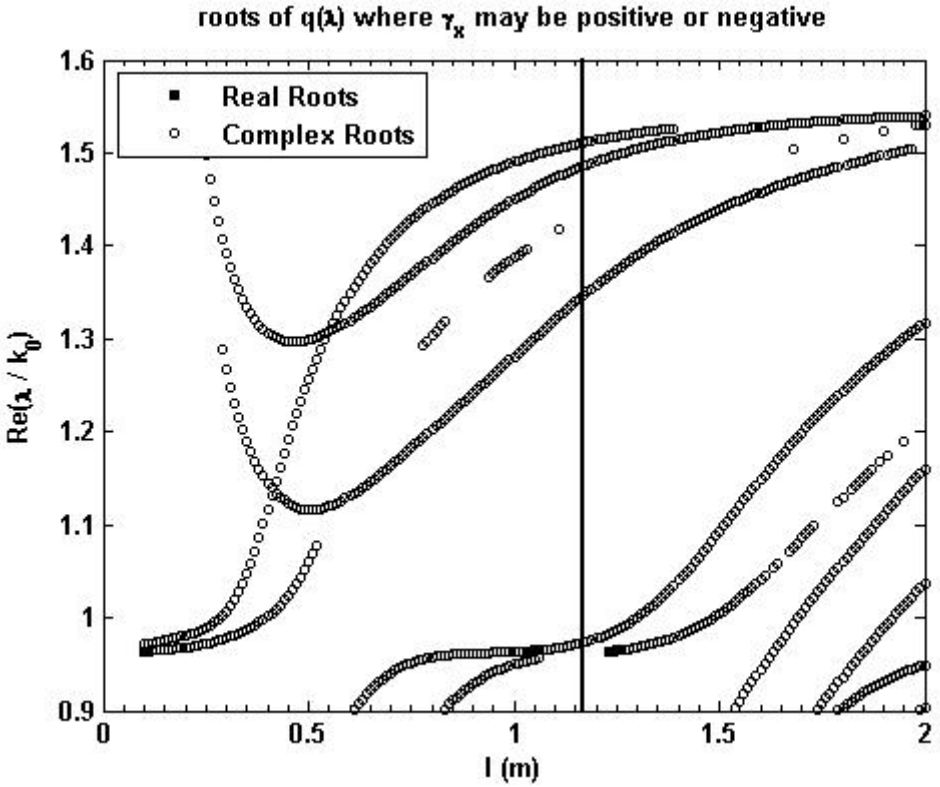

Figure A4-5: Real component of the roots of $q(\lambda)$ vs thickness of the dielectric layer, *l*. The propagation constant may be positive or negative.

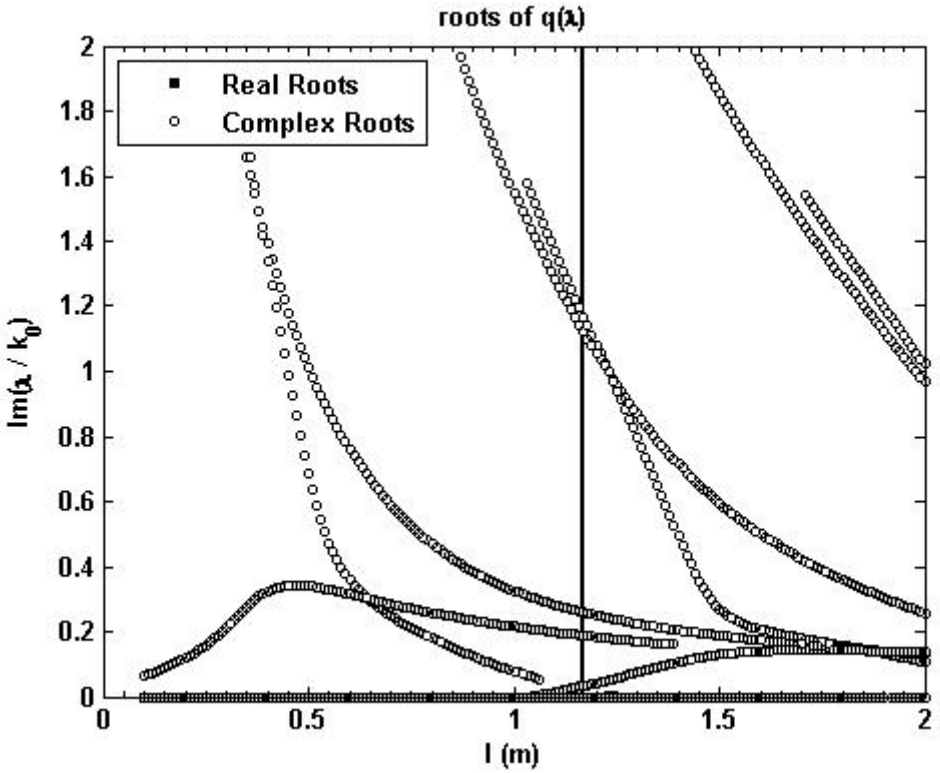

Figure A4-6: Imaginary component of the roots of $q(\lambda)$ vs thickness of the dielectric layer, l. The propagation constant may be positive or negative.

It is clear when comparing the results shown (Figure A4-3-Figure A4-6) here with those of Zhang *et al.* (2004) (Figure A4-1; Figure A4-2) that the results which are comparable are those where the propagation constant is allowed to be positive or negative. The correct results, where the real component of the propagation constant is positive, show fewer roots with a different curve.

When using numerical root finding algorithms, with complex functions, there is always a concern that roots may be missed or values may be erroneously identified as roots. To confirm those results presented above, a graphical representation of the function $q(\lambda)$ is shown below where $l = 0.25$. The roots as shown in Figure A4-3 and Figure A4-4 are supported, whereas the roots shown in Figure A4-1 and Figure A4-2 are not supported.

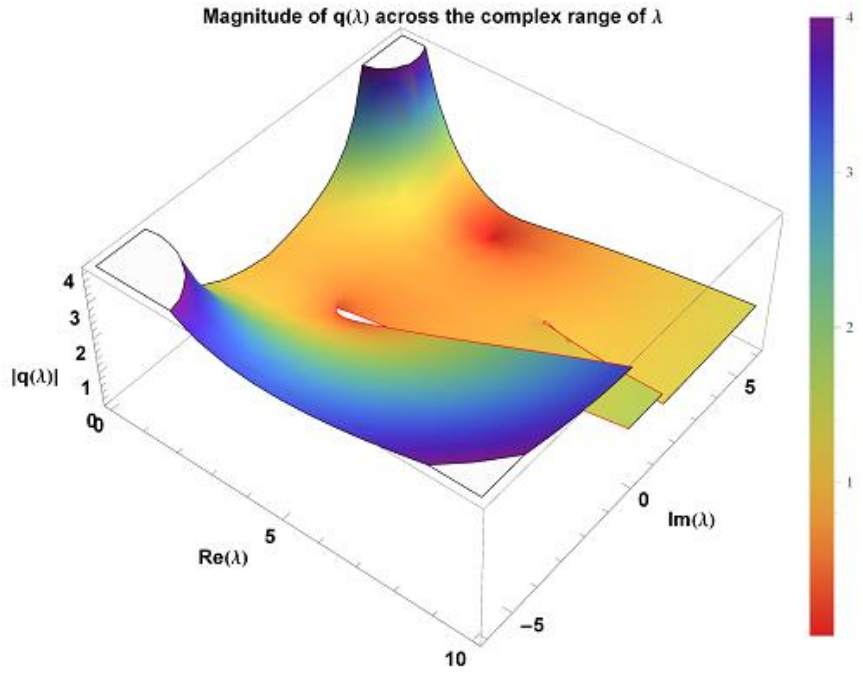

Figure A4-7: Three dimensional graphical representation of $|q(\lambda)|$ where l=0.25 as defined by Zhang *et al.* (2004). A root is visible at $\lambda = 3.1 + 5.2i$. In addition, two branch cuts are shown. The root at approximately $\lambda = 2 + 0.3i$ shown in Figure A4-1 and Figure A4-2 is not present.

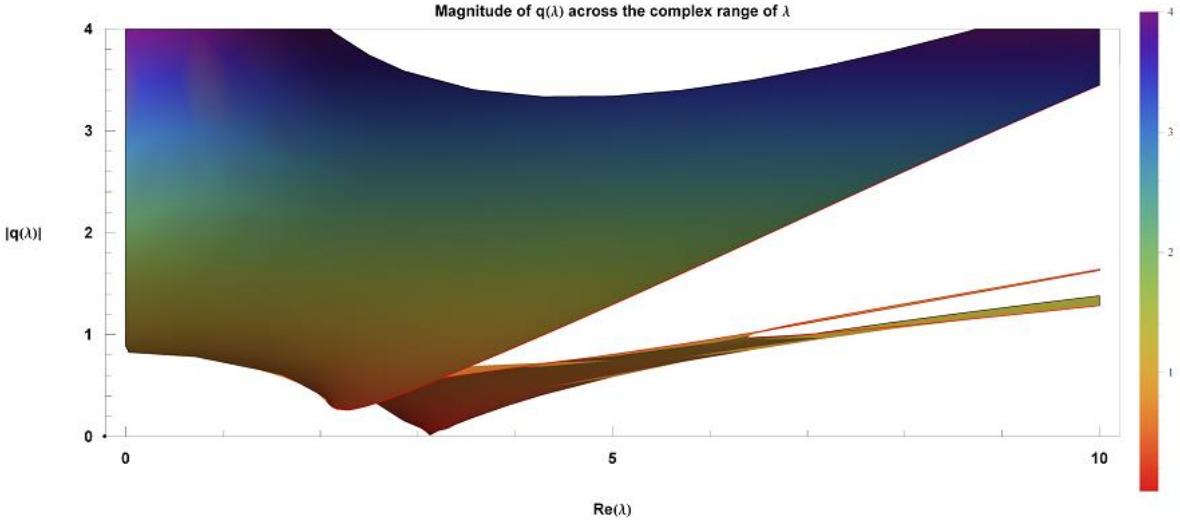

Figure A4-8: Front view of the three dimensional graphical representation of $|q(\lambda)|$ where l=0.25 as defined by Zhang *et al.* (2004). A root is visible at $\lambda = 3.1 + 5.2i$ and can be seen to reach 0. In addition, branch cuts are shown at two points. The root at approximately $\lambda = 2 + 0.3i$ shown in Figure A4-1 and Figure A4-2 is not present.

APPENDIX 5

VALIDATION OF MODEL DERIVED IN CHAPTER 4 BY COMPARING TO PREVIOUS RESULTS

This appendix takes the model derived in Chapter 4 and validates it against two previous publications. This is achieved by making assumptions necessary simplify the model presented in Chapter 4 to the cases covered by the earlier publications. Both simplifications begin from the expression derived for the term *Q:*

$$-Q = \frac{\gamma_0 - \frac{k_0^2\gamma_1}{k_1^2}\frac{\tan(\gamma_1 l_1)\tan(\gamma_2 l_2)\gamma_1\gamma_3 k_2^4 - \gamma_2\gamma_3 k_1^2 k_2^2 + i\gamma_2^2 k_1^2 k_3^2\tan(\gamma_2 l_2) + i\tan(\gamma_1 l_1)\gamma_1\gamma_2 k_2^2 k_3^2}{\gamma_2^2 k_1^2 k_3^2\tan(\gamma_1 l_1)\tan(\gamma_2 l_2) - \gamma_1\gamma_2 k_2^2 k_3^2 + i\tan(\gamma_1 l_1)\gamma_2\gamma_3 k_1^2 k_2^2 + i\tan(\gamma_2 l_2)\gamma_1\gamma_3 k_2^4}}{\gamma_0 + \frac{k_0^2\gamma_1}{k_1^2}\frac{\tan(\gamma_1 l_1)\tan(\gamma_2 l_2)\gamma_1\gamma_3 k_2^4 - \gamma_2\gamma_3 k_1^2 k_2^2 + i\gamma_2^2 k_1^2 k_3^2\tan(\gamma_2 l_2) + i\tan(\gamma_1 l_1)\gamma_1\gamma_2 k_2^2 k_3^2}{\gamma_2^2 k_1^2 k_3^2\tan(\gamma_2 l_2)\tan(\gamma_1 l_1) - \gamma_1\gamma_2 k_2^2 k_3^2 + i\tan(\gamma_1 l_1)\gamma_2\gamma_3 k_1^2 k_2^2 + i\tan(\gamma_2 l_2)\gamma_1\gamma_3 k_2^4}} \quad \text{(A5 - 1)}$$

VALIDATION AGAINST THE THREE LAYERED CASE

The work by Zhang *et al.* (2004) calculated the field due to a vertical electric dipole above a three layered geometry which did not include a perfectly conductive base layer. By assuming that layer 3 has zero thickness, the model presented in Chapter 4 may be simplified to cover the same scenario.

Setting $k_2 = k_3$ and if $l_2 = 0$ allows the following simplification to (A5 - 1):

$$-Q = \frac{\gamma_0 - \frac{k_0^2\gamma_1}{k_1^2}\frac{-\gamma_2\gamma_2 k_1^2 k_2^2 + i\tan(\gamma_1 l_1)\gamma_1\gamma_2 k_2^2 k_2^2}{-\gamma_1\gamma_2 k_2^2 k_2^2 + i\tan(\gamma_1 l_1)\gamma_2\gamma_2 k_1^2 k_2^2}}{\gamma_0 + \frac{k_0^2\gamma_1}{k_1^2}\frac{-\gamma_2\gamma_2 k_1^2 k_2^2 + i\tan(\gamma_1 l_1)\gamma_1\gamma_2 k_2^2 k_2^2}{-\gamma_1\gamma_2 k_2^2 k_2^2 + i\tan(\gamma_1 l_1)\gamma_2\gamma_2 k_1^2 k_2^2}} \quad \text{(A5 - 2)}$$

Which is further simplified to:

$$-Q = \frac{\frac{\gamma_0}{k_0^2} - \left(\frac{-\gamma_1\gamma_2\gamma_2 k_1^2 + i\tan(\gamma_1 l_1)\,\gamma_1\gamma_1\gamma_2 k_2^2}{-\gamma_1\gamma_2 k_1^2 k_2^2 + i\tan(\gamma_1 l_1)\,\gamma_2\gamma_2 k_1^2 k_1^2}\right)}{\frac{\gamma_0}{k_0^2} + \left(\frac{-\gamma_1\gamma_2\gamma_2 k_1^2 + i\tan(\gamma_1 l_1)\,\gamma_1\gamma_1\gamma_2 k_2^2}{-\gamma_1\gamma_2 k_1^2 k_2^2 + i\tan(\gamma_1 l_1)\,\gamma_2\gamma_2 k_1^2 k_1^2}\right)} \qquad \text{(A5 - 3)}$$

By expanding terms and removing the common denominator the following expression is derived:

$$-Q = \frac{\gamma_0\gamma_1\gamma_2 k_1^2 k_2^2 - \gamma_1\gamma_2\gamma_2 k_0^2 k_1^2 - i(\gamma_0\gamma_2\gamma_2 k_1^2 k_1^2 - \gamma_1\gamma_1\gamma_2 k_0^2 k_2^2)\tan(\gamma_1 l_1)}{\gamma_0\gamma_1\gamma_2 k_1^2 k_2^2 + \gamma_1\gamma_2\gamma_2 k_0^2 k_1^2 - i(\gamma_0\gamma_2\gamma_2 k_1^2 k_1^2 + \gamma_1\gamma_1\gamma_2 k_0^2 k_2^2)\tan(\gamma_1 l_1)} \qquad \text{(A5 - 4)}$$

Finally, by multiplying numerator and denominator by $1/k_0^2 k_1^2 k_2^2 \gamma_1\gamma_2$ (A5 - 5) is reached is the equation for the term Q given by Zhang *et al.* (2004).

$$-Q = \frac{\frac{\gamma_0}{k_0^2} - \frac{\gamma_2}{k_2^2} - i\left(\frac{\gamma_0\gamma_2 k_1^2}{\gamma_1 k_0^2 k_2^2} - \frac{\gamma_1}{k_1^2}\right)\tan(\gamma_1 l_1)}{\frac{\gamma_0}{k_0^2} + \frac{\gamma_2}{k_2^2} - i\left(\frac{\gamma_0\gamma_2 k_1^2}{\gamma_1 k_0^2 k_2^2} + \frac{\gamma_1}{k_1^2}\right)\tan(\gamma_1 l_1)} \qquad \text{(A5 - 5)}$$

The remainder of the derivation given in Appendix 3 is based on the expression for Q, shown here to be in agreement with previous publications where the geometry is assumed to be three layered.

VALIDATION AGAINST A SIMPLIFIED FOUR LAYERED CASE

The work by Xu *et al.* (2008) calculated the field due to a vertical electric dipole above a four layered geometry with a perfectly conductive base layer. By assuming that layer 4 has infinite conductivity, the model presented in Chapter 4 may be simplified to cover the same scenario.

Setting $k_3 \to \infty$ allows simplification of (A5 - 1) with the assumption that the fourth layer is perfectly conductive. Considering the numerator of (A5 - 1), expanding the terms, and rearranging so all k_3 terms fall on the denominators gives:

$$Numerator = \gamma_0$$

$$-\left[\frac{\gamma_1^2\gamma_3 k_0^2 k_2^4 \tan(\gamma_1 l_1)\tan(\gamma_2 l_2)}{\gamma_2^2 k_1^4 k_3^2 \tan(\gamma_2 l_2)\tan(\gamma_1 l_1) - \gamma_1\gamma_2 k_1^2 k_2^2 k_3^2 + i\gamma_2\gamma_3 k_1^4 k_2^2 \tan(\gamma_1 l_1) + i\,\gamma_1\gamma_3 k_1^2 k_2^4 \tan(\gamma_2 l_2)}\right.$$

$$-\frac{\gamma_1\gamma_2\gamma_3 k_0^2 k_1^2 k_2^2}{\gamma_2^2 k_1^4 k_3^2 \tan(\gamma_2 l_2)\tan(\gamma_1 l_1) - \gamma_1\gamma_2 k_1^2 k_2^2 k_3^2 + i\gamma_2\gamma_3 k_1^4 k_2^2 \tan(\gamma_1 l_1) + i\,\gamma_1\gamma_3 k_1^2 k_2^4 \tan(\gamma_2 l_2)} \qquad \text{(A5 - 6)}$$

$$+\frac{i\gamma_1\gamma_2^2 k_0^2 k_1^2 \tan(\gamma_2 l_2)}{\gamma_2^2 k_1^4 \tan(\gamma_2 l_2)\tan(\gamma_1 l_1) - \gamma_1\gamma_2 k_1^2 k_2^2 + \frac{i\gamma_2\gamma_3 k_1^4 k_2^2 \tan(\gamma_1 l_1)}{k_3^2} + \frac{i\,\gamma_1\gamma_3 k_1^2 k_2^4 \tan(\gamma_2 l_2)}{k_3^2}}$$

$$\left.+\frac{i\tan(\gamma_1 l_1)\,\gamma_1^2\gamma_2 k_0^2 k_2^2}{\gamma_2^2 k_1^4 \tan(\gamma_2 l_2)\tan(\gamma_1 l_1) - \gamma_1\gamma_2 k_1^2 k_2^2 + \frac{i\gamma_2\gamma_3 k_1^4 k_2^2 \tan(\gamma_1 l_1)}{k_3^2} + \frac{i\,\gamma_1\gamma_3 k_1^2 k_2^4 \tan(\gamma_2 l_2)}{k_3^2}}\right]$$

Elimating terms where $k_3 \to \infty$ gives:

$$Numerator = \gamma_0 + \frac{i\gamma_1 k_0^2}{k_1^2}\left[\frac{\gamma_1 k_2^2 \tan(\gamma_1 l_1) + \gamma_2 k_1^2 \tan(\gamma_2 l_2)}{\gamma_1 k_2^2 - \gamma_2 k_1^2 \tan(\gamma_2 l_2)\tan(\gamma_1 l_1)}\right] \qquad \text{(A5 - 7)}$$

Similarly:

$$Denominator = \gamma_0 - \frac{i\gamma_1 k_0^2}{k_1^2}\left[\frac{\gamma_1 k_2^2 \tan(\gamma_1 l_1) + \gamma_2 k_1^2 \tan(\gamma_2 l_2)}{\gamma_1 k_2^2 - \gamma_2 k_1^2 \tan(\gamma_2 l_2)\tan(\gamma_1 l_1)}\right] \qquad \text{(A5 - 8)}$$

Giving an expression for Q:

$$-Q|_{k_3\to\infty} = \frac{\gamma_0 + \frac{i\gamma_1 k_0^2}{k_1^2}\left[\frac{\gamma_1 k_2^2 \tan(\gamma_1 l_1) + \gamma_2 k_1^2 \tan(\gamma_2 l_2)}{\gamma_1 k_2^2 - \gamma_2 k_1^2 \tan(\gamma_2 l_2)\tan(\gamma_1 l_1)}\right]}{\gamma_0 - \frac{i\gamma_1 k_0^2}{k_1^2}\left[\frac{\gamma_1 k_2^2 \tan(\gamma_1 l_1) + \gamma_2 k_1^2 \tan(\gamma_2 l_2)}{\gamma_1 k_2^2 - \gamma_2 k_1^2 \tan(\gamma_2 l_2)\tan(\gamma_1 l_1)}\right]} \qquad \text{(A5 - 9)}$$

Which is equation 7 from the work by Xu *et al.* (2008). As with the case of the three layered scenario, once Q has been shown to equate to the previous works the remainder of the analysis must be equivalent under this assumption.

APPENDIX 6

SOURCE CODE TO SYNCHRONISE TWO NATIONAL INSTRUMENTS DATA ACQUISITION

CHASSIS USING MATLAB

The complete source code has not been included here. The commands specific to the National Instruments equipment are included which is sufficient for repetition of the method.

RECEIVING CHASSIS (CLOCK RECIPIENT)

```
% Create new task
[Status,TaskNameText,TaskHandle1]  =
calllib('nicaiu','DAQmxCreateTask',InputTaskName,TaskHandle1);

% Create new input voltage channels
[Status,ChannelNameText,c,d]  =
calllib('nicaiu','DAQmxCreateAIVoltageChan',TaskHandle1Numeric,AIConfigStri
ng,'',DAQmx_Val_Diff,minVal,maxVal,DAQmx_Val_Volts,'');

% Configure AI clock timebase source
[Status] =
calllib('nicaiu','DAQmxSetSampClkTimebaseSrc',TaskHandle1Numeric,'/cDAQ1/PF
I0');

% Configure AI clock timebase rate (pre-requisite for external clock)
timebasedata = 2e6;
    [Status] =
calllib('nicaiu','DAQmxSetSampClkTimebaseRate',TaskHandle1Numeric,timebased
ata);
timebasedata = double(InputSamplingRate);
[Status] =
calllib('nicaiu','DAQmxSetSampClkRate',TaskHandle1Numeric,timebasedata);

% Start the task
Status = calllib('nicaiu','DAQmxStartTask',TaskHandle1Numeric);

% Read the data
RecoveredInputData = zeros(InputSamplesPerChannel*NumberOfRXChannels,1);
RecoveredInputDataPtr  =
libpointer('doublePtr',zeros(InputSamplesPerChannel*NumberOfRXChannels,1));
[Status,RecoveredData,DAQmxReadAnalogF64Return1,DAQmxReadAnalogF64Return2]
=
calllib('nicaiu','DAQmxReadAnalogF64',TaskHandle1Numeric,int32(InputSamples
PerChannel),Timeout,FillMode,RecoveredInputDataPtr,uint32(InputSamplesPerCh
annel*NumberOfRXChannels),ReadPtr,ReservedPtr);
RecoveredData =
reshape(RecoveredData,NumberOfRXChannels,InputSamplesPerChannel);

% Stop the task
Status = calllib('nicaiu','DAQmxStopTask',TaskHandle1Numeric);
Status = calllib('nicaiu','DAQmxClearTask',TaskHandle1Numeric);
```

TRANSMITTING CHASSIS (CLOCK SOURCE)

```
% Create New Tasks
[Status,TaskNameText,TaskHandle2]  =
calllib('nicaiu','DAQmxCreateTask',OutputTaskName,TaskHandle2);

% Create Voltage Output Channels
[Status,ChannelNameText,c,d]  =
calllib('nicaiu','DAQmxCreateAOVoltageChan',TaskHandle2Numeric,AOConfigStri
ng,'',minVal,maxVal,DAQmx_Val_Volts,'');

%  Set the analog output to trigger off internal clock
SamplesToAcquire = uint64(TrueOutputSamplesPerChannel);
[Status,ClockSource] =
calllib('nicaiu','DAQmxCfgSampClkTiming',TaskHandle2Numeric,'OnboardClock',
TrueOutputSamplingRate,ActiveEdge,SampleMode,SamplesToAcquire);

% Write Output Signal
SamplesPerChannelWritten = libpointer('int32Ptr',0);
[Status,DAQmxWriteAnalogF64Return1,DAQmxWriteAnalogF64Return2] =
calllib('nicaiu','DAQmxWriteAnalogF64',TaskHandle2Numeric,int32(TrueOutputS
amplesPerChannel),int32(0),double(-
1),DAQmx_Val_GroupByScanNumber,[TXSignal;TriggerSignal],SamplesPerChannelWr
itten,[]);

% Route Sample Clock To PFI0
[Status,SignalExport] =
calllib('nicaiu','DAQmxExportSignal',TaskHandle2Numeric,DAQmx_Val_SampleClo
ck,'/cDAQ1/PFI0');

% Start Task
Status = calllib('nicaiu','DAQmxStartTask',TaskHandle2Numeric);

% Wait for Command To Execute
[Status] = calllib('nicaiu','DAQmxWaitUntilTaskDone',TaskHandle2Numeric,-
1);

% Stop Task
Status = calllib('nicaiu','DAQmxStopTask',TaskHandle2Numeric);
Status = calllib('nicaiu','DAQmxClearTask',TaskHandle2Numeric);

% Disconnect Routing
[Status] =
calllib('nicaiu','DAQmxDisconnectTerms','/cDAQ1/ao/StartTrigger','/cDAQ1/PF
I1');
```

REFERENCES

AGILENT. 2000. Understanding the Fundamental Principles of Vector Network Analysis. Available: http://cp.literature.agilent.com/litweb/pdf/5965-7707E.pdf [Accessed 26 August 2010].

AGILENT 2004. De-embedding and Embedding S-Parameter Networks Using a Vector Network Analyzer.

AKTAS, M. & TUNCER, T. E. 2010. Iterative HOS-SOS (IHOSS) Algorithm for Direction-of-Arrival Estimation and Sensor Localization. *Signal Processing, IEEE Transactions on,* 58, 6181-6194.

AL HAGREY, S. 1994. Electric study of fracture anisotropy at Falkenberg, Germany. *Geophysics,* 59, 881-888.

ANALOG DEVICES INC. 2008. Analog Devices Data Sheet: AD8302. Available: http://www.analog.com/static/imported-files/data_sheets/ad8302.pdf [Accessed 26/02/2013].

ANNAN, A. P. 2002. GPR-History, Trends, and Future Developments. *Subsurface Sensing Technologies and Applications* 3, 18.

AZIZ, P. M., SORENSEN, H. V. & VN DER SPIEGEL, J. 1996. An overview of sigma-delta converters. *Signal Processing Magazine, IEEE,* 13, 61-84.

BAHER, H. 2001. *Analog & digital signal processing,* Chichester, John Wiley & Sons.

BAIER, T. C. 2009. A small, simple, USB-powered vector network analyzer covering 1kHz to 1.3 GHz. *QEX,* January/February 2009, 32 - 36.

BAKER-JARVIS, J. 1990. Transmission / Reflection and Short-Circuit Line Permittivity Measurements. *In:* NIST (ed.). Colorado, USA: NIST.

BAKER-JARVIS, J., JANEZIC, M. D., GROSVENOR JR, J. H.*, et al.* 1992. Transmission/Reflection and Short-Circuit Line Methods for Measuring Permittivity and Permeability. *In:* TECHNOLOGY, N. I. O. S. A. (ed.) *NASA STI/Recon Technical Report N.* Colorado, USA: National Institute of Standards and Technology.

BAKER-JARVIS, J., VANZURA, E. J. & KISSICK, W. A. 1990. Improved technique for determining complex permittivity with the transmission/reflection method. *Microwave Theory and Techniques, IEEE Transactions on,* 38, 1096-1103.

BARKER, B. & TEXAS INSTRUMENTS 2011a. How delta-sigma ADCs work, Part 1. *Analog Applications Journal,* Q3 2011.

BARKER, B. & TEXAS INSTRUMENTS 2011b. How delta-sigma ADCs work, Part 2. *Analog Applications Journal,* Q4 2011.

BARKER, R. D. 1989. Depth of investigation of collinear symmetrical four-electrode arrays. *Geophysics,* 54, 1031-1037.

BASSEN, H. I. & SMITH, G. S. 1983. Electric field probes--A review. *Antennas and Propagation, IEEE Transactions on,* 31, 710-718.

BENDAT, J. S. 1978. Statistical errors in measurement of coherence functions and input/output quantities. *Journal of Sound and Vibration,* 59, 405-421.

BENDAT, J. S. & PIERSOL, A. G. 1971. *Random data : analysis and measurement procedures,* New York ; Chichester, Wiley-Interscience.

BENNETT, W. R. 1948. Spectra of quantized signals. *Bell syst. tech. J,* 27, 446-472.

BIENKOWSKI, P. & TRZASKA, H. 2012. *Electromagnetic measurements in the near field,* Raleigh, N.C., Scitech Pub.

BOIS, K. J., HANDJOJO, L. F., BENALLY, A. D.*, et al.* 1999. Dielectric plug-loaded two-port transmission line measurement technique for dielectric property characterization of granular and liquid materials. *Instrumentation and Measurement, IEEE Transactions on,* 48, 1141-1148.

BOOTON, R. C. 1992. *Computational methods for electromagnetics and microwaves,* New York ; Chichester, Wiley.

BOUGHRIET, A. H., LEGRAND, C. & CHAPOTON, A. 1997. Noniterative stable transmission/reflection method for low-loss material complex permittivity determination. *Microwave Theory and Techniques, IEEE Transactions on,* 45, 52-57.

BOWEN, M., FRASER-SMITH, A. & MCGILL, P. 1992. Long-term averages of globally-measured ELF/VLF radio noise. DTIC Document.

BRILLINGER, D. 1985. A maximum likelihood approach to frequency-wavenumber analysis. *Acoustics, Speech and Signal Processing, IEEE Transactions on,* 33, 1076-1085.

CAMPBELL, J. E. 1990. Dielectric Properties and Influence of Conductivity in Soils at One to Fifty Megahertz. *Soil Science Society of America Journal,* 54, 332-341.

CARTER, G. C. 1987. Coherence and time delay estimation. *Proceedings of the IEEE,* 75, 236-255.

CASSIDY, N. J. 2009. Ground Penetrating Rader Data Processing, Modelling and Analysis. *In:* JOL, H. M. (ed.) *Ground penetrating radar [electronic resource] : theory and applications.* 1st ed. ed. Amsterdam, Netherlands ; Oxford, UK: Elsevier Science.
CHANG, D. & WAIT, J. R. 1974. Extremely Low Frequency (ELF) Propagation Along a Horizontal Wire Located Above or Buried in the Earth. *Communications, IEEE Transactions on,* 22, 421-427.
CHEN, Z., GOKEDA, G. & YU, Y. 2010. *Introduction to direction-of-arrival estimation,* Boston, Artech House.
CHEW, W. C., OLP, K. J. & OTTO, G. P. 1991. Design and Calibration of a Large Broad-Band Dielectric Measurement Cell. *IEEE Transactions on Geoscience and Remote Sensing,* 29, 42-47.
CLARKSON, T. S., GLASSER, L., TUXWORTH, R. W.*, et al.* 1977. An appreciation of experimental factors in time-domain spectroscopy. *Advances in Molecular Relaxation and Interaction Processes,* 10, 173-202.
COMSOL. 2013. Introduction to COMSOL Multiphysics. Available: http://www.comsol.asia/shared/downloads/IntroductionToCOMSOLMultiphysics.pdf [Accessed August 2013].
COOK, P. 1999. *Method and system for detecting and displaying defects in piping*. USA patent application 08/885,367.
COOLEY, J. W. & TUKEY, J. W. 1965. An Algorithm for the Machine Calculation of Complex Fourier Series. *Mathematics of Computation,* 19, 297-301.
CORWIN, D. L. & LESCH, S. M. 2003. Application of Soil Electrical Conductivity to Precision Agriculture. *Agronomy Journal,* 95, 455-471.
COSENZA, P., GHORBANI, A., REVIL, A.*, et al.* 2008. A physical model of the low-frequency electrical polarization of clay rocks. *Journal of Geophysical Research: Solid Earth,* 113, B08204.
COX, H. 1973. Resolving power and sensitivity to mismatch of optimum array processors. *The Journal of the Acoustical Society of America,* 54, 771-785.
CURIONI, G. 2013. *Investigating the seasonal variability of electromagnetic soil properties using field monitoring data from Time-Domain Reflectometry probes* PhD, University of Birmingham.
CURIONI, G., CHAPMAN, D. N., METJE, N.*, et al.* 2012. Construction and calibration of a field TDR monitoring station. *Near Surface Geophysics,* 10, 249 - 261.
DAHLIN, T. 2000. Short note on electrode charge-up effects in DC resistivity data acquisition using multi-electrode arrays. *Geophysical Prospecting,* 48, 181-187.
DAVIS, J. L. & ANNAN, A. P. 1989. Ground-Penetrating Radar for High-Resolution Mapping of Soil and Rock Stratigraphy. *Geophysical Prospecting,* 37, 531-551.
DE MOUSTIER, C. & ALEXANDROU, D. 1991. Angular dependence of 12-kHz seafloor acoustic backscatter. *The Journal of the Acoustical Society of America,* 90, 522-531.
DEGROAT, R. D., DOWLING, E. M. & LINEBARGER, D. A. 1993. The constrained MUSIC problem. *Signal Processing, IEEE Transactions on,* 41, 1445-1449.
DICKIN, F. & WANG, M. 1996. Electrical resistance tomography for process applications. *Measurement Science and Technology,* 7, 247.
DOBSON, M. C., ULABY, F. T., HALLIKAINEN, M. T.*, et al.* 1985. Microwave Dielectric Behavior of Wet Soil-Part II: Dielectric Mixing Models. *Geoscience and Remote Sensing, IEEE Transactions on,* GE-23, 35-46.
DUPRAZ, J. 1986. *Probability, signals, noise,* London, North Oxford Academic.
EARL, S. J. 1998. *Estimation of subsurface electrical resistivity values in 3D.* PhD, University of Bristol.
EBIHARA, S. & HASHIMOTO, Y. 2007. MoM Analysis of Dipole Antennas in Crosshole Borehole Radar and Field Experiments. *Geoscience and Remote Sensing, IEEE Transactions on,* 45, 2435-2450.
EBIHARA, S. & SATO, M. Application of an optical electric field sensor array for direction of arrival estimation in a borehole. Geoscience and Remote Sensing Symposium, 2001. IGARSS '01. IEEE 2001 International, 2001 2001. 1530-1532 vol.3.
EDWARDS, T. C. 1981. *Foundations for microstrip circuit design,* Chichester, Wiley.
EL KORSO, M. N. & PESAVENTO, M. Performance analysis for near field source localization. Sensor Array and Multichannel Signal Processing Workshop (SAM), 2012 IEEE 7th, 17-20 June 2012 2012. 197-200.
ELLIOTT, R. S. 1995. *Electromagnetics : history, theory and applications,* Oxford; New York, Oxford University Press ; IEEE.
EREZ, N. A. & SAMUEL, T. A. 2002. State-Of-The-Art-Review Of No-Dig Technologies for New Installations. *Pipelines 2002.* American Society of Civil Engineers.
FLANAGAN, B. P. & BELL, K. L. 2001. Array self-calibration with large sensor position errors. *Signal Processing,* 81, 2201-2214.
FOO, K. Y., ATKINS, P. R., THOMAS, A. M.*, et al.* Capacitive-Coupled Electric-Field Sensing For Urban Sub-Surface Mapping: Motivations and Practical Challenges. First Internation Conference on Frontiers in Shallow Subsurface Technology, 2010 Delft, Netherlands. 1-5.

FRANZLUEBBERS, A. J. 2002. Water infiltration and soil structure related to organic matter and its stratification with depth. *Soil and Tillage Research,* 66, 197-205.
FRASER-SMITH, A. C. & BOWEN, M. M. 1992. The natural background levels of 50/60 Hz radio noise. *Electromagnetic Compatibility, IEEE Transactions on,* 34, 330-337.
FRENCH, H. & BINLEY, A. 2004. Snowmelt infiltration: monitoring temporal and spatial variability using time-lapse electrical resistivity. *Journal of Hydrology,* 297, 174-186.
FRIEDMAN, S. P. 2005. Soil properties influencing apparent electrical conductivity: a review. *Computers and Electronics in Agriculture,* 46, 45-70.
FRIEL, R. & OR, D. 1999. Frequency analysis of time-domain reflectometry (TDR) with application to dielectric spectroscopy of soil constituents. *Geophysics,* 64, 707-718.
FUCHS, H. V. & RIEHLE, R. 1991. Ten years of experience with leak detection by acoustic signal analysis. *Applied Acoustics,* 33, 1-19.
GARNETT, A. 1984. How useful are today's buried pipe and cable locators? *Wiring Installations and Supplies,* 1984, 24-26.
GETHING, P. J. D. 1978. *Radio direction-finding, and the resolution of multicomponent wave-fields,* Stevenage, Peregrinus [for] the Institution of Electrical Engineeers.
GIESE, K. & TIEMANN, R. 1975. Determination of the complex permittivity from thin-sample time domain reflectometry improved analysis of the step response waveform. *Advances in Molecular Relaxation Processes,* 7, 45-59.
GILCHRIST, A. & ALLOUCHE, E. N. 2005. Quantification of social costs associated with construction projects: state-of-the-art review. *Tunnelling and Underground Space Technology,* 20, 89-104.
GODARA, L. C. 1997. Application of antenna arrays to mobile communications. II. Beam-forming and direction-of-arrival considerations. *Proceedings of the IEEE,* 85, 1195-1245.
GOODWIN, P. 2005. Utilities' Street Works and The Cost of Traffic Congestion. University of West of England.
GOOGLE EARTH. 2013a. *Blagdon Reservoir, $51^0$20'14.03" N $2^0$42'49.65" W elevation: 40m* [Online]. Available: earth.google.com [Accessed 19 August 2013].
GOOGLE EARTH. 2013b. *University of Birmingham, $52^0$27'13.46" N $1^0$55'19.96" W elevation: 130m* [Online]. Available: earth.google.com [Accessed 10 August 2013].
GORRITI, A. G. & SLOB, E. C. 2005a. Comparison of the Different Reconstruction Techniques of Permittivity From S-Parameters. *Geoscience and Remote Sensing, IEEE Transactions on,* 43, 2051-2057.
GORRITI, A. G. & SLOB, E. C. 2005b. A new tool for accurate S-parameters measurements and permittivity reconstruction. *Geoscience and Remote Sensing, IEEE Transactions on,* 43, 1727-1735.
GRAY, D. M. 1973. *Handbook on the principles of hydrology : with special emphasis directed to Canadian conditions in the discussions, applications, and presentation of data,* Port Washington, N.Y., Water Information Center.
GRAY, R. M. 1990. Quantization noise spectra. *Information Theory, IEEE Transactions on,* 36, 1220-1244.
GRCEV, L. & GRCEVA, S. 2009. Comparison Between Exact and Quasi-Static Methods for HF Analysis of Horizontal Buried Wires. *Electromagnetic Compatibility, IEEE Transactions on,* 51, 1051-1054.
GREAT BRITAIN 1996. Pipelines Safety Regulations. London: The National Archives.
GROSICKI, E., ABED-MERAIM, K. & HUA, Y. 2005. A weighted linear prediction method for near-field source localization. *Signal Processing, IEEE Transactions on,* 53, 3651-3660.
HALL, P. S. & VETTERLEIN, S. J. 1990. Review of radio frequency beamforming techniques for scanned and multiple beam antennas. *Microwaves, Antennas and Propagation, IEE Proceedings H,* 137, 293-303.
HALLIKAINEN, M. T., ULABY, F. T., DOBSON, M. C., *et al.* 1985. Microwave Dielectric Behavior of Wet Soil-Part 1: Empirical Models and Experimental Observations. *Geoscience and Remote Sensing, IEEE Transactions on,* GE-23, 25-34.
HANKS, R. J., RITCHIE, J. T., AMERICAN SOCIETY OF, A., *et al.* 1991. *Modeling plant and soil systems,* Madison, Wis, American Society of Agronomy, Crop Science Society of America, Soil Science Society of America.
HARRINGTON, R. 1990. Origin and development of the method of moments for field computation. *Antennas and Propagation Magazine, IEEE,* 32, 31-35.
HARRINGTON, R. F. 1961. *Time-harmonic electromagnetic fields,* New York, McGraw-Hill.
HARRINGTON, R. F. 1987. The Method of Moments in Electromagnetics. *Journal of Electromagnetic Waves and Applications,* 1, 181-200.
HARRINGTON, R. F. 1993. *Field computation by moment methods,* Piscataway, NJ, IEEE Press ; Oxford : Oxford University Press.
HARRIS, F. J. 1978. On the use of windows for harmonic analysis with the discrete Fourier transform. *Proceedings of the IEEE,* 66, 51-83.

HARRIS, N. D., SUGGETT, A. J., BARBER, D. C., *et al.* 1987. Applications of applied potential tomography (APT) in respiratory medicine. *Clinical Physics and Physiological Measurement,* 8, 155.
HASAR, U. C. 2008a. A Fast and Accurate Amplitude-Only Transmission-Reflection Method for Complex Permittivity Determination of Lossy Materials. *Microwave Theory and Techniques, IEEE Transactions on,* 56, 2129-2135.
HASAR, U. C. 2008b. A New Calibration-Independent Method for Complex Permittivity Extraction of Solid Dielectric Materials. *Microwave and Wireless Components Letters, IEEE,* 18, 788-790.
HAYKIN, S. S., JUSTICE, J. H., OWSLEY, N. L., *et al.* 1985. *Array signal processing,* Englewood Cliffs, N.J. ; London, Prentice-Hall.
HEIMOVAARA, T. J. 1994. Frequency domain analysis of time domain reflectometry waveforms: 1. Measurement of the complex dielectric permittivity of soils. *Water Resour. Res.,* 30, 189-199.
HEIMOVAARA, T. J., BOUTEN, W. & VERSTRATEN, J. M. 1994. Frequency domain analysis of time domain reflectometry waveforms: 2. A four-component complex dielectric mixing model for soils. *Water Resources Research,* 30, 201-209.
HEIMOVAARA, T. J., DE WINTER, E. J. G., VAN LOON, W. K. P., *et al.* 1996. Frequency-Dependent Dielectric Permittivity from 0 to 1 GHz: Time Domain Reflectometry Measurements Compared with Frequency Domain Network Analyzer Measurements. *Water Resour. Res.,* 32, 3603-3610.
HEPPNER, J. P., BIELECKI, E. A., AGGSON, T. L., *et al.* 1978. Instrumentation for DC and Low-Frequency Electric-Field Measurements on ISEE-A. *Geoscience Electronics, IEEE Transactions on,* 16, 253-257.
HIEBEL, M. 2008. Vector Network Analyzer Calibration: The Basics. Available: http://cas.web.cern.ch/cas/Denmark-2010/Caspers/RS0908-22VNAWhitePaperV2%20on%20VNA%20calibration%20methods%20CAS%202009%20and%20CAS2010.pdf [Accessed January 2014].
HOBBS, B. A. 1999. Investigating brownfield sites with electrical resistivity. *Physics Education,* 34, 192.
HUANG, Y. 2001. Design, calibration and data interpretation for a one-port large coaxial dielectric measurement cell. *Measurement Science and Technology,* 12, 111.
HUISMAN, J. A., HUBBARD, S. S., REDMAN, J. D., *et al.* 2003. Measuring soil water content with ground penetrating radar: A review. *Vadose Zone Journal,* 2, 476.
HUISMAN, J. A., SNEPVANGERS, J. J. J. C., BOUTEN, W., *et al.* 2002. Mapping spatial variation in surface soil water content: comparison of ground-penetrating radar and time domain reflectometry. *Journal of Hydrology,* 269, 194-207.
HUNT, D. V. L., NASH, D. & ROGERS, C. D. F. 2012. Sustainable utility placement via Multi-Utility Tunnels. *Tunnelling and Underground Space Technology*.
IMAI, T., SAKAYAMA, T. & KANEMORI, T. 1987. Use of ground-probing radar and resistivity surveys for archaeological investigations. *Geophysics,* 52, 137-150.
JACKSON, J. D. 1975. *Classical electrodynamics,* New York; Chichester, Wiley.
JOHNSON, D. H. 1982. The application of spectral estimation methods to bearing estimation problems. *Proceedings of the IEEE,* 70, 1018-1028.
JOHNSON, D. H. & DUDGEON, D. E. 1993. *Array signal processing : concepts and techniques,* Englewood Cliffs, NJ; London, P T R Prentice Hall ; Prentice-Hall International (UK).
JOHNSON, R. L. & MINER, G. E. 1986. Comparison of Superresolution Algorithms for Radio Direction Finding. *Aerospace and Electronic Systems, IEEE Transactions on,* AES-22, 432-442.
JONES, S. B., MACE, R. W. & OR, D. 2005. A Time Domain Reflectometry Coaxial Cell for Manipulation and Monitoring of Water Content and Electrical Conductivity in Variably Saturated Porous Media. *Vadose Zone J.,* 4, 977-982.
JONES, S. B., WRAITH, J. M. & OR, D. 2002. Time domain reflectometry measurement principles and applications. *Hydrological Processes,* 16, 141-153.
JUNG, Y. & SINHA, S. 2007. Evaluation of Trenchless Technology Methods for Municipal Infrastructure System. *Journal of Infrastructure Systems,* 13, 144-156.
KANDA, M. 1993. Standard probes for electromagnetic field measurements. *Antennas and Propagation, IEEE Transactions on,* 41, 1349-1364.
KANTZ, J., WALDMANN, J. & LANDSTORFER, F. M. 2005. Measuring system for time-variant impedances. *Instrumentation and Measurement, IEEE Transactions on,* 54, 258-263.
KAVIAN, M., SLOB, E. C. & MULDER, W. A. Low-Frequency Electrical Properties of Homogeneous and Heterogeneous Sand Samples. Frontiers in Shallow Subsurface Technology, 20 Jan 2010 2010 Delft, Netherlands. 224.
KEAREY, P., BROOKS, M. & HILL, I. 2002. *An introduction to geophysical exploration,* Oxford, Blackwell Science.

KING, R. W. P., OWENS, M. & WU, T. T. 1992. *Lateral electromagnetic waves : theory and applications to communications, geophysical exploration, and remote sensing*, Springer.
KING, R. W. P. & SANDLER, S. S. 1994. The electromagnetic field of a vertical electric dipole in the presence of a three-layered region. *Radio Sci.,* 29, 97-113.
KING, R. W. P. & SANDLER, S. S. 1998. Reply. *Radio Sci.,* 33, 255-256.
KING, R. W. P. & SMITH, G. S. 1981. *Antennas in matter : fundamentals, theory, and applications,* Cambridge, Mass.; London, MIT.
KIRKWOOD, J. G. 1939. The Dielectric Polarization of Polar Liquids. *The Journal of Chemical Physics,* 7, 911-919.
KLEIN, K. & SANTAMARINA, J. C. 1997. Methods for Broad-Band Dielectric Permittivity Measurements (Soil-Water Mixtures, 5Hz to 1.3GHz). *Geotechnical Testing Journal,* 20, 11.
KORMAN, M. S. & SABATIER, J. M. 2004. Nonlinear acoustic techniques for landmine detection. *The Journal of the Acoustical Society of America,* 116, 3354-3369.
KRAFT, C. 1987. Constitutive parameter measurements of fluids and soil between 500 kHz and 5 MHz using a transmission line technique. *Journal of Geophysical Research: Solid Earth,* 92, 10650-10656.
KRAUS, J. D. 1988. *Antennas,* New York ; London, McGraw-Hill.
KRAUS, J. D., FLEISCH, D. A. & RUSS, S. H. 1999. *Electromagnetics : with applications,* Boston, Mass. ; London, WCB/McGraw-Hill.
KREYSZIG, E., KREYSZIG, H. & NORMINTON, E. J. 1999. *Advanced engineering mathematics,* New York ; Chichester, Wiley.
KU, H. H. 1969. Notes on the use of propagation of error formulas. *Journal of Research of the National Bureau of Standards. Section C: Engineering and Instrumentation,* 70C.
KURAS, O., BEAMISH, D., MELDRUM, P. I.*, et al.* 2006. Fundamentals of the capacitive resistivity technique. *Geophysics,* 71, G135-G152.
LAGARIAS, J., REEDS, J., WRIGHT, M.*, et al.* 1998. Convergence Properties of the Nelder--Mead Simplex Method in Low Dimensions. *SIAM Journal on Optimization,* 9, 112-147.
LAMBOT, S., WEIHERMÜLLER, L., HUISMAN, J. A.*, et al.* 2006. Analysis of air-launched ground-penetrating radar techniques to measure the soil surface water content. *Water Resour. Res.,* 42, W11403.
LANZEROTTI, L. J., MACLENNAN, C. G. & FRASERSMITH, A. C. 1990. Background Magnetic Spectra - Approximately 10(-5) to Approximately 10(5) Hz. *Geophysical Research Letters,* 17, 1593-1596.
LECKEBUSCH, J. 2003. Ground-penetrating radar: a modern three-dimensional prospection method. *Archaeological Prospection,* 10, 213-240.
LECKEBUSCH, J. & PEIKERT, R. 2001. Investigating the true resolution and three-dimensional capabilities of ground-penetrating radar data in archaeological surveys: measurements in a sand box. *Archaeological Prospection,* 8, 29-40.
LEE, R. 2002. Soil searching. *IEE Review,* 48, 37-41.
LEICA-GEOSYSTEMS. 2013. Leica Nova MS50 Datasheet. Available: http://www.leica-geosystems.co.uk/en/Leica-Nova-MS50_103592.htm [Accessed 30 August 2013].
LESMES, D. P. & MORGAN, F. D. 2001. Dielectric spectroscopy of sedimentary rocks. *Journal of Geophysical Research: Solid Earth,* 106, 13329-13346.
LEVITSKAYA, T. M. & STERNBERG, B. K. 1996a. Polarization processes in rocks 1. Complex Dielectric Permittivity method. *Radio Sci.,* 31, 755-779.
LEVITSKAYA, T. M. & STERNBERG, B. K. 1996b. Polarization processes in rocks 2. Complex Dielectric Permittivity method. *Radio Sci.,* 31, 781-802.
LI, K. 2009. *Electromagnetic fields in stratified media,* Berlin; Hangzhou, Springer Verlag; Zhejiang University Press.
LIU, L. & LI, K. 2007. Radiation From a Vertical Electric Dipole in the Presence of a Three-Layered Region. *Antennas and Propagation, IEEE Transactions on,* 55, 3469-3475.
LIU, L., LI, K. & PAN, W. Y. 2008. Electromagnetic field from a vertical electric dipole in a four-layered region. *Progress In Electromagnetics Research,* 8, 213-241.
LOGSDON, S. D. 2005. Soil dielectric spectra from vector network analyzer data. *Soil Science Society of America Journal,* 69, 983.
LOGSDON, S. D. & LAIRD, D. A. 2002. Dielectric spectra of bound water in hydrated Ca-smectite. *Journal of Non-Crystalline Solids,* 305, 243-246.
LOWE, M. J. S., ALLEYNE, D. N. & CAWLEY, P. 1998. Defect detection in pipes using guided waves. *Ultrasonics,* 36, 147-154.
LU, Y. L., WANG, Y. L., XU, Y. H.*, et al.* 2009. Electromagnetic field of a horizontal electric dipole buried in a four-layered region. *Progress In Electromagnetics Research,* 16, 247-275.

MAHONY, J. D. 1988. Static fringing capacitance of a dielectric loaded coaxial termination. *Physical Science, Measurement and Instrumentation, Management and Education - Reviews, IEE Proceedings A,* 135, 448-450.
MALONEY, J. G., SMITH, G. S. & SCOTT, W. R. 1990. Accurate computation of the radiation from simple antennas using the finite-difference time-domain method. *Antennas and Propagation, IEEE Transactions on,* 38, 1059-1068.
MANACORDA, G., MINIATI, M., BRACCIALI, S.*, et al.* Development of a bore-head GPR for Horizontal Directional Drilling (HDD) equipment. Ground Penetrating Radar (GPR), 2010 13th International Conference on, 21-25 June 2010 2010. 1-6.
MAROUBY, E., AUBOURG, M. & GUILLON, P. 1990. Application of the finite element method to the design of transitions between coaxial lines. *Microwaves, Antennas and Propagation, IEE Proceedings H,* 137, 219-225.
MATHEWS, J. H. 1992. *Numerical methods for mathematics, science and engineering,* London, Prentice Hall International.
MCDONOUGH, R. N. & WHALEN, A. D. 1995. *Detection of signals in noise,* San Diego, Academic Press.
MCMAHON, W., BURTWELL, M. H. & EVANS, M. 2005. Minimising Street Works Disruption: The Real Costs of Street Works to the Utility Industry and Society. London, UK: UK Water Industry Research.
MEIN, R. G. & LARSON, C. L. 1973. Modeling infiltration during a steady rain. *Water Resources Research,* 9, 384-394.
MERRIAM-WEBSTER. 2013a. Noise. Available: http://www.merriam-webster.com/dictionary/noise [Accessed 20 August 2013].
MERRIAM-WEBSTER. 2013b. Permittivity. Available: http://www.merriam-webster.com/dictionary/permittivity [Accessed June 2013].
METHERALL, P., BARBER, D. C., SMALLWOOD, R. H.*, et al.* 1996. Three-dimensional electrical impedance tomography. *Nature,* 380, 509-512.
METJE, N., ATKINS, P. R., BRENNAN, M. J.*, et al.* 2007. Mapping the Underworld – State-of-the-art review. *Tunnelling and Underground Space Technology,* 22, 568-586.
METJE, N., CHAPMAN, D. N., ROGERS, C. D. F.*, et al.* 2011. Seeing through the Ground: The Potential of Gravity Gradient as a Complementary Technology. *Advances in Civil Engineering,* 2011, 9.
MILLER, D. E. & GARDNER, W. H. 1962. Water Infiltration into Stratified Soil. *Soil Science Society of America Journal,* 26, 115-119.
MINET, J., LAMBOT, S., SLOB, E. C.*, et al.* 2010. Soil Surface Water Content Estimation by Full-Waveform GPR Signal Inversion in the Presence of Thin Layers. *Geoscience and Remote Sensing, IEEE Transactions on,* 48, 1138-1150.
MISAKIAN, M. ELF electric and magnetic field measurement methods. Electromagnetic Compatibility, 1993. Symposium Record., 1993 IEEE International Symposium on, 9-13 Aug 1993 1993. 150-155.
MOLCHANOV, O. A., HAYAKAWA, M. & RAFALSKY, V. A. 1995. Penetration characteristics of electromagnetic emissions from an underground seismic source into the atmosphere, ionosphere, and magnetosphere. *Journal of Geophysical Research: Space Physics,* 100, 1691-1712.
MOTT, H. & BIGGS, A. 1963. Very-low-frequency propagation below the bottom of the sea. *Antennas and Propagation, IEEE Transactions on,* 11, 323-329.
MUGGLETON, J. M. & BRENNAN, M. J. 2008. The design and instrumentation of an experimental rig to investigate acoustic methods for the detection and location of underground piping systems. *Applied Acoustics,* 69, 1101-1107.
MUGGLETON, J. M., BRENNAN, M. J. & ROGERS, C. D. F. 2012. Point vibration measurements for the detection of shallow-buried objects. *Tunnelling and Underground Space Technology*.
MUR, G. & DE HOOP, A. T. 1985. A finite-element method for computing three-dimensional electromagnetic fields in inhomogeneous media. *Magnetics, IEEE Transactions on,* 21, 2188-2191.
NAJAFI, M. & KIM, K. J. 2004. Life-Cycle-Cost Comparison of Trenchless and Conventional Open-Cut Pipeline Construction Projects. *Pipeline Engineering and Construction.*
NATIONAL INSTRUMENTS. 2011. NI cDAQ-917x User Manual. Available: http://www.ni.com/pdf/manuals/372838c.pdf.
NATIONAL INSTRUMENTS. 2012. Operating Instructions and Specifications NI 9229/9239. Available: http://www.ni.com/pdf/manuals/374184j.pdf.
NEAL, A. 2004. Ground-penetrating radar and its use in sedimentology: principles, problems and progress. *Earth-Science Reviews,* 66, 261-330.
NELSON, S. O., STETSON, L. E. & SCHLAPHOFF, C. W. 1974. A General Computer Program for Precise Calculation of Dielectric Properties from Short-Circuited Waveguide Measurements. *Instrumentation and Measurement, IEEE Transactions on,* 23, 455-460.
NEY, M. M. 1985. Method of Moments as Applied to Electromagnetic Problems. *Microwave Theory and Techniques, IEEE Transactions on,* 33, 972-980.

NG, A. P. C. 1995. Direction-of-arrival estimates in the presence of wavelength, gain, and phase errors. *Signal Processing, IEEE Transactions on,* 43, 225-232.
NICOLSON, A. M. & ROSS, G. F. 1970. Measurement of the Intrinsic Properties of Materials by Time-Domain Techniques. *Instrumentation and Measurement, IEEE Transactions on,* 19, 377-382.
NORGREN, M. & HE, S. 1996. An optimization approach to the frequency-domain inverse problem for a nonuniform LCRG transmission line. *Microwave Theory and Techniques, IEEE Transactions on,* 44, 1503-1507.
OBER-SUNDERMEIER, A. & ZACKOR, H. Prediction of congestion due to road works on freeways. Intelligent Transportation Systems, 2001. Proceedings. 2001 IEEE, 2001 2001. 240-244.
OGUS, A. 1999. Nudging and rectifying: the use of fiscal instruments for regulatory purposes*. *Legal Studies,* 19, 245-266.
OH, M., KIM, Y. & PARK, J. 2007. Factors affecting the complex permittivity spectrum of soil at a low frequency range of 1 kHz–10 MHz. *Environmental Geology,* 51, 821-833.
OLDENBORGER, G. A., ROUTH, P. S. & KNOLL, M. D. 2005. Sensitivity of electrical resistivity tomography data to electrode position errors. *Geophysical Journal International,* 163, 1-9.
OPPENHEIM, A. V. & SCHAFER, R. W. 1989. *Discrete-time signal processing,* Englewood Cliffs, N.J. ; London, Prentice Hall ; Prentice-Hall International (UK).
OR, D. & JONES, S. B. Time domain reflectometry (TDR) applications in Earth sciences. Antennas and Propagation Society International Symposium, 2002. IEEE, 2002 2002. 324-327 vol.2.
OR, D. & WRAITH, J. M. 1999. Temperature effects on soil bulk dielectric permittivity measured by time domain reflectometry: A physical model. *Water Resour. Res.,* 35, 371-383.
PADUAN, J. D., KIM, K. C., COOK, M. S., *et al.* 2006. Calibration and Validation of Direction-Finding High-Frequency Radar Ocean Surface Current Observations. *Oceanic Engineering, IEEE Journal of,* 31, 862-875.
PALIOURAS, J. D. & MEADOWS, D. S. 1990. *Complex variables for scientists and engineers,* New York, London, Macmillan Pub. Co., Collier Macmillan.
PAUL, C. R. & NASAR, S. A. 1987. *Introduction to electromagnetic fields,* New York, McGraw-Hill.
PENNOCK, S. R. & REDFERN, M. A. Ultra Wideband Antennas for In-Pipe Ground Penetrating Radar. Antennas and Propagation, 2007. EuCAP 2007. The Second European Conference on, 11-16 Nov. 2007 2007. 1-5.
PEPLINSKI, N. R., ULABY, F. T. & DOBSON, M. C. 1995. Dielectric properties of soils in the 0.3-1.3-GHz range. *Geoscience and Remote Sensing, IEEE Transactions on,* 33, 803-807.
PETHIG, R. 1984. Dielectric Properties of Biological Materials: Biophysical and Medical Applications. *Electrical Insulation, IEEE Transactions on,* EI-19, 453-474.
PING, W., LEWIN, P., GODDARD, K., *et al.* Design and testing of an induction coil for measuring the magnetic fields of underground power cables. Electrical Insulation (ISEI), Conference Record of the 2010 IEEE International Symposium on, 6-9 June 2010 2010. 1-5.
POOR, H. V. 1994. *An introduction to signal detection and estimation,* New York, Springer-Verlag.
POZAR, D. M. 1990. *Microwave engineering,* Reading, Mass., Addison-Wesley.
PRESS, W. H., VETTERLING, W. T. & NUMERICAL RECIPES, S. 1992. *Numerical recipes in C : the art of scientific computing,* Cambridge, Cambridge University Press.
QUAZI, A. 1981. An overview on the time delay estimate in active and passive systems for target localization. *Acoustics, Speech and Signal Processing, IEEE Transactions on,* 29, 527-533.
READ, G. F. 2004. *Sewers: replacement and new construction,* Oxford, UK ; Burlington, MA, Elsevier Butterworth-Heinemann.
ROBERTS, S. & VON HIPPEL, A. 1946. A New Method for Measuring Dielectric Constant and Loss in the Range of Centimeter Waves. *Journal of Applied Physics,* 17, 610-616.
ROBINS, W. P. 1983. *Phase noise in signal sources : theory and applications,* London, Peregrinus, on behalf of the Institution of Electrical Engineers.
ROBINSON, D. A., GARDNER, C. M. K. & COOPER, J. D. 1999. Measurement of relative permittivity in sandy soils using TDR, capacitance and theta probes: comparison, including the effects of bulk soil electrical conductivity. *Journal of Hydrology,* 223, 198-211.
ROBINSON, D. A., JONES, S. B., WRAITH, J. M., *et al.* 2003. A Review of Advances in Dielectric and Electrical Conductivity Measurement in Soils Using Time Domain Reflectometry. *Vadose Zone Journal,* 2, 444-475.
ROBINSON, D. A., SCHAAP, M. G., OR, D., *et al.* 2005. On the effective measurement frequency of time domain reflectometry in dispersive and nonconductive dielectric materials. *Water Resour. Res.,* 41, W02007.
ROYAL, A. C. D., ATKINS, P. R., BRENNAN, M. J., *et al.* 2011. Site Assessment of Multiple-Sensor Approaches for Buried Utility Detection. *International Journal of Geophysics,* 2011.
ROYAL, A. C. D., RIGGALL, T. J. & CHAPMAN, D. N. 2010. Analysis of steering in horizontal directional drilling installations using down-hole motors. *Tunnelling and Underground Space Technology,* 25, 754-765.

RUBIN, J. & STEINHARDT, R. 1963. Soil Water Relations During Rain Infiltration: I. Theory1, 2. *Soil Science Society of America Journal,* 27, 246-251.
ŞAHIN, A. & MILLER, E. L. 2001. Object detection using high resolution near-field array processing. *Geoscience and Remote Sensing, IEEE Transactions on,* 39, 136-141.
SAMOUËLIAN, A., COUSIN, I., TABBAGH, A.*, et al.* 2005. Electrical resistivity survey in soil science: a review. *Soil and Tillage Research,* 83, 173-193.
SANTAMARINA, J. C., KLEIN, K. A. & FAM, M. A. 2001. *Soils and waves,* Chichester, Wiley.
SCHNEIDER, R., FERRARI, V., MATARRESE, S.*, et al.* 2001. Low-frequency gravitational waves from cosmological compact binaries. *Monthly Notices of the Royal Astronomical Society,* 324, 797-810.
SELIGSON, C. D. 1970. Comments on "High-resolution frequency-wavenumber spectrum analysis". *Proceedings of the IEEE,* 58, 947-949.
SHANG, J. Q., ROWE, R. K., UMANA, J. A.*, et al.* 1999. A Complex Permittivity Measurement System for Undisturbed/Compacted Soils. *Geotechnical Testing Journal,* 22, 10.
SHENGLI, Z. & WILLETT, P. 2007. Submarine Location Estimation Via a Network of Detection-Only Sensors. *Signal Processing, IEEE Transactions on,* 55, 3104-3115.
SHEPARD, E. R. 1934. *Electric Measuring Device*. USA patent application.
SHIMIZU, K., ENDO, H. & MATSUMOTO, G. 1989. Fundamental study on measurement of ELF electric field at biological body surfaces. *Instrumentation and Measurement, IEEE Transactions on,* 38, 779-784.
SIXIN, L., MOTOYUKI, S. & KAZUNORI, T. 2004. Application of borehole radar for subsurface physical measurement. *Journal of Geophysics and Engineering,* 1, 221.
SKOMAL, E. N. 1978. *Man-made radio noise,* New York ; London, Van Nostrand Reinhold.
SMITH-ROSE, R. L. 1934. Electrical Measurements on Soil with Alternating Currents. *J. Inst. Electr. Engineers,* 75.
SMITH, S. W. 2003. *Digital signal processing : a practical guide for engineers and scientists,* Amsterdam ; Boston, Newnes.
SOMLO, P. I. 1967. The Computation of Coaxial Line Step Capacitances. *Microwave Theory and Techniques, IEEE Transactions on,* 15, 48-53.
SRINATH, H. & REDDY, V. U. 1991. Analysis of Music Algorithm with Sensor Gain and Phase Perturbations. *Signal Processing,* 23, 245-256.
STUCHLY, M. A. & STUCHLY, S. S. 1980. Coaxial Line Reflection Methods for Measuring Dielectric Properties of Biological Substances at Radio and Microwave Frequencies-A Review. *Instrumentation and Measurement, IEEE Transactions on,* 29, 176-183.
SURKOV, V. V. & HAYAKAWA, M. 2007. ULF electromagnetic noise due to random variations of background atmospheric current and conductivity. *J. Geophys. Res.,* 112, D11116.
TABBAGH, A., HESSE, A. & GRARD, R. 1993. Determination Of Electrical Properties Of The Ground At Shallow Depth With An Electrostatic Quadrupole: Field Trials On Archaeological Sites. *Geophysical Prospecting,* 41, 579-597.
TAFLOVE, A. 1980. Application of the Finite-Difference Time-Domain Method to Sinusoidal Steady-State Electromagnetic-Penetration Problems. *Electromagnetic Compatibility, IEEE Transactions on,* EMC-22, 191-202.
THOMAS, A. M. 2010. *Measurement of Electromagnetic Signal Velocities in Saturated Fine-Grained Soils.* PhD, University of Birmingham.
THOMAS, A. M., CHAPMAN, D. N., ROGERS, C. D. F.*, et al.* 2008. Broadband Apparent Permittivity Measurement in Dispersive Soils Using Quarter-Wavelength Analysis. *Soil Science Society of America Journal,* 72, 1401-1409.
TILLARD, S. 1994. Radar experiments in isotropic and anisotropic geological formations (granite and schists)1. *Geophysical Prospecting,* 42, 615-636.
TOPP, G. C. 2003. State of the art of measuring soil water content. *Hydrological Processes,* 17, 2993-2996.
TOPP, G. C. & DAVIS, J. L. 1985. Measurement of Soil Water Content using Time-domain Reflectrometry (TDR): A Field Evaluation. *Soil Science Society of America Journal,* 49, 19-24.
TOPP, G. C., DAVIS, J. L. & ANNAN, A. P. 1980. Electromagnetic Determination of Soil Water Content: Measurements in Coaxial Transmission Lines. *Water Resources Research,* 16, 574-582.
U.S. DEPARTMENT OF AGRICULTURE. 2013. National Soil Survey Handbook, title 430-VI. Available: http://soils.usda.gov/technical/handbook/ [Accessed July 2013].
VAN DAM, R. L., BORCHERS, B. & HENDRICKX, J. M. Methods for Prediction of Soil Dielectric Properties: A Review. Defense and Security, 2005. International Society for Optics and Photonics, 188-197.
VAN DER ZIEL, A. 1955. *Noise,* London, Chapman & Hall.
VASCO, D., PETERSON, J. & LEE, K. 1997. Ground-penetrating radar velocity tomography in heterogeneous and anisotropic media. *Geophysics,* 62, 1758-1773.

VOLLAND, H. 1995. *Handbook of atmospheric electrodynamics,* Boca Raton, CRC Press.
VOSTEEN, R. E. 1973. *High Level Non-Contacting Dynamic Voltage Follower For Voltage Measurement of Electrostatically Charged Surfaces*. USA patent application.
WAGNER, N., EMMERICH, K., BONITZ, F., *et al.* 2011. Experimental Investigations on the Frequency- and Temperature-Dependent Dielectric Material Properties of Soil. *IEEE Transactions on Geoscience and Remote Sensing,* 49, 2518-2530.
WAIT, J. R. 1953. Propagation of Radio Waves Over Stratified Ground. *Geophysics,* 18, 416-422.
WAIT, J. R. 1962. *Electromagnetic waves in stratified media*, Pergamon.
WAIT, J. R. 1989. Complex resistivity of the earth. *Progress In Electromagnetics Research,* 1.
WAIT, J. R. 1998a. The ancient and modern history of EM ground-wave propagation. *Antennas and Propagation Magazine, IEEE,* 40, 7-24.
WAIT, J. R. 1998b. Comment on "The electromagnetic field of a vertical electric dipole in the presence of a three-layered region" by Ronold W. P. King and Sheldon S. Sandler. *Radio Sci.,* 33, 251-253.
WALKER, R. Bearing accuracy and resolution bounds of high-resolution beamformers. Acoustics, Speech, and Signal Processing, IEEE International Conference on ICASSP '85., Apr 1985 1985. 1784-1787.
WEILAND, T. 1996. Time Domain Electromagnetic Field Computation With Finite Difference Methods. *International Journal of Numerical Modelling: Electronic Networks, Devices and Fields,* 9, 295-319.
WEIR, W. B. 1974. Automatic measurement of complex dielectric constant and permeability at microwave frequencies. *Proceedings of the IEEE,* 62, 33-36.
WEISS, A. J., WILLSKY, A. S. & LEVY, B. C. 1988. Eigenstructure approach for array processing with unknown intensity coefficients. *Acoustics, Speech and Signal Processing, IEEE Transactions on,* 36, 1613-1617.
WENSINK, W. A. 1993. Dielectric Properties Of Wet Soils In The Frequency Range 1-3000 MHz. *Geophysical Prospecting,* 41, 671-696.
WHINNERY, J. R., JAMIESON, H. W. & ROBBINS, T. E. 1944. Coaxial-Line Discontinuities. *Proceedings of the IRE,* 32, 695-709.
WICKENS, T. D. 2002. *Elementary signal detection theory,* New York, Oxford University Press.
WILKINSON, P. B., CHAMBERS, J. E., LELLIOTT, M., *et al.* 2008. Extreme sensitivity of crosshole electrical resistivity tomography measurements to geometric errors. *Geophysical Journal International,* 173, 49-62.
WRAITH, J. M. & OR, D. 1999. Temperature effects on soil bulk dielectric permittivity measured by time domain reflectometry: Experimental evidence and hypothesis development. *Water Resources Research,* 35, 361-369.
XU, X.-L. & BUCKLEY, K. M. 1994. Bias and variance of direction-of-arrival estimates from MUSIC, MIN-NORM, and FINE. *Signal Processing, IEEE Transactions on,* 42, 1812-1816.
XU, Y. H., REN, W., LIU, L., *et al.* 2008. Trapped surface wave and lateral wave in the presence of a four-layered region. *Progress in Electromagnetics Research-Pier,* 82, 271-285.
YORK, D. 1968. Least squares fitting of a straight line with correlated errors. *Earth and Planetary Science Letters,* 5, 320-324.
YOU, K. Y. & ABBAS, Z. 2012. Fringing Field Correction of Admittance Model for Open-Ended Coaxial Sensor. *Sensors Journal, IEEE,* 12, 1468-1469.
YOU, Z., CROSS, J., FOO, K. Y., *et al.* Disposable stepped-frequency GPR and soil measurement devices. Ground Penetrating Radar (GPR), 2010 13th International Conference on, 2010. 1-5.
ZANGWILL, A. 2013. *Modern electrodynamics,* Cambridge, Cambridge University Press.
ZHANG, H. Q., LI, K. & PAN, W. Y. 2004. The electromagnetic field of a vertical dipole on the dielectric-coated imperfect conductor. *Journal of Electromagnetic Waves and Applications,* 18, 1305-1320.
ZHANG, H. Q. & PAN, W. Y. 2002. Electromagnetic field of a vertical electric dipole on a perfect conductor coated with a dielectric layer. *Radio Science,* 37, 13-1-13-7.
ZHOU, W., BECK, B. F. & STEPHENSON, J. B. 2000. Reliability of dipole-dipole electrical resistivity tomography for defining depth to bedrock in covered karst terranes. *Environmental Geology,* 39, 760-766.